



HAL
open science

Rare Earth doped Si based frequency conversion layer for Si Solar Cell

Lucile Dumont

► **To cite this version:**

Lucile Dumont. Rare Earth doped Si based frequency conversion layer for Si Solar Cell. Materials. Normandie Université, France; Université de Caen Normandie, 2016. English. NNT : . tel-01425297

HAL Id: tel-01425297

<https://theses.hal.science/tel-01425297>

Submitted on 3 Jan 2017

HAL is a multi-disciplinary open access archive for the deposit and dissemination of scientific research documents, whether they are published or not. The documents may come from teaching and research institutions in France or abroad, or from public or private research centers.

L'archive ouverte pluridisciplinaire **HAL**, est destinée au dépôt et à la diffusion de documents scientifiques de niveau recherche, publiés ou non, émanant des établissements d'enseignement et de recherche français ou étrangers, des laboratoires publics ou privés.



Normandie Université

THESE

Pour obtenir le diplôme de doctorat

Spécialité Physique

Préparée au sein de l'Université de Caen Normandie

Rare Earth doped Si based frequency conversion layer for Si Solar Cell

Soutenue par
Lucile DUMONT

Thèse soutenue publiquement le 17/11/2016
devant le jury composé de

M. Hervé RINNERT	Professeur des Universités/Université de Lorraine- Institut Jean Lamour (Nancy)	Rapporteur
M. Nicolas BARREAU	Maitre de conférence (HDR)/Institut des Matériaux Jean Rouxel (Nantes)	Rapporteur
M. Didier STIEVENARD	Directeur de Recherche CNRS/ IEMN (Lille)	Examineur
Mme. Marzia CARRADA	Chargée de Recherche CNRS/ CEMES (Toulouse)	Examinatrice
M. Julien CARDIN	Ingénieur de Recherche(HDR)/ CIMAP (Caen)	Co-encadrant de thèse
M. Fabrice GOURBILLEAU	Directeur de Recherche CNRS/ CIMAP (Caen)	Directeur de thèse

Thèse dirigée par Fabrice GOURBILLEAU avec co-encadrement par Julien Cardin, laboratoire CIMAP

Acknowledgement

Already three years have passed, and this stimulating enterprise that is a thesis is close to an end.

I am grateful to the CNRS and the Basse-Normandie region that financed my thesis, to the French National Research Agency that provided support for this work through the GENESE Project (ANR-13-BSS09-0020-01), and to the Hubert Curien Partnership (PHC) that allowed a partnership with Ing-Song Yu assistant professor in the National Dong Hwa University in Taiwan.

I would like, first, to thank the Jury members, Nicolas Barreau, Hervé Rinnert, Marzia Carrada, and Didier Stievenard for agreeing to contribute their expertise to and review this work. I also thank the last two for the constructive talk we had on this work.

I express my sincere gratitude to my thesis director Fabrice Gourbilleau for his guidance and support of my research work as well as for trusting me with the presentation of this work in various conferences over the world. I extend my gratitude to Julien Cardin, my co-supervisor, for his clear and precise explanations and the time he took to discuss with me about the theoretical points of my thesis.

My sincere thanks go to Phillipe Marie for his help with the ellipsometry measurements, Xavier Portier for teaching me the basics of TEM handling and his subsequent help when I was using it, Christophe Labbé for the photoluminescence lifetime measurements he provided and explained, Cedric Frilay for teaching me the fabrication process as well as for always having time to help me, Michael Boisserie for the measurements he performed on several machines, Frank Lemarié for the TEM samples preparation, Patrick Voivenel and Stéphane Renouf for the help they provided when machines encountered technical problems, and Silvain Foubert for manufacturing needed pieces. I also thank Patrizio Benzo for his help during my first year and his contribution to this work. I extend my thanks to Christiane Malot, Delphine Hasley, and Lucie Berker that take care of the administrative part of the research and Cédric Gendreau that maintains the computer network of the laboratory. I would like to thank them all along with Christian Dufour for their acceptance, support and encouragements as well as for the very good times we spent together.

I thank also Ing-Song Yu to whom we were able to deposit our layers on industrial solar cells and that welcomed us warmly in Taiwan.

I acknowledge Marie-Paule Besland who performed XPS measurements on our samples.

I am grateful to Marzia Carrada who made TEM analyses on our samples

I thank all the PhD students, Post-docs, and trainees that shared an office with me for the constructive talks as well as for the good moments and the laughs. I speak about Christian Davesne-Aubert, Ahmed Ziani, Florian Ehre, Nicolas Chery, Jennifer Weimmerskirch-Aubatin, and Clément Guillaume. I thank them as well as Hichem Ben Ammar, Nicolas Guth, and Delphine Marie for their friendship and support.

Last but not least, I would like to thank my family: my parents, my brother as well as my grandparents for their love and support during this thesis and in life generally. I also thank Nicolas Bordes for bearing with me even during the redaction period. I thank him and his family as well as all my friends for their support and encouragements.

Lucile Dumont

Contents

List of abbreviations.....	i
Introduction.....	1
Chapter I: State of the art.....	5
I.1. Silicon solar cells.....	5
I.1.1. Background.....	5
I.1.2. History.....	7
I.1.3. Advantages and drawbacks.....	8
I.2. Efficiency limitations.....	10
I.2.1. Shockley-Queisser limit.....	10
I.2.2. Other efficiency losses.....	12
I.2.3. Exceeding the Shockley-Queisser limit.....	13
I.2.3.1. Multijunction cells.....	13
I.2.3.2. Spectrum conversion.....	14
I.3. Down-conversion principle.....	16
I.3.1. History.....	16
I.3.2. Rare earth ions in the down-conversion process.....	19
I.3.2.1. The rare earth elements.....	19
I.3.2.2. Review of the rare earth ions used for the down-conversion.....	22
I.3.3. Matrix requirements.....	23
I.3.3.1. Silicon solar cell application.....	23
I.3.3.2. The sensitizing matrix.....	24
I.4. Energy transfers.....	25
I.4.1. Matrix to rare earth ions.....	25
I.4.2. Rare earth to rare earth transfer (dipole).....	26

I.4.2.1. Energy transfer between rare earth ions	26
I.4.2.2. Down-conversion possible energy transfers	28
I.4.3. Possible energy losses	29
I.5. Conclusion	31
Bibliography	32
Chapter II: Experimental techniques	41
II.1. Layers fabrication	41
II.1.1. Deposition: Radiofrequency Reactive Magnetron Co-Sputtering	41
II.1.1.1. Principle.....	41
II.1.1.2. Experimental setup	44
II.1.2. Annealing processes.....	44
II.1.2.1. Classical Thermal Annealing	45
II.1.2.2. Rapid Thermal Annealing	46
II.2. Structural and composition characterizations.....	46
II.2.1. Fourier Transform Infrared Spectroscopy.....	46
II.2.1.1. Principle.....	46
II.2.1.2. Experimental setup	47
II.2.2. Transmission Electron Microscopy	49
II.2.2.1. High Resolution Transmission Electron Microscopy	49
II.2.2.2. Energy-Dispersive X-ray spectroscopy	51
II.2.2.3. Sample preparation.....	52
II.2.3. Rutherford Backscattering Spectroscopy.....	52
II.2.3.1. Principle.....	52
II.2.3.2. Experimental setup	53
II.2.3. X-ray Photoelectron Spectroscopy.....	54
II.2.3.1. Principle.....	54
II.2.3.2. Experimental setup	55

II.3. Optical characterizations	56
II.3.1. Ellipsometric spectroscopy	56
II.3.1.1. Experimental setup and principle	56
II.3.1.2. Spectrum modeling.....	58
II.3.2. Photoluminescence Spectroscopy	60
II.3.2.1. General principle	60
II.3.2.2. Energy resolved photoluminescence spectroscopy	60
II.3.2.3. Energy resolved photoluminescence in excitation	62
II.3.2.4. Time resolved photoluminescence	63
II.4. Solar cell characterization.....	65
II.4.1. Photoconductance lifetime	65
II.4.1.1. Principle.....	65
II.4.1.2. Experimental setup	66
II.4.2. External quantum efficiency measurement.....	66
II.4.3. I-V curves.....	68
II.5. Modeling.....	69
II.5.1. Access to optical parameters	69
II.5.2. Propagation of light emission in layered media.....	71
Bibliography.....	73
Chapter III: A study on SiN_x and SiN_x:Tb³⁺ layers	75
III.1. Introduction	75
III.2. SiN _x Matrix.....	75
III.2.1. Composition analyses	76
III.2.1.1. Preliminary results	76
III.2.1.2. Effect of the nitrogen ratio	79
III.2.1.3. Effect of the plasma pressure	80
III.2.1.4. Effect of the annealing temperature	82

III.2.2. Optical properties.....	83
III.2.2.1. Preliminary analyses	84
III.2.2.2. Experiments	86
III.2.2.4. Photoluminescence.....	92
III.2.3. Conclusion	95
III.3. Terbium-doped Matrix, $\text{SiN}_x:\text{Tb}^{3+}$	95
III.3.1. Effect of the plasma pressure and the nitrogen ratio	96
III.3.1.1. Composition analyses	96
III.3.1.2. Optical properties.....	98
III.3.2. Influence of the RF power density on the Tb target on the growth of $\text{SiN}_x:\text{Tb}^{3+}$ film.....	100
III.3.2.1. Composition analyses	100
III.3.2.3. Photoluminescence.....	100
III.3.3. Conclusion	102
III.4. Study of the energy transfer	102
III.4.1. Energy transfer from the matrix to the terbium	102
III.4.1.1. Terbium non-resonant excitation	102
III.4.1.2. Transfer mechanism.....	104
III.4.2. Comparison with a previous study	105
III.4.3. Conclusion	107
III.5. Conclusion.....	108
Bibliography.....	109

Chapter IV: A study of the down-conversion process in the $\text{SiN}_x:\text{Tb}^{3+}-\text{Yb}^{3+}$ and $\text{SiN}_x:\text{Yb}^{3+}/\text{SiN}_x:\text{Tb}^{3+}$ systems

IV.1. Introduction	111
IV.2. $\text{SiN}_x:\text{Tb}^{3+}-\text{Yb}^{3+}$ monolayer system	112
IV.2.1. Structural analyses	112
IV.2.1.1. Effect of the annealing treatment.....	112
IV.2.1.2. Effect of the terbium and ytterbium target power densities.....	114

IV.2.2. Photoluminescence	116
IV.2.2.1. Effect of the terbium target power density	117
IV.2.2.2. Effect of the ytterbium target power density	118
IV.2.3. Other optical properties	120
IV.2.4. Conclusion.....	122
IV.3. Energy transfer and efficiency	122
IV.3.1. Energy transfer from the terbium ions to the ytterbium ions	122
IV.3.2. Down-conversion system efficiency	125
IV.3.2.1. Comparison with a previous study.....	125
IV.3.2.2. Time-resolved photoluminescence and lifetime based efficiency	128
IV.3.3. Conclusion.....	129
IV.3. Multilayer system.....	130
IV.3.1. Principle.....	131
IV.3.2. Effects of the deposition parameters	131
IV.3.2.1. Terbium target power density	132
IV.3.2.2. Ytterbium target power density	133
IV.3.2.3. Terbium-doped sublayer thickness	134
IV.3.2.4. Ytterbium-doped sublayer thickness	135
IV.3.3. Composition properties	136
IV.3.3. Comparison with the monolayer system	136
IV.3.4. Conclusion.....	138
IV.4. Conclusion.....	139
Bibliography.....	140

Chapter V: Application to silicon solar cells	141
V.1. Introduction	141
V.2. Prerequisite to the deposition on silicon solar cells.....	142
V.2.1. Solar cell operating principle	142

V.2.2. Fabrication process	143
V.3. Adaptation of the fabrication parameters of our layers to the silicon solar cell system.....	145
V.3.1. 1 st round -Efficiency improvement	145
V.3.2. Deposition and annealing temperatures studies.....	148
V.3.2.1. Annealing temperature adaptation	149
V.3.2.2. Deposition temperature adaptation	150
V.3.3. Conclusion	151
V.4. Improvement of the fabrication process	152
V.4.1. Study of the annealing temperature	152
V.4.2. Conclusion	155
V.5. Conclusion.....	155
Bibliography.....	156
Conclusion and perspectives	157
Annex 1: Matrix representation and formulation	161
Annex 2: Single emitter modeling.....	165
Annex 3: List of the bonds between the Si, N, H, and O elements and their bands wavenumber in a SiO _x N _y :H material.	169

List of abbreviations

A → Absorbance

A → Activator

APTE → Addition de Photon par Transferts d'Énergie

AR → Anti-reflection

CET → Cooperative energy transfer

CTA → Classical thermal annealing

CZ → Czochralski

DC → Down-conversion

DS → Down-shifting

EDP → Electrons diffraction patterns

EDX → Energy-Dispersive X-ray spectroscopy

EQE → External quantum efficiency

ESA → Excited State Absorption

ET → Energy transfer

ETMM → Extended transfer matrix method

ETU → Energy Transfer Up-conversion

FEG → Field emission gun

FIB → Focus ion beam

FRET → Förster resonant energy transfer

FTIR → Fourier Transform Infrared Spectroscopy

GIEC → Groupe d'experts intergouvernemental sur l'évolution du climat

GSA → Ground State Absorption

HRTEM → High resolution transmission electron microscope

IQE → Internal quantum efficiency

IR → Infrared

LO → Longitudinal optical modes

ML → Multilayer

NIR → Near infrared

OPO → Optical Parametric Oscillator

PECVD → Plasma-enhanced chemical vapor deposition

PIPS → Precision ion polishing system

PL → Energy resolved photoluminescence

PLE → Energy resolved photoluminescence in excitation

PV → Photovoltaic

PVD → Physical vapor deposition

QC → Quantum cutting

QE → Quantum efficiency

R → Reflectance

RBS → Rutherford Backscattering Spectroscopy

RE → Rare earth

RF → Radio frequency

RTA → Rapid thermal annealing

S. H. G → Second Harmonic Generation

S → Sensitizer

SC → Solar cell

sccm → Standard Cubic Centimeters per Minute

SEM → Scanning Electron Microscopy

SHR → Shockley-Read-Hall

S-Q → Shockley-Queisser

STEM-EELS → Scanning Transmission Electron Microscopy- Electron Energy Loss Spectroscopy

T → Transmittance

TEM → Transmission Electron Microscopy

TMM → Transfer matrix method

TO → Transverse optical modes

UC → Up-conversion

UV → Ultraviolet

XPS → X-ray Photoelectron Spectroscopy

Introduction

The use of renewable energies (mainly solar and wind) has been increasing for the past several years as an alternative to fossil fuels. Their use has been limited by their high cost and/or still low efficiency. However, the trend is changing with lower cost and higher efficiency devices being developed. With the recently worldwide signed COP21 agreement aiming to keep the global temperature rise under 2 °C, the renewable energy sources will be even more used. Efficiency improvements have thus to be realized to meet the energy demand.

Solar energy is expected to contribute largely to the future energy supply. The commercial crystalline silicon (*c-Si*) solar cells that currently dominate the market operate with an energy conversion efficiency of at most 20 % for a price lower than 1 \$/W since 2014 while the highest efficiency achieved in laboratory is of 27.6 % which is close to the Shockley-Queisser limit. The major issue leading to such low efficiency is the spectral mismatch (> 50 %) between the solar spectrum and the solar cell material bandgap. Indeed, the AM1.5 solar spectrum includes all photons between 300 and 2500 nm (corresponding to 0.5 to 4.4 eV) while the solar cell optimally used the photons close to their material bandgap. The final converted energy represents a small part of the available energy.

The cells are transparent to the photons with an energy below their material bandgap while absorbing the photons with an energy equal or higher than the material bandgap. However, the excess energy of the photons with an energy above the bandgap is transmitted to the lattice as heat, thus increasing the cells temperature and decreasing the cell efficiency in a so-called thermalization process. This loss of energy may be minimized either by adapting the cells to the solar spectrum, by employing a stack of cells with different bandgap energies called tandem cells, or by adapting the spectrum to the cells thanks to frequency conversion films such as, down-conversion, up-conversion, or down-shifting layers. Frequency conversion processes, and particularly the down-conversion one, thanks to trivalent rare earth ions are promising ways to improve the cells efficiency while keeping a low cost.

The down-conversion process allows to absorb one ultraviolet (UV) photon and emit 2 infrared (IR) ones, thus obtaining a quantum efficiency greater than 1. By choosing the right couple of rare earth ions, the photons with an energy of at least twice of the cells bandgap may be converted in photons of the bandgap energy. Thus the cell receives an increasing number of photons (2 times in the UV range) allowing the increase of the cell efficiency while decreasing the thermalization process.

This down-conversion process has already been achieved in various host matrices doped with various couple of rare earth ions. However, these matrices were not totally compatible with the silicon solar cells process.

Our team (NIMPH team) has already studied rare earth ions doping such as Er^{3+} , Nd^{3+} , Pr^{3+} , Tb^{3+} , and Yb^{3+} in different host matrices. A previous thesis by Y-T. An, was focused on the silicon oxynitride matrix (SiO_xN_y) doped with either the $\text{Pr}^{3+}/\text{Yb}^{3+}$ or the $\text{Tb}^{3+}/\text{Yb}^{3+}$ couple for down-

conversion process. Such Si-based matrix is compatible with the silicon solar cells and thus reduces production cost, but the oxygen it contains favors the rare earth ions clustering that we wish to avoid. Thus in this work, we choose the silicon nitride (SiN_x) as a host matrix. The two rare earth ions couples then studied present energy transfers compatible with the silicon solar cells application but only the second couple has showed promising results of a promising down-conversion process occurring. Thus, this second rare earth ions couple, $\text{Tb}^{3+}:\text{Yb}^{3+}$ is chosen for our work.

The main goal of this thesis is to develop a down-conversion layer having also anti-reflective properties that may be deposited on top of industrial solar cells to increase their efficiency. Other goals are to develop Tb-doped- and Tb-Yb co-doped- layers that have a higher *PL* intensity of the Tb^{3+} and Yb^{3+} peaks respectively than the Tb-doped- and Tb-Yb co-doped- SiO_xN_y layers developed during the precedent work of Y-T An. The main challenge of this work is to optimize the deposition parameters (thus the composition and microstructure of the deposited layers) to achieve a layer with the highest Yb^{3+} *PL* peak intensity possible. For this purpose, the undoped matrix, followed by the Tb-doped layer is first studied before the Tb-Yb co-doped layer systems (monolayer and multilayer) are optimized. The optimized layers obtained are then compared to their SiO_xN_y counterparts before being deposited on industrial solar cells to determine the additional efficiency achieved through down-conversion. The energy transfer mechanisms, between the matrix and the Tb^{3+} ions and then the down-conversion process from the Tb^{3+} ions to the Yb^{3+} ones are also studied.

In the first chapter, the bibliographic study will address the place of the solar cells in the current and future global energy supplies. Various solar cell concepts are introduced as well as their advantages and drawbacks. The mains reasons of the efficiency limit of the solar are detailed and various approaches to overcome this limit are presented among which the frequency conversion (down-conversion, down-shifting, and up-conversion) processes. The choice of the matrix and rare earth ion couple used is detailed. Additionally, the various energy transfers, between the matrix and the rare earth ions, between two rare earth ions, and the possible energy loss paths are exposed.

In the second chapter, the experimental techniques used throughout this work will be detailed beginning by the fabrication process, followed by the characterization techniques, and ending by the modeling of our system. The first is composed of the deposition technique and the annealing process. The second encompasses the structural, composition, and optical characterizations as well as the characterizations specific to solar cells. The third describes the two models used to access optical properties and compare the layers transmission toward the cell efficiencies.

In the third chapter, the undoped- and Tb-doped- SiN_x layers are studied. First the composition and optical properties of the undoped layer are analyzed for various deposition parameters. This undoped layer is optimized to meet the criteria needed both for a down-conversion layer and an anti-reflective one. Second, the Tb-doped composition and optical properties are studied for various deposition parameters in order to optimize their Tb^{3+} *PL* peaks emission. The optimized layer is compared with a similar layer of $\text{SiO}_x\text{N}_y:\text{Tb}^{3+}$ obtained in the previous Y-T An thesis work. The energy transfer between the matrix and the Tb^{3+} ions is studied.

In the fourth chapter, the Tb-Yb co-doped SiN_x layer is studied. First a monolayer is developed and its composition and optical properties studied to achieve the highest Yb³⁺ PL peak emission. Then a multilayer system is devised to act as a model where the rare earth ions concentration in each sublayers is better controlled. The system is optimized and compared to the monolayer one. The optimized monolayer layer is also compared with a similar layer of SiO_xN_y:Tb³⁺-Yb³⁺ obtained in the previous thesis work. The energy transfer between the Tb³⁺ and Yb³⁺ ions is studied.

In the fifth chapter, the above mentioned optimized layers are adapted to the requirements of the silicon solar cells fabrication in an industrial process and deposited on such solar cells. Various parameters are studied to improve the efficiency of the cell but only one example is given that resume the difficulties encountered while going through the scaling from the laboratory experiment from the industrial application.

Chapter I: State of the art

In this first chapter, a brief introduction on the silicon solar cells (*SC*) overviewing their economic and historical backgrounds as well as their advantages and drawbacks will be followed by the origin of their efficiency limitations. Among the several approaches proposed to resolve those limitations, the spectral modification processes, particularly the down-conversion and down-shifting ones, attract our interest. Those processes are developed by doping a matrix with rare earth (*RE*) ions among which the energy transfer takes place. The principle of those processes is overviewed and the choice of the materials employed is explained. The various energy transfers and possible energy losses involved are then detailed.

1.1. Silicon solar cells

1.1.1. Background

The challenge of our century is to maintain the stability of energy supplies with the addition on the network of an increasing share of intermittent energy sources. In fact, the ever growing global population coupled with the raise of the global standard of living increase each year the energy consumption. The energy production has to be increased concurrently which gives rise to resources sustainability problems. Indeed, the main energy sources employed nowadays are fossil fuels that are known to have limited stocks. The current reserves may sustain the energy consumption growth for between tens and hundreds of years depending of the fossil fuel, oil being the most consumed and also the more limited. In addition, for more than twenty years scientists have been warning the world about the effect of the greenhouse gases that may induce a global warming. Nowadays, more and more people realize the need to decrease the emission of those greenhouse gases and particularly the CO₂ one which is a byproduct of our principal energy production processes.

Several ways to decarbonize the energy supply and consumption have been initiated these last years. Therefore actions are taken to save energy in both industry and domestic which entail improving the efficiency of the means of production but also of the consumption of energy. Energy saving allows for a lower growth of the energy demand or its stabilization in the future years depending of the scenarios given by the last GIEC report [1]. Renewable energies are also used to first meet this additional energy need and even substitute the fossil fuels in the long term. Thus, the worldwide investments on renewable energies represented the larger energy supply related investments [2] before the fossil fuels and the nuclear energy in 2014. Moreover, this same year, 8300 TWh of renewable energy were installed which represents almost half of the global energy supply increase. Those two axes will be reinforced following the rating by all the member states of

the COP21 goal, based on the last GIEC report [1]. The goal is to maintain an increase of global temperature below 2 °C.

However, renewable energies have to answer some requirements before being widely used. Renewable energies should have a price comparable with the ones of fossil fuels or nuclear energy to not impact the people finances. In addition the grid should remain stable even with the integration of intermittent energy sources. This point is difficult to satisfy with most of the renewable energy sources that are weather or daytime dependent. Currently the other energy sources (fossils, Nuclear, hydroelectric dam ...) have to compensate the variation of the renewable energies by decreasing or increasing their own production rapidly (*Figure I-1*). In the future, efficient alternatives (batteries or other electrical, and mechanical storage devices [3]) in addition of hydroelectric dam have to be developed to integrate the renewable energies seamlessly to the grid. The efficiency of the production should also be increased to obtain more energy using less space and material.

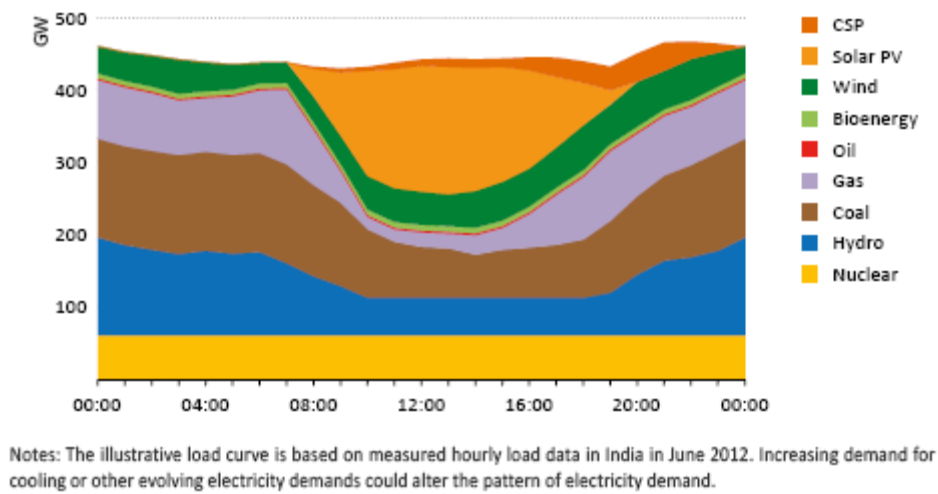


Figure I-1: Example of the impact of intermittent renewable energies (here solar) on the grid; CSP stands for Concentrating Solar Power from [2].

Several renewable energies are used and/or may be developed (*Figure I-1*). The already most employed is the hydroelectric power that is very efficient and can compensate the irregularity of other renewable energy sources. However, the increase of the number of such structures is geographically limited. Come next the wind power and the solar photovoltaic (PV) that are intermittent because dependent of the weather or daytime. The concentrating solar power is more flexible but need a large surface. The geothermal power is used in some specific places but has huge cost of geologic drilling. The bioenergy can also be a solution in region producing a lot of agricultural byproducts but the coupling to the food market of the energy market may result in some food price increase crisis. Other renewable energies are in development such as wave power, tidal power, etc.

1.1.2. History

There are two different technologies using the solar energy to produce electricity, the thermal-, and the photovoltaic- solar.

In the thermal solar technic, mirrors concentrate the light on a specific area where a heat conductive fluid passes. The concentrated light heats this fluid which is then stocked in an insulating heat tank. The heated fluid can then be used anytime allowing a certain flexibility in the electricity production. The thermal solar technic is based on the same principle than used for fossil fuels. Here the heated fluid is used to heat water thus creating steam that will then drive a thermodynamic heat machine allowing the production of electricity [4]. The expensive cost of such structure coupled with the low efficiency of the technic and the need for a large surface prevent this technic to be widely used.

In the photovoltaic solar technic, the solar illumination is used to create directly electricity thanks to the photovoltaic effect. The sunlight striking the cell causes the “release” of electrons and holes that generate an electric current. A photovoltaic panel presents several solar cells linked in parallel and serial which multiply the current and voltage obtained for one cell by the number of cells, hence increasing the total voltage and current obtained [5].

The photovoltaic effect was first mentioned by the French physicist Alexandre-Edmond Becquerel in 1839 [6,7] who found that certain materials produce small amount of electricity when exposed to light. The first practical solar cell was demonstrated in 1954 at Bell laboratories by Chapin et al. [8]. It is only in the 60s that solar cells began to be used in the space industry. From this point, the technology was really developed leading to an increase in efficiency and a decrease of the cost.

The solar cells are usually described into three historical generations [9]:

- The first generation is principally composed of bulk silicon doped with phosphorus and boron creating N- and P-type materials, respectively, to form a P-N junction. The SC exhibits an efficiency from 15 to 20 % and constitutes the major part of the cell market especially on rooftops (85 % of the cells produced). They show a good stability with a lifetime of up to 50 years and a price of up to 3.5 \$/W (*Figure I-2*).
- The second generation was aiming at decreasing the quantity of material used and thus the cost of the thin film cells was decreased to about 1.0 \$/W. Amorphous silicon, cadmium telluride (CdTe), and copper indium gallium diselenide (CIGS) solar cells are the main cells of this generation. Those cells are thinner than the first ones and even flexible. However, their efficiency is lower, varying from 10 to 15 %.
- The third generation aims at increasing the cells efficiency above their thermodynamic limit with 1 sun while keeping a low cost, in most cases below 0.50 \$/W. Several technologies are integrated in this generation and most of them are still ongoing researches. This generation is composed of a lot of technologies among which SCs using new materials but also multijunction cells that demonstrate efficiencies up to 45 % and are considered third generation even if their cost is really high (n times the price of a SC with n the number of junctions). Technologies that aim to increase indirectly the efficiency of the silicon solar cells are also a part of this generation. Those technologies have presently a lower efficiency but are very promising.

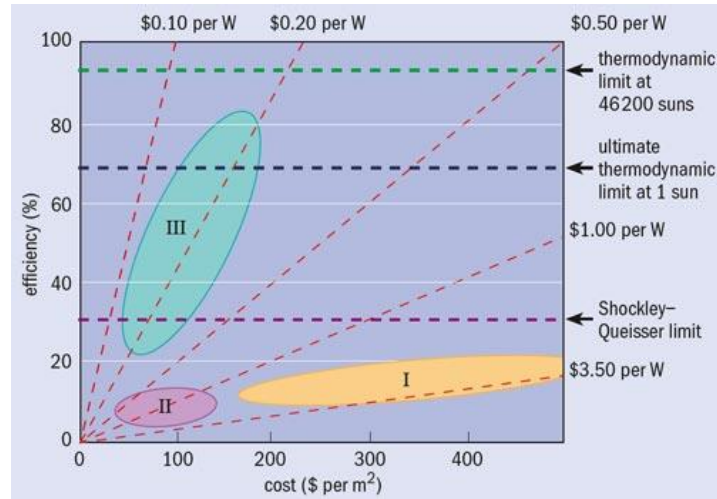


Figure I-2: Efficiency and cost projection for the first (I), second (II), and third (III) generation of photovoltaic solar cells, from [10].

I.1.3. Advantages and drawbacks

Although renewable energies are still expensive and difficult to integrate in the energy grid because of their variability, year after year they constitute a bigger part of the energy production each year. The main advantage of those sustainable energies is to be environment friendly thanks to the absence of greenhouse gases emission while producing energy [11]. However, other points, playing an important part in the fast growth of the renewable energies, may be forward [12]. The leveled cost of those energies (initial and maintenance cost over a long period of time), particularly wind and solar energies, has been steadily decreasing in the recent years [13] thanks to technologic improvements.

Photovoltaic solar cell in particular has those characteristics but presents also some additional [14]. Indeed, solar cells use an energy source that has an infinite duration at our scale (sun life) and is accessible worldwide and in a large amount. Studies show that there is enough solar irradiation available to satisfy 10 times the global energy need [15]. SCs do not require any fuel to work and are silent. They are thus not polluting. SCs are simple to install (do not require drilling, etc.) whether it is to be used in electrical plants or put on individual roofs providing accessible electricity even in the most remote locations. However, the spot on which the solar panels are placed has to be carefully analyzed to avoid shadow, soiling, etc. In addition the production can only take place during the daytime and is very dependent of the weather. The light also heats the cell leading to a temperature increase. Unfortunately, the consequence is a decrease of the cell efficiency by 0.4 %/°C [16]. The development of SCs has to be coupled with the development of energy storage facilities and an adaptation of the grid to intermittent energy sources.

Several types of solar cells have been developed, but the most employed nowadays remains the silicon ones that have the advantage of using the same technology as the microelectronics which allows mass production. Those cells also offer the advantage of being nontoxic. The main drawback

of the silicon remains its low bandgap that does not allow the optimum use of the major part of the sun photons.

There are three types of silicon solar cells [14,17]:

- The monocrystalline silicon (*c-Si*) solar cells that have the best efficiency with 27.6 % (Figure I-3) obtained in laboratory. The cells currently on the market have a maximum of about 20 % efficiency. Those cells have a quite long lifetime of up to 50 years thanks to their low rate degradation. However, their fabrication process needs very high temperature and energy which make them quite expensive compared to other Si SCs (0.75 \$/W [14]). This process also produces quite a lot of wastes such as silicon tetrachloride. The indirect bandgap of the monocrystalline silicon leads to a low optical absorption and thus a thickness of 125 μm is required to absorb 90 % of the incident light. Therefore, the cells are thick so use a lot of materials.
- The polycrystalline silicon (*p-Si*) solar cells present a lower fabrication temperature and produce fewer wastes that allow a cheaper production price (0.62 \$/W). However, their efficiency is also lower, around 15 % with a record at 20.8 %.
- The amorphous silicon (*a-Si*) solar cells are lightweight thin film solar cells that may thus be deposited on flexible substrates and have a cost of 0.69 \$/W. Those cells present a higher bandgap [18] and a higher photo absorbance that allow them to work even in low light conditions. However, their efficiency is really low (around 10 % with a record at 13.6 %) and their lifetime short, around 10 years.

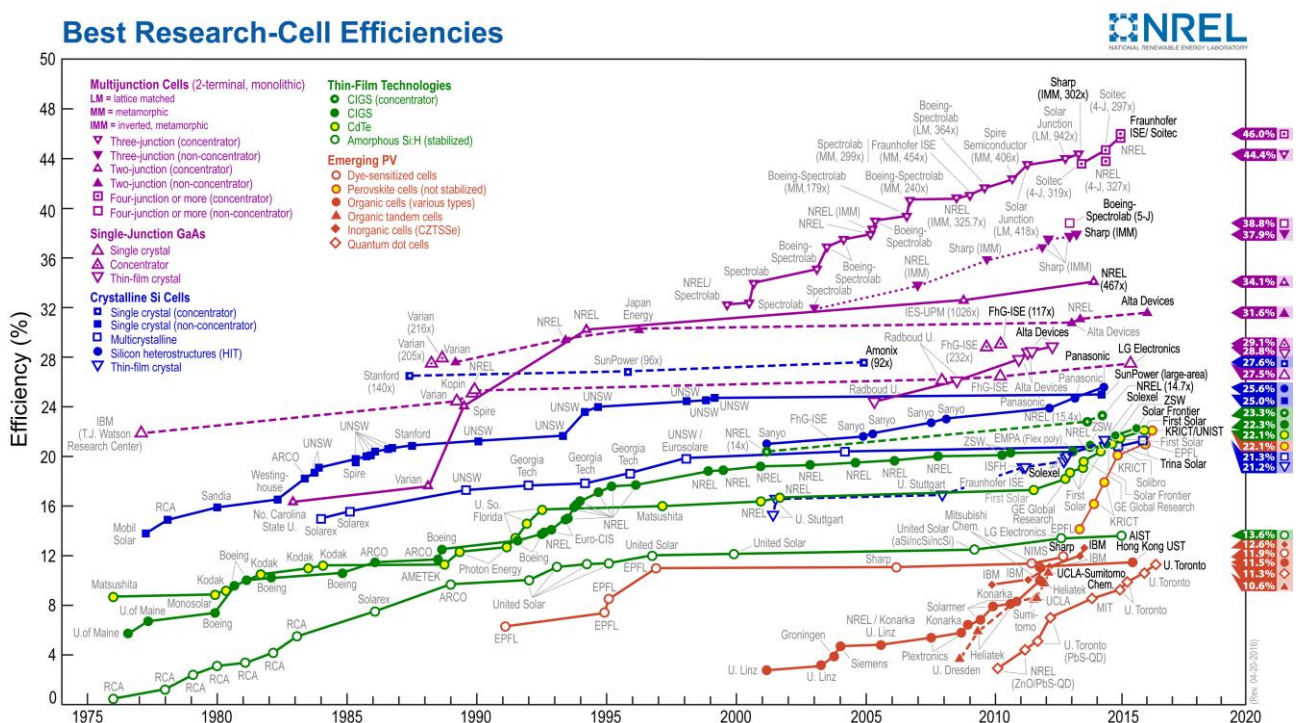


Figure I-3: Best research photovoltaic cell efficiencies Rev. 04-2016 from [19].

1.2. Efficiency limitations

In this work we will focus on improving the silicon solar cells efficiency. However, to succeed in this task, one needs to understand the different loss mechanisms that take place in a solar cell. Based on this understanding, several ways to improve the efficiency will be detailed.

1.2.1. Shockley-Queisser limit

The first solar cells, as most of the solar cells on the market nowadays, are made of on silicon P-N junction. During the photovoltaic process many loss mechanisms may take place. Researches, since the first silicon solar cell demonstration in 1954 [8], have been conducted to improve the efficiency of solar cells. However, in 1961 Shockley and Queisser [20] calculated the theoretical maximum efficiency of a single junction solar cell using P-N junction and called Shockley-Queisser (*S-Q*) limit. Those calculations were based on the detailed balance principle of Pfann and van Roosbroeck [21]. This principle supposes that all the photons above the bandgap are completely absorbed and that carriers mobility is infinite allowing thus the carriers collection even if they are generated outside of the P-N junction space-charge zones. This implies an equivalent recombination rate everywhere in the cell, the bulk or the surface, and equal to the incident radiation exciting rate. *S-Q* limit also considers the solar cell as a blackbody that absorbs all light above its bandgap and none below. The cell has a refractive index of 1, a bandgap of 1.1 eV and operates at a temperature of 300 K under illumination of a blackbody at 6000K (the sun). With the assumptions that the illumination is made by unconcentrated sunlight, that one in-coming photon excites one electron/hole pair, and that the electron/hole pair energy in excess (higher than the bandgap) is relaxed thermally, the *S-Q* limit takes into account:

- The spectral mismatch [22] between the solar spectrum and the cell bandgap that have two components. First, the cell is transparent to the photons with an energy lower than the bandgap which represents a 18% efficiency loss (*Figure I-4 (2)*). And second, the photons with an energy above the bandgap are absorbed but have more energy than necessary for the electron/hole pair excitation. Those electrons (holes) relax to the conduction (valence) band edge by transferring the excess energy to the lattice via phonons [23] that will propagate in the lattice (process called thermalization see *Figure I-4 (1)*). This represents an efficiency loss of 38.2 %. Thus the spectral mismatch leads to an efficiency loss of around 56.2 %.
- The radiative recombinations (*Figure I-4 (3)*) between two charge carriers of opposite sign may occur anywhere in the cell. As an absorbed photon creates an electron/hole pair, the reverse (the recombination of an electron and a hole producing a photon) is also possible and reduces the efficiency by about 10 % for silicon.

The $S-Q$ limit does not take into account the non-radiative recombinations. This calculation leads to an efficiency limit of 33.8 % at 1.1 eV. This limit shows that even if the photovoltaic process itself is perfect, the efficiency would be limited to 33.8%. A recent study by Tiedje et al. [24] implemented the $S-Q$ limit for silicon cells taking into account the non-radiative recombinations. Those non-radiative recombinations account for about another 4 % efficiency loss decreasing to 29.8 % the silicon solar cells efficiency.

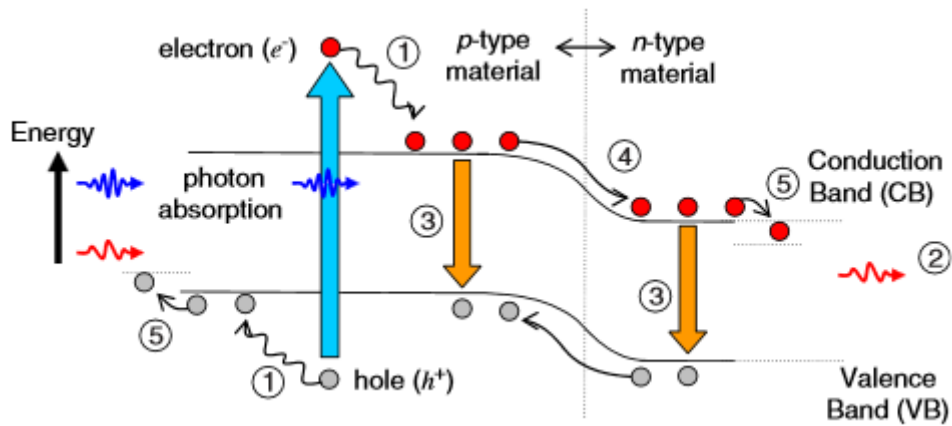


Figure I-4: Loss processes in a single junction solar cell: 1_lattice thermalization losses, 2_transparency, 3_recombination losses, 4_junction losses, and 5_contact voltage, from [25].

1.2.2. Other efficiency losses

In addition of the $S-Q$ limit, other factors may decrease even more the cell efficiency. Resistive losses due to series and shunt resistances [26] contribute to up to another 7 % of the efficiency losses [27]. The series resistance may be due to the carriers motion through the P and N zones of the solar cell, the contact resistance (*Figure I-4 (5)*) between the metal contact and the silicon, and the resistance of the top and rear metal contacts. The shunt resistance (*Figure I-4 (4)*) is mostly due to fabrication defects that provide alternate current leak for the light generated current.

Another factor is the reflection of the light at the surface of the cell that will not be absorbed and used by the cell (*Figure I-5(a)*). This factor counts for around 9 % efficiency loss [27].

Several approaches are currently applied to decrease those losses, for example:

- The optimization of the distance between the contacts lowers the resistivity losses. The metal contact grid should be tight enough to decrease resistivity but not so much as to increase the electrode shadowing effect that would decrease the light absorption in the cell.
- Texturing the cell surface (*Figure I-5(b)*) will enable the reflected light to strike the cell again instead of it going out directly, which reduces significantly the reflection. Different forms and structures of textures have been studied [28,29].
- Depositing an anti-reflection (AR) layer on top of the cell (*Figure I-5(c)*) will result in a net reflected energy equal to zero thanks to the destructive interferences between the beam reflected on the AR layer surface and the one reflected on the solar cell surface. The refractive index of the layer has to be between the one of the air ($n_{\text{air}} = 1$) and the one of the cell ($n_{\text{Si}} = 3.89$ at 1.95 eV). In addition, the couple refractive index and thickness of the layer have to be optimized for an optimal AR process. Models using up to three layers have been studied [30–33].

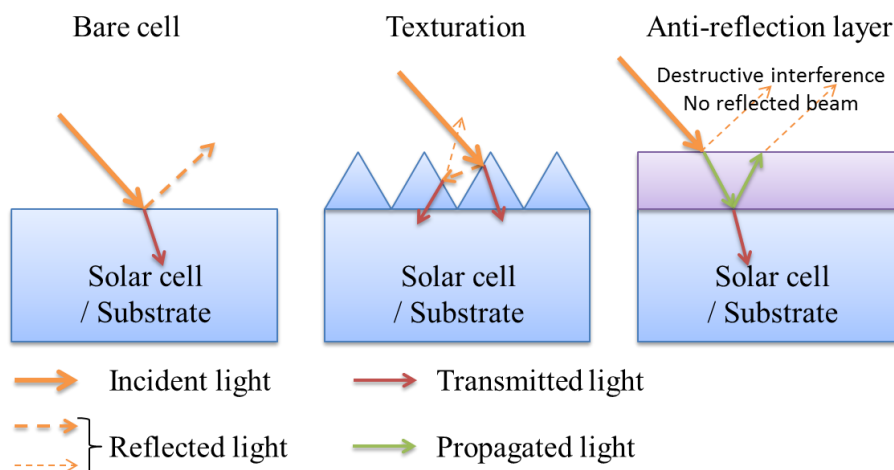


Figure I-5: Schematic of a) a bare solar cell/substrate, b) a textured solar cell/substrate, and c) a solar cell/substrate with an anti-reflection layer on top of it.

1.2.3. Exceeding the Shockley-Queisser limit

Most of the silicon solar cells available on the market are equipped with some of the above technologies which allow to reach 20 % efficiency for crystalline silicon solar cells. However, monocrystalline silicon solar cells displaying up to 27.4 % of efficiency have been developed in laboratory (*Figure I-3*). This value is very close to the $S-Q$ limit of 29.8 %. This closeness shows the need to develop new technics to improve efficiency not by working directly on the cell itself but by finding indirect ways to go over the $S-Q$ limit. Some of those currently research technics to go over the $S-Q$ limit will be described below.

1.2.3.1. Multijunction cells

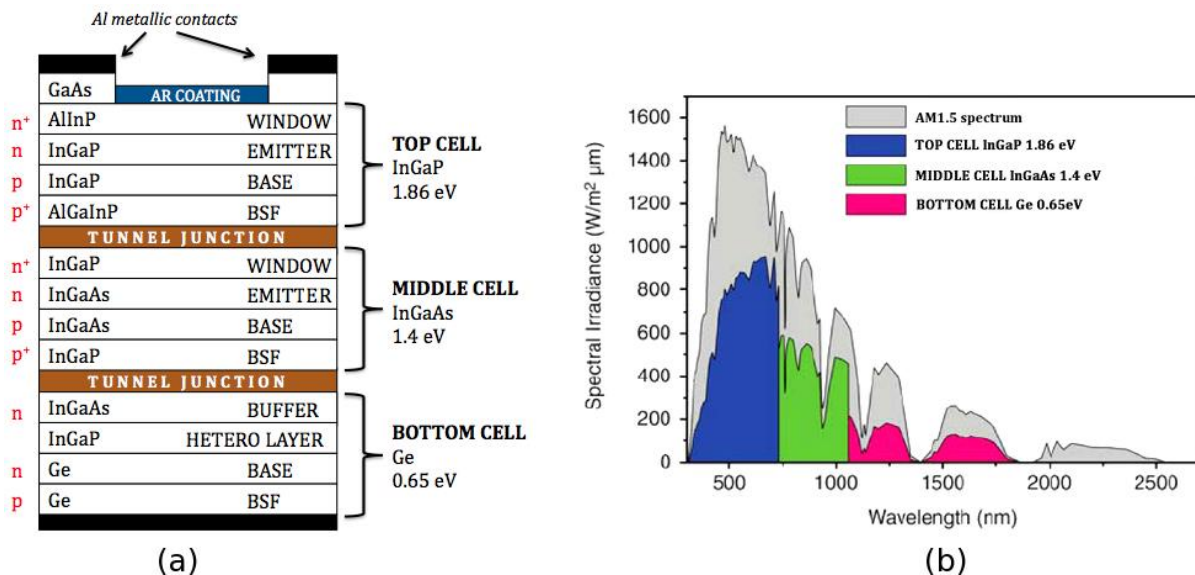


Figure I-6: (a) Schematic of a three-layer cell with tunnel junction. (b) Parts of the solar spectrum used by each of the three cells of the tandem cell from [36].

The $S-Q$ limit calculation shows that over 50 % of the efficiency of a single junction solar cell is lost due to spectral mismatch between the solar spectrum and the solar cell bandgap. One way to improve the absorption of the light is to adapt the cell to the spectrum. For this purpose, multijunction solar cells [34,35] also called tandem cells were developed. Indeed, only the energy of the photons of similar wavelength than the bandgap of the cell (corresponding to a very small part of the solar spectrum) is totally used. Thus stacking cells with different bandgap will increase the part of the solar spectrum for which the energy of the photons is totally used without losses. The cells are stacked according to the value of their bandgap with the larger on top and the smaller at the bottom (*Figure I-6*). The cells may be individual cells or connected in series. However, the cells must have compatible crystalline structures. They must also have the same current going through them. A tunnel junction has to be put between two cells to allow the electrons to flow in the same

direction between the cells without lowering the global voltage and to keep the electric fields of the cells separated.

This technic can increase greatly the solar cells efficiency as the maximum theoretical efficiencies calculated are 60 % and 72 % respectively for multilayer systems with 24 [37] and 36 [38] junctions with different bandgaps. The world record is currently held by Tibbits et al. [39] with a four-layer cell having a measured efficiency of 46.5 %. Those cells are though very expensive and employed only in space projects that favor lightness and efficiency over production cost, and in concentrator systems that need small surface device as the sun light is concentrated on this small area (0.3 to 1 cm² compared to the 25 cm² and more of a standard solar cell).

1.2.3.2. Spectrum conversion

In order to minimize the efficiency losses due to spectral mismatch, another approach may be developed. Instead of adapting the cell to the spectrum, it is the solar spectrum that will be adapted to the cell bandgap. For this purpose, optical frequency conversion technics may be used to fit the solar spectrum to the *SC* bandgap [40].

The cell is transparent for the photons having an energy below the *SC* bandgap. Thanks to the up-conversion (*UC*) process (*Figure I-7*), two photons with at least half the *SC* bandgap energy may be absorbed by a luminescent center which then emits a single photon with an energy higher than the *SC* bandgap energy that will hence be absorbed by the solar cell [41]. The up-converters are placed at the rear part of the solar cell with a bottom/external reflector (*Figure I-8*).

The photons having an energy above the bandgap are absorbed. However the energy in excess of the carriers (higher than the bandgap) is lost in the lattice through a thermalization process. Moreover we already saw that the increase of the cell temperature decreases its efficiency. Two processes allow to absorb high energy photons before they reach the cell and to emit lower energy photons where the internal quantum yield of the cell is higher. The down-conversion (*DC*) process (*Figure I-7*) enables the absorption of one high energy photon leading to the emission of two photons with half the energy of the absorbed one. This process decreases the thermalization of photogenerated carriers while increasing the number of photons that the cell can absorb. The down-shifting (*DS*) process is similar to the down-conversion but leads to the emission of only one lower energy photon per higher energy absorbed photon and the remaining energy is dissipated non-radiatively [42]. This process allows a shifting of the spectrum toward a wavelength range where the cell is more efficient. The down-converters or down-shifters are placed at the front of the cell to tune the spectrum before it interacts with the cell (*Figure II-8*).

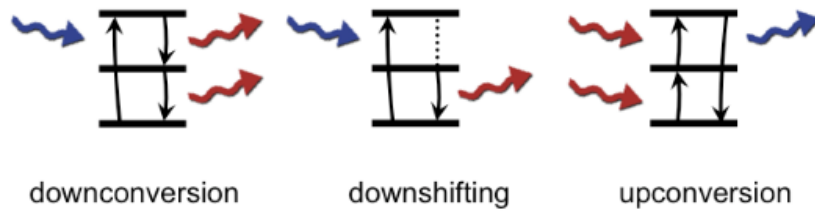


Figure I-7: The three mechanisms of the photon luminescent conversion processes [43].

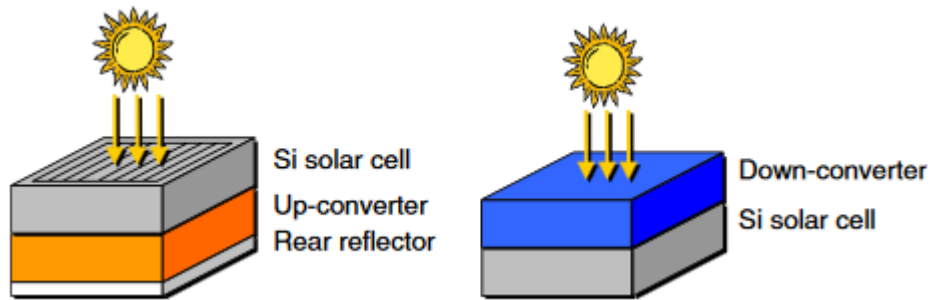


Figure I-8: Diagram of an up-conversion (left) and down-conversion (right) setup [25].

When looking at the solar spectrum received on earth (AM1.5G) (Figure I-9), one can see that the fraction of the energy absorbed by a crystalline silicon solar cell, in green, represents 468 W/cm². Using up conversion layer would potentially allow to use another 164 W/cm² [25] corresponding to 35 % of the absorbed light. Using the down-conversion process will enable to use 149 W/cm² corresponding to 32 % of the absorbed light.

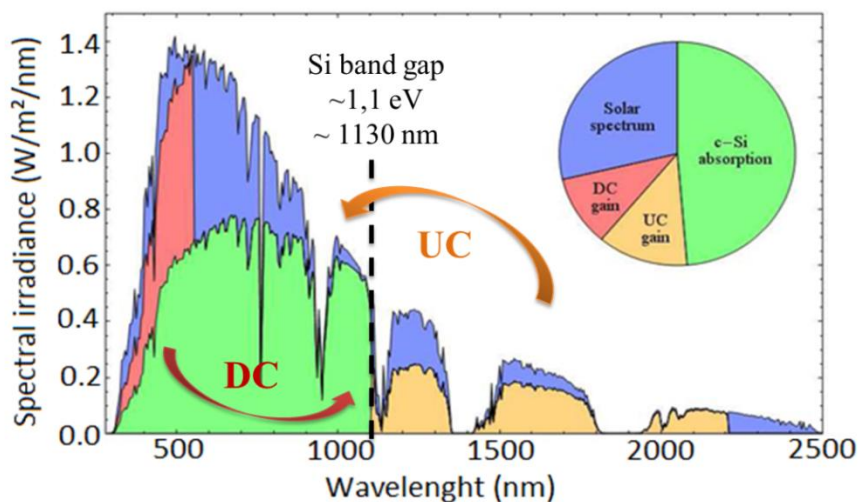


Figure I-9: Solar spectrum received on earth with the parts used by a silicon cell in green, possibly used by down-conversion (DC) in red, and possibly used by up-conversion (UC) in orange. Only the spectral mismatch is considered. From [43].

1.3. Down-conversion principle

1.3.1. History

In 1953, D. L. Dexter published his “theory of sensitized luminescence in solids” [44] that was an extension of the resonance theory of Förster [45] applied to solids. For Dexter this sensitized luminescence takes place between two impurities called sensitizer (S) and activator (A). S will absorb light with certain wavelengths, undergo a Stokes’ shift (because of non-radiative relaxation- NRR - with lattice), and transfers this energy to A (*Figure I-10 (b)*). This last particle will, in turn, undergo a Stokes’ shift before undertaking a radiative or non-radiative transition. This way, A may emit even if its absorption range is different from the one of the exciting light. Indeed, it is S that will have an absorption range compatible with the one of the exciting light and will absorb the energy. As S emitting range encompasses at least to some extent the absorption range of A (*Figure I-10 (a)*), a dipole-dipole interaction occurs leading to the above mentioned process.

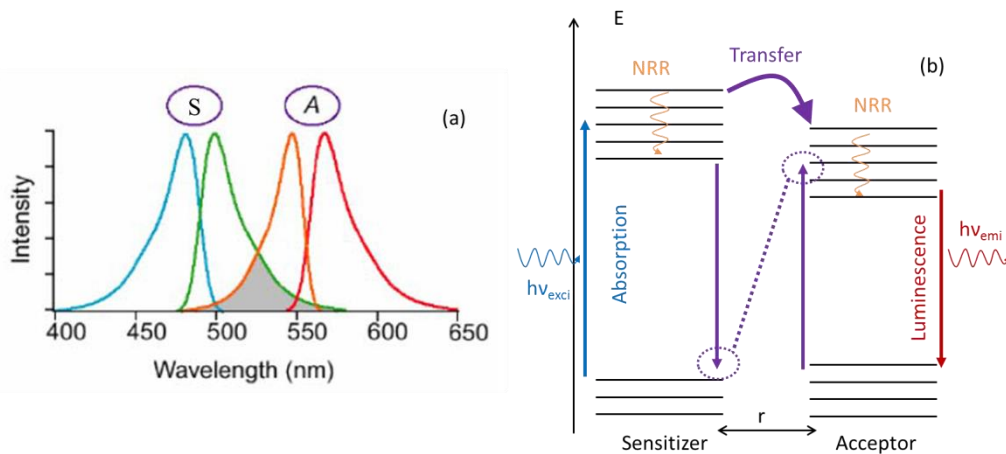


Figure I-10: Overlapping of S emission curves and A absorption ones (a) and schematic of the sensitizer-activator interaction (b). From [46].

A few years later, Dexter was the first to demonstrate the possibility of “luminescent quantum yield greater than unity” [47] happening between S and two A during such sensitized luminescence process. A quantum yield higher than unity may be achieved only in the case of S having three energy levels such that they are separated by an energy in the visible range and that the probability of radiative transitions between those levels is high (*Figure I-11*). It is important to note that for the “photon splitting” to take place, the two activators, A , to which the sensitizer energy is transferred have to be below a certain distance of S .

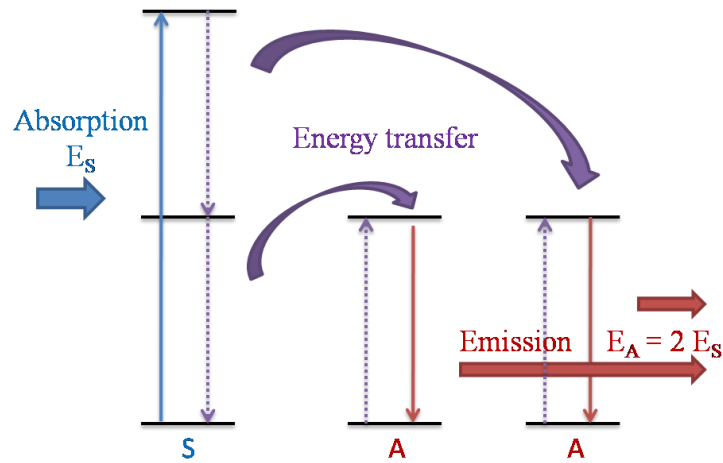


Figure I-11: Schematic of the sensitized luminescence process with a “luminescent quantum yield greater than unity” described by Dexter [47].

The first authors to achieve experimentally such photon splitting also called quantum cutting (*QC*) were Piper et al.[48] and Sommerdijk et al. [49,50]. The *QC* was obtained by doping a lattice of YF_3 with a single rare earth ion (Pr^{3+}). The rare earth ions, after absorbing UV photons, undergo a cascade emission (Figure I-12) leading to the emission of one or two photons of lower energy. They both prove two-photons luminescence from an UV excitation in fluoride doped praseodymium system ($\text{YF}_3:\text{Pr}^{3+}$). Phosphors doped with a single rare earth ions [51–53] present a high UV absorption but a weak visible emission and UV and IR losses.

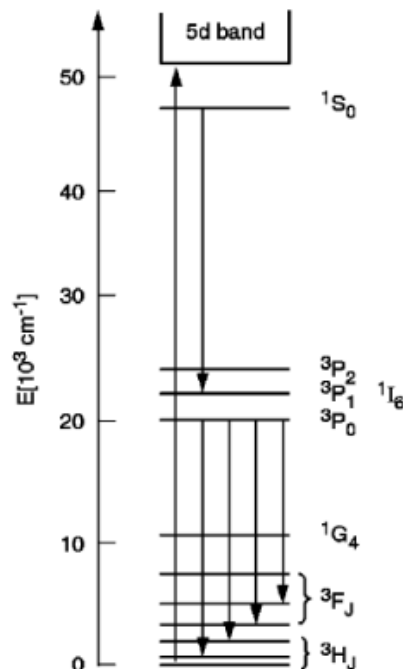


Figure I-12: Quantum cutting (photon cascade emission) for a single ion system, here the Pr^{3+} in YF_3 . From [54].

In 1999, the first system composed of a lattice doped with two rare earth ions $-RE_1$ and RE_2- ($\text{LiGdF}_4:\text{Er}^{3+}$) is published by Wegh et al. [55,56]. This system allows for a still high UV absorption, like the lattice with only one RE ion, but also, contrary to this later, for an enhanced visible and IR emission. The RE_1 ion absorbs photons in the UV range (blue arrow on *Figure I-13*) and transfers part of its energy to two RE_2 ions leading to the emission of two visible photons (red arrows on *Figure I-13*) of half the energy of the UV photon. As the above mentioned energy transfer mechanism has a reverse energy flow compared to the up-conversion energy transfer mechanism described by Auzel in 1990 [57], Wegh et al. called it down-conversion.

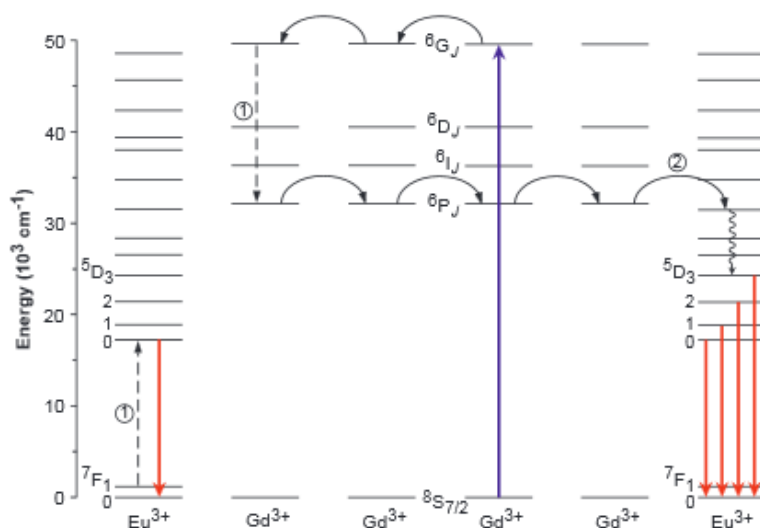


Figure I-13: Visible quantum cutting for a two ions system, here the $\text{Gd}^{3+}-\text{Eu}^{3+}$. From [55].

Wegh et al. also published a down-conversion system with three rare earths ions [58] where the first rare earth absorbs the UV photons and transmits part of its energy to the second ion. This second ion is used as “bridge” to transport the energy to two other ions that will emit visible photons. *Figure I-14* describes this mechanism.

The first mention of down-conversion as a way to go over the $S-Q$ limit and thus increase the solar cells efficiency was made by Trupke et al. [59,60] in 2002-2003. The authors proposed two solar cell/down-conversion layer configurations. The first one consists in putting the down-converters at the back surface of the cell. It was calculated that this method would increase to 39.6 % the solar cell efficiency, far higher than the $S-Q$ limit. However, this method implies to develop new bifacial solar cells. The second one consists in depositing a down-conversion layer on the top surface of the cell. This method leads to a slightly lower efficiency of 38.6 % but allows to use any conventional solar cells. For obvious practical reasons, it’s the second configuration that has been developed up till now. In addition, those same authors explained that down-conversion is particularly efficient for 1.1 eV materials rendering this technic ideal for silicon solar cells.

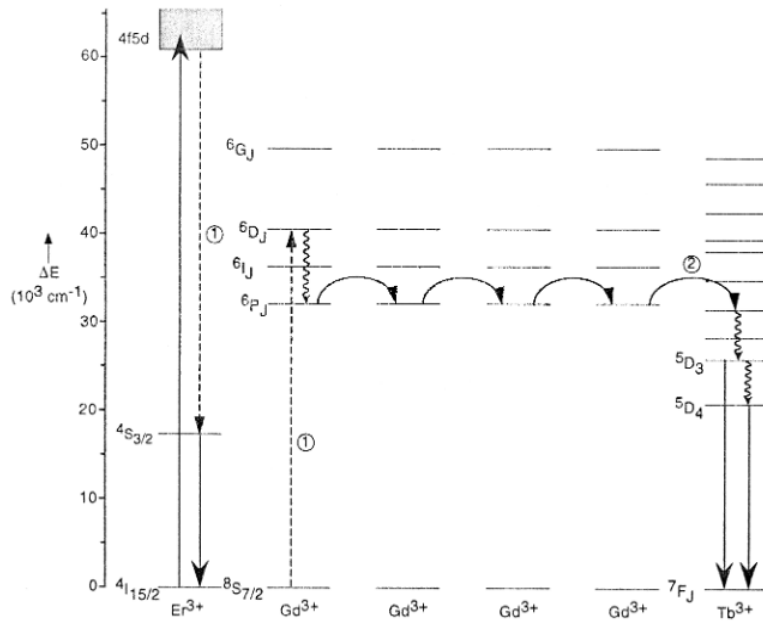


Figure I-14: Visible quantum cutting for a three ions system, here the Er^{3+} - Gd^{3+} - Tb^{3+} . From [58].

1.3.2. Rare earth ions in the down-conversion process

The rare earth ions have been rapidly and extensively used in luminescent devices [52,61]. The motivation of using rare earths comes from their very narrow emission band ranging from the near-infrared (*NIR*) to the ultra-violet (*UV*) thus allowing the production of blue, green, and red emission devices. Moreover, rare earth ions have also been used in laboratory for frequency conversion mechanisms and particularly in *QC* ones that lead to a quantum yield higher than unity that find some applications in lightning industries [54].

1.3.2.1. The rare earth elements

Rare earths are a group of metal elements including the scandium, the yttrium and the fifteen lanthanides elements. Despite their name, rare earths are relatively common in Earth's crust as shown in *Figure I-15*.

In phosphors doped with optically active rare earths, the rare earths occur mainly in the trivalent form (RE^{3+}). However, divalent (RE^{2+}) and tetravalent (RE^{4+}) forms may also be present. Those last forms tend to reduce the luminescence as they act as energy traps.

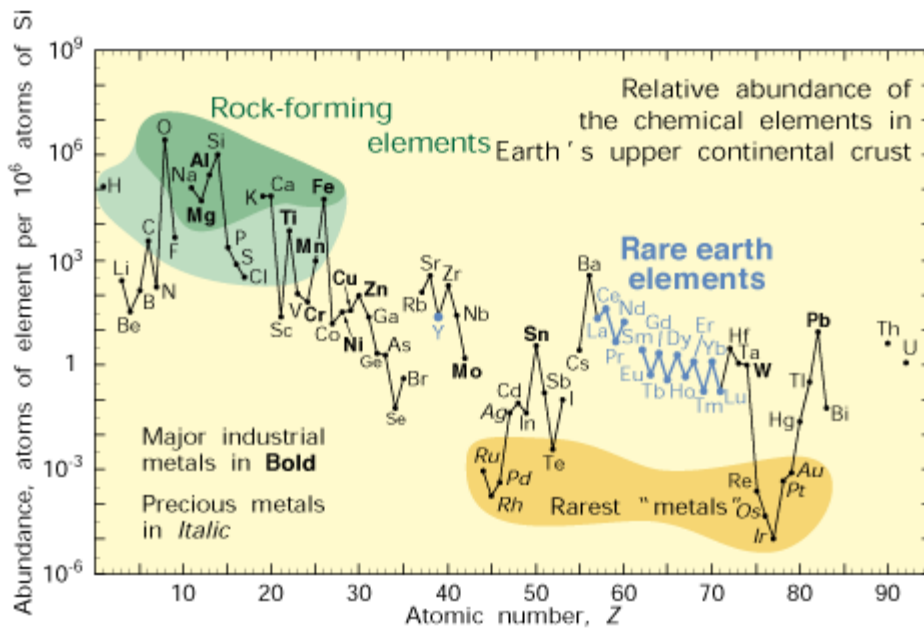


Figure I-15: Abundance of the chemical elements in the Earth's crust. From [62].

The rare earths all have similar chemical and physical properties thanks to their very similar electronic structures. They all have an incomplete 4f electronic orbitals surrounded by 5s, 5p, and 5d complete outer electronic orbitals. The 5s, 5p, and 5d orbitals shield the inner 4f electronic orbitals from the crystal field. The rare earth ions have thus almost kept their atomic character which leads to f-f transitions relatively insensitive to their physical and chemical environment. In addition, the transitions between 4f levels are parity forbidden. However, in case of *RE* ions inside a matrix, the relaxation of selection rules allows the 4f transitions. Therefore, those *RE* ions have a low absorption cross-section (10^{-20} cm^2 [63]) and a long life time (μs to ms [61]).

The 4f orbitals of the rare earths have been determined by Dieke [64] and Carnall et al. [65]; they are shown on *Figure I-16* called Dieke diagram. We can see that the 4f energy levels of the rare earth ions in a matrix are widely distributed between UV and IR allowing absorption and emission in this whole wavelength range.

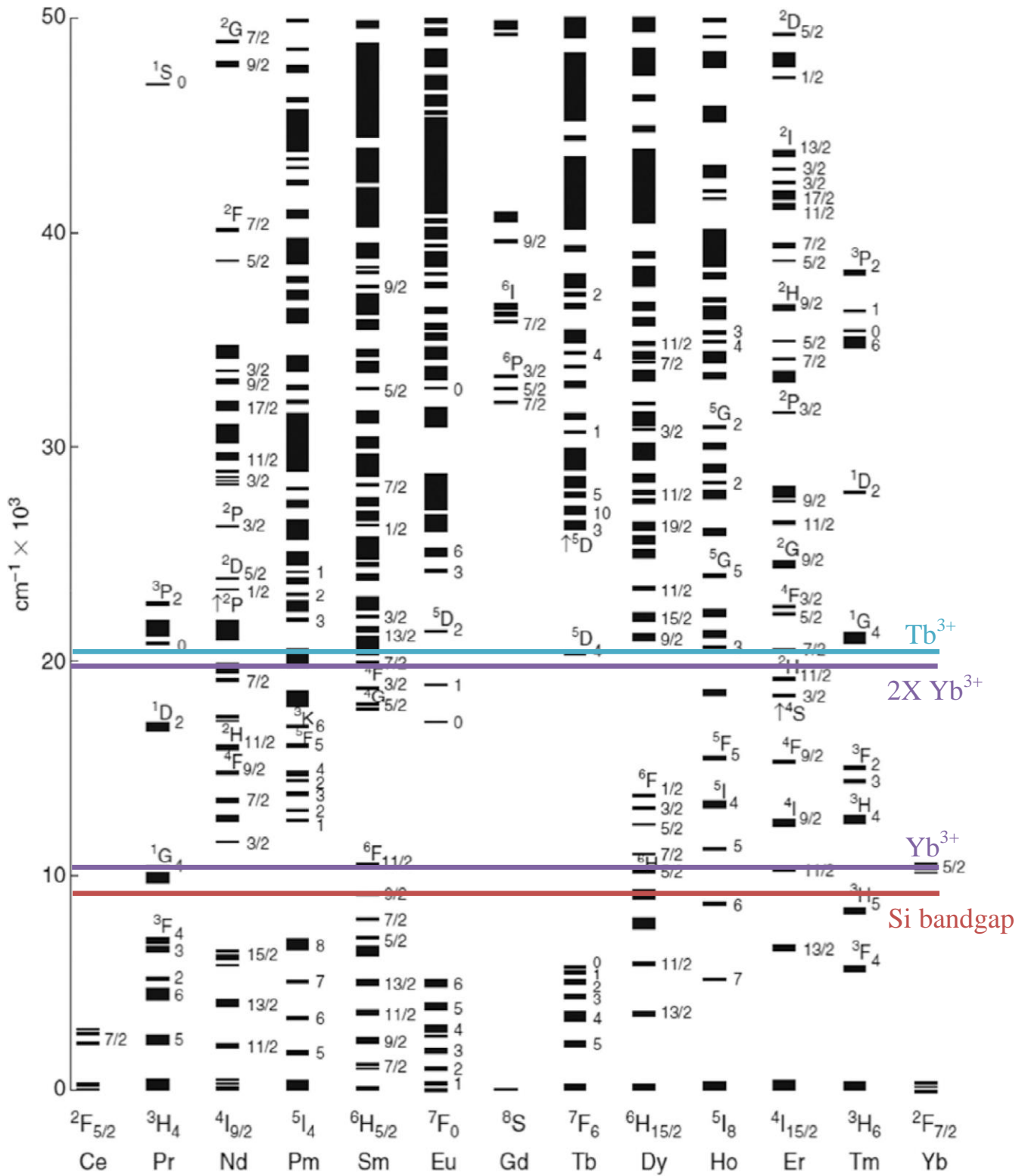


Figure I-16: Dieke diagram [64] with the energy of the silicon bandgap, the $^2F_{5/2}$ energy level of the ytterbium ion, twice the energy of the ytterbium, and the 5D_4 energy level of the terbium ion signaled by color lines.

1.3.2.2. Review of the rare earth ions used for the down-conversion

Thanks to the Dieke diagram (Figure I-16) and the Judd-Ofelt theory [66,67], that allows to determine the possible transitions (radiative or non-radiative) for each rare earth ion and their probabilities, various rare earth ions have been selected to achieve *QC*.

The first studies on *QC* used a single *RE* ion, Pr^{3+} [48,49] or Gd^{3+} [53], that have three energy levels separated by the same amount of energy (Figure I-12). Following the same logic, Eu^{3+} [68] and Dy^{3+} [69] single *RE* ions were studied with different third generation solar cells technologies, resulting in solar cell efficiency improvement.

Most *QC* studies however used two kind of *RE* ions (Figure I-17). In this case, the first *RE* ion— RE_1 — has to have a transition with an energy above twice the energy of the secondary $\text{RE}-\text{RE}_2$ -transition. The first couple investigated was $\text{Gd}^{3+}-\text{Eu}^{3+}$ by Wegh et al. [55]. They proved that a two ions system is more efficient than a single ion one.

In the case of silicon solar cells, the selected *RE* ions couple should lead to the emission of photons with an energy equal to or just above the silicon bandgap ($E_{\text{gSi}} = 1.1$ eV). Thus the RE_2 (Figure I-17) should have a transition with an energy slightly higher than the silicon bandgap to take into account the energy loss due to the matrix relaxation. In a similar way, the RE_1 should have a transition with an energy slightly higher than twice the energy of the RE_2 transition because of the matrix relaxation.

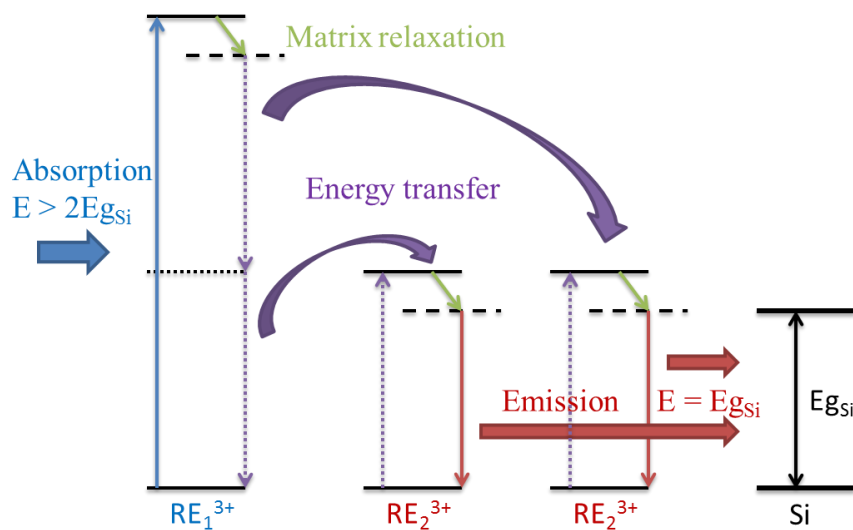


Figure I-17: Schematic of the energy transfers taking place in a down-conversion system applied to solar cells.

Many couples of *RE* ions have been investigated. Systems emitting in the visible range such as $\text{Gd}^{3+}-\text{Eu}^{3+}$ [55,70] or in the far IR range such as $\text{Er}^{3+}-\text{Ce}^{3+}$ and $\text{Nd}^{3+}-\text{Ce}^{3+}$ [71], or $\text{Er}^{3+}-\text{Gd}^{3+}$ (made for germanium *SC*) do not fit the silicon solar cell absorption energy. In order to work with the Si *SC*, the activator ion has to have an energy level just above 1.1 eV (below 1127 nm). Thus Yb^{3+} and Er^{3+} are good candidates. Among them, Yb^{3+} ion is the most used one due to its two levels system

configuration which limits cross-relaxations. By contrast, Er^{3+} ions have multiple energy levels and may therefore present cross-relaxations. Many couples may be formed with the ytterbium ions (see the Dieke diagram on *Figure I-16*). In the Pr^{3+} - Yb^{3+} [72–75], and Er^{3+} - Yb^{3+} [76–78] couples, the sensitizers have an intermediate energy level which may favor cross-relaxation and up-conversion energy loss processes. In the Tm^{3+} - Yb^{3+} [79–81], Eu^{2+} - Yb^{3+} [82], and Ho^{3+} - Yb^{3+} [83] couples, the sensitizers have no exact intermediate energy level but many levels in between the levels used for the *DC* process which may favor multiphonon-relaxation energy loss processes. In the couple Tb^{3+} - Yb^{3+} [84–87], the sensitizer has no intermediate energy level which allows to avoid the above mentioned energy loss processes. In addition, the energy transfers take place between an excited energy level and the ground state instead of between two excited states that then may be relaxed non-radiatively to the ground state thus increasing thermalization. The Ce^{3+} - Yb^{3+} [88] couple offers the advantage to have a higher absorption cross-section than the previous ones (10^{-18} instead of 10^{-21} cm^2 [89]) which favors the light involved in the *DC* process without the need of a sensitizer.

In this work, the couple Tb^{3+} - Yb^{3+} that shows promising results [84,90] will be studied but in a different matrix than the previous works (see § I.3.3).

1.3.3. Matrix requirements

1.3.3.1. Silicon solar cell application

The *QC* systems studied till now were composed of a crystalline- [70,91,92], nanostructured- [77,90,93,94], or amorphous- [78,89,95–97] matrix doped with up to three kinds of rare earth ions that act as impurities [47]. In most of those systems, the matrix is not involved in the *QC* process. The matrix, as the host, is however chosen for its properties relevant for the specific application (lighting, *SC*, ...). Richards, in 2004, listed the properties of luminescent *DC* materials (matrix + *RE* ions) required for lighting, display and photovoltaic applications [98]. All those properties depend on some level of the matrix used. Hence, in the case of photovoltaic applications, the matrix must be stable under high energy photon illumination (*UV*) and should not degrade during the device fabrication. Matrices should also play the part of antireflective layers with a reflective index between the ones of the air and of the cell (see § I.2.2). The matrix should not be toxic and allow for a recycling process.

As the studies focused on lighting applications such as plasma display and mercury-free fluorescent tubes, every kind of glasses have been developed as a host matrix for *RE* ions. Those glasses were mostly fluorides [22,55,70,77,86,87,97,99], borates [89,93,100,101], phosphors [80,84], etc. However, those glasses have a low stability under high energy photon illumination (*UV*) as well as during the solar cell firing process leading to defects formation such as trapped-hole color centers and electrons trapped by RE^{3+} transformed in RE^{2+} [102], and/or diffusion of dopants. Those defects play the role of traps for the photons. Most glasses also involve environmental and safety issues due to the presence of heavy metals like cadmium [103], or lead [78]. Thus, silicon oxide

[104] and silicon oxynitride [105] matrices that are compatible with the silicon solar cell fabrication process have been developed.

In this work an amorphous silicon nitride matrix, SiN_x , free of oxygen will be studied. The absence of oxygen allows for a higher RE ions concentration in the matrix before photoluminescence quenching [106]. SiN_x offers the advantage of being largely used in microelectronics and especially as anti-reflective layers on actual silicon solar cells that eases the fabrication of both a DC and anti-reflective layer. This material is also highly compatible with the fabrication processes of the silicon solar cells. Silicon and nitrogen are also non-toxic and very common elements. The fact that the matrix is amorphous also decreases the chance of carrier recombinations that usually occur at the grain boundaries.

1.3.3.2. The sensitizing matrix

Richards shows that experimental external quantum yields are lower than the theory because of the poor absorption cross section of RE ions [98]. Indeed, most of the rare earth ions have a small absorption cross-section (around 10^{-20} cm^2 [63]) which decreases the efficiency of the system. In order to increase the absorption, a sensitizer has to be used. Such sensitizer has an absorption cross-section higher than the rare earth ions and will absorb the photons before transferring their energy to the ions. Two kinds of sensitizer have been described by Dexter. The first kind is a dopant that may be another rare earth that have higher absorption cross-section such as the Ce^{3+} (10^{-18} cm^{-1} [107]). They also have broader absorption and emission cross-section enabling an excitation and an energy transfer over a broader spectral range. They are then used in three rare earths systems [108,109]. The second is the matrix itself that have an absorption coefficient of around 10^3 cm^{-1} (at 0.8 eV) [110]. In this case the matrix should be chosen for its bandgap that must have an energy higher than the absorption energy of the selected rare earth ions. In that way, the matrix will absorb the photons in a wide range of energy and transmits easily the energy to the surrounding rare earth ions (at the RE energy of absorption). It is important to note that the ideal matrix should absorb the photons with an energy higher than twice the energy of the bandgap of the SC but be transparent for all the photons with a lower energy. Indeed, absorption of photons below this limit will decrease the cell efficiency under its usual efficiency without the DC layer [22].

In this work, we will use the silicon nitride, SiN_x , that showed large emission due to defect states in its bandgap formed by either an excess of nitrogen or silicon [111,112].

1.4. Energy transfers

Several energy transfer mechanisms in systems containing up to three rare earth ions have been reported. In this section, we will first review the energy transfer mechanisms from the matrix to the *RE* ions. The various energy transfers in between *RE* ions will then be described. Finally, the energy losses that might happen in such systems will be exposed.

1.4.1. Matrix to rare earth ions

As exposed above (§ 1.3.3. (a)), the 4f-4f transitions of the *RE* ions having a low absorption cross-section, a more effective excitation of those transitions is obtained by using matrix-assisted excitation via energy transfer. In silicon nitride matrices, SiN_x , free of Si clusters, the origin of the sensitization towards the *RE* ions are mainly the band tails and the deep states in the bandgap that have a much higher absorption cross-section than the 4f-4f transition direct excitation of the *RE* ions.

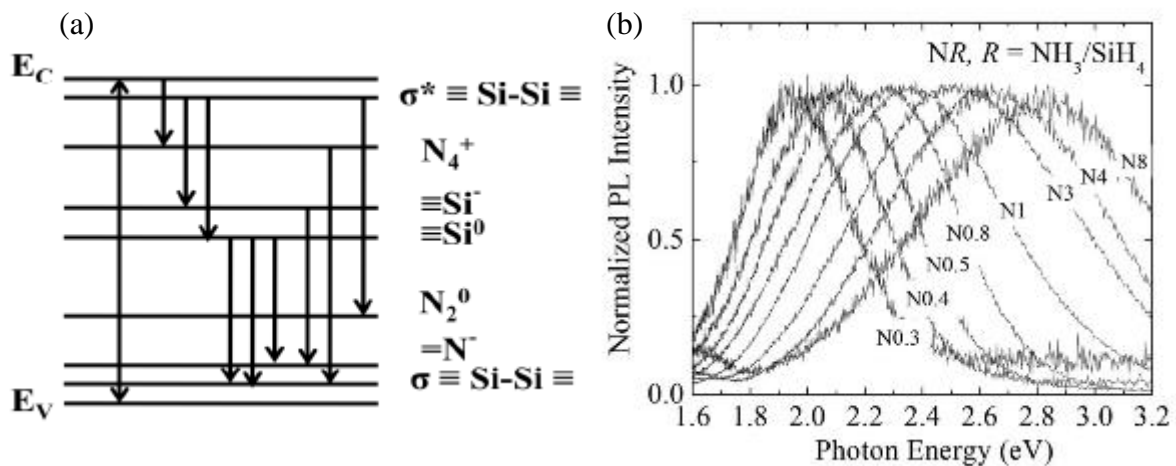


Figure I-18: (a) Density of states of the different defects and their energy, from [104]. (b) PL spectra normalized to the peak intensity for various R ($[\text{N}]/[\text{Si}]$ ratio), from [113].

The SiN_x matrix, as an amorphous dielectric material, shows local fluctuations in the interatomic distances and the bonding angles which create localized states near the band edges capable of trapping the charge carriers. Those localized states leads to band tails with exponential shape density of states extending in the bandgap [114]. The matrix also contains structural defects that are broken or unsaturated bonds such as dangling bonds ($\equiv \text{Si}^-$, $\equiv \text{Si}^0$, $=\text{N}^-$) and the unit ($\equiv \text{Si-Si} \equiv$, $=\text{N}_2^0$, $=\text{N}_4^+$) [111]. Those defects create distinct energy states inside the bandgap of SiN_x . Levels may be localized near the conduction and/or valence bands thus extending their states that are then called localized states (Figure I-18). Levels may also be localized in the middle of the bandgap creating what are called deep states.

The SiN_x matrix containing Si or N excess has been widely studied [115–117]. It has been demonstrated [111,112,118–120] that the defects due to the disorder of the non-stoichiometric material create various states (*Figure I-18 (a)*):

- the $\equiv\text{Si}-\text{Si}\equiv \sigma$ and σ^* centers levels situated just in the gap at 0.4 eV and 5.0 eV, respectively
- the $=\text{N}^-$ centers level situated at 0.5 eV
- the $=\text{N}_2^0$ centers level situated at 1.8 eV
- the $\equiv\text{Si}^0$ centers level situated just above midgap at 2.7 eV
- the $\equiv\text{Si}^-$ centers level situated below the conduction band at 3.0 eV
- the $=\text{N}_4^+$ centers level situated at 3.6 eV

It has been shown that by tuning the material composition and particularly the $[\text{N}]/[\text{Si}]$ ratio, the width of the band tails may be monitored [116,121,122]. Wang et al. [113] and Kistner et al. [123] have demonstrated that by varying the nitrogen content, the disorder of the matrix may be increased (*Figure I-18 (b)*) which leads to the creation of deeper band tail states and a shift in the PL emission.

This tuning of the band tails width may be used to obtain a matrix emission that overlap the *RE* ions energy absorption band. Previous studies on Erbium-doped systems have proven that: first, the band tails can transfer energy within a broad spectral range from 2 to 4 eV directly to the Er^{3+} ions [124], and second, that the band tails excitation of Er^{3+} ions is prevailing for a material annealed at lower temperature than 1050°C (at higher temperature the excitation via Si-nanoparticles is dominant) [125].

1.4.2. Rare earth to rare earth transfer (dipole)

1.4.2.1. Energy transfer between rare earth ions

Several energy transfer mechanisms may take place between rare earth ions. Such mechanisms have been described by Auzel [57] and are shown on the *Figure I-19*. Those mechanisms involve the energy transfer from a sensitizer, *S*, to an acceptor, *A*, following different mechanisms:

- The resonant radiative energy transfer in which *S* emits a photon that will then be absorbed by *A* (*Figure I-19 (a)*). In this case the lifetime of *S* remains constant with the concentration increase of *A*.
- The resonant non-radiative energy transfer in which *S* excites *A* by a non-radiative channel (*Figure I-19 (b)*). In such case, the lifetime of *S* is strongly dependent of the concentration of *A* as the non-radiative transitions contribute to depopulate the excited energy levels.

- The phonon-assisted energy transfer that is required when there is an energy mismatch between the excited levels of S and A (Figure I-19 (c)). This mechanism has to be considered as soon as the mismatch reaches several thousand of reciprocal centimeters. However, the probability of an energy transfer is smaller for a bigger mismatch.

- The cross-relaxation that occurs when S and A are identical ions (Figure I-19 (d)). Also called self-quenching, it involves two identical ions, one in an excited state and the other in the ground state, exchanging energy which results in the two ions being in an intermediate excited state.

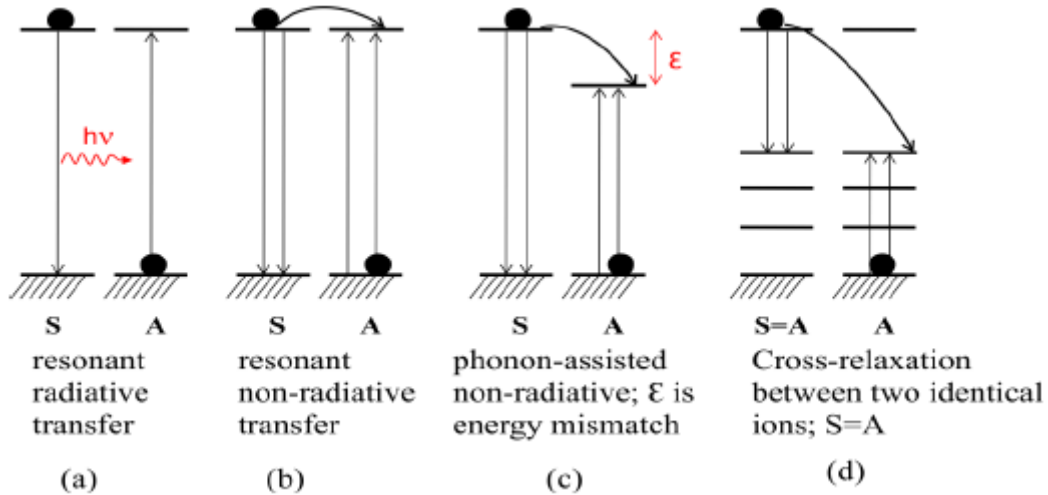


Figure I-19: Schematic diagram describing the energy transfer possible between two RE ions. From [57].

For a non-radiative energy transfer, several mechanisms may occur: the magnetic-, the exchange-, and the dipole-dipole- interaction. In the case of RE ions, only the electrostatic dipole-dipole interaction or FRET (Förster resonant energy transfer) [126] is probable. This non-radiative mechanism is favored by: (i) the overlapping of the emission and absorption spectra of S and A respectively, (ii) the S lifetime larger than the energy transfer time, and (iii) the short S and A inter-distance. The energy transfer efficiency decreases with a power 6 when the distance S - A increases over 1 nm. The FRET is characterized by a decrease of the S luminescence and an increase of the A one. In addition, the lifetime of S decreases.

Indeed, the transfer efficiency of this interaction [127,128] is given by:

$$E_{dd} = \frac{1}{1 + \left(\frac{R}{R_0}\right)^6} \propto \left(\frac{R_0}{R}\right)^6 \quad \text{I-1}$$

With R the average distance between S and A , and R_0 the Förster radius which is the distance (typically between 5 and 10 nm) corresponding to an interaction efficiency of 50 %.

1.4.2.2. Down-conversion possible energy transfers

The goal of this work is to develop a down-conversion thin layer to put on top of Si SC. To this purpose, a two RE ions doped system is used in which several energy transfer mechanisms may take place (Figure I-20):

- The quantum cutting (QC) on a single RE ion (I) by sequential emission of two IR photons is theoretically possible (a).
- The emission of two IR photons from a pair of RE ions (II) is possible via a two steps mechanism: a cross-relaxation followed by a resonant energy transfer (b).
- The emission of two IR photons by the two RE ions (I and II) involved via a single cross-relaxation mechanism (c) and (d).

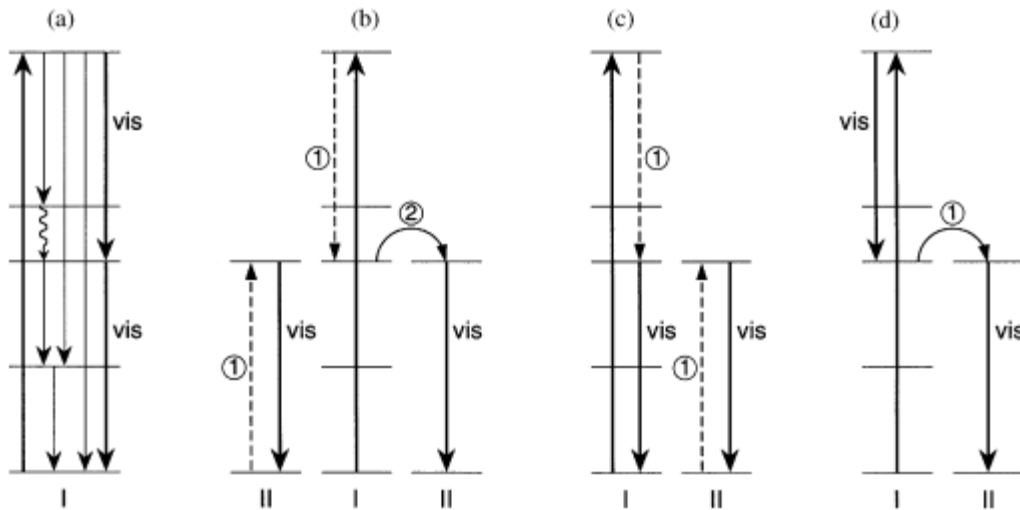


Figure I-20: Possible QC mechanisms for two RE ions (I and II) (1) indicate a cross-relaxation between I and II and (2) an energy transfer from I to II. From [55].

In the case of the system with a sensitizer interacting with a pair of identical activators, the accretive and cooperative transitions [129] (Figure I-21) are competing. The accretive transition is a first order energy transfer and is thus dominant over the second order energy transfers such as the cooperative transition [22]. However, the accretive transition needs an intermediate energy level to take place. Thus, in systems doped with three energy levels systems, with intermediate level, RE ions such as Pr^{3+} , the accretive mechanism (Figure I-21 (b)) is dominant [74]. However, in systems doped with two energy levels systems, without intermediate level, RE ions such as Tb^{3+} , the first order mechanism is not possible. So, the second order mechanism that is the cooperative one may happen. Veerger et al. [84] verified this hypothesis by comparing the experimental luminescent decay time curve of Tb^{3+} for different Yb^{3+} concentrations to the Monte Carlo simulated decay time curves. For this purpose, they have taken into account the three energy transfers possible that are the cooperative, the accretive, and the phonon-assisted energy transfers. The cooperative energy

transfer simulated curve was found to fit particularly well the experimental curve proving that the cooperative mechanism is dominant for two energy levels *RE* ions.

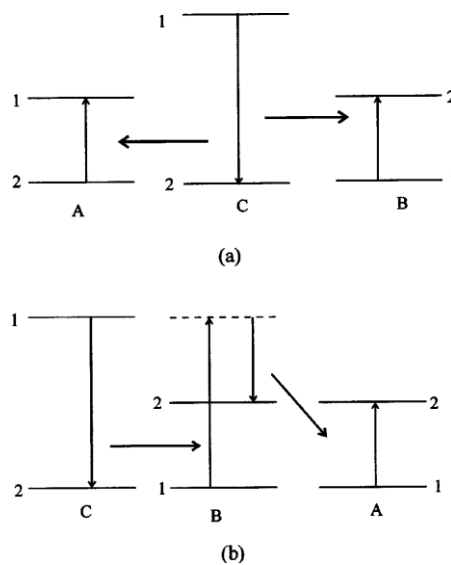


Figure I-21: Energy level diagram of a three *RE* ions system for *QC* (a) cooperative and (b) accretive. From [129].

I.4.3. Possible energy losses

Though, if the *DC* process enables an increase of the cell efficiency, several energy loss mechanisms may reduce this efficiency improvement:

The up-conversion may take place using the same *RE* ions but in an energy transfer opposite to *DC*. In this case, two photons with energy equal to the silicon bandgap are absorbed and a UV photon is emitted. Auzel [57] suggested six mechanisms the up-conversion might follow (*Figure I-22*). In the case of a Tb-Yb co-doped material, the *APTE* (for Addition de Photon par Transferts d'Énergie) or *ETU* (for Energy Transfer Up-conversion) (*Figure I-22* (a)) and the 2-step-absorption or *GSA* (for Ground State Absorption) + *ESA* (for Excited State Absorption) processes (*Figure I-22* (b)) cannot take place as they need a three level acceptor. In addition the *S. H. G.* (for Second Harmonic Generation) (*Figure I-22* (e)) and the 2-photon-absorption excitation or multi-photon excitation processes (*Figure I-22* (f)) might only take place under high excitation energies of the order of 10^{10} times the integrated intensity of the terrestrial solar spectrum [40]. Those processes are thus not happening in our system. The two processes that may occur in our Tb-Yb co-doped system are the cooperative sensitization (*Figure I-22* (c)) and the cooperative luminescence (*Figure I-22* (d)).

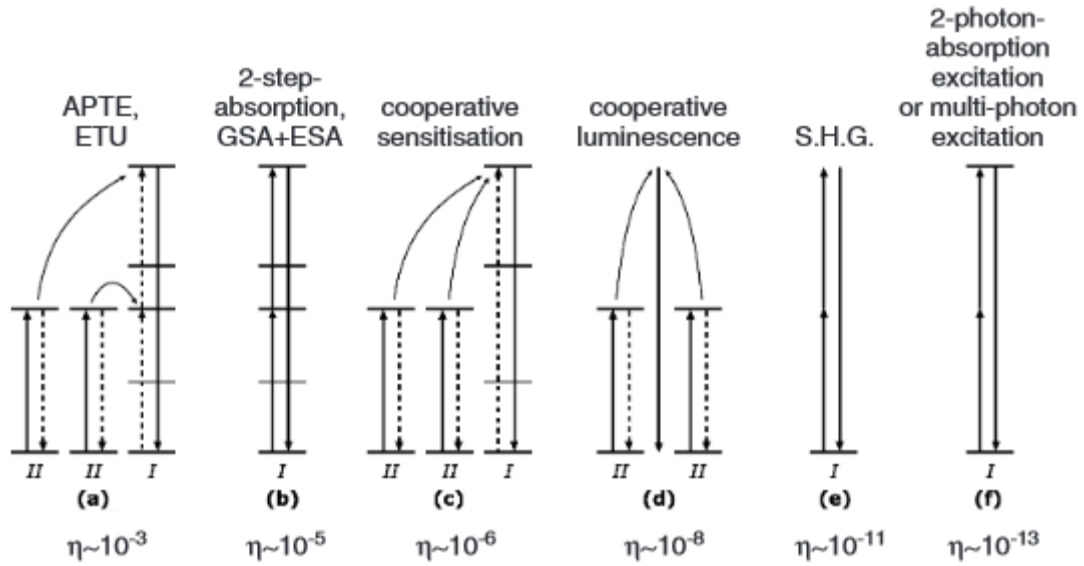


Figure I-22: Schematics of the different up-conversion processes with the quantum efficiency. The quantum efficiencies of the cooperative sensitization and luminescence processes were obtained in materials doped Tb^{3+} and Yb^{3+} , and Yb^{3+} alone, respectively. From [22,57].

The multiphonon-relaxation [130] might also occur at any stage of the DC process (in the terbium or ytterbium ions). An excited impurity (here RE ion) may relax radiatively or non-radiatively. In the case of the non-radiative decay, if the difference in level energies is higher than the energy of a single phonon, several phonons may be created simultaneously. However, the rate of this transition is dependent of the number of phonons emitted so of the width between the energy levels and the maximum energy of a phonon in the matrix. The more phonons are created, the smaller the transition rate is. For more than 4 to 6 phonons, the multiphonon-relaxation transition will be negligible compared to the radiative ones [131,132]. In our case, the phonon energy in the SiN_x matrix is 484 cm^{-1} [133]. Table I-1 shows that in both cases, Tb and Yb, the number of phonons created to relax to the closest energy level is far higher than 6. Consequently, the multiphonon-relaxation is negligible in front of the radiative transitions in our system.

	levels	Energy	Phonon number
Tb	$^5D_4 \rightarrow ^7F_0$	15000 cm^{-1}	31
Yb	$^2F_{5/2} \rightarrow ^2F_{7/2}$	10100 cm^{-1}	21

Table I-1: Number of phonons necessary to achieve a multiphonon-relaxation transition between two closest energy levels of Tb and Yb.

The cross-relaxation (Figure I-23 (a)) between two identical RE ions also called self-quenching might also decrease the DC process efficiency. The cross-relaxation happens between an ion in its excited state and another one in its ground state. During this energy transfer, the drop in energy of

the first ion is equal to the increase in energy of the second. This way, they both end up in an intermediate excited state. In our system, Tb^{3+} ion does not have an intermediate energy level. Thus, the cross-relaxation will not take place in our system.

The migration (*Figure I-23 (b)*) between identical *RE* ions (sensitizers) may be detrimental to the *DC* process efficiency if, instead of transporting the energy to the activator, it transports it to a defect that will trap the energy.

Thus, the processes that may decrease the *DC* process efficiency in our system are the two cooperative up-conversion transfers and the migration to a defect.

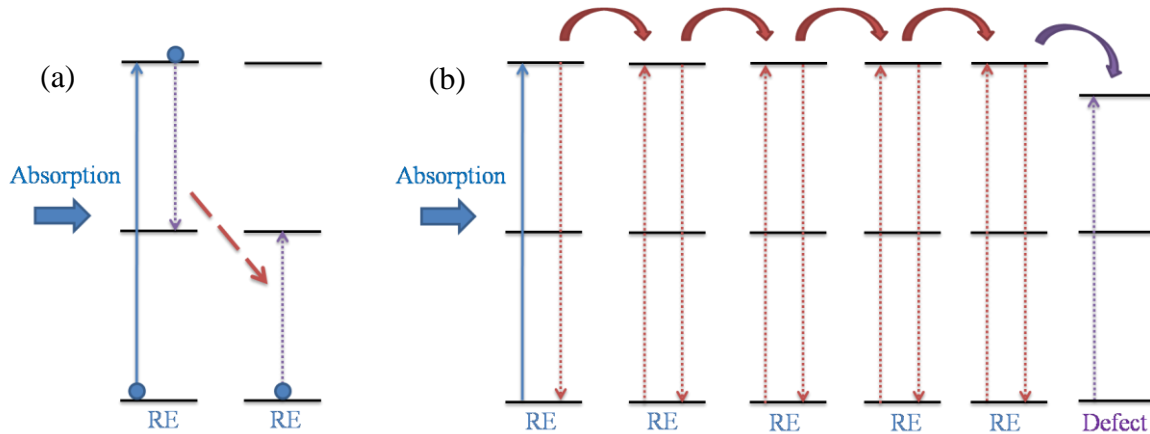


Figure I-23: Mechanisms of the (a) cross section and (b) migration processes.

1.5. Conclusion

The major aim of this thesis is to develop a *DC* layer compatible with the silicon solar cells fabrication process that will increase the efficiency of the cells. For this purpose, our layer should present an efficiency as high as possible. As reference, we would like to create a layer that shows a higher efficiency than the 186 % internal quantum yield of the $SiO_xN_y:Tb^{3+}-Yb^{3+}$ layer obtained by a previous work done by our team [134].

The $Tb^{3+}-Yb^{3+}$ couple has been studied extensively and proved to display an efficient energy conversion process [84,135] that leads to the emission of IR photons which energy corresponds perfectly to the silicon bandgap [22]. We thus use this couple in our study. The SiO_xN_y matrix was previously chosen for its compatibility with *c-Si* solar cells. However, the oxygen of the matrix is thought to favor the formation of oxide *RE* clusters [136,137] that would reduce the *RE* ions emission. Thus, in this study we investigate the silicon nitride matrix that is compatible with *c-Si* solar cells since such layers are widely used in the Si solar cell industry as anti-reflective [138] or passivation [139] layers.

Bibliography

- [1] IPCC Intergovernmental Panel on Climate Change, (n.d.). http://www.ipcc.ch/home_languages_main_french.shtml.
- [2] WEO2015SpecialReportonEnergyandClimateChange.pdf, (n.d.). <https://www.iea.org/publications/freepublications/publication/WEO2015SpecialReportonEnergyandClimateChange.pdf> (accessed January 18, 2016).
- [3] J.-M. Tarascon, Stockage et conversion de l'énergie: synthèse et perspectives, (2011). https://www.college-de-france.fr/media/jean-marie-tarascon/UPL19361_tarascon_20110323.pdf (accessed April 18, 2016).
- [4] http://www.eia.gov/Energyexplained/?page=solar_thermal_power_plants, (n.d.).
- [5] How do Photovoltaics Work? - NASA Science, (n.d.). <http://science.nasa.gov/science-news/science-at-nasa/2002/solarcells/> (accessed January 20, 2016).
- [6] A.E. Becquerel, Mémoire sur les effets électriques produits sous l'influence des rayons solaires, *Comptes Rendus À Académie Sci.* (1839) 561.
- [7] A.E. Becquerel, Recherches sur les effets de la radiation chimique de la lumière solaire au moyen des courants électriques, *Comptes Rendus À Académie Sci.* (1839) 145.
- [8] D. Chapin, Fuller, Pearson, A new silicon p-n junction photocell for converting solar radiation into electrical power, *J. Appl. Phys.* 25 (1954) 676.
- [9] Solar Cells, (2008). <http://org.ntnu.no/solarcells/index.php>.
- [10] Bright outlook for solar cells, *Environ. Res. Web.* (n.d.). <http://environmentalresearchweb.org/cws/article/news/30489>.
- [11] I. Dincer, Renewable energy and sustainable development: a crucial review, *Renew. Sustain. Energy Rev.* 4 (2000) 157–175.
- [12] CEF Converse Energy Future, (n.d.). <http://www.conserve-energy-future.com/>.
- [13] Energy Innovation_Policy and technology LLC, (2015). <http://energyinnovation.org/2015/02/07/levelized-cost-of-energy/>.
- [14] Energy Informative, The homeowner's guide to solar panels, (n.d.). <http://energyinformative.org>.
- [15] EPIA, Solar Generation 6_Solar Photovoltaic Electricity Empowering the World, (2011). <http://www.greenpeace.org/international/Global/international/publications/climate/2011/Final%20SolarGeneration%20VI%20full%20report%20lr.pdf>.
- [16] INES Education, Cours solaire thermique - INES Education, (n.d.). <http://ines.solaire.free.fr/solpv/page0.html> (accessed October 2, 2014).
- [17] Solar Facts and Advice, (n.d.). <http://www.solar-facts-and-advice.com/>.
- [18] N. Cheung, Solar Cells Fabrication Technologies, (2010). http://www-inst.eecs.berkeley.edu/~ee143/fa10/lectures/Lec_26.pdf (accessed April 18, 2016).
- [19] NREL, (n.d.). <http://www.nrel.gov/ncpv/>.
- [20] W. Shockley, H.J. Queisser, Detailed Balance Limit of Efficiency of p-n Junction Solar Cells, *J. Appl. Phys.* 32 (1961) 510–519. doi:10.1063/1.1736034.
- [21] W.G. Pfann, W. Van Roosbroeck, Radioactive and Photoelectric p-n Junction Power Sources, *J. Appl. Phys.* 25 (1954) 1422. doi:10.1063/1.1721579.
- [22] B.M. van der Ende, L. Aarts, A. Meijerink, Lanthanide ions as spectral converters for solar cells, *Phys. Chem. Chem. Phys.* 11 (2009) 11081. doi:10.1039/b913877c.
- [23] J.P. Wolfe, Thermodynamics of excitons in semiconductors, *Phys. Today.* 35 (1982) 46. doi:10.1063/1.2914968.
- [24] T. Tiedje, E. Yablonovitch, G.D. Cody, B.G. Brooks, Limiting Efficiency of Silicon Solar Cells, *IEEE Trans. Electron Devices.* (1984) 711.
- [25] B.S. Richards, Enhancing the performance of silicon solar cells via the application of passive luminescence conversion layers, *Sol. Energy Mater. Sol. Cells.* 90 (2006) 2329–2337.

doi:10.1016/j.solmat.2006.03.035.

- [26] PVEducation, (n.d.). <http://www.pveducation.org/>.
- [27] Solar cell operating principles, (n.d.). <http://ocw.tudelft.nl/fileadmin/ocw/courses/SolarCells/res00019/!37204c6f7373657320616e64206f7074696d697a6174696f6e.pdf>.
- [28] E. Yablonovitch, G.D. Cody, Intensity Enhancement in Textured Optical Sheets.pdf, IEEE Trans. Electron Devices. ED-29 (1982) 300–305.
- [29] H. Sai, Y. Kanamori, K. Arafune, Y. Ohshita, M. Yamaguchi, Light trapping effect of submicron surface textures in crystalline Si solar cells, Prog. Photovolt. Res. Appl. 15 (2007) 415–423. doi:10.1002/pip.754.
- [30] J. Zhao, M. Green, others, Optimized antireflection coatings for high-efficiency silicon solar cells, Electron Devices IEEE Trans. On. 38 (1991) 1925–1934.
- [31] D. Bouhafs, A. Moussi, A. Chikouche, J.M. Ruiz, Design and simulation of antireflection coating systems for optoelectronic devices: Application to silicon solar cells, Sol. Energy Mater. Sol. Cells. 52 (1998) 79–93.
- [32] M. Cid, N. Stem, C. Brunetti, A.F. Beloto, C.A.S. Ramos, Improvements in anti-reflection coatings for high-efficiency silicon solar cells, Surf. Coat. Technol. 106 (1998) 117–120.
- [33] D.N. Wright, E.S. Marstein, A. Holt, Double layer anti-reflective coatings for silicon solar cells, in: Photovolt. Spec. Conf. 2005 Conf. Rec. Thirty-First IEEE, IEEE, 2005: pp. 1237–1240. http://ieeexplore.ieee.org/xpls/abs_all.jsp?arnumber=1488363 (accessed December 14, 2015).
- [34] R.W. Miles, K.M. Hynes, I. Forbes, Photovoltaic solar cells: An overview of state-of-the-art cell development and environmental issues, Prog. Cryst. Growth Charact. Mater. 51 (2005) 1–42. doi:10.1016/j.pcrysgrow.2005.10.002.
- [35] M. Yamaguchi, T. Takamoto, K. Araki, N. Ekins-Daukes, Multi-junction III–V solar cells: current status and future potential, Sol. Energy. 79 (2005) 78–85. doi:10.1016/j.solener.2004.09.018.
- [36] N.V. Yastrebova, High-efficiency multi-junction solar cells: Current status and future potential, (2007). <http://sunlab.eecs.uottawa.ca/wp-content/uploads/2014/pdf/HiEfficMjSc-CurrStatusFuturePotential.pdf>.
- [37] N.A. Gokcen, J.J. Loferski, Efficiency of tandem solar cell systems as a function of temperature and solar energy concentration ratio, Sol. Energy Mater. 1 (1979) 271–286.
- [38] C.H. Henry, Limiting efficiencies of ideal single and multiple energy gap terrestrial solar cells, J. Appl. Phys. 51 (1980) 4494. doi:10.1063/1.328272.
- [39] T.N.D. Tibbits, P. Beutel, New efficiency frontiers with wafer-bonded multi-junction solar cells, in: Amsterdam, 2014. https://www.ise.fraunhofer.de/de/veroeffentlichungen/konferenzbeitraege/konferenzbeitraege-2014/29th-eupvsec/tibbits_-4cp.2.1.pdf (accessed January 26, 2016).
- [40] C. Strümpel, M. McCann, G. Beaucarne, V. Arkhipov, A. Slaoui, V. Švrček, C. del Cañizo, I. Tobias, Modifying the solar spectrum to enhance silicon solar cell efficiency—An overview of available materials, Sol. Energy Mater. Sol. Cells. 91 (2007) 238–249. doi:10.1016/j.solmat.2006.09.003.
- [41] T. Trupke, A. Shalav, B.S. Richards, P. Würfel, M.A. Green, Efficiency enhancement of solar cells by luminescent up-conversion of sunlight, Sol. Energy Mater. Sol. Cells. 90 (2006) 3327–3338. doi:10.1016/j.solmat.2005.09.021.
- [42] E. Klampaftis, D. Ross, K.R. McIntosh, B.S. Richards, Enhancing the performance of solar cells via luminescent down-shifting of the incident spectrum: A review, Sol. Energy Mater. Sol. Cells. 93 (2009) 1182–1194. doi:10.1016/j.solmat.2009.02.020.
- [43] W.G.J.H.M. van Stark, A. Meijerink, R.E.I. Schropp, Chap 1: Solar Spectrum Conversion for Photovoltaics Using Nanoparticles of Third Generation Photovoltaics, Vasilis Fthenakis. (2012). doi:10.5772/39213.

- [44] D.L. Dexter, A Theory of Sensitized Luminescence in Solids, *J. Chem. Phys.* 21 (1953) 836–850. doi:10.1063/1.1699044.
- [45] T. Förster, Zwischenmolekulare Energiewanderung und Fluoreszenz, *Ann. Phys.* 2 (1948) 55.
- [46] J. Cardin, Synthèse, caractérisation et modélisation de matériaux en couches minces pour l'optique en vue d'applications, HDR, 2016. <https://hal.archives-ouvertes.fr/tel-01271560/document> (accessed May 24, 2016).
- [47] D.L. Dexter, Possibility of Luminescent Quantum Yields Greater than Unity, *Phys. Rev.* 108 (1957) 630–633. doi:10.1103/PhysRev.108.630.
- [48] W.W. Piper, J.A. DeLuca, F.S. Ham, Cascade fluorescent decay in Pr³⁺-doped fluorides: Achievement of a quantum yield greater than unity for emission of visible light, *J. Lumin.* 8 (1974) 344–348. doi:10.1016/0022-2313(74)90007-6.
- [49] J.L. Sommerdijk, A. Bril, A.W. de Jager, Two photon luminescence with ultraviolet excitation of trivalent praseodymium, *J. Lumin.* 8 (1974) 341–343. doi:10.1016/0022-2313(74)90006-4.
- [50] J.L. Sommerdijk, A. Bril, A.W. de Jager, Luminescence of Pr³⁺-Activated fluorides, *J. Lumin.* 9 (1974) 288–296. doi:10.1016/0022-2313(74)90041-6.
- [51] R. Pappalardo, Calculated quantum yields for photon-cascade emission (PCE) for Pr³⁺ and Tm³⁺ in fluoride hosts, *J. Lumin.* 14 (1976) 159–193. doi:10.1016/S0022-2313(76)90592-5.
- [52] C.R. Ronda, Phosphors for lamps and displays: an applicational view, *J. Alloys Compd.* 225 (1995) 534–538. doi:10.1016/0925-8388(94)07065-2.
- [53] R.T. Wegh, H. Donker, A. Meijerink, R.J. Lamminmäki, J. Hölsä, Vacuum-ultraviolet spectroscopy and quantum cutting for Gd³⁺ in LiYF₄, *Phys. Rev. B.* 56 (1997) 13841–13848. doi:10.1103/PhysRevB.56.13841.
- [54] C. Ronda, Luminescent materials with quantum efficiency larger than 1, status and prospects, *J. Lumin.* 100 (2002) 301–305.
- [55] R.T. Wegh, H. Donker, K.D. Oskam, A. Meijerink, Visible Quantum Cutting in LiGdF₄:Eu³⁺ Through Downconversion, *Science.* 283 (1999) 663–666. doi:10.1126/science.283.5402.663.
- [56] R.T. Wegh, H. Donker, K.D. Oskam, A. Meijerink, Visible quantum cutting in Eu³⁺-doped gadolinium fluorides via downconversion, *J. Lumin.* 82 (1999) 93–104. doi:10.1016/S0022-2313(99)00042-3.
- [57] F. Auzel, Upconversion processes in coupled ion systems, *J. Lumin.* 45 (1990) 341–345. doi:10.1016/0022-2313(90)90189-I.
- [58] R.T. Wegh, E.V.D. van Loef, A. Meijerink, Visible quantum cutting via downconversion in LiGdF₄: Er³⁺, Tb³⁺ upon Er³⁺ 4f¹¹→4f¹⁰5d excitation, *J. Lumin.* 90 (2000) 111–122. doi:10.1016/S0022-2313(99)00621-3.
- [59] T. Trupke, M.A. Green, P. Würfel, Improving solar cell efficiencies by down-conversion of high-energy photons, *J. Appl. Phys.* 92 (2002) 1668–1674. doi:10.1063/1.1492021.
- [60] T. Trupke, P. Würfel, M. Green, others, Up-and down-conversion as new means to improve solar cell efficiencies, in: *Photovolt. Energy Convers. 2003 Proc. 3rd World Conf. On, IEEE*, 2003: pp. 67–70. http://ieeexplore.ieee.org/xpls/abs_all.jsp?arnumber=1305221 (accessed January 29, 2016).
- [61] C.R. Ronda, T. Jüstel, H. Nikol, Rare earth phosphors: fundamentals and applications, *J. Alloys Compd.* 275 (1998) 669–676.
- [62] G.B. Haxel, J.B. Hedrick, G.J. Orris, P.H. Stauffer, J.W. Hendley II, Rare earth elements: critical resources for high technology, 2002. <http://pubs.er.usgs.gov/publication/fs08702>.
- [63] R. Paschotta, J. Nilsson, P.R. Barber, J.E. Caplen, A.C. Tropper, D.C. Hanna, Lifetime quenching in Yb-doped fibres, *Opt. Commun.* 136 (1997) 375–378. doi:10.1016/S0030-4018(96)00720-1.
- [64] G.H. Dieke, Spectra and Energy Levels of Rare Earth Ions in Crystals, (1968). <http://tocs.ulb.tu-darmstadt.de/22403175.pdf> (accessed January 29, 2016).
- [65] W.T. Carnall, G.L. Goodman, K. Rajnak, R.S. Rana, A systematic analysis of the spectra of

- the lanthanides doped into single crystal LaF₃, *J. Chem. Phys.* 90 (1989) 3443–3457.
doi:10.1063/1.455853.
- [66] B.R. Judd, Optical absorption intensities of rare-earth ions, *Phys. Rev.* 127 (1962) 750.
- [67] G.S. Ofelt, Intensities of Crystal Spectra of Rare-Earth Ions, *J. Chem. Phys.* 37 (1962) 511.
doi:10.1063/1.1701366.
- [68] C.-L. Cheng, J.-Y. Yang, Hydrothermal Synthesis of Eu³⁺-Doped Y(OH)₃ Nanotubes as Downconversion Materials for Efficiency Enhancement of Screen-Printed Monocrystalline Silicon Solar Cells, *IEEE Electron Device Lett.* 33 (2012) 697–699.
doi:10.1109/LED.2012.2187771.
- [69] J. Liu, Q. Yao, Y. Li, Effects of downconversion luminescent film in dye-sensitized solar cells, *Appl. Phys. Lett.* 88 (2006) 173119. doi:10.1063/1.2198825.
- [70] B. Liu, Y. Chen, C. Shi, H. Tang, Y. Tao, Visible quantum cutting in BaF₂: Gd, Eu via downconversion, *J. Lumin.* 101 (2003) 155–159.
- [71] T.T. Basiev, M.E. Doroshenko, V.V. Osiko, Cooperative nonradiative cross-relaxation in crystals of La (1- x) CexF₃ solid solutions, *J. Exp. Theor. Phys. Lett.* 71 (2000) 8–11.
- [72] D. Chen, Y. Wang, Y. Yu, P. Huang, F. Weng, Near-infrared quantum cutting in transparent nanostructured glass ceramics, *Opt. Lett.* 33 (2008) 1884–1886.
- [73] B.M. van der Ende, L. Aarts, A. Meijerink, Near-Infrared Quantum Cutting for Photovoltaics, *Adv. Mater.* 21 (2009) 3073–3077. doi:10.1002/adma.200802220.
- [74] K. Deng, X. Wei, X. Wang, Y. Chen, M. Yin, Near-infrared quantum cutting via resonant energy transfer from Pr³⁺ to Yb³⁺ in LaF₃, *Appl. Phys. B.* 102 (2011) 555–558.
doi:10.1007/s00340-011-4413-7.
- [75] Y.-S. Xu, F. Huang, B. Fan, C.-G. Lin, S.-X. Dai, L.-Y. Chen, Q.-H. Nie, H.-L. Ma, X.-H. Zhang, Quantum cutting in Pr³⁺-Yb³⁺ codoped chalcogenide glasses for high-efficiency c-Si solar cells, *Opt. Lett.* 39 (2014) 2225. doi:10.1364/OL.39.002225.
- [76] J.J. Eilers, D. Biner, J.T. van Wijngaarden, K. Krämer, H.-U. Güdel, A. Meijerink, Efficient visible to infrared quantum cutting through downconversion with the Er³⁺-Yb³⁺ couple in Cs₃Y₂Br₉, *Appl. Phys. Lett.* 96 (2010) 151106. doi:10.1063/1.3377909.
- [77] V.D. Rodríguez, V.K. Tikhomirov, J. Méndez-Ramos, A.C. Yanes, V.V. Moshchalkov, Towards broad range and highly efficient down-conversion of solar spectrum by Er³⁺-Yb³⁺ co-doped nano-structured glass-ceramics, *Sol. Energy Mater. Sol. Cells.* 94 (2010) 1612–1617. doi:10.1016/j.solmat.2010.04.081.
- [78] V.K. Tikhomirov, V.D. Rodríguez, J. Méndez-Ramos, J. del-Castillo, D. Kirilenko, G. Van Tendeloo, V.V. Moshchalkov, Optimizing Er/Yb ratio and content in Er-Yb co-doped glass-ceramics for enhancement of the up- and down-conversion luminescence, *Sol. Energy Mater. Sol. Cells.* 100 (2012) 209–215. doi:10.1016/j.solmat.2012.01.019.
- [79] S. Ye, B. Zhu, J. Luo, J. Chen, G. Lakshminarayana, J. Qiu, Enhanced cooperative quantum cutting in Tm³⁺-Yb³⁺ codoped glass ceramics containing LaF₃ nanocrystals, *Opt. Express.* 16 (2008) 8989–8994.
- [80] L. Xie, Y. Wang, H. Zhang, Near-infrared quantum cutting in YPO₄:Yb³⁺, Tm³⁺ via cooperative energy transfer, *Appl. Phys. Lett.* 94 (2009) 061905.
doi:10.1063/1.3078823.
- [81] W.J. Park, S.J. Oh, J.K. Kim, J. Heo, T. Wagner, L. Strizik, Down-conversion in Tm³⁺/Yb³⁺ doped glasses for multicrystalline silicon photo-voltaic module efficiency enhancement, *J. Non-Cryst. Solids.* 383 (2014) 181–183.
doi:10.1016/j.jnoncrysol.2013.03.037.
- [82] Y. Tai, G. Zheng, H. Wang, J. Bai, Broadband down-conversion based near infrared quantum cutting in Eu²⁺-Yb³⁺ co-doped SrAl₂O₄ for crystalline silicon solar cells, *J. Solid State Chem.* 226 (2015) 250–254. doi:10.1016/j.jssc.2015.02.020.
- [83] K. Deng, T. Gong, L. Hu, X. Wei, Y. Chen, M. Yin, Efficient near-infrared quantum cutting in NaYF₄: Ho³⁺, Yb³⁺ for solar photovoltaics, *Opt. Express.* 19 (2011) 1749–1754.

doi:10.1364/OE.19.001749.

- [84] P. Vergeer, T.J.H. Vlugt, M.H.F. Kox, M.I. den Hertog, J.P.J.M. van der Eerden, A. Meijerink, Quantum cutting by cooperative energy transfer in $\text{YbxY}_{1-x}\text{PO}_4:\text{Tb}^{3+}$, *Phys. Rev. B.* 71 (2005) 014119. doi:10.1103/PhysRevB.71.014119.
- [85] J.-L. Yuan, X.-Y. Zeng, J.-T. Zhao, Z.-J. Zhang, H.-H. Chen, X.-X. Yang, Energy transfer mechanisms in Tb^{3+} , Yb^{3+} codoped Y_2O_3 downconversion phosphor, *J. Phys. Appl. Phys.* 41 (2008) 105406. doi:10.1088/0022-3727/41/10/105406.
- [86] Q. Duan, F. Qin, D. Wang, W. Xu, J. Cheng, Z. Zhang, W. Cao, Quantum cutting mechanism in Tb^{3+} - Yb^{3+} co-doped oxyfluoride glass, *J. Appl. Phys.* 110 (2011) 113503. doi:10.1063/1.3662916.
- [87] Z. Pan, G. Sekar, R. Akrobetu, R. Mu, S.H. Morgan, Visible to near-infrared down-conversion luminescence in Tb^{3+} and Yb^{3+} co-doped lithium–lanthanum–aluminosilicate oxyfluoride glass and glass-ceramics, *J. Non-Cryst. Solids.* 358 (2012) 1814–1817. doi:10.1016/j.jnoncrysol.2012.05.028.
- [88] H. Lin, S. Zhou, H. Teng, Y. Li, W. Li, X. Hou, T. Jia, Near infrared quantum cutting in heavy Yb doped $\text{Ce}_{0.03}\text{Yb}_{3x}\text{Y}_{(2.97-3x)}\text{Al}_5\text{O}_{12}$ transparent ceramics for crystalline silicon solar cells, *J. Appl. Phys.* 107 (2010) 043107. doi:10.1063/1.3298907.
- [89] D. Chen, Y. Wang, Y. Yu, P. Huang, F. Weng, Quantum cutting downconversion by cooperative energy transfer from Ce^{3+} to Yb^{3+} in borate glasses, *J. Appl. Phys.* 104 (2008) 116105. doi:10.1063/1.3040005.
- [90] Q.Y. Zhang, C.H. Yang, Z.H. Jiang, X.H. Ji, Concentration-dependent near-infrared quantum cutting in $\text{GdBO}_3:\text{Tb}^{3+}, \text{Yb}^{3+}$ nanophosphors, *Appl. Phys. Lett.* 90 (2007) 061914. doi:10.1063/1.2472195.
- [91] X. Chen, J. Wu, X. Xu, Y. Zhang, N. Sawanobori, C. Zhang, Q. Pan, G.J. Salamo, Three-photon infrared quantum cutting from single species of rare-earth Er^{3+} ions in $\text{Er}_0.3\text{Gd}_0.7\text{VO}_4$ crystalline, *Opt. Lett.* 34 (2009) 887–889.
- [92] C. Ming, F. Song, L. An, X. Ren, Highly efficient quantum cutting in Yb/Pr-codoped $\text{NaY}(\text{WO}_4)_2$ crystal, *Curr. Appl. Phys.* 14 (2014) 1028–1030. doi:10.1016/j.cap.2014.05.012.
- [93] Q.Y. Zhang, C.H. Yang, Y.X. Pan, Cooperative quantum cutting in one-dimensional $(\text{YbxGd}_{1-x})\text{Al}_3(\text{BO}_3)_4:\text{Tb}^{3+}$ nanorods, *Appl. Phys. Lett.* 90 (2007) 021107. doi:10.1063/1.2430942.
- [94] H. Lin, D. Chen, Y. Yu, A. Yang, Y. Wang, Near-infrared quantum cutting in $\text{Ho}^{3+}/\text{Yb}^{3+}$ codoped nanostructured glass ceramic, *Opt. Lett.* 36 (2011) 876.
- [95] G. Lakshminarayana, J. Qiu, Near-infrared quantum cutting in $\text{RE}^{3+}/\text{Yb}^{3+}$ ($\text{RE}=\text{Pr}, \text{Tb}$, and Tm): $\text{GeO}_2\text{-B}_2\text{O}_3\text{-ZnO-L}_a\text{F}_3$ glasses via downconversion, *J. Alloys Compd.* 481 (2009) 582–589. doi:10.1016/j.jallcom.2009.03.034.
- [96] Y. Teng, J. Zhou, X. Liu, S. Ye, J. Qiu, Efficient broadband near-infrared quantum cutting for solar cells, *Opt. Express.* 18 (2010) 9671–9676. doi:10.1364/OE.18.009671.
- [97] B. Dieudonné, B. Boulard, G. Alombert-Goget, A. Chiasera, Y. Gao, S. Kodjikian, M. Ferrari, Up- and down-conversion in $\text{Yb}^{3+}\text{-Pr}^{3+}$ co-doped fluoride glasses and glass ceramics, *J. Non-Cryst. Solids.* 377 (2013) 105–109. doi:10.1016/j.jnoncrysol.2012.12.025.
- [98] B.S. Richards, Luminescent layers for enhanced silicon solar cell performance: Down-conversion, *Sol. Energy Mater. Sol. Cells.* 90 (2006) 1189–1207. doi:10.1016/j.solmat.2005.07.001.
- [99] D. Chen, Y. Yu, Y. Wang, P. Huang, F. Weng, Cooperative Energy Transfer Up-Conversion and Quantum Cutting Down-Conversion in $\text{Yb}^{3+}:\text{TbF}_3$ Nanocrystals Embedded Glass Ceramics, *J. Phys. Chem. C.* 113 (2009) 6406–6410. doi:10.1021/jp809995f.
- [100] J. Zhou, Y. Zhuang, S. Ye, Y. Teng, G. Lin, B. Zhu, J. Xie, J. Qiu, Broadband downconversion based infrared quantum cutting by cooperative energy transfer from Eu^{2+} to Yb^{3+} in glasses, *Appl. Phys. Lett.* 95 (2009) 141101. doi:10.1063/1.3242335.
- [101] X. Liu, S. Ye, Y. Qiao, G. Dong, B. Zhu, D. Chen, G. Lakshminarayana, J. Qiu, Cooperative

- downconversion and near-infrared luminescence of Tb³⁺–Yb³⁺ codoped lanthanum borogermanate glasses, *Appl. Phys. B.* 96 (2009) 51–55. doi:10.1007/s00340-009-3478-z.
- [102] F. Mady, J.-B. Duchez, Y. Mebrouk, M. Benabdesselam, A physical model of the photo- and radiation-induced degradation of ytterbium-doped silica optical fibres, in: *AIP Conf. Proc.*, 2014. <https://hal.archives-ouvertes.fr/hal-01223816/> (accessed April 21, 2016).
- [103] I.A.A. Terra, L.J. Borrero-González, T.R. Figueredo, J.M.P. Almeida, A.C. Hernandez, L.A.O. Nunes, O.L. Malta, Down-conversion process in Tb³⁺–Yb³⁺ co-doped Calibo glasses, *J. Lumin.* 132 (2012) 1678–1682. doi:10.1016/j.jlumin.2012.02.019.
- [104] Y.T. An, Rare Earth doped Silicon based thin film for quantum cutting in solar cell, Université de Caen Basse Normandie, 2013.
- [105] Y.-T. An, C. Labbé, J. Cardin, M. Morales, F. Gourbilleau, Highly Efficient Infrared Quantum Cutting in Tb³⁺- Yb³⁺ Codoped Silicon Oxynitride for Solar Cell Applications, *Adv. Opt. Mater.* 1 (2013) 855–862.
- [106] L. Dumont, J. Cardin, P. Benzo, M. Carrada, C. Labbé, A.L. Richard, D.C. Ingram, W.M. Jadwisienczak, F. Gourbilleau, SiN_x:Tb³⁺–Yb³⁺, an efficient down-conversion layer compatible with a silicon solar cell process, *Sol. Energy Mater. Sol. Cells.* 145 (2016) 84–92. doi:10.1016/j.solmat.2015.09.031.
- [107] J. Weimmerskirch-Aubatin, Propriétés de luminescence et caractérisation structurale de films minces d'oxyde de silicium dopés au cérium et co-dopés cérium-ytterbium, Université de Lorraine, 2014. http://docnum.univ-lorraine.fr/public/DDOC_T_2014_0180_WEIMMERSKIRCH.pdf (accessed January 22, 2016).
- [108] X.Y. Huang, D.C. Yu, Q.Y. Zhang, Enhanced near-infrared quantum cutting in GdBO₃:Tb³⁺, Yb³⁺ phosphors by Ce³⁺ codoping, *J. Appl. Phys.* 106 (2009) 113521. doi:10.1063/1.3267484.
- [109] Q. Zhang, J. Wang, G. Zhang, Q. Su, UV photon harvesting and enhanced near-infrared emission in novel quantum cutting Ca₂BO₃Cl:Ce³⁺, Tb³⁺, Yb³⁺ phosphor, *J. Mater. Chem.* 19 (2009) 7088. doi:10.1039/b906954b.
- [110] S. Yerci, R. Li, S.O. Kucheyev, T. van Buuren, S.N. Basu, L. Dal Negro, Energy transfer and 1.54 μm emission in amorphous silicon nitride films, *Appl. Phys. Lett.* 95 (2009) 031107. doi:10.1063/1.3184790.
- [111] J. Robertson, M.J. Powell, Gap states in silicon nitride, *Appl. Phys. Lett.* 44 (1984) 415–417. doi:10.1063/1.94794.
- [112] C. Mo, L. Zhang, C. Xie, T. Wang, Luminescence of nanometer-sized amorphous silicon nitride solids, *J. Appl. Phys.* 73 (1993) 5185–5188. doi:10.1063/1.353796.
- [113] M. Wang, M. Xie, L. Ferraioli, Z. Yuan, D. Li, D. Yang, L. Pavesi, Light emission properties and mechanism of low-temperature prepared amorphous SiN_x films. I. Room-temperature band tail states photoluminescence, *J. Appl. Phys.* 104 (2008) 083504. doi:10.1063/1.2996292.
- [114] Chapter2 Fundamentals, in: n.d. http://www.diss.fu-berlin.de/diss/servlets/MCRFileNodeServlet/FUDISS_derivate_000000001571/02_Chapter2.pdf?hosts= (accessed May 24, 2016).
- [115] S. Hasegawa, M. Matsuda, Y. Kurata, Bonding configuration and defects in amorphous SiN_x:H films, *Appl. Phys. Lett.* 58 (1991) 741. doi:10.1063/1.104533.
- [116] H. Kato, N. Kashio, Y. Ohki, K.S. Seol, T. Noma, Band-tail photoluminescence in hydrogenated amorphous silicon oxynitride and silicon nitride films, *J. Appl. Phys.* 93 (2003) 239. doi:10.1063/1.1529292.
- [117] M. Molinari, H. Rinnert, M. Vergnat, Evolution with the annealing treatments of the photoluminescence mechanisms in a-SiN_x:H alloys prepared by reactive evaporation, *J. Appl. Phys.* 101 (2007) 123532. doi:10.1063/1.2749283.
- [118] S.V. Deshpande, E. Gulari, S.W. Brown, S.C. Rand, Optical properties of silicon nitride films

- deposited by hot filament chemical vapor deposition, *J. Appl. Phys.* 77 (1995) 6534–6541. doi:10.1063/1.359062.
- [119] W.L. Warren, J. Kanicki, J. Robertson, P.M. Lenahan, Energy level of the nitrogen dangling bond in amorphous silicon nitride, *Appl. Phys. Lett.* 59 (1991) 1699–1701. doi:10.1063/1.106222.
- [120] L. Zhang, H. Jin, W. Yang, Z. Xie, H. Miao, L. An, Optical properties of single-crystalline α -Si₃N₄ nanobelts, *Appl. Phys. Lett.* 86 (2005) 061908. doi:10.1063/1.1862753.
- [121] J.M. Shannon, S.C. Deane, B. McGarvey, J.N. Sandoe, Current induced drift mechanism in amorphous SiN_x:H thin film diodes, *Appl. Phys. Lett.* 65 (1994) 2978. doi:10.1063/1.112482.
- [122] F. Giorgis, P. Mandracci, L. Dal Negro, C. Mazzoleni, L. Pavesi, Optical absorption and luminescence properties of wide-band gap amorphous silicon based alloys, *J. Non-Cryst. Solids.* 266 (2000) 588–592.
- [123] J. Kistner, X. Chen, Y. Weng, H.P. Strunk, M.B. Schubert, J.H. Werner, Photoluminescence from silicon nitride—no quantum effect, *J. Appl. Phys.* 110 (2011) 023520. doi:10.1063/1.3607975.
- [124] S. Yerci, Rui Li, S.O. Kucheyev, T. van Buuren, S.N. Basu, L. Dal Negro, Visible and 1.54 μm Emission From Amorphous Silicon Nitride Films by Reactive Cosputtering, *IEEE J. Sel. Top. Quantum Electron.* 16 (2010) 114–123. doi:10.1109/JSTQE.2009.2032516.
- [125] E. Steveler, H. Rinnert, X. Devaux, M. Dossot, M. Vergnat, Indirect excitation of Er³⁺ ions in silicon nitride films prepared by reactive evaporation, *Appl. Phys. Lett.* 97 (2010) 221902. doi:10.1063/1.3521279.
- [126] T. Förster, 10th Spiers Memorial Lecture. Transfer mechanisms of electronic excitation, *Discuss Faraday Soc.* 27 (1959) 7–17. doi:10.1039/DF9592700007.
- [127] Fluorescence Resonance Energy Transfer (FRET), (n.d.). <https://www.amherst.edu/media/view/106141/original/FRET.pdf> (accessed May 24, 2016).
- [128] S.A. Hussain, An introduction to fluorescence resonance energy transfer (FRET), *ArXiv Prepr. ArXiv09081815*. (2009). <http://arxiv.org/abs/0908.1815> (accessed May 24, 2016).
- [129] D.L. Andrews, R.D. Jenkins, A quantum electrodynamical theory of three-center energy transfer for upconversion and downconversion in rare earth doped materials, *J. Chem. Phys.* 114 (2001) 1089. doi:10.1063/1.1323958.
- [130] S.A. Egorov, J.L. Skinner, On the theory of multiphonon relaxation rates in solids, *J. Chem. Phys.* 103 (1995) 1533. doi:10.1063/1.469775.
- [131] S. Tanabe, H. Hayashi, T. Hanada, N. Onodera, Fluorescence properties of Er³⁺ ions in glass ceramics containing LaF₃ nanocrystals, *Opt. Mater.* 19 (2002) 343–349.
- [132] M.J. Weber, Selective Excitation and Decay of Er³⁺ Fluorescence in La F₃, *Phys. Rev.* 156 (1967) 231.
- [133] K.A. Nasyrov, V.A. Gritsenko, Y.N. Novikov, E.H. Lee, S.Y. Yoon, C.W. Kim, Two-bands charge transport in silicon nitride due to phonon-assisted trap ionization, *J. Appl. Phys.* 96 (2004) 4293–4296.
- [134] Y.-T. An, C. Labbé, M. Morales, P. Marie, F. Gourbilleau, Fabrication and photoluminescence properties of Tb-doped nitrogen-rich silicon nitride films, *Phys. Status Solidi C.* 9 (2012) 2207–2210.
- [135] Y. Wang, L. Xie, H. Zhang, Cooperative near-infrared quantum cutting in Tb³⁺, Yb³⁺ codoped polyborates La_{0.99-x}Yb_xBaB₉O₁₆:Tb_{0.01}, *J. Appl. Phys.* 105 (2009) 023528. doi:10.1063/1.3056382.
- [136] A. Monteil, S. Chaussedent, G. Alombert-Goget, N. Gaumer, J. Obriot, S.J.L. Ribeiro, Y. Messaddeq, A. Chiasera, M. Ferrari, Clustering of rare earth in glasses, aluminum effect: experiments and modeling, *J. Non-Cryst. Solids.* 348 (2004) 44–50. doi:10.1016/j.jnoncrysol.2004.08.124.
- [137] M.J. Lochhead, K.L. Bray, Rare-earth clustering and aluminum codoping in sol-gel silica: investigation using europium (III) fluorescence spectroscopy, *Chem. Mater.* 7 (1995) 572–

577.

- [138] W.R. Taube, A. Kumar, R. Saravanan, P.B. Agarwal, P. Kothari, B.C. Joshi, D. Kumar, Efficiency enhancement of silicon solar cells with silicon nanocrystals embedded in PECVD silicon nitride matrix, *Sol. Energy Mater. Sol. Cells.* 101 (2012) 32–35.
doi:10.1016/j.solmat.2012.02.010.
- [139] C. Leguijt, P. Lölgen, J.A. Eikelboom, A.W. Weeber, F.M. Schuurmans, W.C. Sinke, P.F.A. Alkemade, P.M. Sarro, C.H.M. Maree, L.A. Verhoef, Low temperature surface passivation for silicon solar cells, *Sol. Energy Mater. Sol. Cells.* 40 (1996) 297–345.

Chapter II: Experimental techniques

In this chapter we will review the different techniques employed to analyze the properties of our layers. First, the layer fabrication steps, that are the deposition and the annealing processes, will be detailed. Then, the structural characterization techniques followed by the optical ones will be exposed. Last, the simulation models used to interpret the results will be described.

II.1. Layers fabrication

The layers were deposited by radiofrequency reactive magnetron co-sputtering which principle will be explained in the following section. The experimental setup employed will also be described as well as the specificities of our particular sputtering machine. After the deposition process, the layers were annealed. The two possible annealing processes are detailed.

II.1.1. Deposition: Radiofrequency Reactive Magnetron Co-Sputtering

II.1.1.1. Principle

The sputtering technique is a physical vapor deposition (*PVD*) technique that enables the deposition of nanometers thin to micrometers thick layers. This technique condenses elements on a substrate from the sputtering of solid phase materials called targets.

In a chamber under vacuum (10^{-7} mTorr) (*Figure II-1*) a plasma is created from an inert gas such as argon. The association of the negative polarization of the target (cathode) with a rarefied atmosphere of argon leads to the creation of an electrical glow discharge between the target and the chamber walls, which leads to the formation of a plasma. The plasma positive ions are accelerated toward the target by the potential difference in between the target (charged negatively) and the substrate, and chamber walls (charged positively). Those ions thus acquire energy that will be released during the ions collision with the target surface. Multiple effects may then take place (*Figure II-2*). (i) an atom may be ejected because of its high energy. (ii) the incident ion may be implanted in the target. (iii) the incident ion may be backscattered at the target surface and then be neutralized by charge transfer. (iv) secondary electrons may also be emitted and will sustain the plasma. All these phenomena are called sputtering. The influence of those different phenomena is dependent of the discharge characteristics, and of the chemical and physical properties of the target. The sputtering yield Y , corresponding to the number of sputtered atoms divided by the number of

incident atoms, increases linearly with the ion energy. Y is also inversely proportional to the sublimation energy of the material. Y is also dependent on the respective masses of the ion and of the target material.

The mobility and the energy of the species arriving on the substrate are dependent of the sputtering parameters such as the target power density, the chamber pressure, the deposition temperature, and the distance between the target and the substrate.

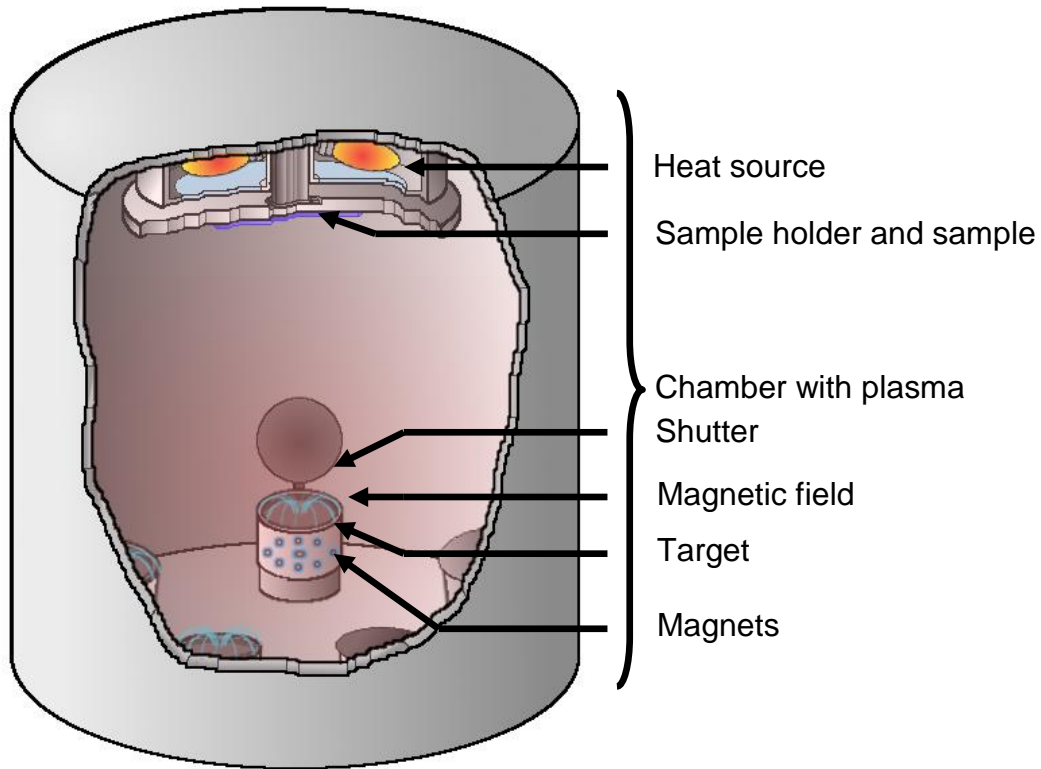


Figure II-1: Reactive magnetron co-sputtering diagram.

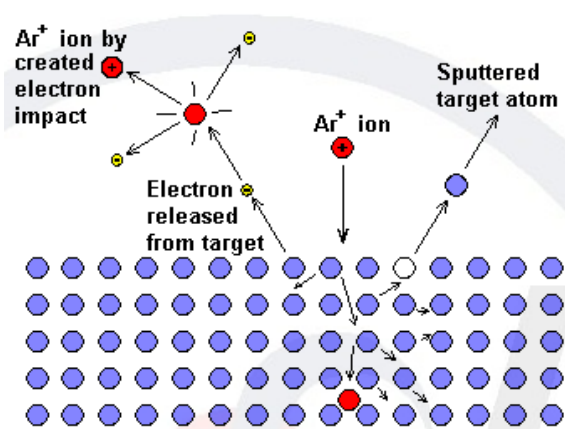


Figure II-2: Scheme of the different interactions of the plasma ions with the target. From [1].

The description above represents the basic working of a sputtering machine. The machine we employed has various improvements described below:

a) Co-sputtering

Several targets may be used simultaneously with a confocal setup. The targets are slightly inclined toward the interior of the chamber so that the substrate is situated at the focal point of all the targets leading to the deposition of a homogeneous layer on the substrate. Using several targets instead of only one allows to deposit more complex materials.

b) Magnetron sputtering

A magnetic field is generated by magnets, placed in circle with one bigger in the center, below each target (*Figure II-1*). This principle consists in applying a magnetic field in the vicinity of the targets to favor the species sputtering which accelerate the low pressure deposition rate. The emitted electrons are confined in the vicinity of the surface of the targets by the magnetic field. The plasma density is thus increased by around one order of magnitude.

c) Reactive sputtering

It consists in introducing in the chamber a chemically non-inert gas (H_2 , O_2 , N_2) in addition of the inert gas. This gas will chemically react in the plasma and at the substrate surface with the sputtered species. Reactive sputtering is commonly used to deposit oxides, carbides, or nitrides. The composition of the layer may be monitored by controlling the respective flux of inert and non-inert gases in the chamber, $f(Ar)$ and $f(N_2)$ respectively. In this study, we will speak of nitrogen ratio, rN_2 , given by the following equation:

$$rN_2(\%) = \left(\frac{f(N_2)}{f(N_2) + f(Ar)} \right) \times 100\% \quad \text{II-1}$$

d) Radiofrequency sputtering

In the case of insulating materials, the use of a DC power supply is impossible. Indeed, positive charges accumulate at the top of the target because the current cannot go through the target. This accumulation of charges then stops the sputtering process as the cations of the plasma are not attracted anymore toward the target. To overcome this problem, the use of a AC system is recommended.

II.1.1.2. Experimental setup

The thin layers of this study were deposited using an Orion 5 UHV magnetron sputtering machine from AJA international. The machine is made up of five targets. Up to four targets can be used simultaneously. The substrate is placed at the same distance of all the targets (10 cm) and is rotating at 20 rpm during the whole deposition process to ensure the layer homogeneity (~ 1 nm difference on a 4" wafer). Prior to deposition, the vacuum in the chamber is between 10^{-7} and 10^{-8} mTorr. The pressure is maintained by the combination of a molecular turbo-pump and a primary pump. Two halogen lamps situated above the substrate holder heat the substrate up to 850 °C.

In case of our Tb-Yb co-doped silicon nitride, the layers are deposited using solid targets which are metallic for terbium, and ytterbium and semiconductor for silicon. The reactive sputtering is obtained by introducing nitrogen as well as argon in the chamber during deposition.

During this work, the deposition parameters that are investigated are: (i) the plasma pressure (between 2 and 4 mTorr), (ii) the nitrogen ratio (between 14 and 30 %), the terbium target power density (between 0.3 and 1.8 W/cm²), and the ytterbium target power density (between 0.1 and 0.55 W/cm²). The silicon target power density is fixed at 4.5 W/cm². The layers deposited are around 90 nm thick for a better comparison between them.

II.1.2. Annealing processes

After being deposited, the layers are annealed in order to improve their optical properties [2]. The annealing allows the recovery of the defects of the matrix (vacancy, dangling bonds) as well as the reorganization of the material, if the energy provided via the heat is higher than the atomic motion barrier that will let the atoms diffuse through the material. However, annealing the samples at too high a temperature might also contribute to the formation of silicon and/or rare earth nanoparticles.

Two types of annealing approaches were employed in this study: classical thermal annealing (*CTA*), and rapid thermal annealing (*RTA*). Those two approaches follow the same four steps but are dissimilar regarding how each step is running (*Figure II-X2*).

II.1.2.1. Classical Thermal Annealing

The tubular furnace (*Figure II-3*) is first heated to the required annealing temperature, ranging from 200 °C to 1000 °C, under vacuum (~15 mTorr). A 48 sccm (Standard Cubic Centimeters per Minute) N₂ flow is then injected in the furnace during 20 min to lower the oxygen content in the furnace. The sample is placed in a nacelle (at the load lock) and transferred to the furnace. A previous study [3] determined that the transfer time is fixed at 90 s by the motorization of the transfer system. The same study gave a 2 to 12 °C/s temperature rising rate of the sample once in the furnace depending of the annealing temperature. The sample is then annealed under vacuum (~37 mTorr) and a N₂ flow (48 sccm) for a determined time (usually 1 h). Then, the sample is removed from the furnace and cooled under N₂ (*Figure II-4 (left)*).

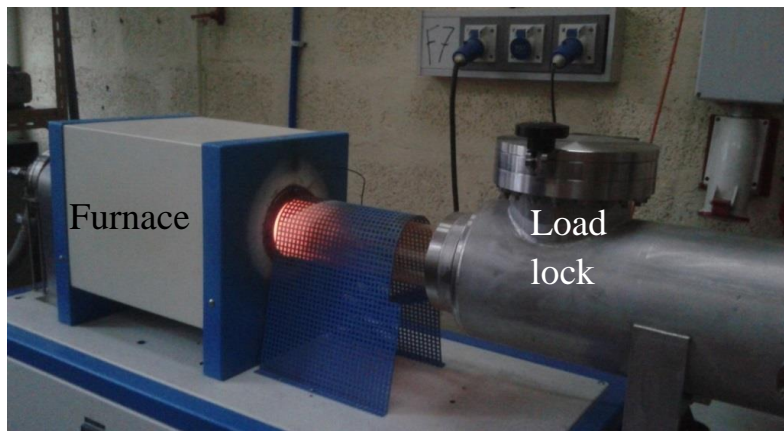


Figure II-3: Tubular furnace used to make CTA processes.

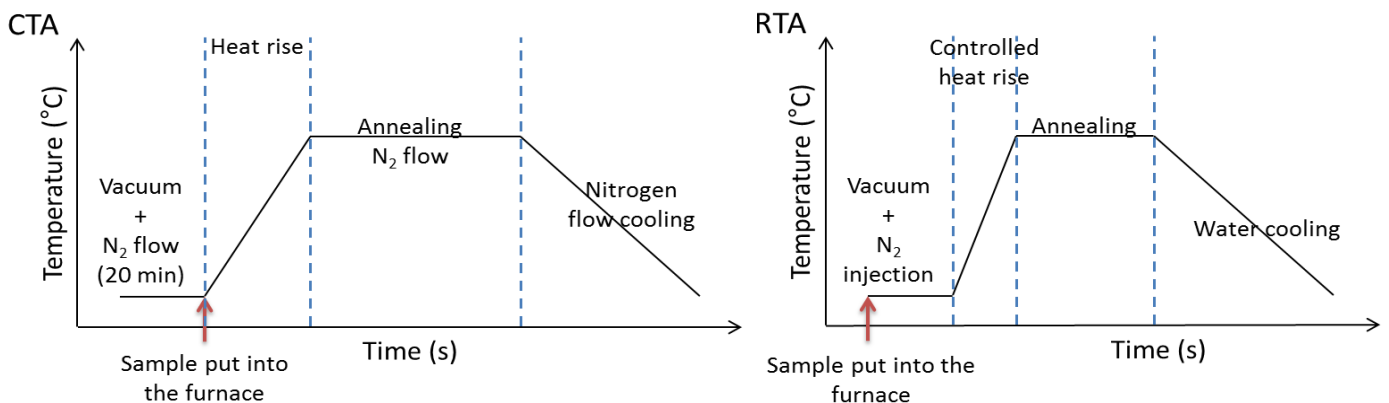


Figure II-4: Schematics of the CTA (left) and RTA (right) annealing cycles.

II.1.2.2. Rapid Thermal Annealing

The furnace is entirely automated. In this case the sample is placed directly in the furnace at room -temperature and -pressure. The furnace is first pumped to ~15 mTorr pressure. N₂ is then injected until room pressure is reached. The heating lamps are switched on and the temperature rising rate is fixed at 20 °C/s. The sample stays at temperature during a given time (about 10 min). At the end of the fixed annealing time, the lamps are switched off and the furnace is cooled down by a circulating water flow in its chamber walls (*Figure II-4 (right)*).

II.2. Structural and composition characterizations

In this part we will review the principle and the setup used of the structural and composition characterization technics employed in this work namely the Fourier Transform Infrared spectroscopy, the Transmission Electron Microscopy, the Rutherford Backscattering Spectroscopy, and the X-ray Photoelectron Spectroscopy.

II.2.1. Fourier Transform Infrared Spectroscopy

II.2.1.1. Principle

The Fourier Transform Infrared Spectroscopy (*FTIR*) enables the study of the chemical bonds between the different atoms of a molecule. This method is based on the molecule vibrational states. The most common schemes used are two heteroatoms systems (that are dependent of their surrounding in the molecule) (*Figure II-5 (a) and (b)*). Several vibrational mode types exist: (i) the stretching vibrations, ν_{AB} (*Figure II-5 (a)*), and (ii) the bending vibrations, δ_{AB} (*Figure II-5 (b)*). Such system will vibrate (or rotate) only if the received energy is equal to the energy difference between two of its vibrational levels:

$$\Delta E = E_1 - E_2 \quad \text{II-2}$$

Thus, when an IR beam interacts with the system, only the parts of the beam that have frequencies ν corresponding to the ΔE of the system will be absorbed following the equation:

$$\Delta E = h \cdot \nu \quad \text{II-3}$$

With $h = 6.626 \cdot 10^{-34}$ Js, the Planck constant

The absorption spectrum ensuing from the polychromatic mid-IR beam interaction with the sample is characteristic of its constituting molecules. The spectrum gives qualitative (nature of the bonds) and quantitative (concentrations of the various elements of the material) information on the sample.

In this work most of the vibrational modes observed are stretching modes and particularly symmetric stretching (also called breathing) modes that see the atoms vibrating in phase with each other along the bonds. Other vibrational modes may have been observed such as the asymmetric stretching mode that reflects the atoms vibrating out of phase with each other along the bonds, the rocking mode representing the atoms oscillating together in a direction perpendicular to the bonds plan, and the rocking mode coming from the oscillation of the atoms together in the same direction in the bonds plan.

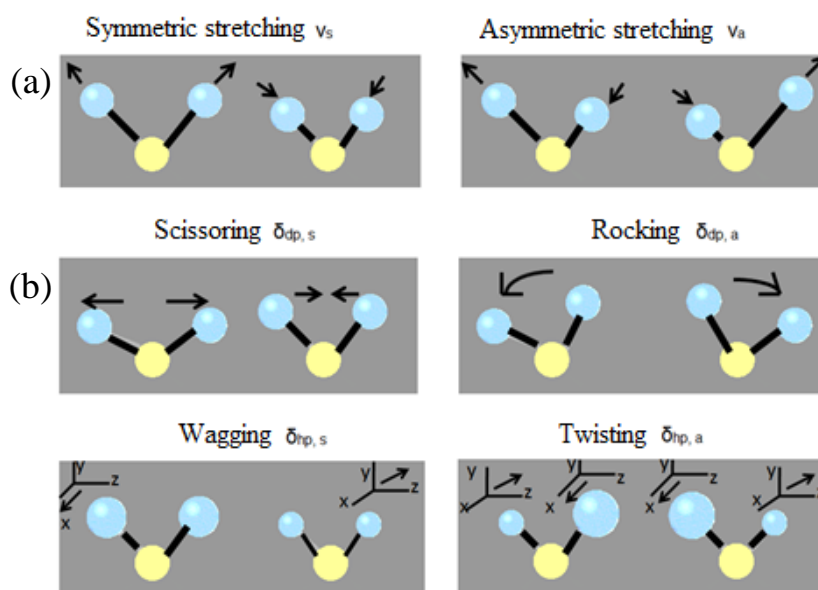


Figure II-5: Vibrational states: (a) Stretching vibrations, and (b) bending vibrations.

II.2.1.2. Experimental setup

The *FTIR* measurements were performed with a Thermo Nicolet Nexus 750-II that can record a spectrum on the 4000 to 400 cm^{-1} range with a 5 cm^{-1} resolution at room temperature. All the measurements were carried out in transmission mode.

The machine (*Figure II-6 (a)*) presents two light sources. The first one is a laser He-Ne 633 nm that enables in the one hand to align the system before any measurement, and in the other hand to trigger the interferometer operation during a measurement. The second one is a tungsten filament lamp that emits between 2.5 and $25\text{ }\mu\text{m}$ and is used for the measurements. The tungsten lamp generates a middle IR-polychromatic beam that goes through a Michelson interferometer. Thanks to a beam splitter and two mirrors, one fixed and the other mobile (*Figure II-6 (b)*), the incoming polychromatic beam is turned into an interferogram.

This interferogram has the particularity that each of its composing data point has information about every infrared frequency of the initial beam. Thus all frequencies are measured simultaneously, which provide results extremely fast. In order to obtain a frequency spectrum that enables interpretation, a Fourier transform is applied on the interferogram.

The signal of the beam that goes through the sample is attenuated at some specific wavelengths characteristic of the bonds of the material creating peaks. Those peaks called absorption peaks allow to determine the material composition. However, to obtain a spectrum representative of the material, the spectra of the substrate alone as well as of H₂O and CO₂ have to be subtracted from the experimental spectrum.

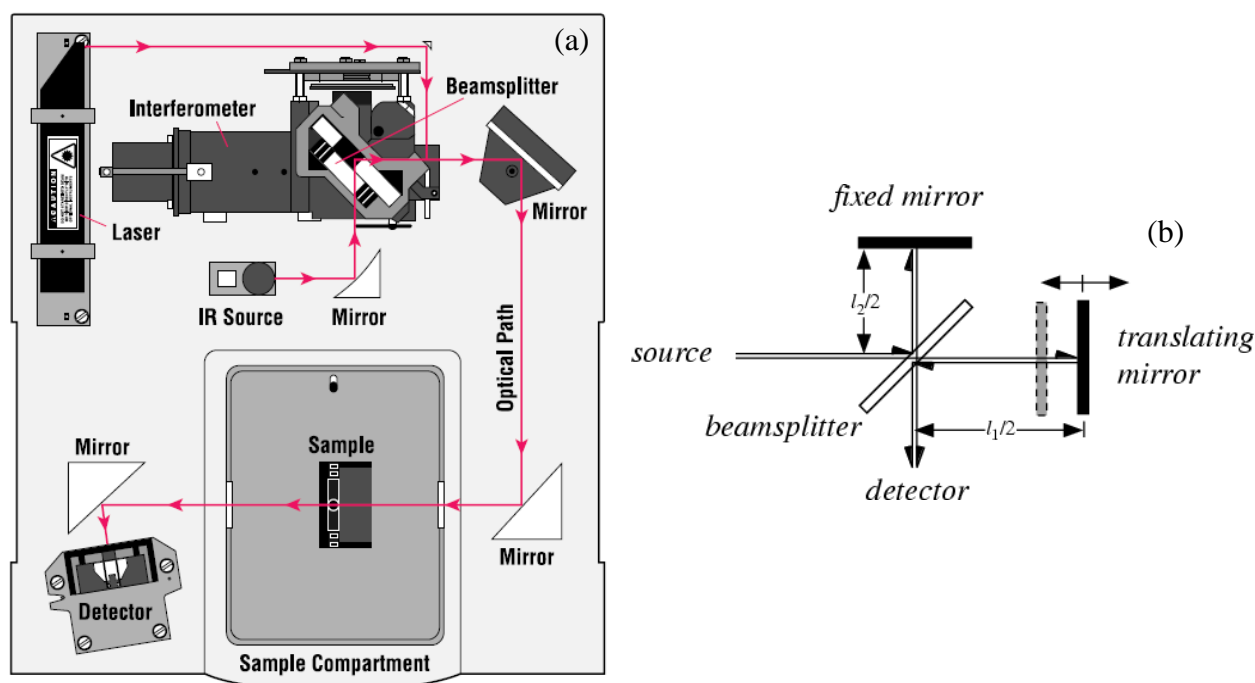


Figure II-6: FTIR operation diagram from [4] (a) and detail of the Michelson interferometer from [5] (b).

The sample is placed in a closed chamber that is continuously purged with N₂. The beam interacts with the sample at normal angle or at Brewster angle (65°).

The normal incidence spectrum only displays the transverse optical modes (TO) corresponding to the excitation of the vibrational modes parallel to the sample surface [6] while the Brewster angle spectrum displays both the transverse optical modes (TO) and the longitudinal optical modes (LO), this last corresponding to the excitation of the vibrational modes perpendicular to the sample surface.

II.2.2. Transmission Electron Microscopy

II.2.2.1. High Resolution Transmission Electron Microscopy

a) Principle

The Transmission Electron Microscopy (*TEM*) is the most powerful technique to investigate materials at the nanometer scale. A coherent electron beam is sent on a sample. If the sample is thin enough, below 40 nm, the principle of a photonic optical microscope applies. Using electrons instead of photons allows for a better resolution (10 000 times better) due to their lower wavelength as Abbe equation shows:

$$R = \frac{0.61\lambda}{n \sin u} \quad \text{II-4}$$

With n the refractive index between the objective and the material, u the objective aperture, 0.61 a coefficient linked to the Fraunhofer scattering, and λ the beam wavelength.

The electrons are focalized on the sample with which they interact with a spatial contrast corresponding to a variation of density and/or composition of the material. They are then collected by a detector that transforms the signal in a comprehensible image.

b) Experimental setup

An electron source produces an electron beam that is accelerated by an anode before going through condenser lenses that focus the beam on the sample. The electrons interacting with the sample are either absorbed or scattered (they disappeared from the beam), or transmitted depending of the density and or the composition. The transmitted electrons arrived at the bottom of the column (*Figure II-7*) and hit a fluorescent screen that allows the visualization of the sample image. The image obtained may also directly be recorded by a CCD camera.

Images of this study were obtained on several machines. Some micrographies were achieved in our laboratory by means of a JEOL 2010 FEG (using a field emission gun). In this case, the experiments were performed by Xavier Portier and myself. Other pictures were made with a Cs corrected TEM-FEG microscope Tecnai F20S in the CEMES in Toulouse where Marzia Carrada operated as part of a METSA project and the GENESE ANR project.

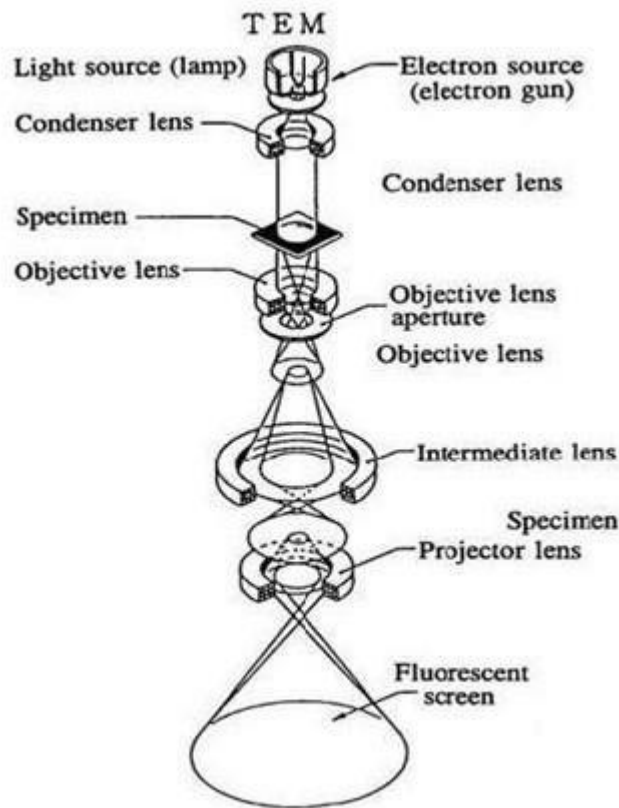


Figure II-7: TEM operation system (from [7]).

c) Modes

The microscope can be used in diffraction mode that uses the elastically scattered electrons. The lattice acts like a grating for the electrons [8] that are diffracted according to the plan perpendicular to the incident electron beam. This mode allows to access the electrons diffraction patterns (*EDP*) which is characteristic of the sample crystallographic structure. For an amorphous and nanostructured sample the *EDP* is constituted of more or less broad rings depending of the organization level of the matter.

The microscope can also be used in image mode. In this case, three types of contrast are available:

- The absorption contrast that uses all the transmitted, diffused, and diffracted electrons. As the only electrons not used are the absorbed ones, the darker areas are the ones that absorb the most. The elements with higher Z number absorbing more the electrons, they appear in darker shades.
- The diffraction contrast that can be separated in two imaging modes. The bright field mode uses only the transmitted beam that is directly collected. The areas that transmitted the most the beam are seen in bright while the areas that diffracted the beam appear in dark. The dark field mode uses only a part of the beam that has been diffracted (diaphragm). Only the areas that diffracted this particular beam direction will appear in bright. As the elements with

higher Z number scatter electrons at higher angles, they are seen in darker shades with the bright field mode and in brighter shades using the dark field mode. Those modes allow to detect crystallized particles that appears in darker shades with the bright field mode and in brighter shades with the dark field mode [9].

- The phase contrast or high resolution mode that is obtained by the interference of the transmitted beam with one diffracted one. The image ensuing displays the periodic potential created by the atoms. This allows to see the plans and columns formed by the atoms if the area observed is well aligned with respect to the electron beam.

II.2.2.2. Energy-Dispersive X-ray spectroscopy

Energy-Dispersive X-ray spectroscopy (*EDX*) analyses were performed with a *TEM* setup on the samples. This technique is used to determine the composition of the sample. The electron beam interacts with the inner shell electrons of the sample atoms and ejects them (*Figure II-8*). When outer shell electrons take their place they lose their excess energy by emitting X-rays. The X-ray energy depends of the energy level of the atoms. Thus a set of peaks is characteristic of an element. The emitted X-ray beam is directed on an X-ray detector that transforms X-ray energy into voltage. The signal is then measured by a pulsed processor and transferred to an analyzer that displays an understandable graph.

Such analysis is more accurate for heavy atoms than light ones. Moreover, the analysis precision increases for elements that are around the same weight. Only relative concentration may be obtained (concentration compared to ones of the other elements of the layer). In addition, using a *TEM* instead of a *SEM* (Scanning Electron Microscopy) allows for a better spacial resolution.

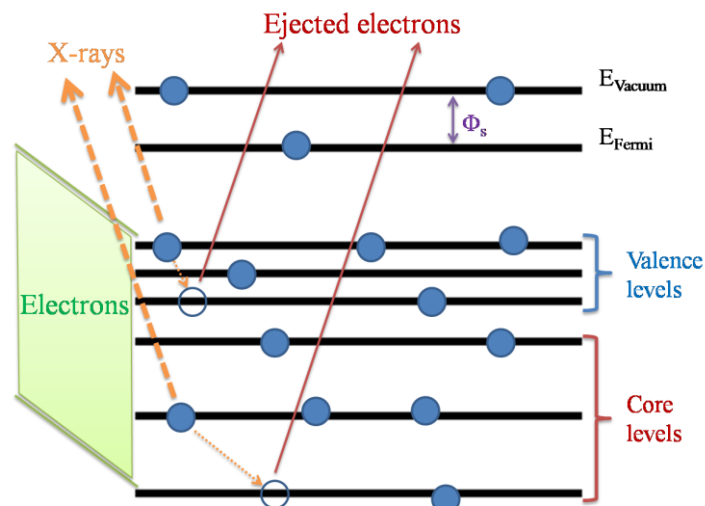


Figure II-8: Schematic of the X-rays generation from the interaction of an electron beam with an atom.

II.2.2.3. Sample preparation

Samples have to be thinned to tens of nanometers, until they are transparent to electrons. For this purpose, three methods were employed: mechanical etching with a tripod, ion etching with a precision ion polishing system (*PIPS*-Gatan), or with a focus ion beam (*FIB*-FEI).

A comparison (made in the CEMES) between the two first techniques showed a damaging of part of the sample using *PIPS* while using tripod led to an homogeneous sample.

In the CIMAP, the samples were prepared thanks to a *FIB*.

II.2.3. Rutherford Backscattering Spectroscopy

II.2.3.1. Principle

The Rutherford Backscattering Spectroscopy (*RBS*) is a quantitative analytical method. High energy ions are bombarded on a sample and are backscattered when they come into contact with the atoms of the sample. The energy of the backscattered ions depends of the element with which it interacts as well as of the distance to the sample surface this interaction occurred. Thus *RBS* allows the determination of the quantitative concentration of the elements (without the need of a calibration) as well as the depth profiling of each elements of the sample (when the *RBS* is associated with ion etching).

When a flux of high energy particles irradiates a material most of them are implanted and do not go out of the material as they have a diameter ($\sim 1e^{-15}$ m) far smaller than the spacing in between the material atoms ($\sim 2e^{-10}$ m). A small part undergoes direct elastic collision with an atom and is backscattered at an angle θ (*Figure II-9*). The backscattered particles will lose energy during the collision in itself. The amount of momentum transferred to the collided atoms depends of their mass. If the collision occurs with an atom in depth, other energy losses will take place while passing through the material both before and after the collision. The importance of the energy loss depends of the stopping power of the material (the different elements and their density) and of the velocity of the particle. Typical energy loss for 2 MeV He ranges between 100 and 800 eV/nm.

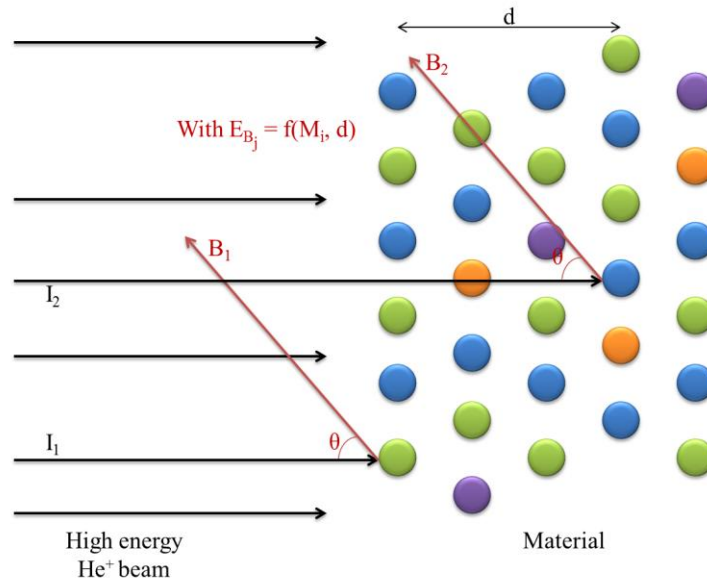


Figure II-9: Schematic of the RBS principle with I_j and B_j the incident and backscattered ions, θ the backscattering angle, d the sample thickness at which the atom is, M_i the atom atomic mass and E_{Bj} the energy of the backscattered ions. The different colors represent each a different atom.

II.2.3.2. Experimental setup

The particles irradiating the sample are He^+ ions that are obtained from He precursors. The He^+ ion beam is focalized by a quadrupole magnet into the sample in the chamber (Figure II-10). After being backscattered the ions are detected by one or several detectors that may be fixed or mobile depending of the machine. The entire machine is under vacuum (1 to 10 mTorr).

During this study, RBS measurements were performed at the Edwards Accelerator Laboratory of Ohio University by Wojciech M. Jadwisienczak using a 4.5 MV tandem accelerator. Samples, oriented with an angle of 7.5° toward beam direction, were irradiated with a 2.2 MeV $^4\text{He}^+$ ion beam. The energy resolution obtained on the sample was 20-30 keV, depending on the depth at which the analysis was performed. The elemental concentrations were calculated by fitting the data using the RUMP simulation software [10]. Stoichiometric fitting, based upon growth conditions, was completed but provided an unsatisfactory representation of the data. In order to fit the data better, non-stoichiometric fitting was completed, leading to composition errors as follows: 10 % for the silicon content, 10 % for the rare earth content, and 12.5 % for the N content.

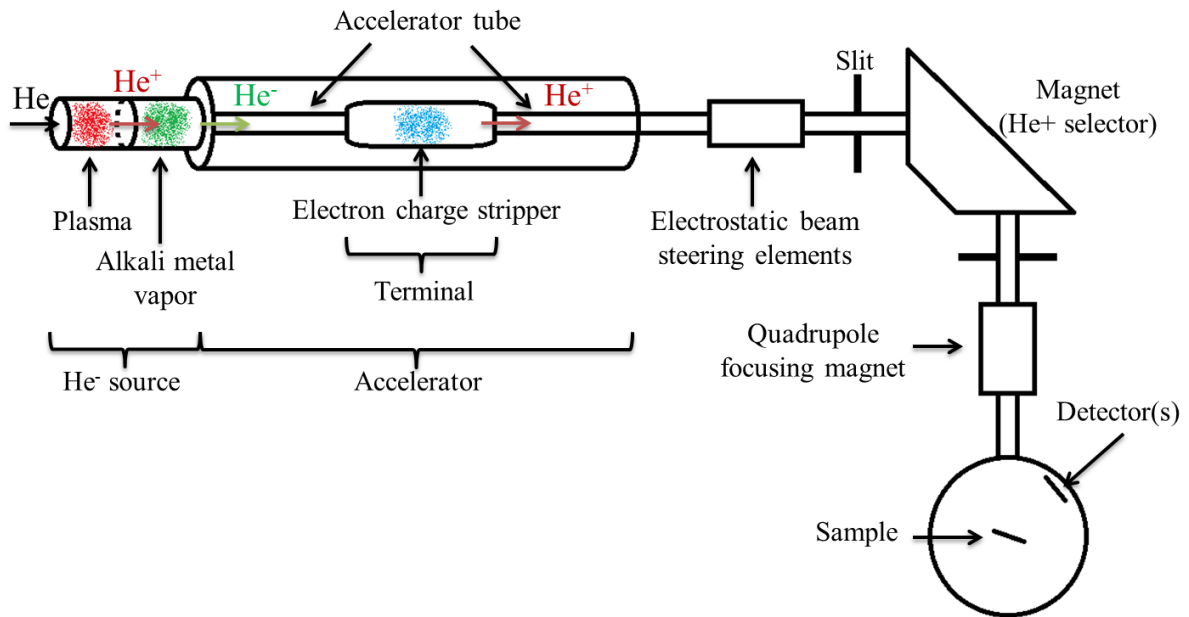


Figure II-10: RBS operation scheme.

II.2.3. X-ray Photoelectron Spectroscopy

II.2.3.1. Principle

X-ray Photoelectron Spectroscopy (*XPS*) is a non-destructive quantitative surface analysis. Thanks to the kinetic energy of heart electrons emitted after X-ray irradiation, not only the various composing elements of a material can be detected but their relative concentrations as well as their electronic states are achievable.

When a material receives an $h\gamma$ energy X-ray beam (*Figure II-11*), some of its heart or valence electrons that have an energy smaller than $h\gamma$ are ejected. During the interaction with the atom, part of the X-ray beam energy is used to break the bond and is called binding energy, E_b . The other part of the X-ray beam energy is transferred to the electron in the form of kinetic energy, E_k . The three energies are linked as follow:

$$h\gamma = E_b + E_k + \Phi_s \quad \text{II-5}$$

With Φ_s the work function (minimum thermodynamic work needed to remove an electron from a material to a point in the vacuum at the surface of this material) depending of the machine and the material.

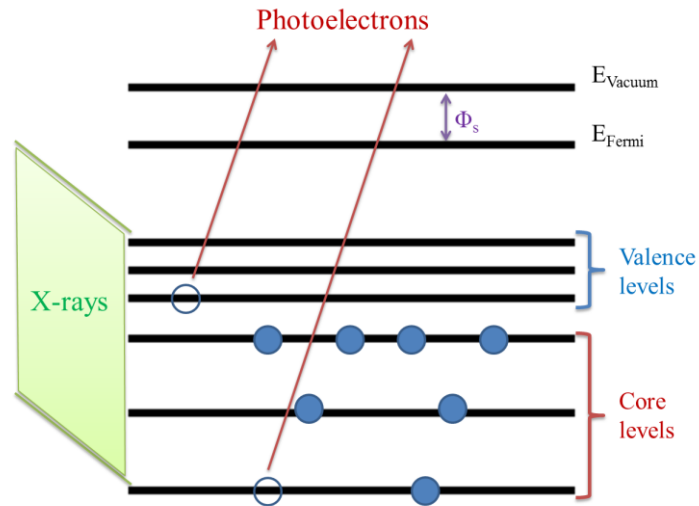


Figure II-11: Schematic of the photoelectrons generation from the interaction of an X-ray beam with an atom.

II.2.3.2. Experimental setup

An X-ray source irradiates a sample at around a 45° angle. The atoms reemit photogenerated electrons that come mainly from a 2 to 10 nm thick volume at the sample surface. Indeed the depth of analysis is dependent of inelastic mean free path of the electrons in the material that itself depends of the kinetic energy of the electron and of matrix surrounding the element. The electron beam obtained is then directed toward the analyzer and focalized on his slit. The analyzer is composed of two hemispherical electrodes that will spread the electron accordingly to their kinetic energy (Figure II-12). An electron detector is situated at the end of the analyzer and will detect the number of electron for each kinetic energy. After using the Equation II-5, a spectrum is obtained displaying the number of electrons according to their binding energy.

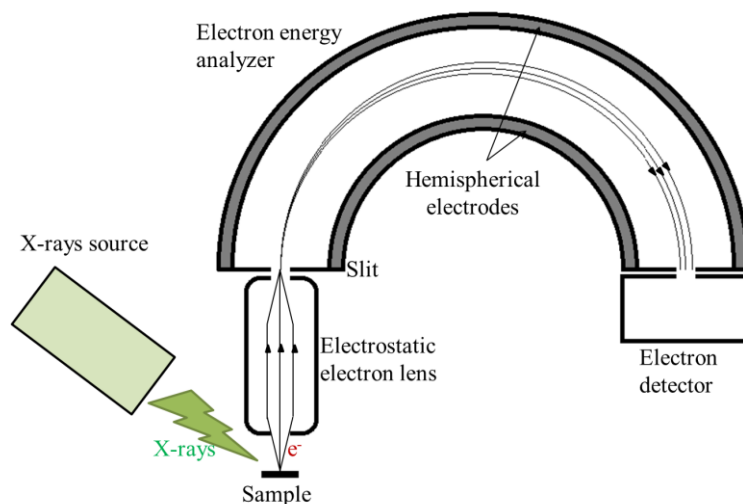


Figure II-12: XPS operating scheme.

The binding energy is characteristic of the atomic energy levels and the valence of the different elements. Thus, the position (in energy) of the peaks obtained allows to determine the elements present in the materials as well as their valence. All the elements except H and He can be detected. The detection limit is sets at 0.1 at.% concentration.

The peaks intensity is linked to the concentration of the element from which the photoelectrons are coming. The concentration of an element A, C_A , is always determined compared to another element B, C_B , (relative concentration) following the relation:

$$\frac{C_A}{C_B} = \frac{I_A \sigma_B l_B T_B}{I_B \sigma_A l_A T_A} \quad \text{II-6}$$

With σ the photoionization cross section (ionization probability in the heart level considered), l the photoelectrons mean free path, and T the spectrometer transmission.

The variation of the atom chemical surrounding influences the heart energy levels. This phenomenon is called chemical shift is expressed by a binding energy variation. This phenomenon may have various origins such as electronic state-, degree of oxidation-, or chemical bond nature-variation. Such phenomenon, and in particular the change of degree of oxidation, is expressed by the decomposition of one peak into several ones.

In this study, samples were analyzed by Marie-Paul Besland using the XPS from the Jean Rouxel Institut of Nantes.

II.3. Optical characterizations

In this part we will present the optical characterization techniques used through this study. After describing the ellipsometric spectroscopy, and the various photoluminescence spectroscopies, we will also introduce the photoconductance lifetime and external quantum efficiency measurements.

II.3.1. Ellipsometric spectroscopy

II.3.1.1. Experimental setup and principle

The phase modulated ellipsometric spectroscopy is a non-destructive technic allowing the access to a sample thickness and optical properties such as the refractive index ($\tilde{n} = n - ik$). This technique is based on measurements of the variation of the polarization state of a light beam that is reflected at the surface of a sample. The thickness of a sample can be determined from a few nm to 1 μm (the accuracy is inversely proportional to the thickness).

The ellipsometer used is a Jobin-Yvon UVISEL with an incident fixed angle of 66.2° and a spectral range of 1.5 -6 eV with a 0.05 eV resolution.

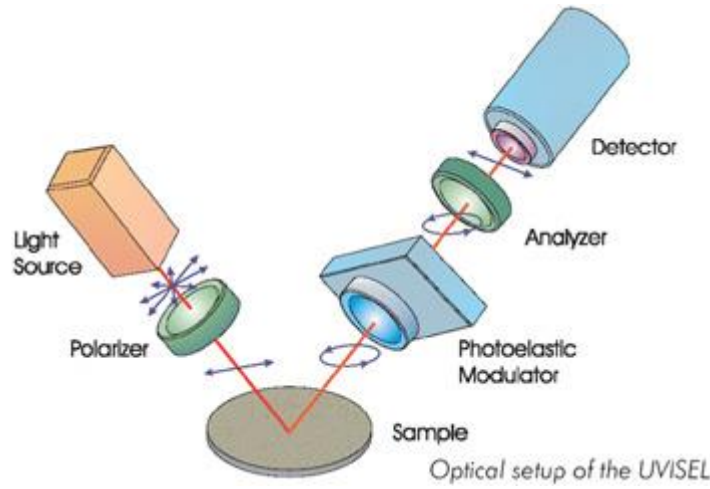


Figure II-13: Experimental setup of the UVISEL phase modulated ellipsometric spectrometer.

A large spectral range (1.5 to 6 eV) non-polarized light source (Xenon lamp) emits a beam that goes through a rectilinear polarizer set at 45° to reflect at oblique angle (66.2°) from the sample studied (Figure II-13). The reflected light then goes through a photo-elastic modulator (fused silica bar rendered bi-refractive because of an applied constrain) set at a 0° and that introduces a modulated phase shift, following the sinusoidal time depending function $\varphi(t)$, between the parallel and perpendicular components of the beam electric field. Then, the beam goes through an analyzing polarizer set at a 45° and that resolves the polarization state of the reflected light before a grating monochromator directs each wavelength sequentially toward the detector.

The detected signal I takes the form:

$$I = I_0 + I_s \sin(\varphi(t)) + I_c \cos(\varphi(t)) \quad \text{II-7}$$

With

$$I_0 = \frac{E_0^2}{4} \left(|r_p|^2 + |r_s|^2 \right) \quad \text{II-8}$$

$$I_s = I_0 \sin(2\Psi) \sin(\Delta) \quad \text{II-9}$$

$$I_c = I_0 \sin(2\Psi) \cos(\Delta) \quad \text{II-10}$$

With E_0 the electric field amplitude of the incident beam, and Ψ and Δ the ellipsometric angles that can be linked to the ratio ρ of the parallel, r_p , and perpendicular, r_s , reflection coefficients:

$$\rho = \frac{r_p}{r_s} = \tan \Psi . e^{i\Delta} \quad \text{II-11}$$

II.3.1.2. Spectrum modeling

The dielectric constants n and k , the thickness, and the roughness cannot be obtained directly from the recorded (I_s , I_c) spectra. The (I_s , I_c) spectra are characteristic of the whole sample (substrate + layer). In order to access the thickness, optical parameters and roughness of the layer specifically, we need to model our sample (*Figure II-14(1)*). This model has to correspond to the structure of the analyzed sample. In our case, a crystalline silicon substrate supporting a thin layer that may or may not display roughness.

It is also necessary to model the (I_s , I_c) spectra of both the layer and the substrate with a dispersion law model. In this study, the model called “New Amorphous” that derives from the Forouhi-Bloomer [11] model has been used and is presented below:

$$\begin{cases} k(E) = \frac{f_j(\omega - \omega_g)^2}{(\omega - \omega_j)^2 + \Gamma_j^2} & \text{si } \omega > \omega_g \\ k(E) = 0 & \text{si } \omega < \omega_g \\ n(E) = n_\infty + \frac{B(\omega - \omega_j) + C}{(\omega - \omega_j)^2 + \Gamma_j^2} \end{cases} \quad \text{II-12}$$

With:

$$\begin{cases} B = \frac{f_j}{\Gamma_j} [\Gamma_j^2 - (\omega_j - \omega_g)^2] \\ C = 2f_j\Gamma_j(\omega_j - \omega_g) \end{cases} \quad \text{II-13}$$

n_∞ , Γ_j , f_j , ω_j , and ω_g are the tunable parameters.

With n_∞ the refractive index while the energy tends to infinity, ω_g the wave energy in eV, f_j the oscillator strength of the electrons that oscillate at the resonant energy ω_j , and Γ_j the damping coefficient that models the absorption phenomenon.

The program first displays the dispersion (I_s , I_c) spectra corresponding to the initial material used (thin line). The program then adjusts the model parameters using iterative calculi (*Figure II-14(2)*) in order to obtain a modeled dispersion curve as close as possible to the experimental one by minimizing the χ^2 . The parameters of the substrate are known and fixed. Only the layer parameters are adjusted to fit the experimental (I_s , I_c) spectra. Once the experimental data fitted by the model, the optical constants n and k can then be deduced versus the wavelength (*Figure II-14(3)*) along with the layer thickness.

The absorption coefficient α can be calculated from the extinction coefficient k :

$$\alpha = \frac{4\pi k}{\lambda} = \frac{4\pi k \omega}{hc}$$

II-14

With c the speed of light, h the Planck constant, and λ the wavelength

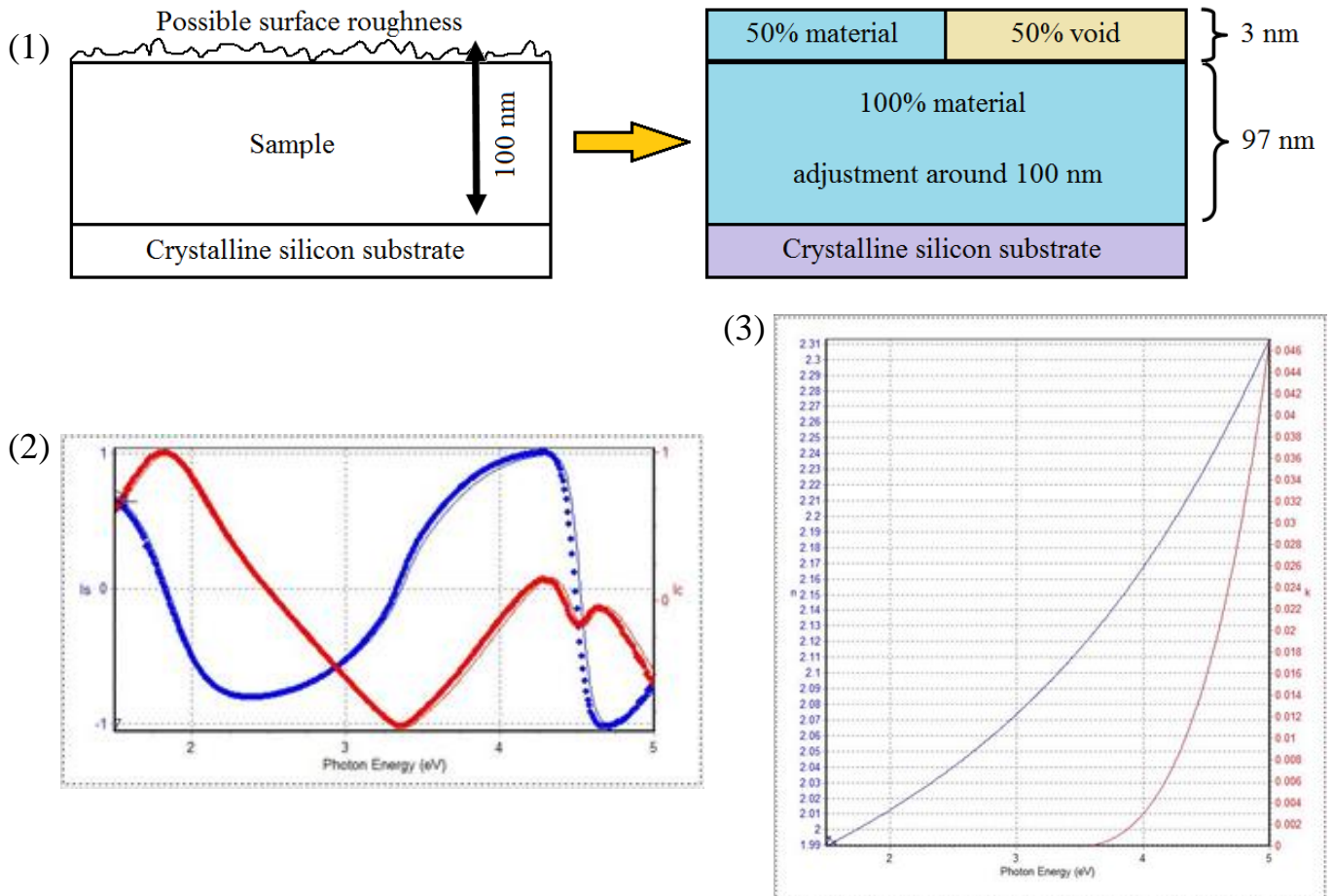


Figure II-14: Steps of the ellipsometry modelling process. (1): modelling of the sample, (2): experimental (points) and fitted (thin line) (I_s , I_c), (3): n and k resulting from the modelled material.

II.3.2. Photoluminescence Spectroscopy

II.3.2.1. General principle

The photoluminescence spectroscopy allows to investigate the electronic structure of a material. A monochromatic light beam is sent on the sample that absorbs the incident photons and acquires energy in the process (*Figure II-15*). This energy excites the electrons of the material that are then able to go from the valence band or some excited states to allowed excited energy levels. Those now excited electrons are finally de-excited toward their ground states by either a non-radiative relaxation (no light emission) or a radiative one (light emission). The radiative process emits photons and is called photoluminescence. The emitted photons go through a monochromator before being detected by a photomultiplier.

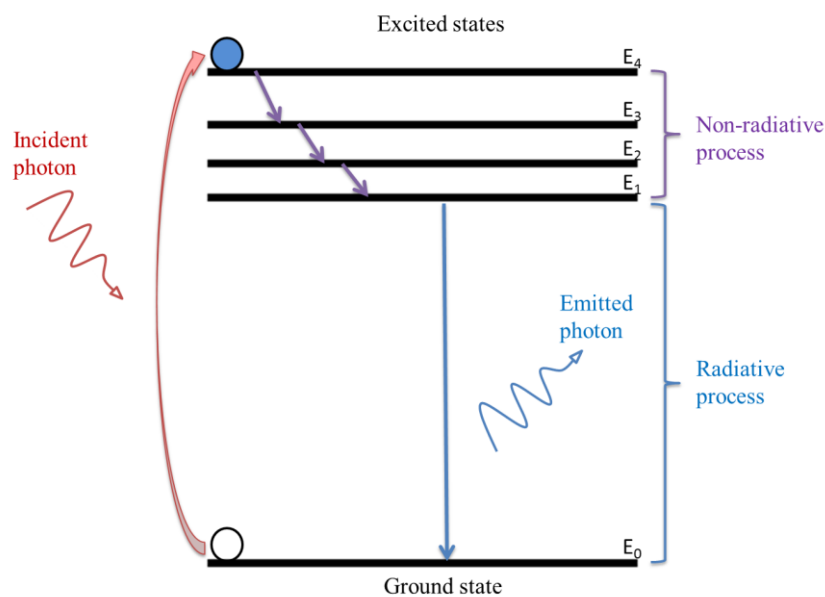


Figure II-15: Excitation and de-excitation process.

II.3.2.2. Energy resolved photoluminescence spectroscopy

a) Principle

For the energy resolved photoluminescence spectroscopy that will be called photoluminescence (*PL*) from this point, the excitation wavelength is fixed while the detector scans the whole range of reemitted wavelengths. We obtain graphs representing the reemitted light intensity according to the detected wavelengths at one excitation wavelength which gives us the energy levels of the material thus its optical characteristics.

b) Experimental setup

The measurements are carried out at room temperature. *Figure II-16* exhibits the experimental setup used to measure photoluminescence spectra. The optical excitation source is either an argon laser or a Lot-Oriel 1 kW Xenon white lamp with an OMNI300 monochromator selecting the wavelength. The laser source has a higher power density with high spectral resolution at the expense of the available wavelengths. The light beam thus emitted is chopped at 87 Hz. The light beam is then focused by lenses on the sample with an angle of incidence of 45° . A Part of the PL emitted light is collected and focused by new lenses toward the entrance slit of a MSH 300 OMNI monochromator. The collected light is then dispersed by the monochromator and detected at its exit slit by means of a Hamamatsu (R5108) photomultiplier tube. The signal thus detected is amplified and converted in a voltage signal by a trans-impedance amplifier FEMTO. The obtained signal containing all frequencies is transmitted to and filtered by the SR830 lock-in amplifier. This later referred to chopper frequency to select the intensity accordingly with the chopper frequencies. The selected signal is recorded by the computer. A LABVIEW developed software (created by Julien Cardin and Patrick Voivenel) is used as interface with the machine.

In case of comparison between layers, the *PL* intensity of each layer is divided by its thickness in μm .

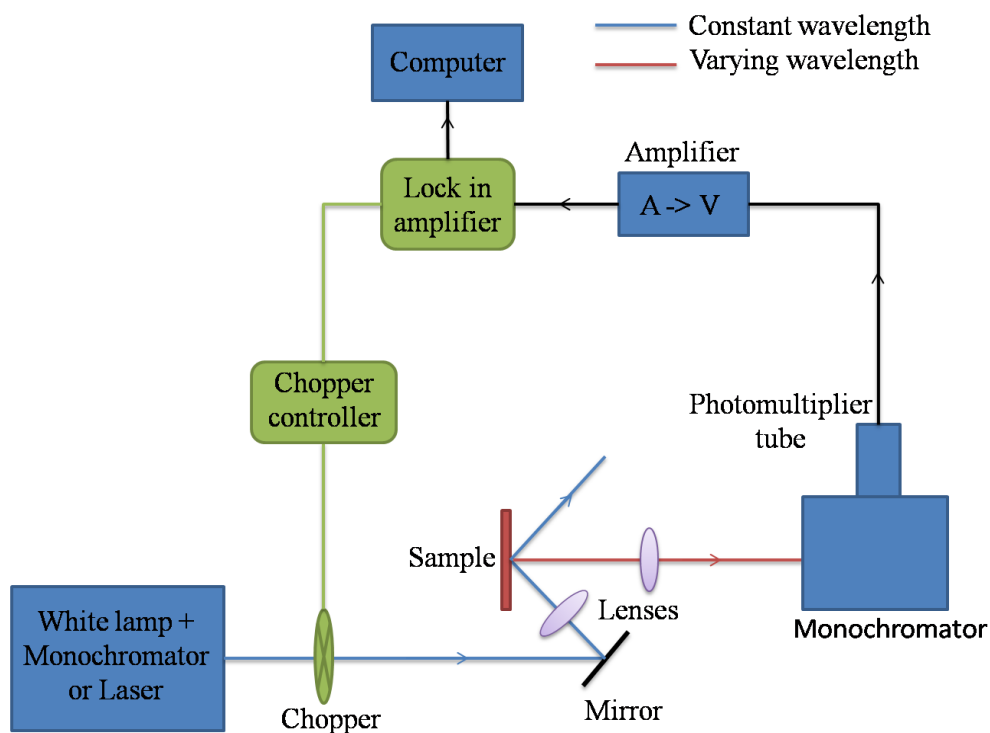


Figure II-16: Schematic of the photoluminescence experimental setup.

II.3.2.3. Energy resolved photoluminescence in excitation

a) Principle

For the energy resolved photoluminescence in excitation (*PLE*), the detected wavelength is kept constant. In this configuration, the excitation wavelength is varied over a wide range of energy. Here, the *PLE* spectra are constituted by the intensity of the *PL* emitted light at the one detection wavelength versus the excitation wavelength.

b) Experimental setup

The measurements are completed at room temperature. As represented by *Figure II-17*, the optical excitation source is a Lot-Oriel 1 kW Xenon white lamp with an OMNI300 monochromator scanning the wavelength range. The light beam (one for each excitation wavelengths) thus emitted goes through a chopper set at 87 Hz. The light beam is then focalized by lenses on the sample following a 45°. Part of the *PL* emitted light is collected and focused by other lenses toward entrance slit of a MSH 300 OMNI monochromator. The collected light is then spread by the monochromator which selects the one detected wavelength expected (exit slit). This wavelength is detected by a Hamamatsu (R5108) photomultiplier tube. The signal thus detected is amplified and converted in a voltage signal by a SR830 transimpedance amplifier. The signal processing is the same than for the energy resolved photoluminescence. Here again, in case of comparison between layers, the *PL* intensity of each layer is divided by its thickness in μm .

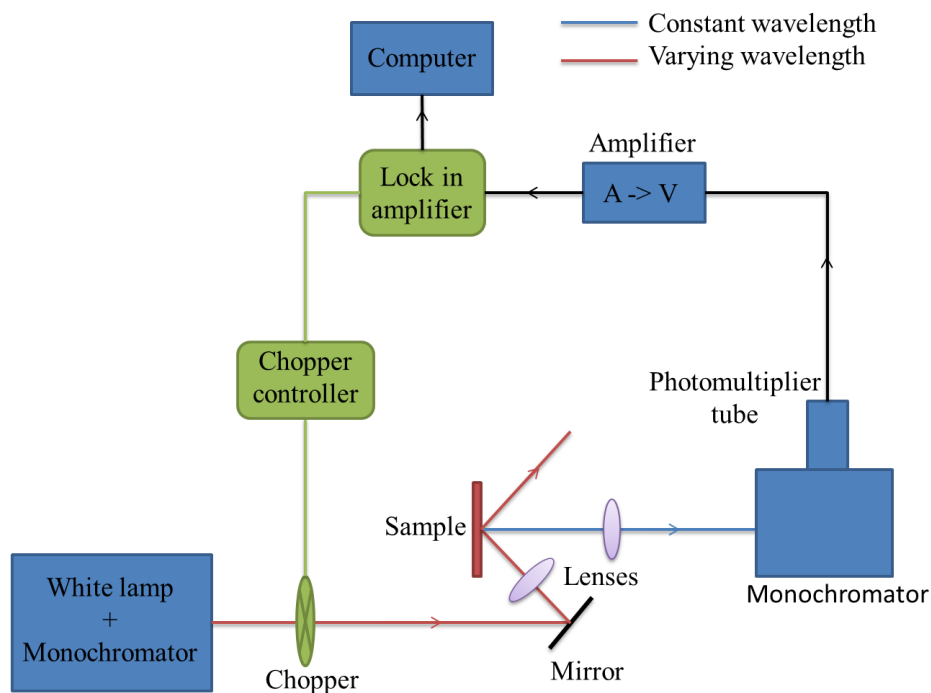


Figure II-17: Schematic of the photoluminescence in excitation experimental setup.

II.3.2.4. Time resolved photoluminescence

a) Principle

When a material is excited by a photon flux, the excited electrons have two ways to go back to their ground states: or they follow a non-radiative way (emission of a phonon, Auger de-excitation, and surface or defects recombination) or they follow a radiative way and emit photons. The emitted light intensity and the lifetime of the emission (time for which the sample emits after the end of the excitation) depend of the kind of emitting elements and of their surroundings.

Let's take a two levels system (*Figure II-18 (a)*) that is excited by a photon flux Φ_i . Part of the electrons of the level *A* goes from the ground state *A* to the excited states *B*. Then, during the de-excitation, part of the *B* population is relaxed by non-radiative or radiative processes. This relaxation is characterized by its lifetime, τ_e , that can be determined thanks to the time resolved photoluminescence experiment. The de-excitation of the *B* state can then be expressed by N_B/τ_e .

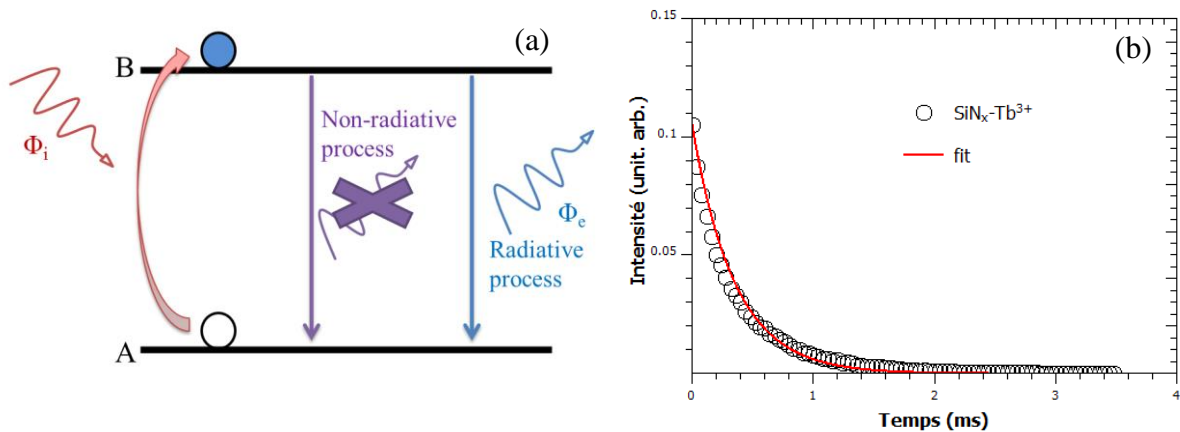


Figure II-18: Two levels system (a) and lifetime example with an integral fit (b).

The lifetime is dependent of the radiative process lifetime, τ_r , but also of the non-radiative process lifetime, τ_{nr} , following the equation:

$$\frac{1}{\tau_e} = \frac{1}{\tau_r} + \frac{1}{\tau_{nr}} \quad \text{II-15}$$

The time resolved photoluminescence (or lifetime measurement) consists in sending a light beam at regular intervals on a sample and measuring the time the sample emits light afterward. The photoluminescence decrease is recorded according to the time in order to access the lifetime of the sample charge carriers.

For simple cases, lifetime is obtained by fitting the experimental curve by a decreasing exponential function:

$$y = A_0 \cdot e^{-\left(\frac{t}{\tau_e}\right)} \quad \text{II-16}$$

When the single decreasing exponential curve does not fit the experimental curve, decreasing multi-exponential function model with a mean lifetime, τ_m , may be employed:

$$\tau_m = \int_0^{\infty} \frac{I(t)}{I_0} dt \quad \text{II-17}$$

With $I(t)$ the intensity for a given time t and I_0 the maximum intensity of $I(t)$ (or the initial at time assume to be 0). For difficult cases, stretch decreasing exponential [12] may also be used:

$$y = y_0 + A_0 \cdot e^{-\left(\frac{t-t_0}{\tau_e}\right)^\beta} \quad \text{II-18}$$

With β the dispersion factor (the farther from 1 β is, the more important the dispersion is).

Figure II-18 (b) shows the fit between the experimental curve and the curve obtained while using the mean lifetime. The fit is not perfect because of the weight difference between the long and the short lifetimes.

b) Experimental setup

As shown on *Figure II-19*, a laser NT340 EKSPLA Optical Parametric Oscillator (OPO) pumped by a Nd:YAG pulsed laser at 355 nm provides a wavelength tunable light beam with a 5 ns FWHM (full width at half maximum) pulse at room temperature. This beam is focalized with lenses on the sample at a 45° incident angle. Following the photoluminescence process described above, the sample reemits light. A part of the emitted light is focalized by lenses on the slit of a THR1000 Jobin Yvon monochromator. This later spreads the light that is then detected by a liquid-nitrogen-cooled Hamamatsu-NIR PMT R5509_73 InP/InGaAs photomultiplier tube. The signal is amplified and converted to voltage by an amplifier and the data are acquired on a Tektronix TDS3012B oscilloscope and recorded on a computer by means of a Labview interface (made by P. Voivenel and J. Cardin).

The decay time measurements were performed at an excitation wavelength of 244 nm with an average power of 40 mW, and with a repetition rate of 10 Hz at room temperature.

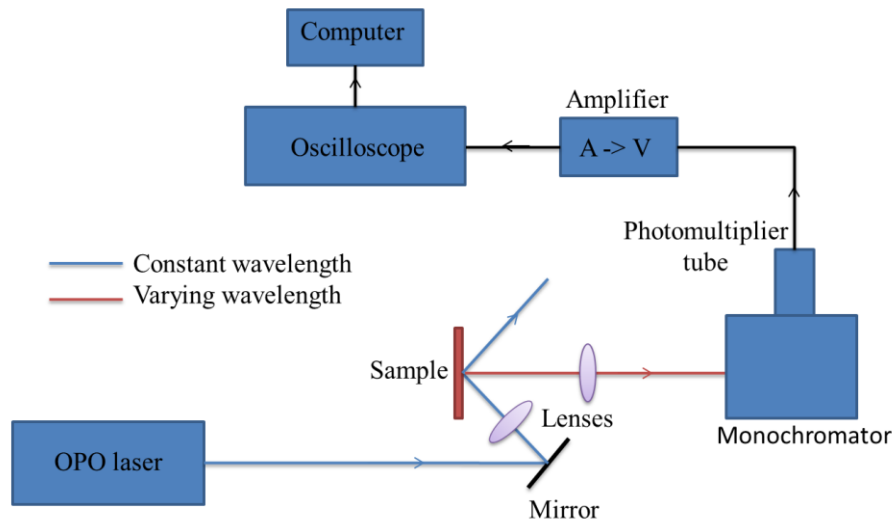


Figure II-19: Time-resolved photoluminescence operation diagram.

II.4. Solar cell characterization

II.4.1. Photoconductance lifetime

II.4.1.1. Principle

The access to the lifetime of minority carriers (from generation to recombination) is very interesting to preview the potential efficiency of solar cells. This analysis is complex and depends of the material quality, the doping level, and the illumination level.

The sample is irradiated with light which generates carriers. The carriers then might de-excite by recombination. The lifetime has two components, the bulk lifetime, τ_b , and the surface lifetime, τ_s . In the bulk of the material, several recombinations having each a lifetime may take place: the radiative (band-to-band) recombination, τ_{rad} , the Auger recombination, τ_A , and the recombination through defect levels or Shockley-Read-Hall (*SRH*) recombination, τ_{SRH} , due to traps within the band gap leading to the relation:

$$\frac{1}{\tau_b} = \frac{1}{\tau_{rad}} + \frac{1}{\tau_A} + \frac{1}{\tau_{SRH}} \quad \text{II-19}$$

In semiconductor such as silicon, τ_{rad} is very large and may be neglected. The Auger lifetime may be calculated accurately with theoretical models but the *SRH* lifetime is more difficult to calculate as is depending of the number of defects in the material.

The surface lifetime may also be very important and complicate the measurement. However, surface lifetime can be well modeled and specific cases may simplify it. Perfectly passivated

surface leads to $\tau_s = \infty$. The surface recombination may then be neglected thus easing the effective lifetime calculation.

The effective lifetime may be expressed as followed:

$$\frac{1}{\tau_{eff}} = \frac{1}{\tau_b} + \frac{1}{\tau_s} \quad \text{II-20}$$

II.4.1.2. Experimental setup

The lifetime of carriers was measured in the National Dong Hwa University, Taiwan, by Dr. Ing-Song Yu in the frame of the ORCHID-PHC bilateral project with a WCT-120 Lifetime Test Instrument by Sinton Instruments. A Xenon flash lamp illuminates a 2" diameter wafer and an eddy-current conductance sensor. As the carriers' lifetime is smaller than 200 μ s the Quasi-Steady-State-Photoconductance method was employed [13]: (i) slowly-decaying continuous light source with a decay constant 10 times slower than the lifetime of carriers, (ii) simultaneous measurement of the sample conductivity and intensity of the light, (iii) sample conductivity and light intensity converted into the average excess carrier density Δn and the electron/hole pairs generation rate G respectively, and (iv) calculus of the lifetime τ following the equation:

$$\Delta n = G\tau \quad \text{II-21}$$

The standard WCT-120 software provided the data.

II.4.2. External quantum efficiency measurement

The quantum efficiency (QE) indicates a solar cell efficiency in converting light to electron as a function of the wavelength. It is given by the number of generated carriers over the number of incident photons for a given wavelength. The external quantum efficiency (EQE) includes the optical losses that are the light transmission through the cell and the reflection of the light away from the cell, while the internal quantum efficiency (IQE) does not and take into account only the absorbed photons. Thus, the relation between the two is:

$$IQE = \frac{EQE}{(1-R-T)} \propto \frac{EQE}{(1-R)} \quad \text{II-22}$$

With R the reflectance of the cell and T its transmittance that may be considered equal to zero considering the thickness of a cell (200 μ m).

A method of measuring the *EQE* is to record the current of the cell and the incident beam power according to the wavelength of the incident photons [14].

As shown on *Figure II-20*, a monochromatic light produce by a white lamp source followed by a monochromator and chopped is incident on both the sample and the reference detector. The bias light provides a power of 0.3 to 0.5 suns allowing to reach the operation point of the cell. The current of the cell is recorded for each wavelength as well as the incident power given by the reference photodetector. The *EQE* is then calculated from the experimental values of current and incident power by the computer.

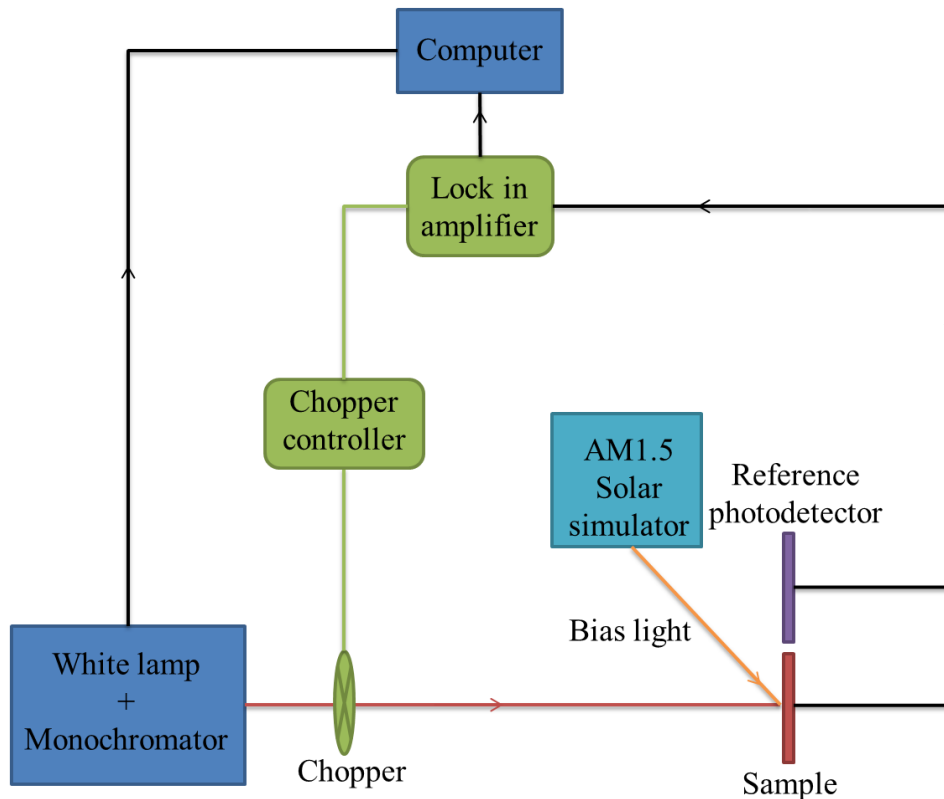


Figure II-20: EQE measurement operation diagram.

The *EQE* of the system constituted of our layers deposited on a silicon solar cell is measured in Hualien, Taiwan by Dr. Ing-Song Yu of the Department of Material Science and Engineering of the National Dong Haw University.

II.4.3. I-V curves

The current-voltage characteristic curve, or I-V curve, of a solar cell reflects the operation of its P-N junction. The I-V curve (*Figure II-21*) gives the possible operation couple intensity/voltage of the cell under 1 sun illumination with no shading and for a standard cell temperature (25 °C). The obtained curve is the result of the addition of the I-V curve of the SC in the dark (acting as a diode) and the light generated current.

The maximum voltage called open-circuit voltage (V_{OC}) occurs at zero current so when the circuit is open (infinite resistance). The maximum current called short-circuit (I_{SC}) current occurs at zero voltage so when there is no resistance in the circuit. The power available from the cell (in Watts) is given by the product of the current by the voltage and displayed on the P-V curve (*Figure II-21*). The maximum power generated by the cell (P_{max}) is obtained at the “knee” of the I-V curve for the couple of the maximum power current (I_{mp}) and voltage (V_{mp}). The evolution of this curve will be detailed more precisely in Chapter V.

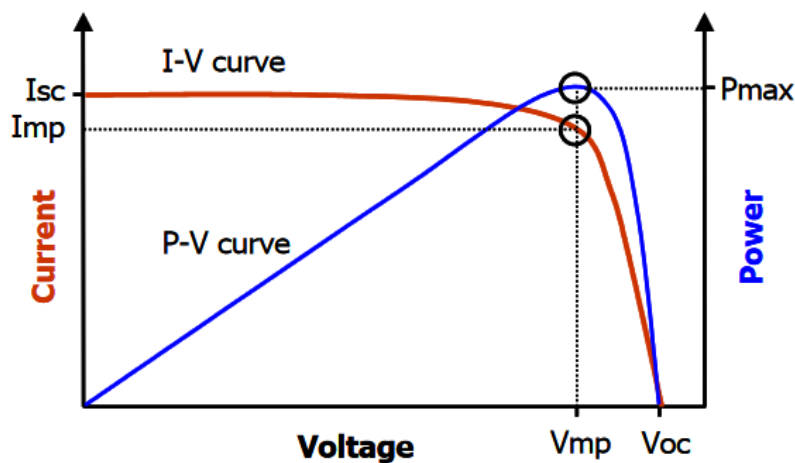


Figure II-21: Typical I-V and P-V curve of a solar cell. From [15].

The I-V curve measurements are performed on the silicon solar cells in Hualien, Taiwan by Dr. Ing-Song Yu of the Department of Material Science and Engineering of the National Dong Haw University.

II.5. Modeling

II.5.1. Access to optical parameters

A simulation program based on the transfer matrix method (*TMM*) [16] described in *Annex I* was run using the refractive indexes of each medium as well as the thickness and the possible roughness of the layer obtained from the ellipsometric measurements performed on the sample. The simulation program will then calculate the absorbance A , reflectance R , and transmittance T of the layer deposited on top of a silicon wafer as a function of λ (*Figure II-22*).

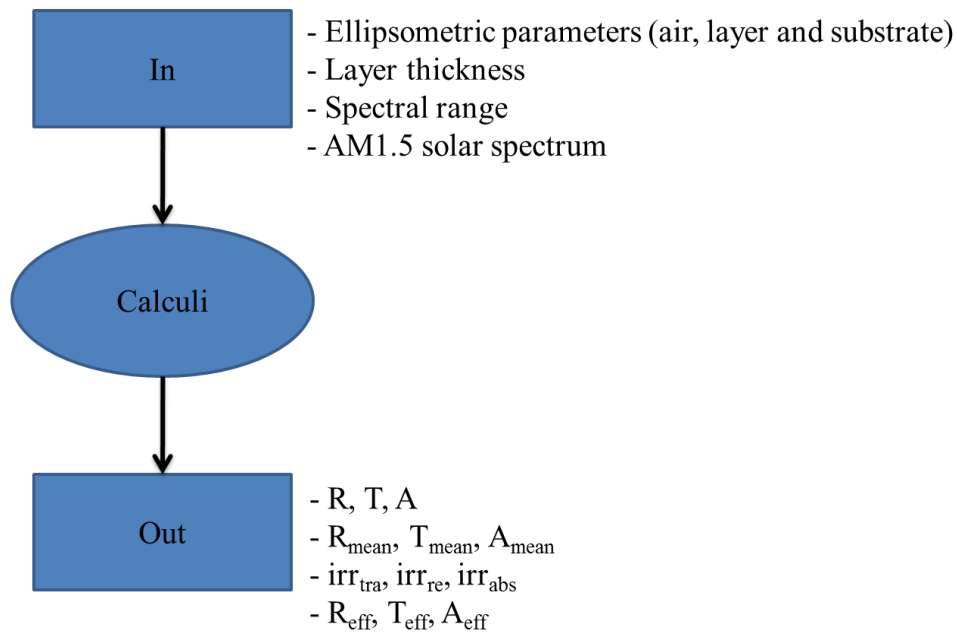


Figure II-22: Diagram representing the TMM program.

From those spectral values, mean values integrated and normalized over specific λ ranges may be calculated following:

$$A_{mean} = \frac{\int_{\lambda_{min}}^{\lambda_{max}} A(\lambda) d\lambda}{\int_{\lambda_{min}}^{\lambda_{max}} d\lambda}, \quad \text{II-23}$$

$$R_{mean} = \frac{\int_{\lambda_{min}}^{\lambda_{max}} R(\lambda) d\lambda}{\int_{\lambda_{min}}^{\lambda_{max}} d\lambda}, \quad \text{and} \quad \text{II-24}$$

$$T_{mean} = \frac{\int_{\lambda_{min}}^{\lambda_{max}} T(\lambda) d\lambda}{\int_{\lambda_{min}}^{\lambda_{max}} d\lambda} \quad \text{II-25}$$

The mean -absorbance A_{mean} , -reflectance R_{mean} , and -transmittance T_{mean} do not depend of the spectral range as they are normalized by it. Thus those mean values may be compared over different wavelength ranges. Moreover, they globally describe in a unique scalar value the absorbance, reflectance, or transmittance curves in a given range which allow for an easier comparison between the samples.

In addition, values representing the layer and its interaction with the AM1.5 solar spectrum $L_{AM1.5}(\lambda)$ [17] are defined. The absorption, reflection, and transmission irradiances that will be called irr_{abs} , irr_{re} , and irr_{tra} respectively are given in W/m² and represent the proportion of the sun light that is absorbed, reflected and transmitted by the layer over a given spectral range:

$$irr_{abs} = \int_{\lambda_{min}}^{\lambda_{max}} A(\lambda) L_{AM1.5}(\lambda) d\lambda, \quad \text{II-26}$$

$$irr_{re} = \int_{\lambda_{min}}^{\lambda_{max}} R(\lambda) L_{AM1.5}(\lambda) d\lambda, \text{ and} \quad \text{II-27}$$

$$irr_{tra} = \int_{\lambda_{min}}^{\lambda_{max}} T(\lambda) L_{AM1.5}(\lambda) d\lambda \quad \text{II-28}$$

By normalizing those last values by the incident solar spectrum AM1.5 $L_{AM1.5}(\lambda)$, we obtain normalized values convoluted by the AM1.5 solar spectrum that are the absorbance, reflectance, and transmittance efficiencies called A_{eff} , R_{eff} , and T_{eff} respectively. Those values may be compared over different wavelength ranges and also allow an easy comparison between samples.

$$A_{eff} = \frac{\int_{\lambda_{min}}^{\lambda_{max}} A(\lambda) L_{AM1.5}(\lambda) d\lambda}{\int_{\lambda_{min}}^{\lambda_{max}} L_{AM1.5}(\lambda) d\lambda} \quad \text{II-29}$$

$$R_{eff} = \frac{\int_{\lambda_{min}}^{\lambda_{max}} R(\lambda) L_{AM1.5}(\lambda) d\lambda}{\int_{\lambda_{min}}^{\lambda_{max}} L_{AM1.5}(\lambda) d\lambda} \quad \text{II-30}$$

$$T_{eff} = \frac{\int_{\lambda_{min}}^{\lambda_{max}} T(\lambda) L_{AM1.5}(\lambda) d\lambda}{\int_{\lambda_{min}}^{\lambda_{max}} L_{AM1.5}(\lambda) d\lambda}$$

II.5.2. Propagation of light emission in layered media

The light emission and propagation in our samples were studied thanks to an extended transfer matrix method (ETMM) following the model of the single emitter [18,19] described in Annex 2. This method is based on the same matrix model as above (detailed in Annex 1) and [16] uses the ellipsometric parameters (refractive indexes and thicknesses) of the samples and the surrounding media. With this method we can access the distribution of emission as a function of the wavelength and of the emission angle in each considered medium (Figure II-23).

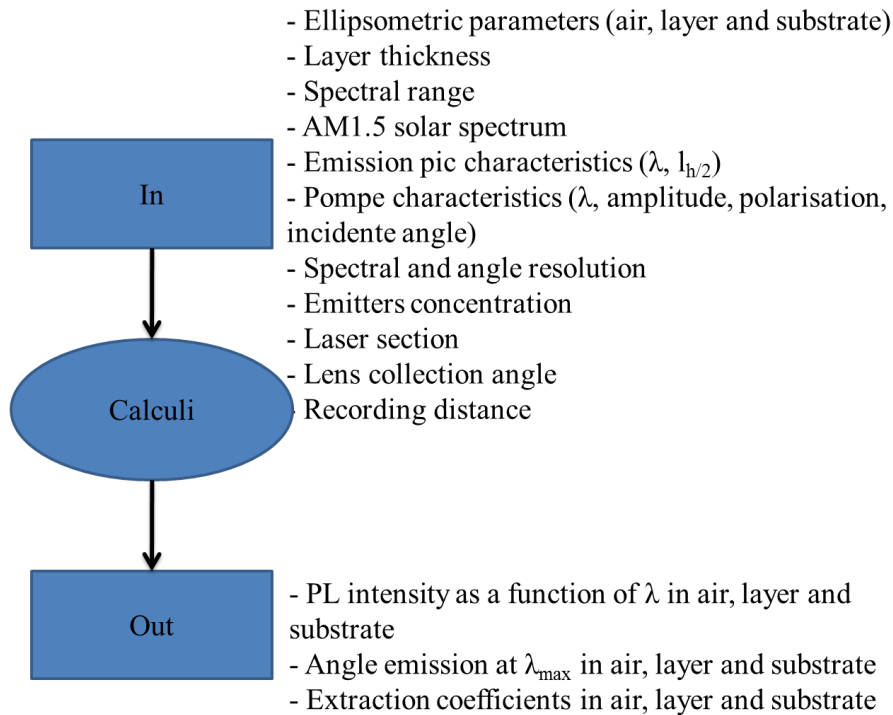


Figure II-23: Diagram representing the ETMM program.

The Yb^{3+} spectral line shape was assumed to be described by a Gaussian function. PL spectra were obtained by the integration over emission angles in the conversion layer, air, and silicon materials. A supplementary integration led us to the total power densities in three media leading to the global emission properties:

$$\eta_i = \int_{Tot} I_i(\lambda) d\lambda \quad \text{II-32}$$

With i the medium either the air, the layer or the substrate.

The luminescence efficiencies in each medium are obtained by defining the luminescence efficiency as the ratio of the power density in the medium i over the total emitted power density:

$$\eta_i^{lum} = \frac{\eta_i}{\eta_{air} + \eta_{layer} + \eta_{substrate}} \quad \text{II-33}$$

Bibliography

- [1] Oxford Vacuum Science High vacuum science and technology, (n.d.). http://www.oxford-vacuum.com/background/thin_film/sputtering.htm.
- [2] L. Dumont, J. Cardin, P. Benzo, M. Carrada, C. Labbé, A.L. Richard, D.C. Ingram, W.M. Jadwisieniczak, F. Goubilleau, SiNx:Tb3+–Yb3+, an efficient down-conversion layer compatible with a silicon solar cell process, *Sol. Energy Mater. Sol. Cells.* 145 (2016) 84–92. doi:10.1016/j.solmat.2015.09.031.
- [3] C.-H. Liang, Propriétés optiques des films minces à base de Si dopé Nd: Vers un amplificateur optique, Université de Caen, 2013. <http://tel.archives-ouvertes.fr/tel-00926053> (accessed January 22, 2014).
- [4] Thermo Nicolet Corporation, Introduction to Fourier Transform Infrared Spectrometry, (2001). <http://mmrc.caltech.edu/FTIR/FTIRintro.pdf>.
- [5] Fourier Transform Spectrometer, Scienceworld.wolfram.com. (n.d.). <http://scienceworld.wolfram.com/physics/FourierTransformSpectrometer.html>.
- [6] G. Dupont, H. Caquineau, B. Despax, R. Berjoan, A. Dollet, Structural properties of N-rich a-Si-N: H films with a low electron-trapping rate, *J. Phys. Appl. Phys.* 30 (1997) 1064.
- [7] Transmission Electron Microscopy (TEM), (n.d.). <http://www2.warwick.ac.uk/fac/sci/physics/current/postgraduate/regs/mpags/ex5/techniques/structural/tem/>.
- [8] N. Menguy, Caractérisations des nanomatériaux par microscopies électroniques, (n.d.). http://www-ext.imPMC.upmc.fr/~menguy/PDFs/MET_MEB/ED_Poitiers_A.pdf (accessed May 19, 2016).
- [9] N. Menguy, Microscopie Électronique en Transmission Imagerie Haute Résolution Imagerie Haute Résolution Spectroscopie EELS Spectroscopie EELS, (n.d.). http://www-ext.imPMC.upmc.fr/~menguy/PDFs/MET_MEB/Cours_MET_part_2.pdf (accessed May 19, 2016).
- [10] Computer Graphic Service.htm, (n.d.).
- [11] A.R. Forouhi, I. Bloomer, Optical dispersion relations for amorphous semiconductors and amorphous dielectrics, *Phys. Rev. B.* 34 (1986) 7018–7026. doi:10.1103/PhysRevB.34.7018.
- [12] A.F. van Driel, I.S. Nikolaev, P. Vergeer, P. Lodahl, D. Vanmaekelbergh, W.L. Vos, Statistical analysis of time-resolved emission from ensembles of semiconductor quantum dots: Interpretation of exponential decay models, *Phys. Rev. B.* 75 (2007). doi:10.1103/PhysRevB.75.035329.
- [13] Sinton-WCT-120PL-product-note.pdf, (n.d.). <http://sintoninstruments.com/PDFs/Sinton-WCT-120PL-product-note.pdf> (accessed July 13, 2016).
- [14] C.-F. Lin, M. Zhang, S.-W. Liu, T.-L. Chiu, J.-H. Lee, High Photoelectric Conversion Efficiency of Metal Phthalocyanine/Fullerene Heterojunction Photovoltaic Device, *Int. J. Mol. Sci.* 12 (2011) 476–505. doi:10.3390/ijms12010476.
- [15] Guide to Interpreting I-V Curves.pdf, (n.d.). <http://resources.solmetric.com/get/Guide%20to%20Interpreting%20I-V%20Curves.pdf> (accessed June 28, 2016).
- [16] P. Yeh, *Optical waves in layered media*, New York: Wiley, 1988.
- [17] Solar Spectral Irradiance ASTM G-173.htm, (n.d.).
- [18] H. Benisty, R. Stanley, M. Mayer, Method of source terms for dipole emission modification in modes of arbitrary planar structures, *JOSA A.* 15 (1998) 1192–1201.
- [19] J.-P. Weber, S. Wang, A new method for the calculation of the emission spectrum of DFB and DBR lasers, *IEEE J Quantun Electron.* 27 (1991) 2256.
- [20] Y.G. Boucher, Theoretical investigation of amplified spontaneous emission in an active structure by extended (3×3) transfer matrix formalism: The case of a non-uniform longitudinal distribution of emitters, *J. Eur. Opt. Soc. Rapid Publ.* 1 (2006).

Chapter III: A study on SiN_x and $\text{SiN}_x:\text{Tb}^{3+}$ layers

III.1. Introduction

To develop an efficient down-converter layer, it is necessary, due to its complexity to optimize each step of the fabrication. Thus, in this chapter, we describe the optimization first of the SiN_x host matrix, and then of the Tb-doped SiN_x film. For the former, the aim is to develop a matrix that will meet the requirements of both the frequency conversion process and the anti-reflective layers as described in the first chapter. For this purpose, the layer should absorb high energy photons (at least twice the silicon bandgap energy) while being transparent to lower energy photons. In addition, the layer reflectance at the air/layer interface should be very low in order to reduce the amount of reflected photons. Concerning the $\text{SiN}_x:\text{Tb}^{3+}$ system, the effect of the different deposition parameters on the structural and optical properties are analyzed. We investigate the energy transfer taking place from the matrix to the terbium ions thanks to *PL*, *PLE* and time-resolved photoluminescence. As one of our objectives is to develop a Tb-doped SiN_x layer with a higher Tb^{3+} *PL* peak intensity than the Tb-doped SiO_xN_y layers developed during the precedent work of Y-T An, the efficiency of our optimized Tb-doped layer is compared to the optimized Tb-doped SiO_xN_y layer obtained during this previous work.

III.2. SiN_x Matrix

The first step of our work on the *DC* layers concerns the optimization of the undoped matrix. The layers are deposited in our laboratory by *RF* reactive magnetron sputtering of a pure silicon target in a nitrogen-rich plasma on a silicon P-type *CZ* (Czochralski) wafer. The deposition is performed with the values of the Si target power density, the substrate-target distance (*d*) and the substrate rotation fixed at 4.5 W/cm², 10 cm, and 20 rpm (rotation per minute), respectively. The plasma pressures (*P*) investigated are 2, 3, and 4 mTorr and the nitrogen ratio is varied from 14 % to 30 %. The deposition time (*t_d*) was adjusted in each case to obtain 90 nm thick layers. Unless otherwise stated, the layers studied are non-annealed. The structural, optical properties of the matrix are studied as a function of the nitrogen ratio and the plasma pressure as well as the annealing temperature. Those studies allow to determine an optimized matrix that combines efficient absorption characteristic in the UV range with suitable anti-reflective property and rare earth sensitizing effect.

III.2.1. Composition analyses

III.2.1.1. Preliminary results

In the first instance, general observations on the matrix have to be made before focusing into the effect of the deposition parameters.

A transmittance *FTIR* study is conducted at both normal and Brewster (65°) angles on the produced layers. It is worth noting that all the *FTIR* spectra exhibit only two vibration bands peaking at 1121 cm^{-1} and at 847 cm^{-1} . Thanks to the deposition method of the SiN_x layers no hydrogen has been incorporated into the matrix. However, oxygen might be incorporated afterward during open-air storage. *Annex 3* lists all the possible bands resulting from the binding between those elements. Some of them are resumed in *Table III-1*. We can see that, apart the Si-N bonds, TO_3 mode of the Si-O bond between 1060 and 1050 cm^{-1} and the Si-H bond between 907 and 845 cm^{-1} can be at the origin of these two vibration bands. However such O- or H-bonds have also their signature between 1215 and 1256 cm^{-1} , 2200 and 2000 cm^{-1} , and 3320 and 2500 cm^{-1} corresponding to Si-O, Si-H, and N-H bonds, respectively. None of these vibrations band can be seen on *Figure III-1*. This confirms that our films are free from O and H and that the two bands are only due to the *LO* and *TO* modes of the Si-N bond. Ordinarily, only the *TO* band at 847 cm^{-1} may be seen under normal incidence analysis, but the amorphous character of the layers leads to a possible contribution of the *LO* peaks even under at such incidence angle [1].

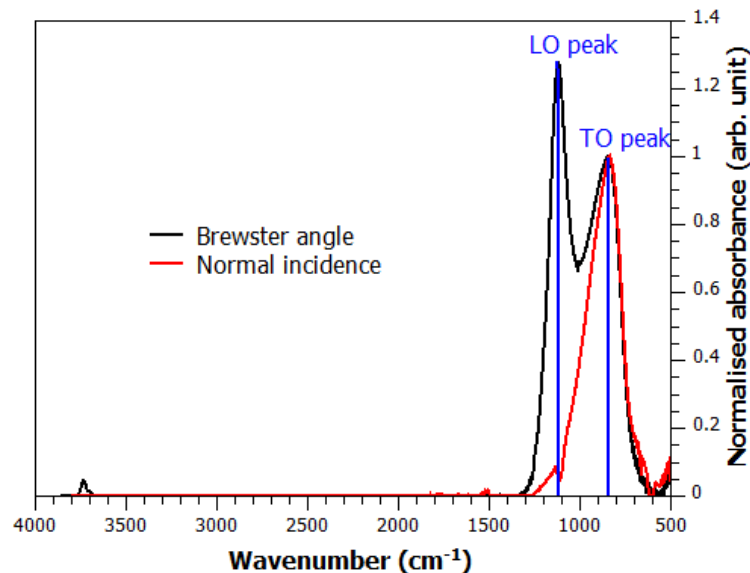


Figure III-1: FTIR spectra of the SiN_x matrix at normal (red) and at Brewster (black) incidence angles.

Position (cm ⁻¹)	Name	Bond	Position (cm ⁻¹)	Name	Bond
3500-3320		N-H	1070-1030	LO	Si-N
2220-2000		Si-H	907-845		Si-H
1550		N-H	880-810	TO	Si-N
1215-1256	LO ₃	Si-O	650-630		Si-H
1200-1140		N-H	600-400		Si-N
1060-1050	TO ₃	Si-O			

Table III-1: Summary of the list (see Annex 3) of the bond between the Si, N, H, and O elements and their vibration bands wavenumber.

Ellipsometry measurements are also undertaken on every layer. It appears that their refractive indexes at 1.95 eV, n , are lower than the refractive index (2.03) of the stoichiometric Si₃N₄ material [2]. The refractive indexes of silicon and nitrogen at 1.95 eV being 3.89 [3] and 1.00 [4], respectively, a n higher than the one of the stoichiometric material signifies an excess of silicon, whereas a n lower an excess of nitrogen. The deposited layers are then non stoichiometric and have an excess of nitrogen. However, it is possible that the obtained refractive index at 1.95 eV is lower than the value in bulk material because of the presence of porosity in the microstructure as observed previously by O. Debieu et al. [5].

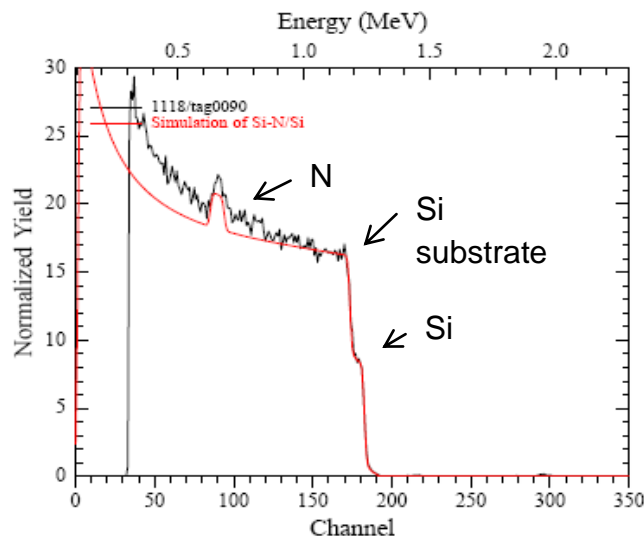


Figure III-2: RBS spectra of a SiN_x layer.

Figure III-2 shows the *RBS* analysis and its corresponding fit of a SiN_x layer. The presence of silicon from both the substrate and the layer as well as of nitrogen in the layer is confirmed. The fit shows an excess of nitrogen which is in agreement with the ellipsometry measurements. Moreover, no peak corresponding to oxygen near the nitrogen one is detected which confirms the absence of oxygen in our layer.

Nevertheless, it is important to underline the difficulties we had to determine the composition of our samples. Indeed, several measurement techniques were employed with different outcomes. The ellipsometry, *FTIR* and *RBS* experiments do not detect oxygen in the layers whereas *EDS-TEM* and *XPS* detect oxygen and carbon. This may be explained by the fact that *XPS* measurements samples are more sensitive to the surface of the layers and the presence of oxygen can be the result of surface oxidation. The surface of the samples studied by *EDS-TEM* may also have been oxidized during preparation. *EDS* and *XPS* measurements also lead to a silicon excess while *RBS* leads to a nitrogen excess or a stoichiometry. This uncertainty may be explained by the uncertainty of the various measurements (10 % for the *RBS*) coupled with the near stoichiometric composition of our samples. Similar difficulties are faced when doping the host matrix with rare earth ions and will be described in the next chapter.

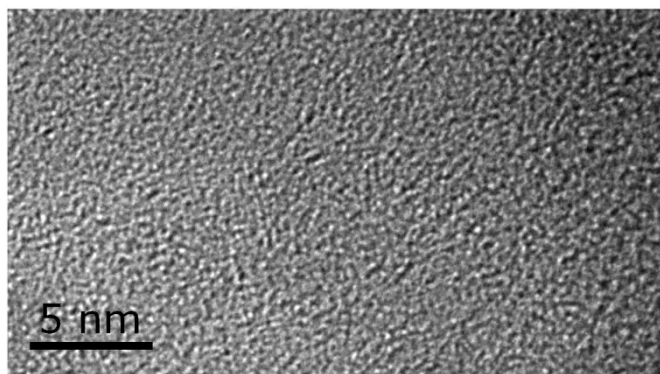


Figure III-3: HRTEM picture of a typical SiN_x layer annealed by CTA at 850 °C during 1 h.

HRTEM analyses (*Figure III-3*) carried out on such SiN_x layer annealed by *CTA* at 850 °C during 1 h show that the layer is amorphous and homogeneous with no clusters (crystalline or amorphous) at the observation scale.

III.2.1.2. Effect of the nitrogen ratio

Figure III-4 shows the evolution of the position of the *LO* band of the Si-N bond as well as the refractive index value at 1.95 eV as a function of the nitrogen ratio rN_2 . The *LO* band position shifts toward the high wavenumbers (blueshift) by 10 cm^{-1} which is a small variation. The refractive index at 1.95 eV value decreases with the increase of rN_2 . Such evolution has already been observed by Debieu et al. [5] with a larger variation (50 cm^{-1}) but over a larger range of rN_2 (0 to 29 %). A smaller *LO* peak shift is consistent with a smaller rN_2 range. According to the work of Debieu et al. [5] and Huang et al. [6] on O- or H-free SiN_x films, a blueshift of the *LO* band position can be ascribed to an increase in the $[\text{N}]/[\text{Si}]$ ratio. This shift can be attributed to a shortening of the Si-N bond caused by a change in the matrix composition [7]. The shift may also come with an increase in the matrix disorder due to nitrogen excess. This is the reason why a decrease of the refractive index at 1.95 eV that can be attributed both to the disorder- and nitrogen excess- increases has been observed (Figure III-4).

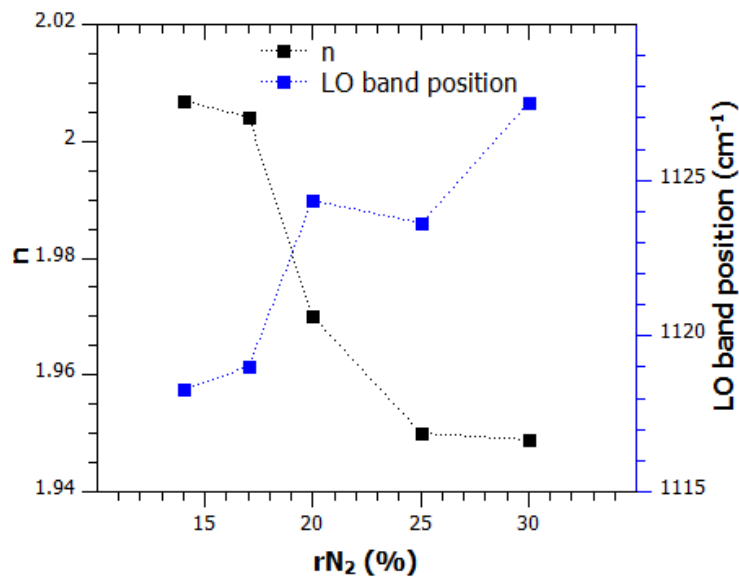


Figure III-4: Si-N bond *LO* band position and refractive index at 1.95 eV as a function of the nitrogen ratio for a plasma pressure fixed at 3 mTorr.

The refractive index values are linked to x , the [N]/[Si] ratio, determined by Makino [8] as the bonding-density-weighted linear combination of reference refractive indexes taken at $x = 0$ (for $n = n_{Si}$) and $x = 4/3$ (for $n = n_{Si_3N_4}$) using the relation:

$$n(x) = \frac{N_{Si-N}n_{Si_3N_4} - N_{Si-Si}n_{Si}}{N_{Si-N} + N_{Si-Si}} \quad \text{III-1}$$

With $n(x)$ the refractive index of the material and N_{Si-N} and N_{Si-Si} the bonding density of the Si-N and Si-Si bonds that may be known thanks to the equation of state:

$$SiN_x \leftrightarrow \left(1 - \frac{3x}{4}\right)Si + \frac{x}{4}Si_3N_4 \quad \text{III-2}$$

Which gives:

$$\frac{N_{Si-N}}{N_{Si-Si}} = \frac{3 \cdot \frac{x}{4}}{\left(1 - \frac{3x}{4}\right) \frac{1}{2}} = \frac{3x}{2\left(1 - \frac{3x}{4}\right)} \quad \text{III-3}$$

Using Equation III-3 in Equation III-1, we obtain:

$$n(x) = \frac{\left(\frac{N_{Si-N}}{N_{Si-Si}}\right)n_{Si_3N_4} - n_{Si}}{\left(\frac{N_{Si-N}}{N_{Si-Si}}\right) + 1} = \frac{\left(\frac{3x}{2\left(1 - \frac{3x}{4}\right)}\right)n_{Si_3N_4} - n_{Si}}{\left(\frac{3x}{2\left(1 - \frac{3x}{4}\right)}\right) + 1} = \frac{\frac{3}{2}xn_{Si_3N_4} + 2n_{Si} - \frac{3x}{2}n_{Si}}{\frac{3x}{2} + 2} \quad \text{III-4}$$

Thus one can deduce the ratio x :

$$x = \frac{4(n_{Si} - n(x))}{3(n(x) + n_{Si} - 2n_{Si_3N_4})} \quad \text{III-5}$$

With $n(x)$ the refractive index of the layer at 1.95 eV, $n_{Si_3N_4} = 2.03$ [2], and $n_{a-Si} = 4.20$ [9].

In our calculations, we take into account an amorphous silicon, as such SiN_x layer are free of crystalline clusters (*Figure III-3*). In addition the equation is considered valid for materials with N excess. The results of this calculus (*Equation III-5*) are displayed on *Figure III-5* in which one can see that x increases with the nitrogen ratio and stays above 1.33. Such evolution means that there is an excess of N in the layers which increases with rN_2 .

III.2.1.3. Effect of the plasma pressure

Figure III-6 (a) shows a decrease of the refractive index at 1.95 eV by 0.11 (4 times the measurement uncertainty) while the plasma pressure increases. Such an evolution can be attributed to the increase of the relative content of nitrogen in the layers with the plasma pressure. As

described above, this decrease of the refractive index at 1.95 eV may also express the higher matrix disorder that accompanies the increase of the nitrogen content. The $[N]/[Si]$ ratio, x , is above 1.33 and increases with the plasma pressure (*Figure III-6 (b)*) confirming that the plasma pressure favors the nitrogen incorporation.

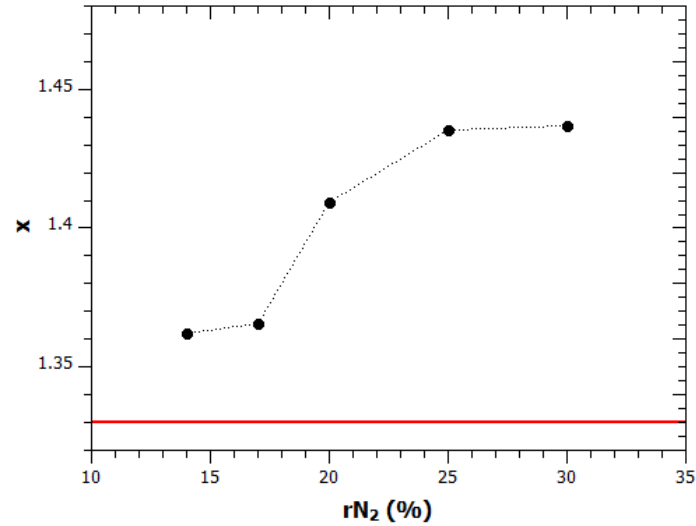


Figure III-5: The $[N]/[Si]$ ratio, x , as a function of the nitrogen ratio for a plasma pressure fixed at 3 mTorr. The red line represents the x of the stoichiometric material Si_3N_4 (at $x = 1.33$).

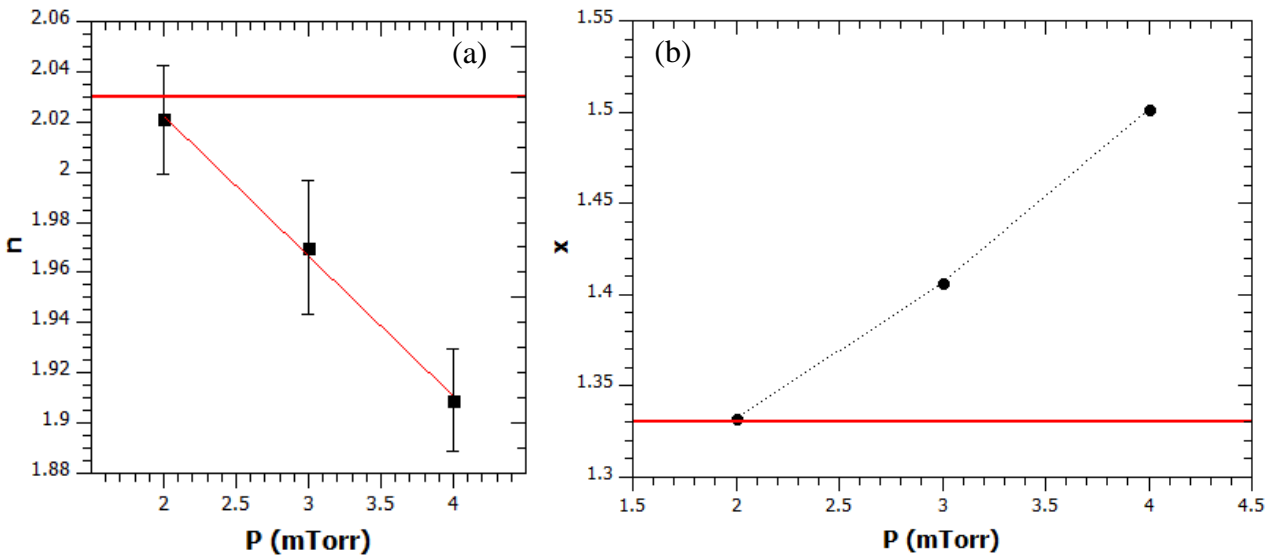


Figure III-6: Refractive index at 1.95 eV values (a), and $[N]/[Si]$ ratio, x (b), as a function of the plasma pressure for a nitrogen ratio fixed at 20 %.

III.2.1.4. Effect of the annealing temperature

The influence of the annealing temperature after deposition has also been studied and the corresponding *FTIR* spectra registered under Brewster incidence are presented in *Figure III-7 (a)*. For this purpose, the layers were annealed using the conventional approach (*CTA*) for 1 h at 750, 850, and 950 °C under a pure N₂ flow. The increase of the annealing temperature leads to an increase of the Si-N bond *LO* band intensity accompanied by a blueshift of its position. We consider that the composition of the layers remains unchanged during the annealing process as the refractive index at 1.95 eV of the annealed layers (*Figure III-7 (b)*) remains unchanged. The *LO* band evolutions are consequently attributed to the decrease of the disorder resulting from the reorganization of the matrix upon annealing. This is confirmed by the decreasing overlapping of *TO* and *LO* bands around 1000 cm⁻¹ [5].

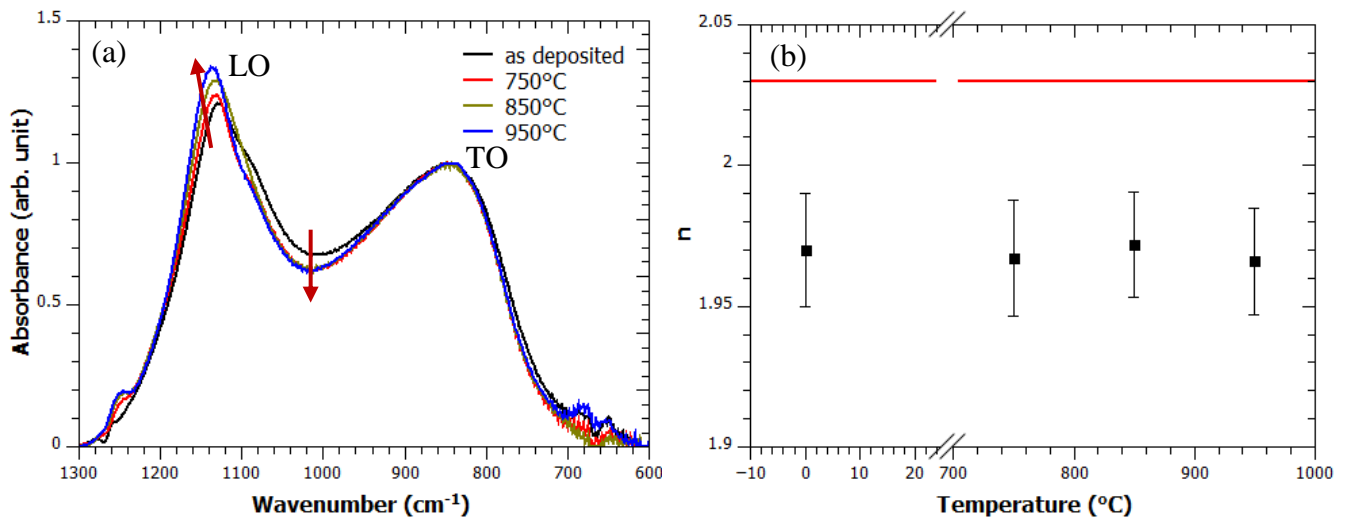


Figure III-7: (a) FTIR spectra for different annealing temperatures. The red arrows illustrate the evolution of the Si-N bond LO band and the overlapping of Si-N bond TO and LO bands. (b) Refractive index at 1.95 eV as a function of the annealing temperature.

III.2.2. Optical properties

The SiN_x layers we develop will be used as host matrix for frequency conversion layers (down-shifting -*DS*- or down-conversion -*DC*-) and should thus meet several important criteria before being used. First, due to the low absorption cross-section of the rare earth ions, the layers should play the role of efficient sensitizer toward them. Thus, the layers should absorb the UV photons (above 2.2 eV or below 564 nm) and transfer their energy to the rare earth ions to promote at least the excitation of the electron from the ⁷F₆ to the ⁵D₄ level of the Tb³⁺ ions. Moreover, the *DC*- or *DS*-layer are placed on top of the *SC*, and thus have to be transparent to the lower energy photons ($E < 2.2$ eV or $\lambda > 564$ nm). Thus, besides a high absorption above 2.2 eV, this nitride layer should have a high irradiance coupled with an absorption as low as possible in the visible range (below 2.2 eV) to preserve the *SC* efficiency. Furthermore, our layer should also display anti-reflective properties. Consequently, the reflectance at the interface air/layer has to be as low as possible in order to transmit the light through the layer and toward the *SC*.

In order to determine the deposition parameters leading to the most appropriate layer according to those criteria, the reflectance R , absorbance A , and transmittance T of the layers have been determined using the thickness and the parameters of the “New Amorphous” dispersion law model fitted from the ellipsometry measurements in the transfer matrix method (*TMM*) program.

III.2.2.1. Preliminary analyses

Before depositing our layers, we study the R_{eff} , A_{eff} , and T_{eff} described in the second chapter (§II.4.1.) which represent the reflectance, absorbance, and transmittance normalized and convoluted by the AM1.5 spectrum. They have been analyzed as a function of the refractive index n at 1.95 eV and the thickness of the layer d for an extinction coefficient constant ($k=0.008$).

Two wavelength domains have to be defined before any analyses. One where the Tb-Yb co-doped layer will play its role of frequency conversion, which corresponds to the 300-550 nm range noted *DC*, and one where the layer should be as transparent as possible. This later ranges between 550 and 1200 nm is noted *Non-DC*.

As previously mentioned, we want a layer having a high absorbance and low transmittance in the *DC* range and in the same time, low absorbance and high transmittance in the *Non-DC* range. In addition, the reflectance has to be low on the whole spectral range.

Figure III-8 displays A_{eff} and T_{eff} as a function of n and d in the *DC* (a, c) and *Non-DC* (b, d) ranges. The absorbance and the transmittance should thus ideally be gate functions. However the monotony of the refractive index of the materials used does not allow such behavior. A compromise has to be done between high absorbance in the *DC* range and high transmittance in the *Non-DC* one. Such gate function behavior may be obtained by using Bragg systems but it is not the object of this study. The thickness should stay under 100 nm and the refractive index at 1.95 eV under 2.2.

Figure III-9 shows R_{eff} as a function of n and d in the total range (300-1200 nm). The couple $n = 2.0$ and $d = 80$ nm shows good anti-reflectance properties (real *SC*) but if n increases d should decrease so the couple $n = 2.2$ and $d = 70$ nm is also good.

Thus, the layer thickness should not go over 100 nm with a preference for 80 to 70 nm and the refractive index at 1.95 eV should stay between 2.0 and 2.2.

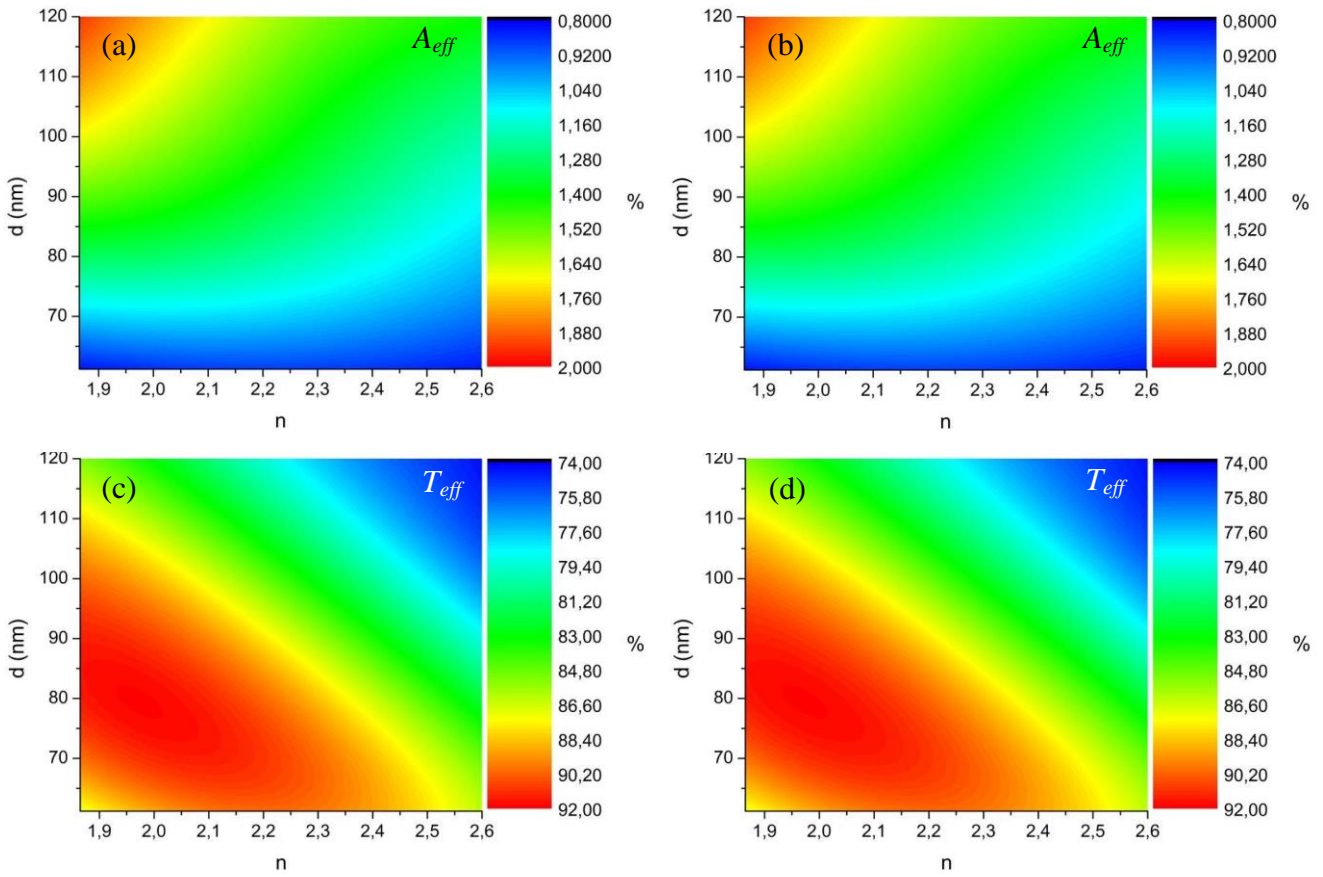


Figure III-8: A_{eff} as a function of n and d in the DC (a) and Non-DC (b) ranges, and T_{eff} as a function of n and d in the DC (c) and Non-DC (d) ranges.

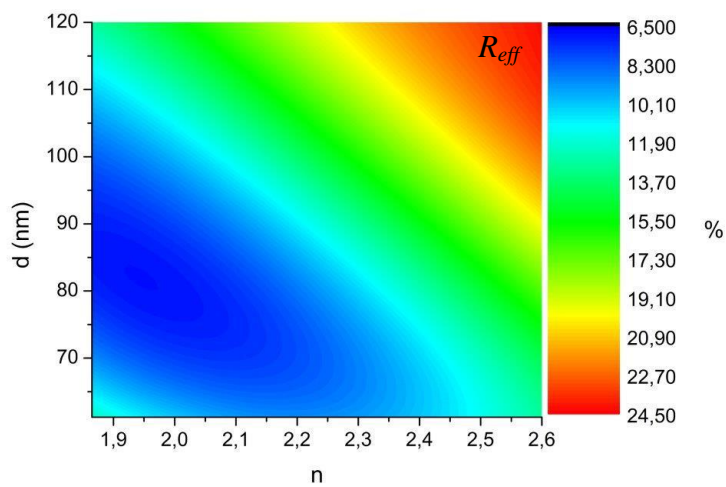


Figure III-9: R_{eff} as a function of n and d in the total range (300-1200 nm).

III.2.2.2. Experiments

After determining the optimal range for the thickness and refractive index at 1.95 eV of our layers, we deposit SiN_x layers varying the plasma pressure and the nitrogen ratio. Examples of the reflectance R , absorbance A , and transmittance T curves of the deposited layers are displayed on *Figure III-10*. However, it is difficult to compare the different layers based only on such curves. Thus, we will use the mean absorbance A_{mean} , reflectance R_{mean} , and transmittance T_{mean} as well as the absorbance A_{eff} , reflectance R_{eff} , and transmittance T_{eff} efficiencies convoluted by the AM1.5 solar spectrum as described in the second chapter (§I.4.1.). Those scalars allow an easier comparison between the layers and between the spectral ranges.

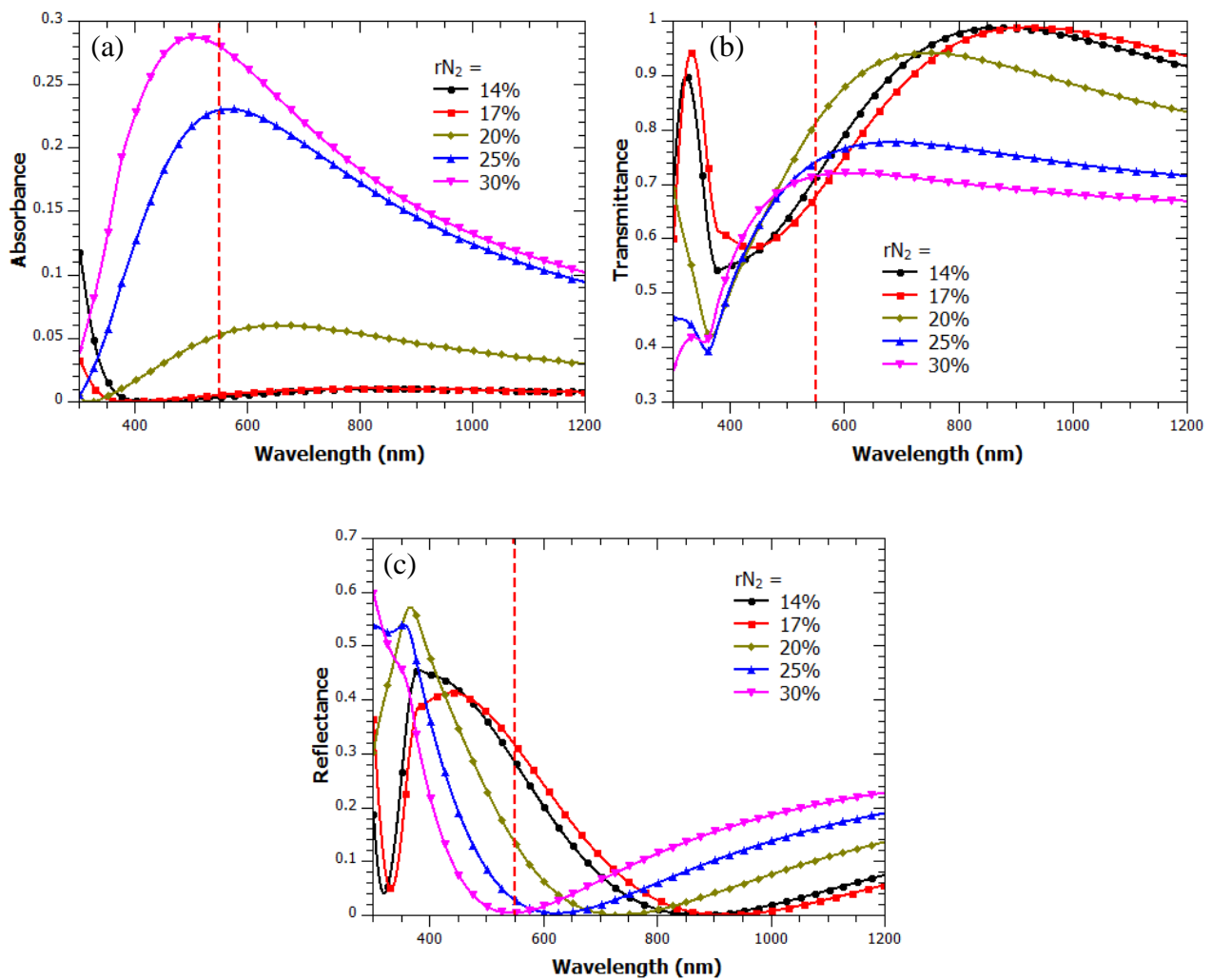


Figure III-10: Absorbance A (a), Transmittance T (b), and Reflectance R (c) curves of the deposited layers for different rN_2 . The red dotted line split the total spectral range (300-1200 nm) in two between the DC range (300-550 nm) and the Non-DC range (550-1200 nm).

a) Mean values

The mean reflectance integrated and normalized over specific λ ranges (R_{mean}) (see §I.4.1.) on the 300-1200 nm range corresponding to the whole solar spectrum is reported on *Figure III-11* as a function of the nitrogen ratio (*Figure III-11 (a)*), and of the plasma pressure (*Figure III-11 (b)*). Those values are compared to the R_{mean} of a Si_3N_4 reference layer (red line). Both figures display a decrease in the R_{mean} with the plasma pressure and the nitrogen ratio.

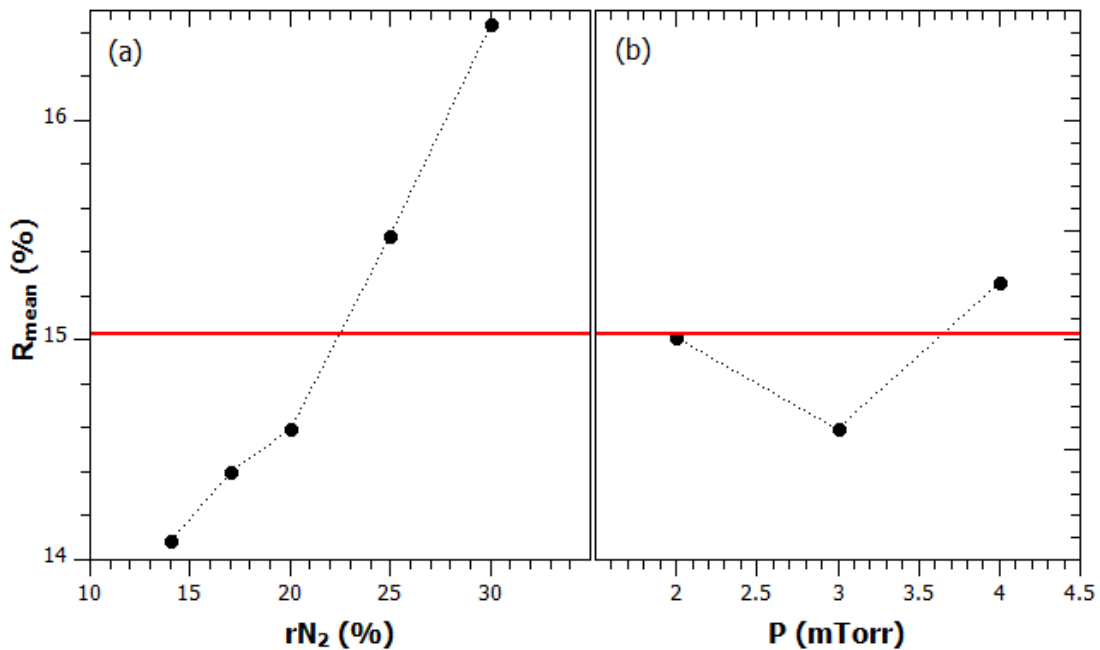


Figure III-11: Integrated normalized reflectance R_{mean} at the air/layer interface of SiN_x layers as a function of the nitrogen ratio for plasma pressure fixed at 3 mTorr (a) and as a function of the plasma pressure for a nitrogen ratio fixed at 20 % (b). The red line corresponds to the reflectance of a Si_3N_4 anti-reflective layer as a reference.

The layers displaying the best anti-reflective properties are those fabricated with $P = 3$ mTorr and $rN_2 = 14$ %. However, considering our reference, the layers fabricated with rN_2 between 14 and 20 % have a R_{mean} below the red line and present good anti-reflectance characteristics. Moreover, the plasma pressure has a minimal effect on the reflectance as R_{mean} stays around the red line with the increase of the plasma pressure. Though, the layer deposited at 4 mTorr has a R_{mean} higher than Si_3N_4 . Thus, P and rN_2 values under 3 mTorr and 20 % respectively are to be favored to produce layers meeting one of the above-mentioned criteria.

The absorbance and transmittance properties of the layer are studied similarly by calculating the mean absorbance and transmittance integrated and normalized over specific λ ranges (A_{mean} and T_{mean}) (see §I.4.1.). *Figure III-12* exhibits A_{mean} and T_{mean} of the same previous samples for different nitrogen ratios for plasma pressure fixed at 3 mTorr (*Figure III-12 (a) and (c)*) and for different P with a nitrogen ratio fixed at 20 % (*Figure III-12 (b) and (d)*). The red lines represent the Si_3N_4 reference. It is important to note that the values of A_{mean} and T_{mean} are similar in the two ranges which is explained by the monotony of the refractive index.

Regarding the effect of the nitrogen ratio, A_{mean} increases and T_{mean} decreases with the increase of rN_2 . The increase or decrease is more pronounced for the layers with a rN_2 higher than 20 %. For those last two layers the absorbance is very high, and the transmittance very low, in the *DC* range but also in the *Non-DC* one which is a major drawback for solar cell applications. For nitrogen ratios of 14 and 17 %, the absorbance is closer to the one of the Si_3N_4 reference which is interesting for the *Non-DC* part but useless in the *DC* one since it will not favor the sensitization of the rare earth ions. The best compromise is then the layer deposited with a nitrogen ratio rN_2 of 20 %.

Regarding the effect of the plasma pressure, the best layer in the *DC* part is the one deposited with a P of 4 mTorr with high absorbance and low transmittance. However, its absorbance is also very high, and its transmittance very low, in the *Non-DC* part of the spectrum that will strongly decrease the efficiency of the Si solar cell. The analyses of the two other samples deposited with a plasma pressure of 2 mTorr and 3 mTorr present lower absorbances and higher transmittances in the *Non-DC* range with a slightly higher absorbance and lower transmittance for the 2 mTorr layer (by 4 % and 0.72 % respectively). However, they also present lower similar absorbances in the *DC* one with respect to the 4 mTorr-layer. Thus, the best compromise is the layer deposited under a 3mTorr pressure and a nitrogen ratio rN_2 of 20 %, even if in the *Non-DC* part, such a SiN_x layer absorbs more photons than the Si_3N_4 one.

The increase of absorbance with the nitrogen ratio and the plasma pressure may be linked to the increase of nitrogen in the matrix. Indeed, adding more nitrogen above the stoichiometric amount will create more nitrogen defects. Thus nitrogen defects states will be created in the gap of the matrix and will absorb photons.

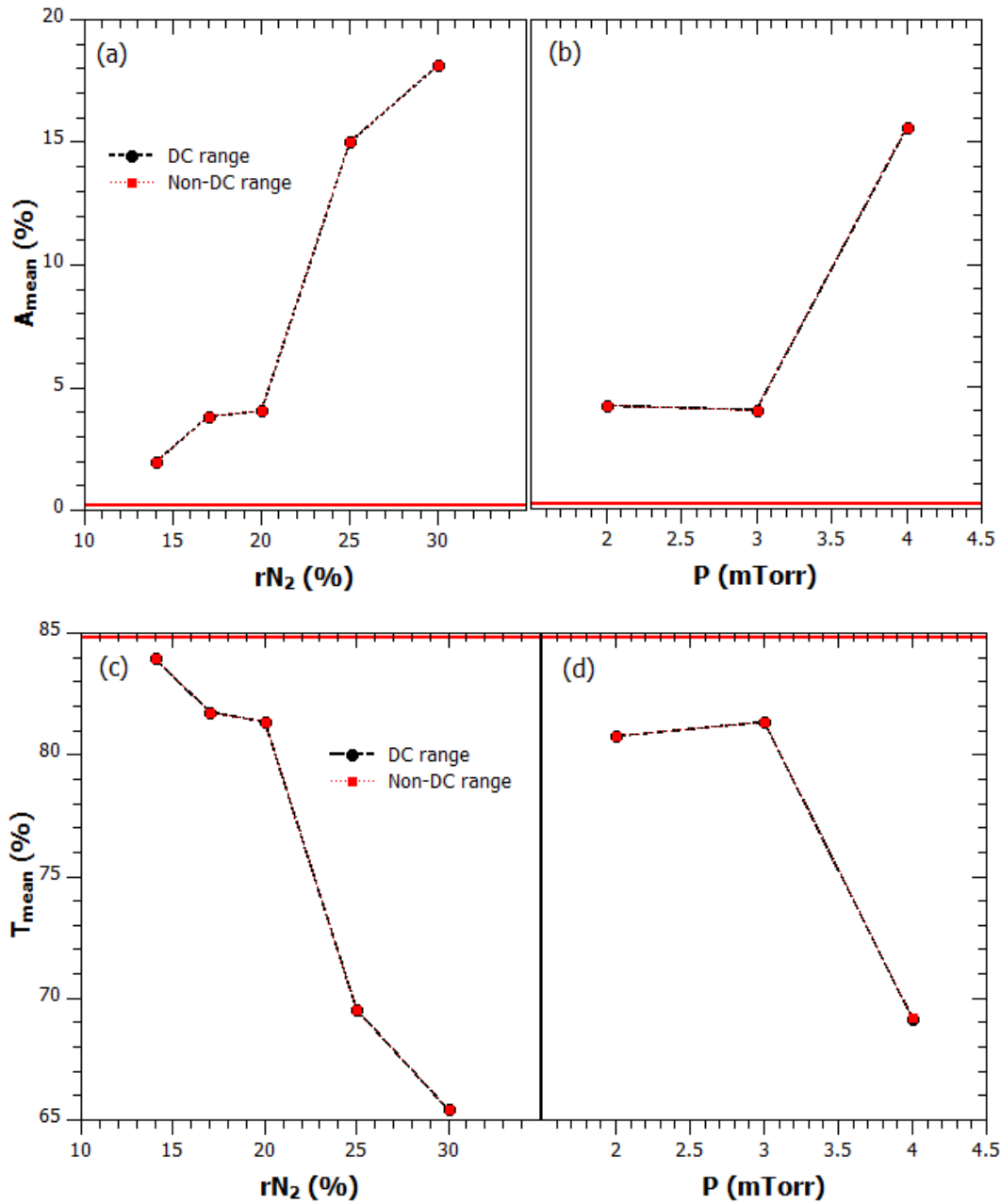


Figure III-12: Integrated normalized absorbance A_{mean} and transmittance T_{mean} of SiN_x layers on the DC and Non-DC ranges as a function of the nitrogen ratio for plasma pressure fixed at 3 mTorr (a) and (c) and as a function of the plasma pressure for a nitrogen ratio fixed at 20 % (b) and (d). The red line corresponds to the reflectance of a Si_3N_4 anti-reflective layer as a reference.

b) Values convoluted by the solar spectrum

The absorbance A_{eff} , reflectance R_{eff} , and transmittance T_{eff} efficiencies convoluted by the AM1.5 solar spectrum allow to access the interaction between the light of the AM1.5 solar spectrum and the layer and thus study the compatibility of the layer with the sun light.

The reflectance efficiency (R_{eff}) (see §I.4.1.) integrated and normalized over the 300-1200 nm range corresponding to the whole solar spectrum is reported on *Figure III-13* as a function of the plasma pressure (*Figure III-13 (a)*), and of the nitrogen ratio (*Figure III-13 (b)*). Those values are compared to the R_{eff} of a Si_3N_4 reference layer (red line).

While taking into account the interaction between the layer and the AM1.5 solar spectra, the layers displaying the best anti-reflective properties are those fabricated with $P = 4$ mTorr and $rN_2 = 25$ %. However, considering our reference, the layers fabricated with $P = 2$ and 3 mTorr and $rN_2 = 20$ % have a R_{eff} close to the red line and present good reflectance characteristics. Thus, the plasma pressure P does not seem to have a big influence on the R_{eff} while the rN_2 values have to be between 20 and 25 % to produce layers meeting one of the above-mentioned criteria.

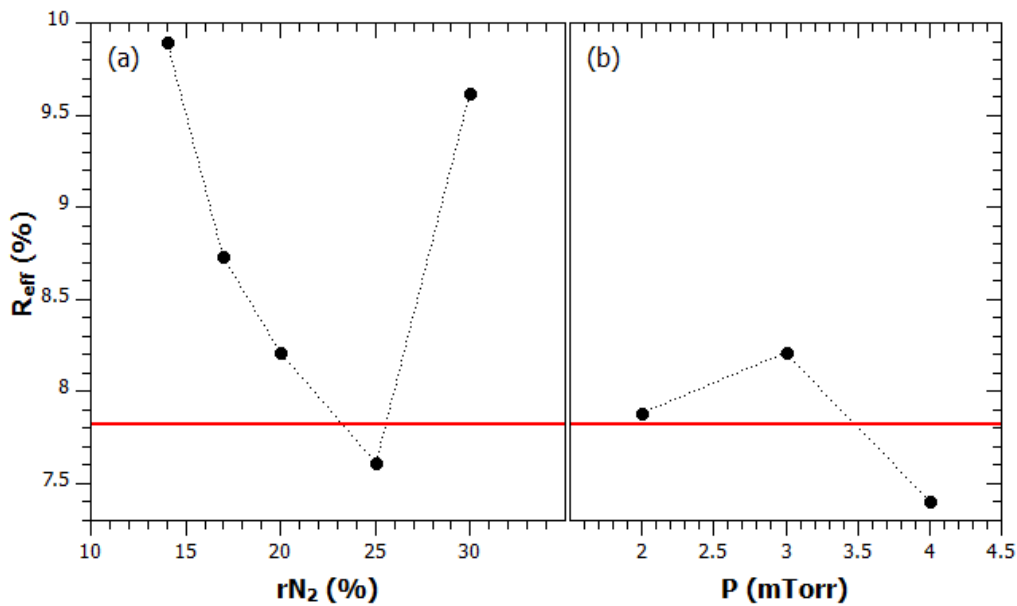


Figure III-13: Reflectance efficiency R_{eff} at the air/layer interface of SiN_x layers as a function of the nitrogen ratio for plasma pressure fixed at 3 mTorr (a) and as a function of the plasma pressure for a nitrogen ratio fixed at 20 % (b). The red line corresponds to the reflectance of a Si_3N_4 anti-reflective layer as a reference.

The absorbance and transmittance efficiencies integrated and normalized over specific λ ranges (A_{eff} and T_{eff}) of the layer are studied as above (see §I.4.1.). *Figure III-14* exhibits A_{eff} and T_{eff} of the same previous samples for different nitrogen ratios with plasma pressure fixed at 3 mTorr (*Figure III-14 (a) and (c)*) and plasma pressures with a nitrogen ratio fixed at 20 % (*Figure III-14 (b) and (d)*). The red lines represent the Si_3N_4 reference. It is important to note that the values of A_{eff} and T_{eff}

are similar in the two ranges which is explained by the monotony of the refractive index. Contrary to the reflectance efficiency R_{eff} that has an evolution opposite to the mean reflectance R_{mean} , A_{eff} and T_{eff} have a similar evolution to A_{mean} and T_{mean} . Thus, A_{eff} increases and T_{eff} decreases with the increase of rN_2 , with a pronounced increase or decrease after 20 %. The similar evolution is seen also with the increase of P .

According to the absorbance and transmittance, the criteria previously mentioned (low reflectance on the whole solar spectrum, absorbance high and transmittance low in the *DC* range, and absorbance low and transmittance high in the *Non-DC* range) are reached in the range of rN_2 is between 14 and 20 %, and P below 3 mTorr. However, the reflectance measurements show that it might be interesting to also look for rN_2 between 20 and 25 % to improve the anti-reflective properties of the layers. **The best compromise is thus the layer deposited with a nitrogen ratio rN_2 of 20 % and a plasma pressure P of 3 mTorr.**

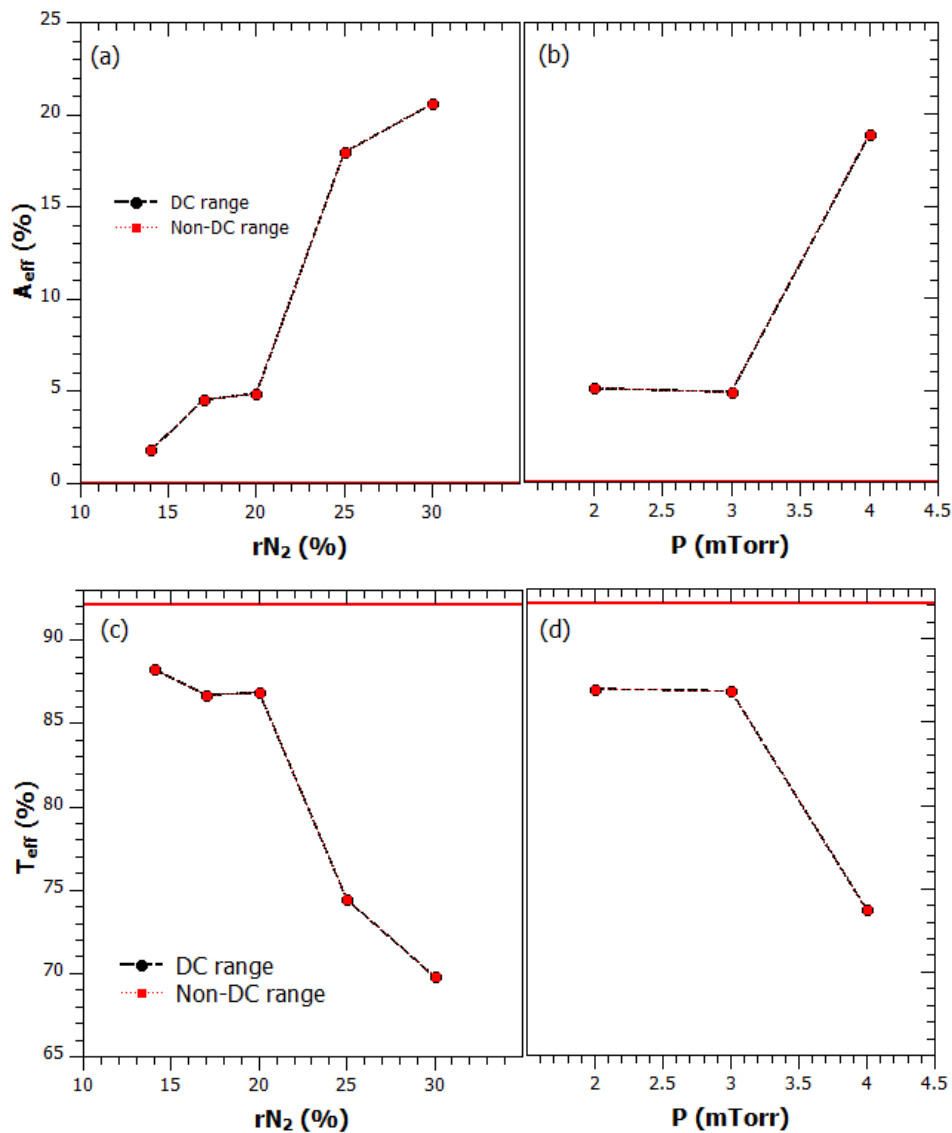


Figure III-14: Integrated normalized reflectance A_{eff} and T_{eff} of SiN_x layers on the DC and Non-DC ranges as a function of the nitrogen ratio for plasma pressure fixed at 3 mTorr (a) and (c) and as a function of the plasma pressure for a nitrogen ratio fixed at 20 % (b) and (d). The red line corresponds to the reflectance of a Si_3N_4 anti-reflective layer as a reference.

III.2.2.4. Photoluminescence

Photoluminescence measurements of SiN_x layers as a function of the plasma pressure and the nitrogen ratio were made with two different gratings. The first that is blazed at 300 nm with 1200 lines per mm and denoted [1200-300] is more dispersive than the second one blazed at 750 nm with 600 lines per mm and denoted [600-750].

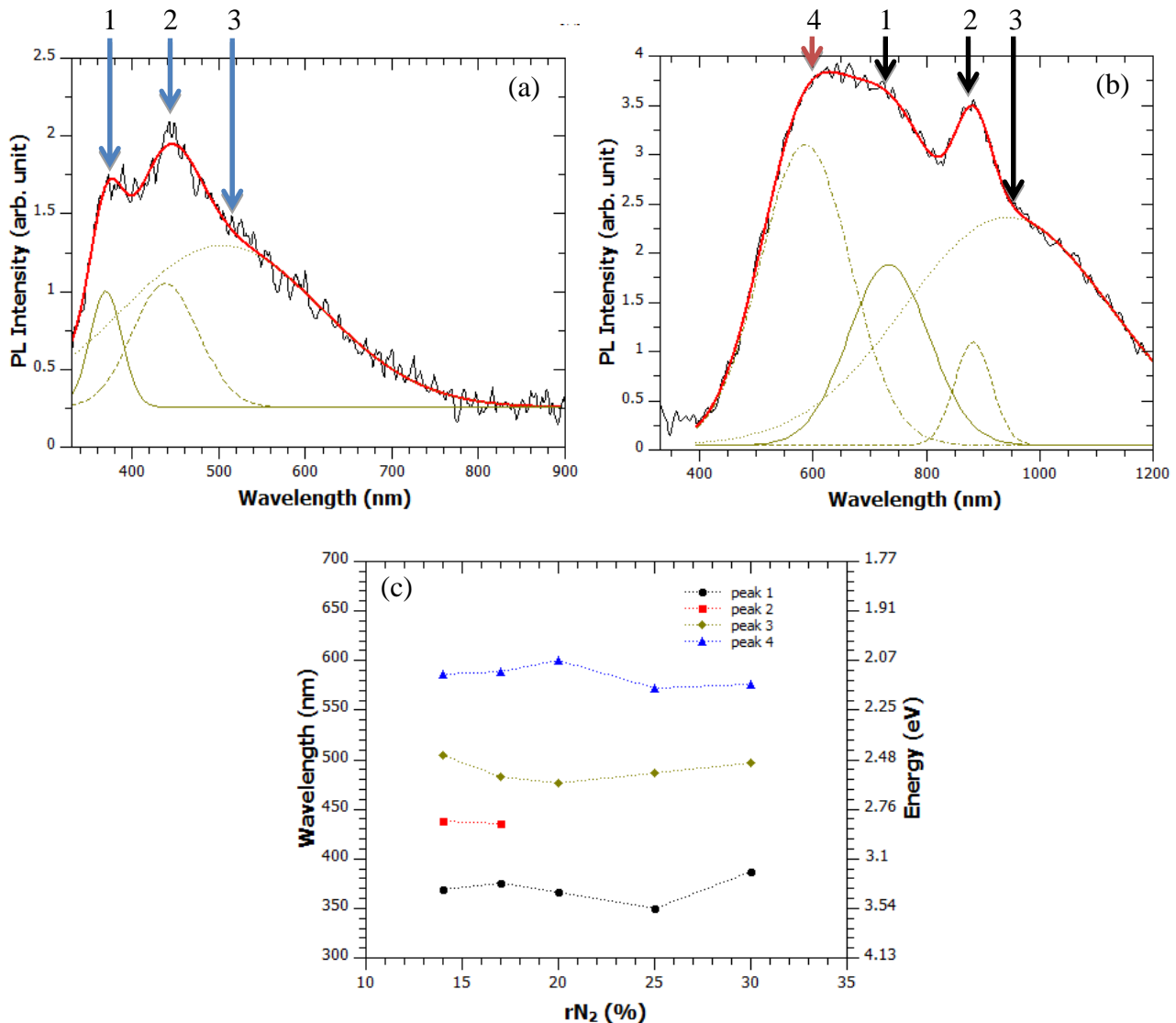


Figure III-15: Photoluminescence spectra (black curves) of the SiN_x layers with the [1200-300] (a) and the [600-750] (b) gratings for a 20 % nitrogen ratios and a 3 mTorr plasma pressure. The experiments are carried out with an excitation wavelength of 285 nm. The red curves are the fit made of several Gaussian curves (green curves). Position of the various peaks as a function of the nitrogen ratio (c).

Several peaks can be detected with both gratings (Figure III-15). In the case of the [600-750] grating on Figure III-15 (b), the addition of filters up to 645 nm before the detection eliminates the peaks from 700 nm to 1200 nm (marked by black arrows). Those peaks were found to be the second

order of the three first peaks (marked by blue arrows) of the spectra measured with the [1200-300] grating on *Figure III-15 (a)*. In some cases (25 % and 30 %), the signal being low ($5 \cdot 10^{-6}$ arb. unit), it merges with the background noise ($1 \cdot 10^{-6}$ arb. unit) and peaks are difficult to determine.

Previous studies focused on the emission of the SiN_x matrix and its origin [14–18], demonstrated that defects of the SiN_x material such as dangling bonds ($\equiv\text{Si}^-$, $\equiv\text{Si}^0$, $=\text{N}^-$) and the unit ($\equiv\text{Si-Si}\equiv$, $=\text{N}_2^0$, $=\text{N}_4^+$) create energy levels inside the bandgap (of 5.4 eV).

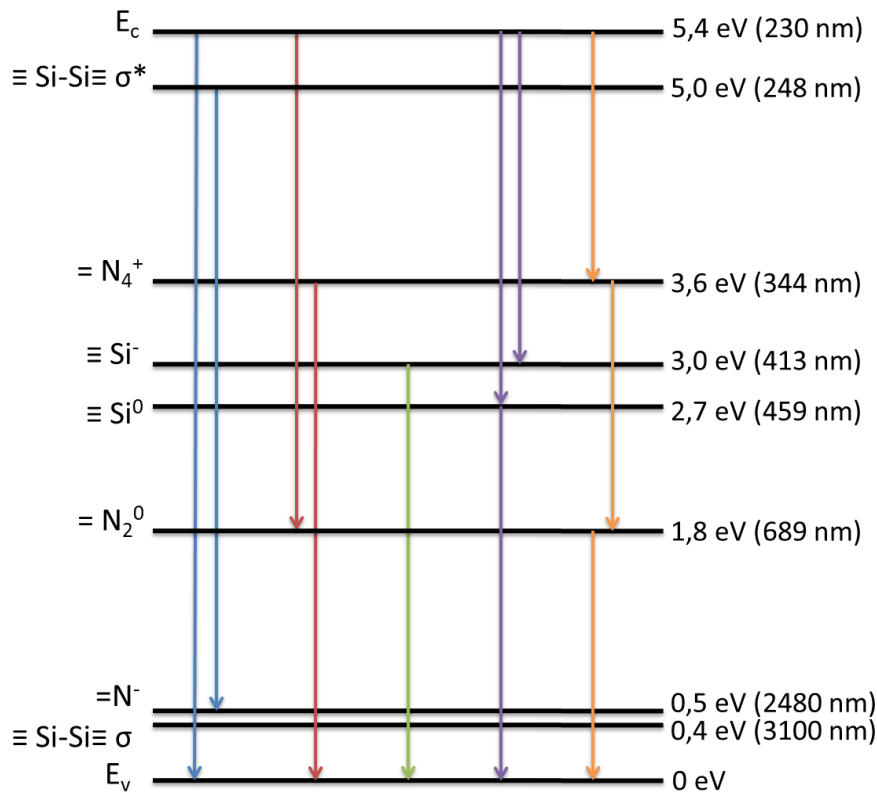


Figure III-16: Energy level diagram of the SiN_x matrix with the energy transitions (arrows) observed in the literature [14–18].

The PL spectra of the annealed (CTA 850 °C 1 h) SiN_x layer deposited with 14 % $r\text{N}_2$ and 3 mTorr is reported on *Figure III-15 (a) and (b)*. A multi-peaks fit (modeling peaks thanks to Gaussian curves) shows that the photoluminescence spectra are composed of three to four peaks depending on the deposition parameters. The position of those broad peaks due to the density of states of the defects is displayed on *Figure III-15 (c)*. A correspondence is found between the experimental and theoretical energy transitions that may thus be associated to specific electronic transitions, as reported on *Figure III-16*:

- The first peak at 370 nm (3.3 eV) may correspond to the 3.1 to 3.6 eV transitions associated to the E_c or $\equiv\text{Si-Si}\equiv\sigma^* \rightarrow =\text{N}_2^0$ and $=\text{N}_4^+ \rightarrow =\text{N}^-$, $\equiv\text{Si-Si}\equiv\sigma$, or E_v electronic transitions (red arrows).
- The second peak at 440 nm (2.8 eV) may correspond to the 2.5 to 3.0 eV transitions associated to the $\equiv\text{Si}^- \rightarrow =\text{N}^-$, $\equiv\text{Si-Si}\equiv\sigma$, or E_v electronic transitions (green arrow).

- The third peak at 490 nm (2.5 eV) may correspond to the 2.2 to 2.7 eV transitions associated to the E_c or $\equiv\text{Si-Si}\equiv \sigma^* \rightarrow \equiv\text{Si}^0$ and $\equiv\text{Si}^0 \rightarrow =\text{N}^-$, $\equiv\text{Si-Si}\equiv \sigma$, or E_v electronic transitions. It also might correspond to the 2.0 to 2.4 eV associated to the E_c or $\equiv\text{Si-Si}\equiv \sigma^* \rightarrow \equiv\text{Si}^-$ electronic transitions (violet arrows).
- The fourth peak at 585 nm (2.1 eV) may correspond to 1.3 to 1.8 eV transitions associated to the E_c or $\equiv\text{Si-Si}\equiv \sigma^* \rightarrow =\text{N}_4^+$, the $=\text{N}_2^0 \rightarrow =\text{N}^-$, $\equiv\text{Si-Si}\equiv \sigma$, or E_v , and $=\text{N}_4^+ \rightarrow =\text{N}_2^0$ the electronic transitions (orange arrows).

It is important to note that the energy levels associated to the $\equiv\text{Si-Si}\equiv \sigma$ and σ^* as well as $=\text{N}^-$ centers are close to the conduction and valence bands (0.5 eV or less). Therefore, it is difficult to determine from or to which of those energy levels or bands the energy transfers are made. It may result in a broad *PL* peak.

It is interesting to note that the second peak, from $\equiv\text{Si}^- \rightarrow =\text{N}^-$, $\equiv\text{Si-Si}\equiv \sigma$, or E_v (at 440 nm or 2.8 eV), appears only for the values of rN_2 of 14 % and 17 %. This may be due to the decreasing silicon content proportionally to the nitrogen one that will decrease the number of Si-Si bonds and thus favors the Si-N one, as well as the number of electron trapping silicon defects thus decreasing the $\equiv\text{Si}^- \rightarrow =\text{N}^-$, $\equiv\text{Si-Si}\equiv \sigma$, or E_v transfers.

Following the same reasoning the E_c or $\equiv\text{Si-Si}\equiv \sigma^* \rightarrow \equiv\text{Si}^-$ electronic transitions (violet arrow to the right) is less probable than the E_c or $\equiv\text{Si-Si}\equiv \sigma^* \rightarrow \equiv\text{Si}^0$ and $\equiv\text{Si}^0 \rightarrow =\text{N}^-$, $\equiv\text{Si-Si}\equiv \sigma$, or E_v electronic transitions. Indeed, the third peak is present for all the nitrogen ratios while the second peak that features the $\equiv\text{Si}^-$ energy level is present only for the lowest rN_2 values.

Thus the defect states in the bandgap are at the origin of the emissions at around 370, 440, and 490 nm and might be resonant with the energy level of the terbium ions. The matrix may thus transfer energy to the terbium ions.

III.2.3. Conclusion

The optical properties as a function of the plasma pressure and the nitrogen ratio in the plasma have been studied in order to determine the deposition parameters. The optimized frequency conversion layer meets the required criteria of high absorbance and low transmittance on the *DC* range and low absorbance and high transmittance for the *Non-DC* range coupled with a low reflectance on the whole solar spectrum. Following those criteria, the layer deposited with a plasma pressure of 3 mTorr and a nitrogen ratio of 20 % is the best compromise. Photoluminescence measurements on the same layers show the existence of distinct states in the bandgap of the matrix but cannot determine the terbium ions excitation efficiency. Thus, a study of the Tb-doped layer as a function of the plasma pressure and the nitrogen ratio in the plasma is needed to determine the best deposition parameters.

III.3. Terbium-doped Matrix, SiN_x:Tb³⁺

Once the fabrication conditions for an optimized matrix are known, the second step consists in incorporating terbium ions in this matrix. The system SiN_x:Tb³⁺ will be optimized mainly through the photoluminescence intensity of the terbium peaks. In this part, the layers are deposited in our laboratory by *RF* reactive magnetron co-sputtering of a pure silicon target and a metallic terbium one in a nitrogen-rich plasma on a silicon P-type *CZ* (Czochralski) wafer. The deposition is performed with the values of the Si target power density, the substrate-target distance (*d*) and the substrate rotation fixed at 4.5 W/cm², 10 cm, and 20 rpm, respectively. The plasma pressures (*P*) investigated are 2, 3, and 4 mTorr and the nitrogen ratio *rN₂* is varied from 14 % to 30 %. The *RF* power density applied on the terbium target (*RFP_{Tb}*) varies from 0.3 to 1.8 W/cm². The deposition time (*t_d*) was adjusted in each case to obtain 90nm-thick layers. Unless otherwise stated, the layers are annealed by means of conventional furnace (*CTA*) at 850 °C for 1 h under nitrogen flow. Prior to analyze the terbium incorporation effect, the structural, optical properties of the matrix are studied as a function of the two variable deposition parameters that are the nitrogen ratio and the plasma pressure. Those studies allow to determine an optimized system that may be used as a down-shifting (*DS*) system or as a base to develop a down-conversion (*DC*) layer.

III.3.1. Effect of the plasma pressure and the nitrogen ratio

III.3.1.1. Composition analyses

As observed on *Figure III-17*, the Tb-doped layer has a higher refractive index at 1.95 eV than the stoichiometric material ($n_{\text{Si}_3\text{N}_4} = 2.03$ at 1.95 eV) and also than the undoped material. The higher values of n achieved at 1.95 eV for Tb-doped layers might be due:

- to a change of the relative content of Si and N due to a modification of the deposition rate of the species by the addition of Tb in the plasma during deposition.
- to the incorporation of terbium ions in the matrix inducing higher disorder due to large RE ions atomic radius. Indeed, a n that goes away from $n_{\text{Si}_3\text{N}_4}$, being lower or higher, traduces a matrix of higher disorder than the well-ordered stoichiometric material.

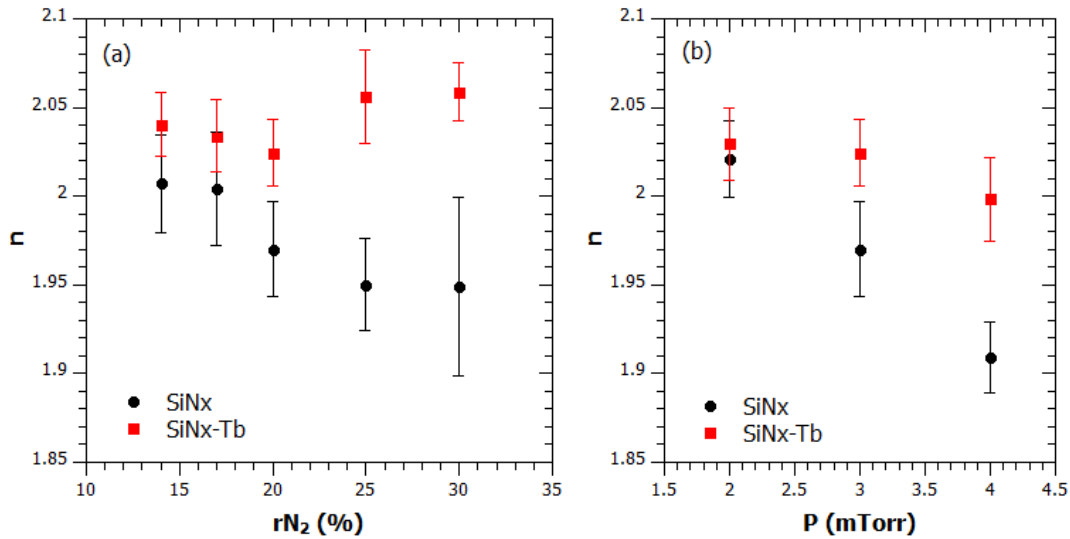


Figure III-17: Refractive index values of the undoped (black) and Tb-doped (red) layers at 1.95 eV as a function of the plasma pressure for a nitrogen ratio fixed of 20 % (a) and of the nitrogen ratio for a plasma pressure fixed at 3 mTorr (b).

Figure III-18 shows the Si-N bond LO band position and intensity for the Tb-doped and the undoped layers, as a function of the nitrogen ratio rN_2 and the plasma pressure P . We can see that the LO peak position shifts toward the low wavenumbers (redshift) and its intensity is lower for the Tb-doped layers than for the undoped ones for the variation of rN_2 . The shift of the LO band toward the low wavenumbers (redshift) with the incorporation of Tb^{3+} ions is here again small but validated by the work of O. Debieu [5] and may express either a decrease in the relative N content (thus an increase of the Si relative content) or an increase of the disorder of the matrix. The decrease of the LO band intensity may point toward an increase in the matrix disorder.

To investigate the origin of this evolution, RBS analyses are performed on one Tb-doped- and one undoped- layers (see *Table III-2*). From the atomic concentration, the relative amounts of each

species can be calculated. While taking into account solely the Si and N species, their relative amounts are the same for the two samples, 43 % and 57 %, respectively. Those results rule out the hypothesis of a change in the relative proportions of Si and N. Thus, the refractive index variation at 1.95 eV as well as the FTIR peak shift is due to the increase of the matrix stress induced by the addition of large diameter rare earths ions.

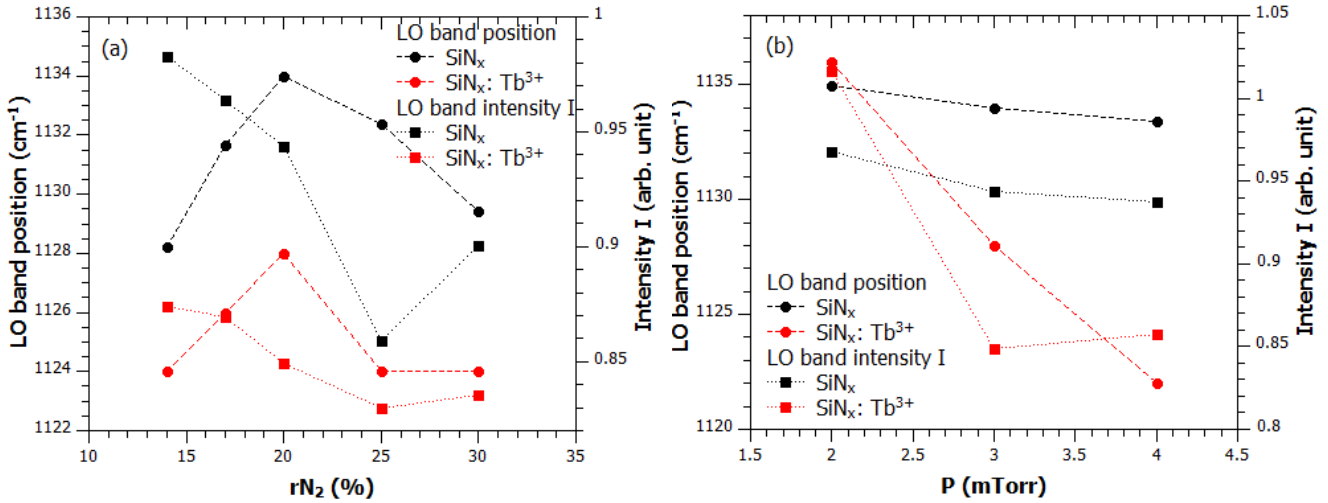


Figure III-18: Si-N bond LO band position and intensity of the matrix (black) and the Tb-doped system (red) as a function of the plasma pressure for a nitrogen ratio fixed at 20 % (a) and of the nitrogen ratio for a plasma pressure fixed at 3 mTorr (b).

Sample	Si ($\times 10^{15}$ atoms/cm ²)	N ($\times 10^{15}$ atoms/cm ²)	Tb ($\times 10^{15}$ atoms/cm ²)
SiN _x (3 mTorr, 20 %)	360	480	/
SiN _x :Tb ³⁺ (3 mTorr, 20 %, 0.45 W/cm ²)	294	392	12.74

Table III-2: RBS results obtained for the undoped and Tb-doped layer.

III.3.1.2. Optical properties

Figure III-19 exhibits the evolution of the PL intensity for the four characteristic peaks of the terbium ions corresponding to the 5D_4 to 7F_3 , 7F_4 , 7F_5 , and 7F_6 transitions at 629 nm, 594 nm, 550 nm, and 493 nm, respectively [10]. This evolution is given for different nitrogen ratios rN_2 in the plasma (Figure III-19 (a)) and different plasma pressures (Figure III-19 (b)).

The PL intensity of the terbium ions peaks increases slightly with the nitrogen ratio till 20 % and then decreases. Similarly, the PL peaks intensity attained a maximum for 3 mTorr while the plasma pressure increases. However, the peaks intensities achieved for 14 % and 17 % nitrogen ratios are very close and inside the 10 % uncertainty of the measurement.

The higher Tb^{3+} PL peaks intensity is obtained for deposition parameters fixed at 20 % for rN_2 and 3 mTorr for the plasma pressure.

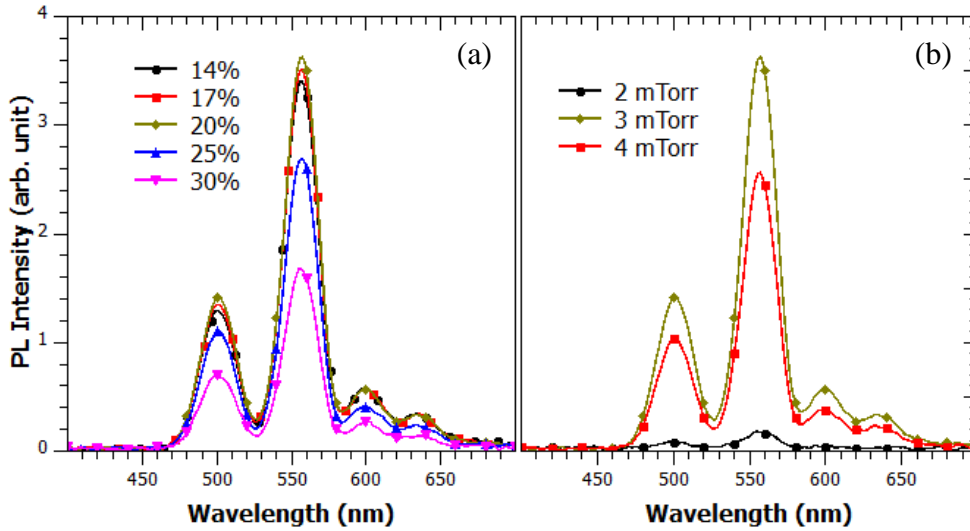


Figure III-19: PL measurements of $SiN_x:Tb^{3+}$ system for different nitrogen ratios and a plasma pressure fixed at 3 mTorr (a), for different plasma pressures and a nitrogen ratio fixed of 20 % (b). The excitation wavelength used is 285 nm with a [1200-300] grating.

Figure III-20 shows that R_{eff} , A_{eff} and T_{eff} of the Tb-doped layers are similar to the ones of the undoped layers studied previously (§ III.2.). The R_{mean} , A_{mean} and T_{mean} of the Tb-doped layers are also similar to the ones of the undoped layers but are not shown here. Thus reflectance, absorbance and transmittance are stable with the incorporation of terbium in the layer. It means that the favorable deposition parameters are still between 20 and 25 % rN_2 and a plasma pressure of 3 mTorr for reflectance and between 14 and 20 % rN_2 and up to 3 mTorr for the absorbance and transmittance. So, the compromise of fixing the deposition parameters at 20 % for rN_2 and 3 mTorr for P is still valid. **Taking into account the various criteria mentioned above as well as the terbium PL intensity, the optimal layer is deposited with a nitrogen ratio in the plasma of 20 % and a plasma pressure of 3 mTorr. Those parameters are fixed for the rest of the study.**

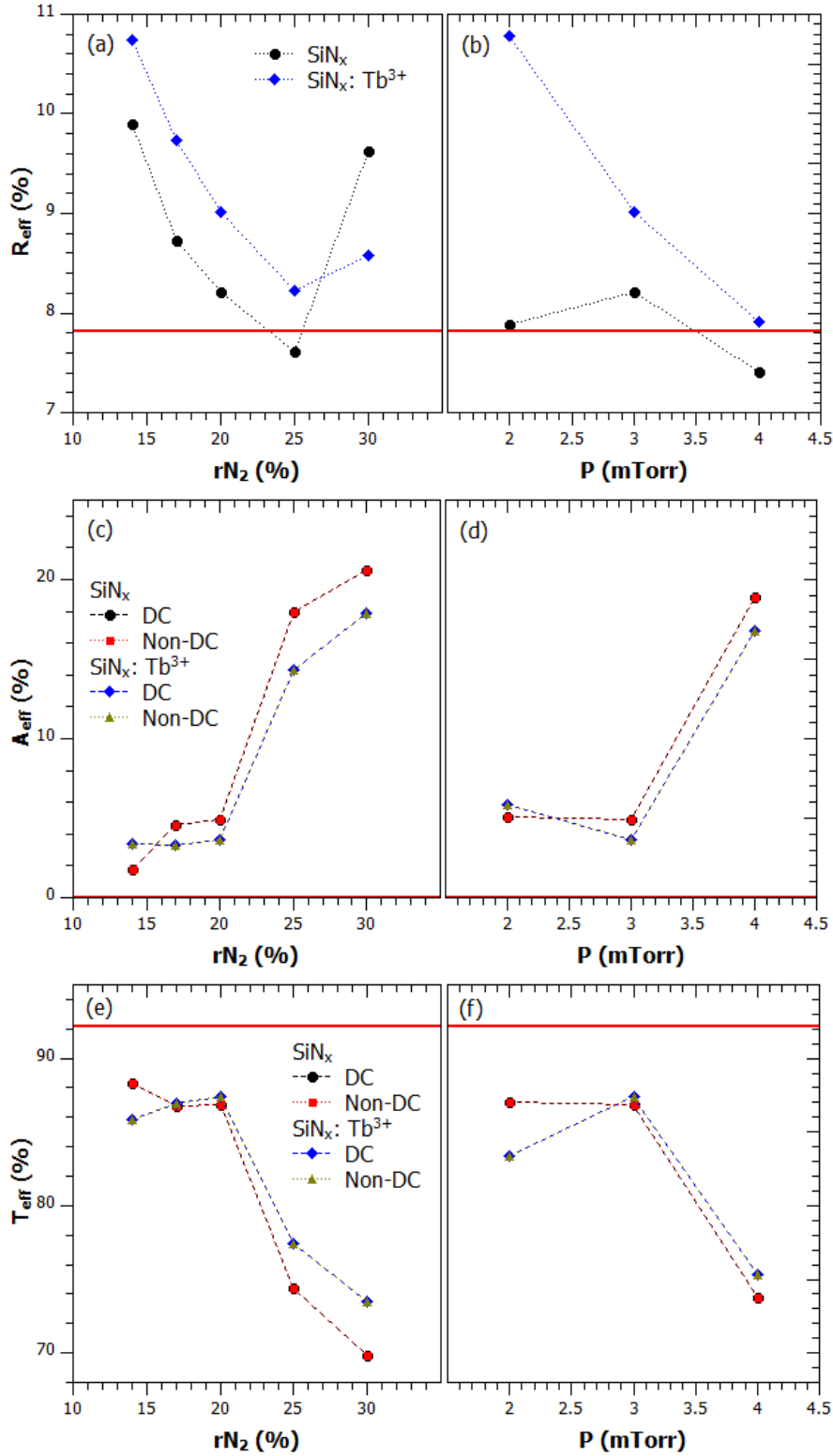


Figure III-20: R_{eff} , A_{eff} , and T_{eff} of non-annealed Tb-doped- and undoped- layers as a function of the nitrogen ratio for a plasma pressure fixed at 3 mTorr ((a), (c), and (e)) and of the plasma pressure for a nitrogen ratio fixed at 20 % ((b), (d), and (f)). The red lines represent the characteristics of a Si_3N_4 reference [11]. III.3.2. Influence of the RF power density on the Tb target on the growth of $SiN_x:Tb^{3+}$ film.

III.3.2. Influence of the RF power density on the Tb target on the growth of SiN_x: Tb³⁺ film

III.3.2.1. Composition analyses

FTIR measurements were also pursued on non-annealed samples doped with terbium as a function of the terbium target power density RFP_{Tb} (Figure III-21 (a)). The Si-N bond LO band shifts toward the lower wavenumbers (redshift) and its intensity decreases quite spectacularly while the Tb target power density increases. Coupled with the increase of the refractive index at 1.95 eV with the RFP_{Tb} (Figure III-21 (b)), such behavior characterizes an important increase of disorder in the matrix provoked by the addition of an increasing quantity of large rare earth ions. This important increase of disorder is confirmed by the increase of the overlapping of the TO-LO bands around 1000 cm⁻¹.

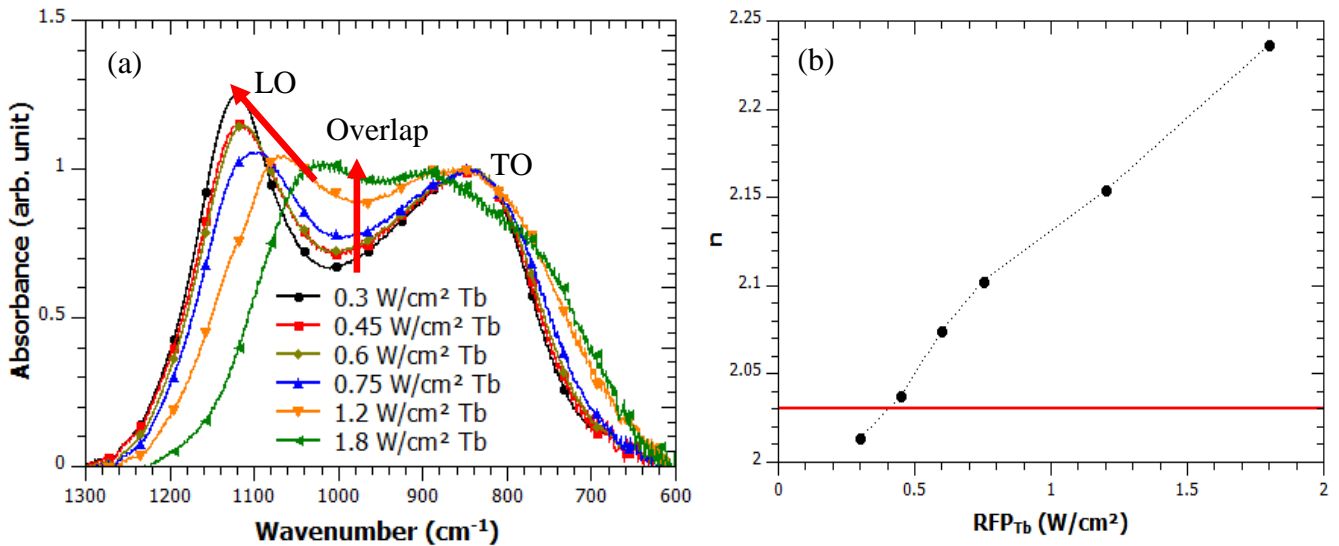


Figure III-21: FTIR spectra (a) and refractive index at 1.95 eV (b) of non-annealed SiN_x:Tb³⁺ layers as a function of the Tb target power densities for fixed nitrogen ratio (20 %) and plasma pressure (3 mTorr). The red line corresponds to the refractive index of the stoichiometric Si₃N₄.

III.3.2.3. Photoluminescence

The effect of the terbium incorporation on the emission properties of the SiN_x:Tb³⁺ layers is reported on Figure III-22 (a) in which the photoluminescence spectra are displayed for different values of RFP_{Tb} . The terbium peaks intensity increases with RFP_{Tb} and reaches a maximum for 0.45 W/cm² before decreasing (Figure III-22 (c)). The increase of intensity of the Tb³⁺ emission before 0.45 W/cm² associated with the constant lifetime may be explained by the addition of optically active terbium ions. The decrease of intensity with RFP_{Tb} is attributed to a concentration quenching process [12] due the large number of Tb³⁺ ions incorporated in the matrix. This is the signature of

clustering of rare earth ions and/or an increase of the matrix disorder. This last point is confirmed by both the lifetime measurements (Figure III-22 (b) and (c)) and the FTIR analyses previously detailed (Figure III-21 (a)). In the former, the terbium lifetime of the $^5D_4-^7F_5$ transition stays stable up to $0.45 \text{ W/cm}^2 \text{ RFP}_{Tb}$ meaning that the addition of terbium ions does not create new non-radiative de-excitation ways. For higher values of RFP_{Tb} , a decrease of the terbium lifetime is observed and is the signature of new non-radiative de-excitation ways. They may be due to the formation of defects in the matrix that can trap photons and/or energy migration between terbium ions that become close enough to transfer their energy to each other till encountering a defect that will once again trap the energy. Concerning the FTIR measurements, the overlap intensity of the LO-TO pair around 1000 cm^{-1} as well as the decrease and the shift toward the high wavelengths of the LO peak are the signature of an increasing disorder and thus an increasing number of defects that may be responsible for the PL emission quenching observed. **Thus our optimum settings leading to the higher Tb^{3+} PL peaks intensity are 0.45 W/cm^2 terbium target power density with 20 % nitrogen ratio, and 3 mTorr plasma pressure.**

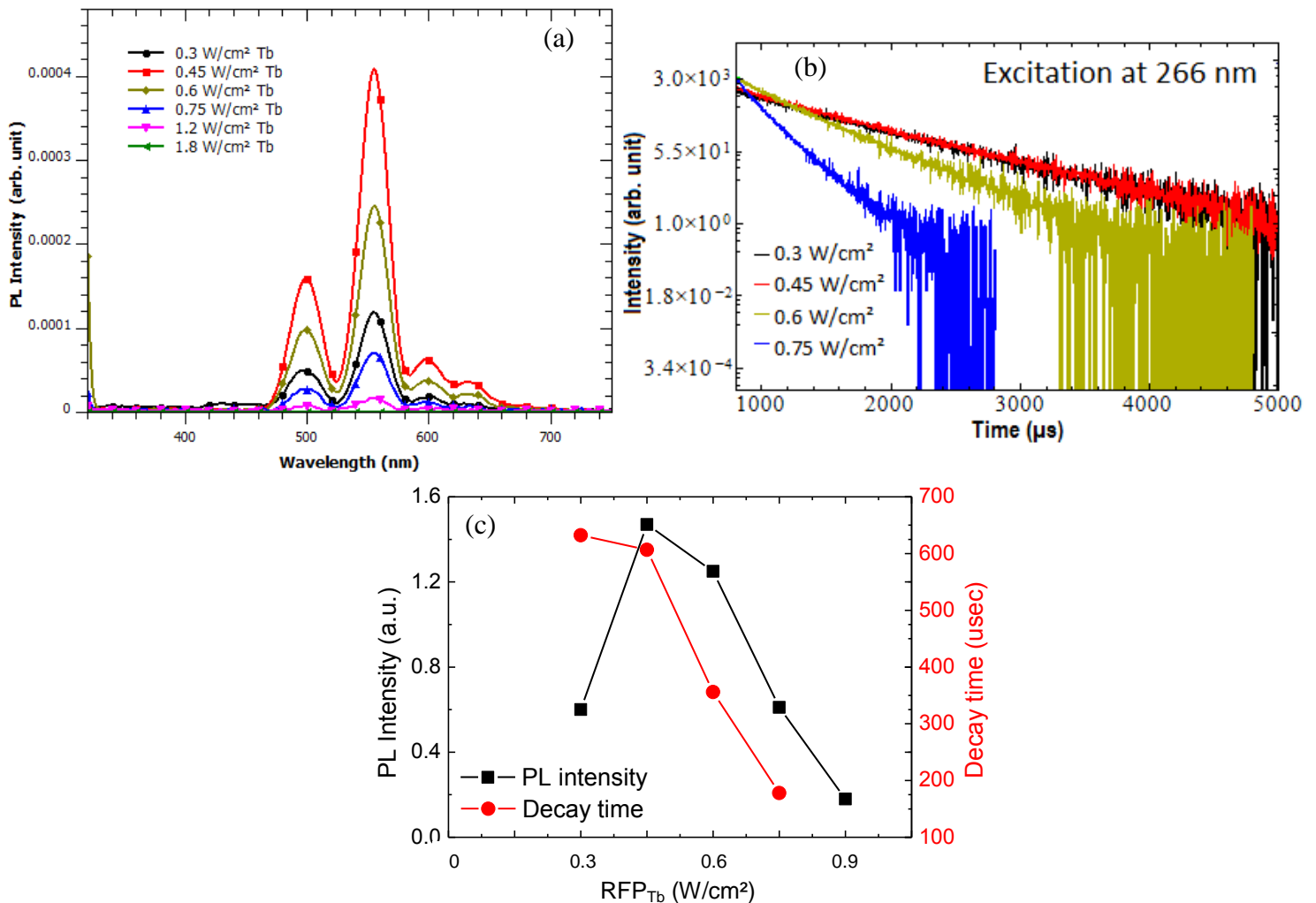


Figure II-22: PL curves for an excitation at 285 nm and a [1200-300] grating (a), and lifetime measurements (b) of the $\text{SiN}_x:\text{Tb}^{3+}$ layers for different RFP_{Tb} . PL intensity maximum at 550 nm and Tb lifetime values as a function of the RFP_{Tb} (c).

III.3.3. Conclusion

In a first time, the reflectance, absorbance, and transmittance as well as the photoluminescence of the Tb-doped layer were studied as function of the nitrogen ratio and of the plasma pressure. We determine the deposition parameters that leads to a layer meeting the criteria awaited of a frequency conversion layer coupled with an anti-reflective layer (low reflectance on the whole solar spectrum, absorbance high and transmittance low in the *DC* range, and absorbance low and transmittance high in the *Non-DC* range) and showing the Tb³⁺ peaks higher *PL* intensity. The deposition parameters of 20 % for the nitrogen ratio and 3 mTorr for the plasma pressure were confirmed as leading to the optimal layer regarding the above mentioned criteria. In a second time, the photoluminescence was studied as a function of the radio frequency power density on the terbium target and the 0.45 W/cm² *RFP_{Tb}* was determine to lead to the layer showing the higher Tb³⁺ *PL* intensity. The evolution of the *PL* intensity was studied and explanations put forward. The layer thus obtained may be used as a base toward the optimization of a down-conversion layer. Such layer may also be used alone on Si *SC* as a down-shifting layer to increase the cell efficiency.

III.4. Study of the energy transfer

An optimized SiN_x:Tb³⁺ layer requires to study the energy transfer from the matrix to the terbium. The purpose of this part is to analyze the transfer mechanism in the studied system. At the end, the properties of the optimized SiN_x:Tb³⁺ layer will be compared with the ones of SiO_xN_y:Tb³⁺ previously studied in our team [13] .

III.4.1. Energy transfer from the matrix to the terbium

III.4.1.1. Terbium non-resonant excitation

As shown in the §III.2.2.4. and on *Figure III-15*, SiN_x *PL* emission covers the range between 320 nm and 488 nm which may allow an energy transfer to the terbium (which ⁵D₄ level is situated at 488 nm). However, the occurrence of such a transfer is not demonstrated.

This energy transfer from the matrix to the terbium ions was tested by exciting the Tb-doped layer at a non-resonant excitation wavelength for the terbium ions. The resulting *PL* spectrum evidences the presence of the four characteristic peaks of the terbium ions corresponding to the ⁵D₄ to ⁷F₃, ⁷F₄, ⁷F₅, and ⁷F₆ energy transfers at 629 nm, 594 nm, 550 nm, and 493 nm (*Figure III-23*). This is a signature of an energy transfer from the matrix to the Tb³⁺ ions.

In addition, *Figure III-24* shows the evolution of the $\text{SiN}_x:\text{Tb}^{3+}$ PL spectrum in the 330 to 460 nm and 460 to 750 nm ranges, corresponding to the host matrix emission and to the terbium ions emission, respectively. The PL emission has been recorded as a function of the terbium target power density. It is noticeable that the matrix emission is quenched as soon as Tb^{3+} ions are incorporated in the matrix. It is another evidence of the energy transfer mechanism taking place between the matrix transfers energy and the Tb^{3+} ions.

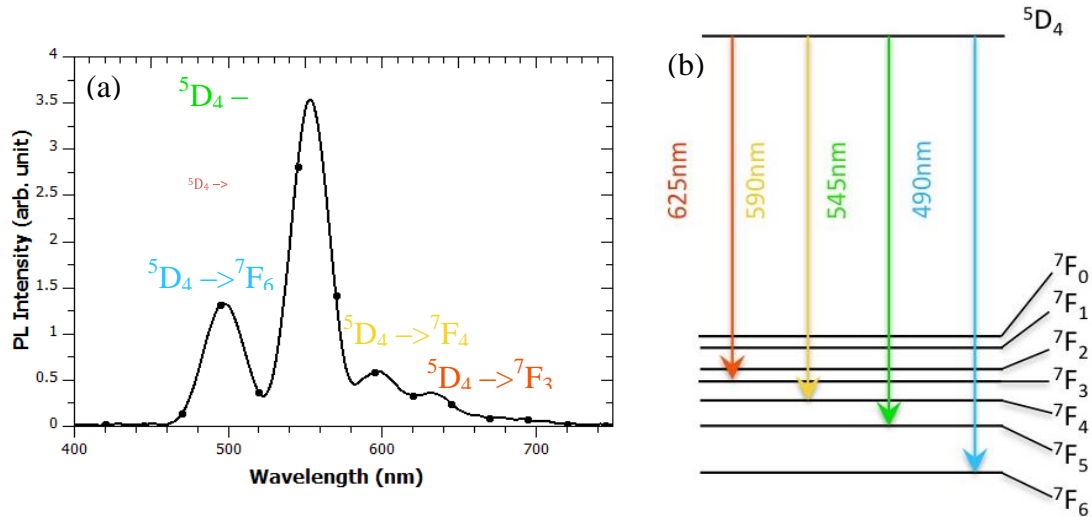


Figure III-23: (a) PL measurement of the terbium-doped matrix for an excitation wavelength of 300 nm measured with the [1200-300] grating. (b) Energy levels of the Tb^{3+} ions and energy transfers corresponding to the PL peaks obtained.

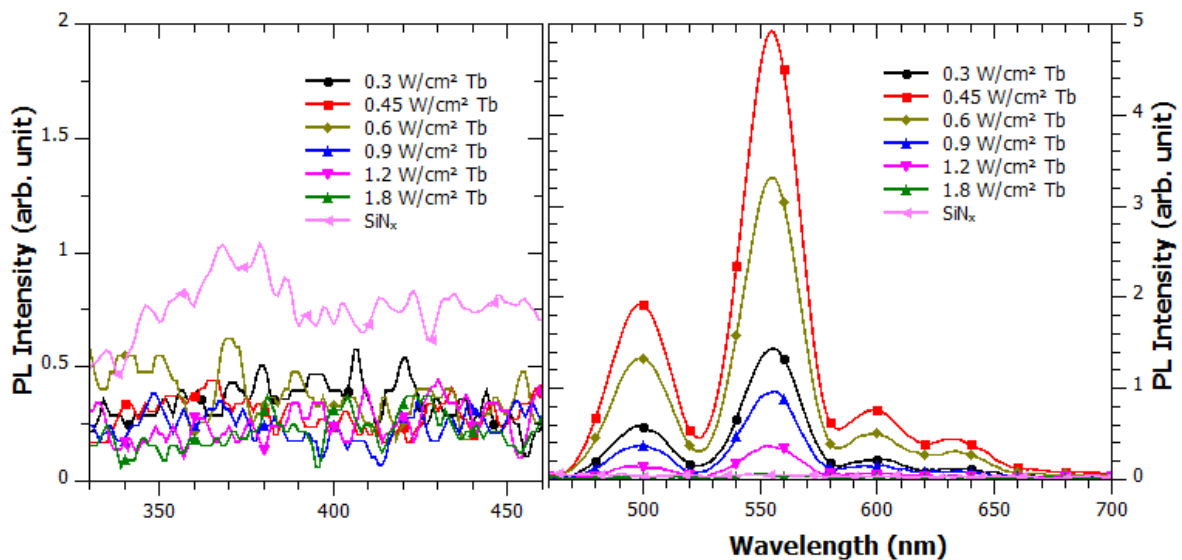


Figure III-24: PL measurements of the $\text{SiN}_x:\text{Tb}^{3+}$ layers for various Tb target power densities applied and compared to the undoped- SiN_x matrix for an excitation wavelength of 285 nm and the [1200-300] grating.

III.4.1.2. Transfer mechanism

Once the transfer from the host matrix to the terbium is demonstrated, the transfer mechanism is detailed. A photoluminescence in excitation of the Tb-doped system spectrum at a detection wavelength of 545 nm (corresponding to the $^5D_4 \rightarrow ^7F_6$ energy transition) is displayed *Figure III-25*. The *PLE* signal is intense from 240 to 290 nm and decreases then to the limit of detectability for wavelengths above 335 nm (3.7 eV). It shows that the Tb-doped system is mainly excited by wavelengths between 240 and 290 nm corresponding to 4.3 to 5.2 eV. This energy range may be associated with the E_c or $\equiv\text{Si-Si}\equiv \sigma^* \rightarrow =\text{N}^-$, $\equiv\text{Si-Si}\equiv \sigma$, or E_v electronic transfers of the matrix that was not previously mentioned (§III.4.1.1.) because the lowest limit of the *PL* setup measurement range is 320 nm. The multiple transfers close in energy that may take place explain that we obtained *PLE* bands instead of peaks. The direct excitation of the Tb^{3+} ions by the sun light may also be considered and act in parallel of the matrix path. Indeed, the *PLE* spectrum on *Figure III-25* ends at around 310 nm while a previous study [19] exposed an important Tb^{3+} ions excitation up to 380 nm.

Figure III-25 also shows that the **terbium ions, being discrete, are excited mostly in their high energy levels such as the $4f^75d$ energy band and the 4F_7 and $^5H_{6,7,8}$ energy levels by the E_c or $\equiv\text{Si-Si}\equiv \sigma^* \rightarrow =\text{N}^-$, $\equiv\text{Si-Si}\equiv \sigma$, or E_v electronic transfers of the matrix (ranging from 4.5 to 5.4 eV or 230 to 275 nm). The terbium ions then undergo non-radiative de-excitation till reaching the 5D_4 energy level from which the four characteristic radiative energy transitions take place.**

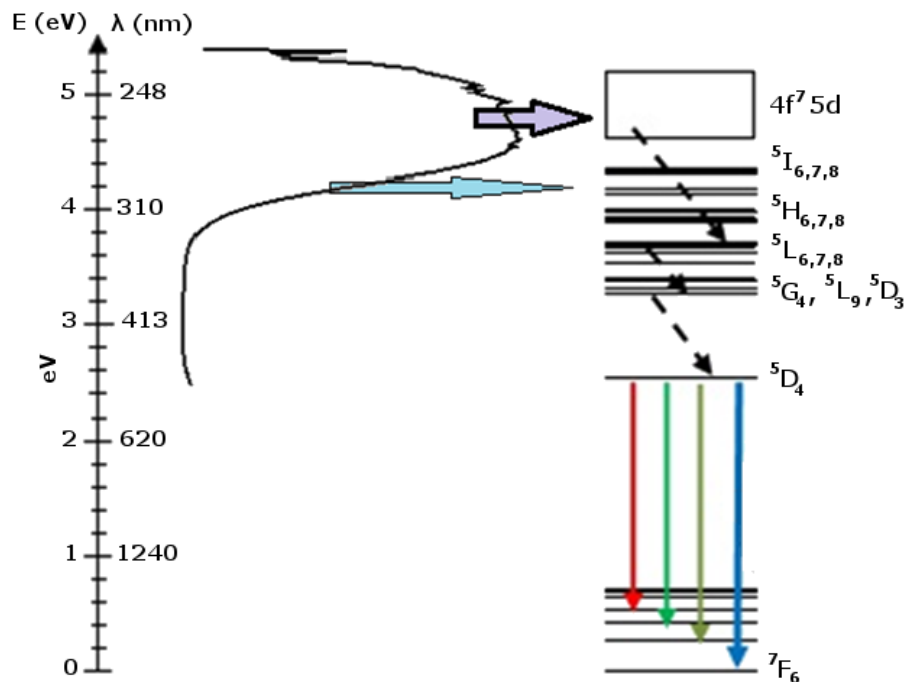


Figure III-25: PLE spectrum of the $\text{SiN}_x:\text{Tb}^{3+}$ system for a detection wavelength of 550 nm and energy level diagram of the Tb^{3+} ion with the energy transfer from the matrix in blue and violet arrows, the non-radiative de-excitation in black straight dashed line arrows, and the radiative de-excitation in colored arrows.

III.4.2. Comparison with a previous study

One of our objectives is to develop a Tb-doped layer that have a higher *PL* intensity of the Tb³⁺ peak than the Tb-doped SiO_xN_y layer developed during the precedent work of Y-T An. The optimized Tb-doped SiN_x layer obtained in this work is thus compared to a similar one constituted by Tb³⁺ ions incorporated in a silicon oxynitride host-matrix, SiO_xN_y [13]. The *PL* intensity at 629 nm, 594 nm, 550 nm, and 493 nm of our optimized sample is found to be 2.34 times more intense than the optimized sample obtained on the SiO_xN_y:Tb³⁺ system (*Figure III-26*). The objective of a higher *PL* peak intensity is reached and, from this point, we also go further and determine how much more light a Si *SC* topped with our Tb-doped SiN_x layer would receive compared to one topped with the Tb-doped SiO_xN_y layer.

Indeed, it has been shown [20] that the Yb³⁺ *PL* intensity, I_{PL} , is given by:

$$I_{PL} = \frac{N^* \cdot V}{\tau_{rad}}, \quad \text{III-6}$$

with V being the volume on which the *PL* excitation is applied, N^* being the excited state population density, and τ_{rad} being the Tb³⁺ radiative lifetime. In our experiment, the volume of interaction and the pump power density (1.9×10^{15} photons/cm² at 285 nm) are constant. Assuming a constant τ_{rad} (around 620 μ s in both matrices) and using *Equation III-6*, we obtain the Tb³⁺ excited state ratio $N^*_{SiN_x}(Tb^{3+})/N^*_{SiO_xN_y}(Tb^{3+}) = 2.34$, which demonstrates the higher *PL* efficiency of the SiN_x:Tb³⁺ system.

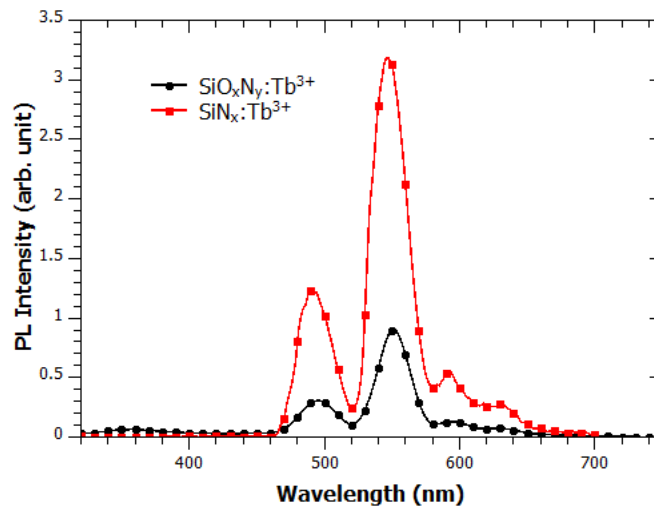


Figure III-26: Photoluminescence spectra of the optimized samples obtained of SiO_xN_y and SiN_x doped terbium matrices for an excitation wavelength of 285 nm measured with the [600-750] grating.

In the same way, the absorbance of both $\text{SiO}_x\text{N}_y:\text{Tb}^{3+}$ and $\text{SiN}_x:\text{Tb}^{3+}$ samples exhibiting the highest Tb^{3+} PL emission are estimated to be 23.2 % and 10.3 %, respectively, for an excitation at 285 nm and 1.9×10^{15} photons/cm². This difference can be attributed to opto-geometrical differences between the two studied layers ($\text{SiO}_x\text{N}_y:\text{Tb}^{3+}$ and $\text{SiN}_x:\text{Tb}^{3+}$), where the layers have different thicknesses (225 nm and 93 nm) and different refractive indexes (1.65 and 2.02).

The *ETMM* program yields the luminescence ratios in the layer, in the air, and in the substrate; the last two may also be called extraction efficiencies. The luminescence ratios are the ratio of the emission in the medium we seek (air, layer or substrate) over the total emission, they are given in *Table III-3*. We can see that the SiN_x layer transfers more to the *SC* (modeled here by the Si) than the SiO_xN_y layer.

For both samples, assuming that their *PL* intensity is proportional to a global efficiency, η^{glo} , composed of the absorbance, the luminescence, and the internal efficiencies:

$$I_{PL} \propto \eta^{glo} = \eta^{abs} \eta^{int} \eta^{lum} . \quad \text{III-7}$$

The luminescence ratios, η^{lum} , defined for each medium are given in *Table III-3*. The absorbance efficiencies represents the propagation with partial absorption of the signal at 501 nm and 557 nm (Tb^{3+}) to the interfaces of the emitting medium and corresponds to the absorbances at the excitation wavelength: $\eta^{abs}(\text{SiN}_x) = 10.3$ % and $\eta^{abs}(\text{SiN}_x\text{O}_y) = 23.2$ %. The internal efficiency represents the *DS* conversion efficiency as well as the efficiency of the energy transfer between the matrix and the terbium ions.

As previously mentioned, the Tb^{3+} excited state ratio of SiN_x *DS* layer (*Figure III-26*) was found to be 2.34 times higher than the one for SiN_xO_y layers with the same *PL* experimental conditions (1.9×10^{15} photons/cm² at 285 nm). From this ratio and with relationship (Equation III-7) we determined the internal efficiency ratio:

$$\eta^{int}(\text{SiN}_x) / \eta^{int}(\text{SiN}_x\text{O}_y) = 2.85 . \quad \text{III-8}$$

This internal efficiency improvement of the *DS* SiN_x layer compared to the thicker SiN_xO_y can be attributed to following improvements: (i) the optically active *RE* content, (ii) the *DS* conversion, or/and (iii) the 501 nm and 557 nm photons propagation.

The *PL* intensity represents the global efficiency in the air, however in the silicon solar cell application, we may be interested in the global efficiency in the silicon *SC*. In order to evaluate this global efficiency in silicon, we use the *Equation III-7* replacing the extraction ratio in the air by the extraction ratio in the silicon (*Table III-3*). The ratio of global efficiency of *DS* layers with emission in the Si substrate leads to:

$$\eta^{glo}(\text{SiN}_x) / \eta^{glo}(\text{SiN}_x\text{O}_y) = 2.14 . \quad \text{III-9}$$

This ratio shows the improvement of the global efficiency of the *DS* SiN_x layer transmitted to the silicon substrate compared to the thicker SiN_xO_y one (assumed to be representative of the silicon *SC*). **For the conditions of thickness and refractive index employed in this work, the silicon, and thus the silicon solar cells, would receive 2.14 times more light at 501 nm and 557 nm from the Tb-doped SiN_x layer compared to the thicker SiN_xO_y one for an excitation at 285 nm.**

$\eta^{\text{lum}}(\%)$	Air	Layer	Silicon
SiN _x	19.3	61.6	19.1
SiN _x O _y	24.4	64.3	11.3

Table III-3: Luminescence ratio of the SiN_x and SiO_xN_y matrixes in the air, the layer, and the silicon.

III.4.3. Conclusion

The energy transfer from the matrix to the terbium ions was proven by the presence of the four characteristic *PL* peaks of Tb³⁺ ions for an excitation non-resonant with the Tb³⁺ ions. The energy transfer was investigated thanks to *PL* and *PLe* measurements of both the undoped and Tb-doped layers. It was found that the Tb³⁺ ions are excited in there high energy levels (4f⁷5d energy band and the ⁴F₇ and ⁵H_{6,7,8} energy levels) by the E_c → =N⁻ electronic transfer of the matrix as well as the gap, before de-exciting non-radiatively to the ⁵D₄ level from which the radiative transitions take place.

The optimized Tb-doped (or *DS*) layer was compared to the optimized layer of a previous study on the SiO_xN_y:Tb³⁺ system and found to have a *PL* intensity 2.34 times higher which leads to the silicon solar cells receiving 2.14 times more light at 501 nm and 557 nm from the Tb-doped SiN_x layer compared to the thicker SiN_xO_y one. Thus, a first objective is reached.

III.5. Conclusion

In this work, both layers of SiN_x and layers of $\text{SiN}_x:\text{Tb}^{3+}$ deposited by reactive magnetron co-sputtering have been studied in order to obtain an optimized thin layer that emits a maximum at 629 nm, 594 nm, 550 nm, and 493 nm (terbium peaks) and has also good anti-reflective properties. This layer may be used as base to the development of a down-conversion layer. Such layer may also be deposited as such on Si *SC* to be used as down-shifting (*DS*) layer to increase the cell efficiency.

The undoped layer was first investigated and its optical properties studied as a function of the nitrogen ratio and the plasma pressure in order for the layers to meet the criteria awaited of a frequency conversion layer coupled with an anti-reflective layer (low reflectance on the whole solar spectrum, absorbance high and transmittance low in the *DC* range, and absorbance low and transmittance high in the *Non-DC* range). A compromise was found for 20 % nitrogen ratio and 3 mTorr plasma pressure.

Those values were then confirmed by a similar study made on Tb-doped layers. The power density applied the terbium target was next investigated through the Tb^{3+} photoluminescence. The higher intensity was obtained for a 0.45 W/cm² terbium target power density.

The energy transfer from the matrix to the terbium ions was proven and investigated. It was found that the Tb^{3+} ions are excited in there high energy levels ($4f^75d$ energy band and the 4F_7 and $^5H_{6,7,8}$ energy levels) by the $E_c \rightarrow =N^-$ electronic transfer of the matrix as well as the gap, before de-exciting non-radiatively to the 5D_4 level from which the radiative transitions take place.

This optimized Tb-doped (or *DS*) layer was compared to the optimized layer of a previous study on the $\text{SiO}_x\text{N}_y:\text{Tb}^{3+}$ system and found to have a *PL* intensity 2.34 times higher which leads to the silicon solar cells receiving 2.14 times more light at 501 nm and 557 nm from the Tb-doped SiN_x layer compared to the thicker SiN_xO_y one. One of our objectives is thus reached.

Bibliography

- [1] T. Li, J. Kanicki, Observation of incident angle dependent phonon absorption in hydrogenated amorphous silicon nitride thin films, *Appl. Phys. Lett.* 73 (1998) 3866. doi:10.1063/1.122919.
- [2] E.D. Palik, *Handbook of Optical Constants of Solids*, Academic Press, Boston, 1985. <http://www.sciencedirect.com/science/article/pii/B9780080547213500010> (accessed March 31, 2016).
- [3] G.E. Jellison, Optical functions of silicon determined by two-channel polarization modulation ellipsometry, *Opt. Mater.* 1 (1992) 41–47.
- [4] E.R. Peck, B.N. Khanna, Dispersion of Nitrogen*, *JOSA.* 56 (1966) 1059–1063.
- [5] O. Debieu, R.P. Nalini, J. Cardin, X. Portier, J. Perrière, F. Gourbilleau, Structural and optical characterization of pure Si-rich nitride thin films, *Nanoscale Res. Lett.* 8 (2013) 1–13.
- [6] L. Huang, K.W. Hipps, J.T. Dickinson, U. Mazur, X.D. Wang, Structure and composition studies for silicon nitride thin films deposited by single ion beam sputter deposition, *Thin Solid Films.* 299 (1997) 104–109. doi:10.1016/S0040-6090(96)09446-1.
- [7] S. Hasegawa, L. He, Y. Amano, T. Inokuma, Analysis of SiH and SiN vibrational absorption in amorphous SiN_x:H films in terms of a charge-transfer model, *Phys. Rev. B.* 48 (1993) 5315–5325. doi:10.1103/PhysRevB.48.5315.
- [8] T. Makino, Composition and structure control by source gas ratio in LPCVD SiN_x, *J. Electrochem. Soc.* 130 (1983) 450–455.
- [9] D.T. Pierce, W.E. Spicer, Electronic structure of amorphous Si from photoemission and optical studies, *Phys. Rev. B.* 5 (1972) 3017.
- [10] Z. Yuan, D. Li, M. Wang, P. Chen, D. Gong, L. Wang, D. Yang, Photoluminescence of Tb³⁺-doped SiN_x films grown by plasma-enhanced chemical vapor deposition, *J. Appl. Phys.* 100 (2006) 83106. doi:10.1063/1.2358301.
- [11] Filmetrics, *Refractive Index of Si₃N₄, Silicon Nitride, SiN, SiON*, (n.d.). <https://www.filmetrics.com/refractive-index-database/Si3N4/SiN-SiON-Silicon-Nitride>.
- [12] F. Benz, J.A. Guerra, Y. Weng, A.R. Zanatta, R. Weingärtner, H.P. Strunk, Concentration quenching of the green photoluminescence from terbium ions embedded in AlN and SiC matrices, *J. Lumin.* 137 (2013) 73–76. doi:10.1016/j.jlumin.2012.12.028.
- [13] Y.-T. An, C. Labbé, M. Morales, P. Marie, F. Gourbilleau, Fabrication and photoluminescence properties of Tb-doped nitrogen-rich silicon nitride films, *Phys. Status Solidi C.* 9 (2012) 2207–2210.
- [14] S.V. Deshpande, E. Gulari, S.W. Brown, S.C. Rand, Optical properties of silicon nitride films deposited by hot filament chemical vapor deposition, *J. Appl. Phys.* 77 (1995) 6534–6541. doi:10.1063/1.359062.
- [15] C. Mo, L. Zhang, C. Xie, T. Wang, Luminescence of nanometer-sized amorphous silicon nitride solids, *J. Appl. Phys.* 73 (1993) 5185–5188. doi:10.1063/1.353796.
- [16] J. Robertson, M.J. Powell, Gap states in silicon nitride, *Appl. Phys. Lett.* 44 (1984) 415–417. doi:10.1063/1.94794.
- [17] W.L. Warren, J. Kanicki, J. Robertson, P.M. Lenahan, Energy level of the nitrogen dangling bond in amorphous silicon nitride, *Appl. Phys. Lett.* 59 (1991) 1699–1701. doi:10.1063/1.106222.
- [18] L. Zhang, H. Jin, W. Yang, Z. Xie, H. Miao, L. An, Optical properties of single-crystalline α -Si₃N₄ nanobelts, *Appl. Phys. Lett.* 86 (2005) 61908. doi:10.1063/1.1862753.
- [19] D. Umamaheswari, B.C. Jamalalah, T. Sasikala, T. Chengaiah, I.-G. Kim, L. Rama Moorthy, Photoluminescence and decay behavior of Tb³⁺ ions in sodium fluoro-borate glasses for display devices, *J. Lumin.* 132 (2012) 1166–1170. doi:10.1016/j.jlumin.2011.12.080.
- [20] D. Navarro-Urrios, Y. Lebour, O. Jambois, B. Garrido, A. Pitanti, N. Dalosso, L. Pavesi, J.

- Cardin, K. Hijazi, L. Khomenkova, F. Gourbilleau, R. Rizk, Optically active Er³⁺ ions in SiO₂ codoped with Si nanoclusters, *J. Appl. Phys.* 106 (2009) 93107. doi:10.1063/1.3253753.
- [21] J. Bandet, B. Despax, M. Caumont, Nitrogen bonding environments and local order in hydrogenated amorphous silicon nitride films studied by Raman spectroscopy, *J. Appl. Phys.* 85 (1999) 7899. doi:10.1063/1.370604.
- [22] A. Aydinli, A. Serpengüzel, D. Vardar, Visible photoluminescence from low temperature deposited hydrogenated amorphous silicon nitride, *Solid State Commun.* 98 (1996) 273–277.
- [23] S. Charvet, A. Zeinert, C. Gonçalves, M. Goës, Effect of small nitrogen dilution on the microstructure of hydrogenated silicon thin films deposited by magnetron radiofrequency sputtering, *Thin Solid Films.* 458 (2004) 86–91. doi:10.1016/j.tsf.2003.11.307.
- [24] J.W. Osenbach, W.R. Knolle, A model describing the electrical behavior of a-SiN:H alloys, *J. Appl. Phys.* 60 (1986) 1408. doi:10.1063/1.337318.
- [25] G. Scardera, T. Puzzer, I. Perez-Wurfl, G. Conibeer, The effects of annealing temperature on the photoluminescence from silicon nitride multilayer structures, *J. Cryst. Growth.* 310 (2008) 3680–3684. doi:10.1016/j.jcrysgro.2008.05.018.
- [26] Z. Yin, F.W. Smith, Optical dielectric function and infrared absorption of hydrogenated amorphous silicon nitride films: Experimental results and effective-medium-approximation analysis, *Phys. Rev. B.* 42 (1990) 3666.
- [27] J.-F. Lelievre, Elaboration de SiN_x: H par PECVD: optimisation des propriétés optiques, passivantes et structurales pour applications photovoltaïques, INSA de Lyon, 2007. https://www.researchgate.net/profile/Jean-Francois_Lelievre/publication/251238424_Elaboration_de_SiNxH_par_PECVD__optimisation_des_propriets_optiques_passivantes_et_structurales_pour_applications_photovoltaiques/links/0c96051efcca550e81000000.pdf (accessed April 1, 2016).
- [28] H. Ono, T. Ikarashi, K. Ando, T. Kitano, Infrared studies of transition layers at SiO₂/Si interface, *J. Appl. Phys.* 84 (1998) 6064–6069. doi:10.1063/1.368917.
- [29] F. Rebib, E. Tomasella, J.P. Gaston, C. Eypert, J. Cellier, M. Jacquet, Determination of optical properties of a-SiO_xN_y thin films by ellipsometric and UV-visible spectroscopies, *J. Phys. Conf. Ser.* 100 (2008) 82033. doi:10.1088/1742-6596/100/8/082033.
- [30] G. Dupont, H. Caquineau, B. Despax, R. Berjoan, A. Dollet, Structural properties of N-rich a-Si-N: H films with a low electron-trapping rate, *J. Phys. Appl. Phys.* 30 (1997) 1064.
- [31] K. Lau, J. Weber, H. Bartzsch, P. Frach, Reactive pulse magnetron sputtered SiO_xN_y coatings on polymers, *Thin Solid Films.* 517 (2009) 3110–3114. doi:10.1016/j.tsf.2008.11.084.

Chapter IV: A study of the down-conversion process in the $\text{SiN}_x:\text{Tb}^{3+}-\text{Yb}^{3+}$ and $\text{SiN}_x:\text{Yb}^{3+}/\text{SiN}_x:\text{Tb}^{3+}$ systems

IV.1. Introduction

The purpose of this chapter is to fabricate and study the $\text{SiN}_x:\text{Tb}^{3+}-\text{Yb}^{3+}$ system as a potential down-converter layer. This study is eased by the previous determination of the two deposition parameters that are the plasma pressure and the nitrogen ratio in the plasma allowing to optimize the optical properties of the Tb-doped nitride thin film.

In the first part, the Tb-Yb co-doped layer is studied. Ytterbium ions are added to the previous optimized $\text{SiN}_x:\text{Tb}^{3+}$ layer. *FTIR* and ellipsometric spectroscopies as well as *TEM* analyses are carried out to determine the structural properties. Photoluminescence spectroscopy measurements and Transfer Matrix method (*TMM*) program computation are performed to determine the optical properties.

In the second part, the energy transfer mechanism from the terbium ions and the ytterbium ones is investigated. The efficiency of the *DC* system is determined both for the layer alone and for the layer deposited on a solar cell. As one of our objectives is to develop a Tb-Yb co-doped SiN_x layer with a higher Yb^{3+} *PL* peak intensity than the Tb-Yb co-doped SiO_xN_y layers developed during the precedent work of Y-T An, the efficiency of the optimized *DC* layer obtained is compared to the optimized Tb-Yb co-doped SiO_xN_y *DC* layer developed by our group in this previous study [1].

In the third part of this chapter, a multilayer system composed of a stack of either Tb- or Yb-doped sublayers is studied to increase the efficiency of the frequency conversion system. The multilayer and monolayer systems efficiency are then compared.

IV.2. $\text{SiN}_x:\text{Tb}^{3+}-\text{Yb}^{3+}$ monolayer system

After optimizing the undoped- and Tb-doped- matrix, the incorporation of Yb^{3+} ions in this later is studied. The $\text{SiN}_x:\text{Tb}^{3+}-\text{Yb}^{3+}$ layer is optimized by determining the deposition parameters leading to the highest ytterbium *PL* peak intensity. In this part, the layers are deposited in our laboratory by *RF* reactive magnetron co-sputtering of silicon-, terbium- and ytterbium-targets in a nitrogen-rich plasma on a silicon P-type *CZ* wafer. The deposition is performed with the values of the Si target power density (RFP_{Si}), the plasma pressure (P), the nitrogen ratio (rN_2), the substrate-target distance (d) and the substrate rotation fixed at 4.5 W/cm², 3 mTorr, 20 %, 10 cm, and 20 rpm, respectively. The *RF* power density applied on the terbium target (RFP_{Tb}) varies from 0.45 to 1.5 W/cm² while the one applied on the ytterbium target (RFP_{Yb}) varies from 0.1 to 0.55 W/cm². Deposition time (t_d) was adjusted in each case to obtain 90 nm thick layers. Unless otherwise stated, the layers are annealed by classical thermal approach (*CTA*) at 850 °C for 1 h under nitrogen flow. Microstructure and composition of rare earth-doped layers will be first investigated. Their optical properties will then be studied as a function of deposition and annealing parameters. Spectral absorbance, reflectance, and luminance of a typical layer will be studied and compared to standard Si_3N_4 material used as a solar cell antireflective layer.

IV.2.1. Structural analyses

IV.2.1.1. Effect of the annealing treatment

A transmittance *FTIR* analysis is conducted at Brewster angle on the annealed produced Tb-Yb co-doped layers. The curves obtained are reported on *Figure IV-1*. First, it is worth noting the small peak appearing around 1250 cm⁻¹ only for annealed layers. It corresponds to the longitudinal LO_3 vibrational band of the Si-O bond according to *Table III-1*. This is a signature of an oxidation either of the layer and/or of the wafer during annealing. However, no oxygen peak has been detected on the *RBS* spectrum, attesting that the layer does not contain oxygen according to the detection threshold of 0.2 at.%. Consequently, we assume that the presence of the LO_3 vibration band results from the oxidation of the Si wafer. The deposited layers are oxygen free. The two other peaks obtained are, from left to right, still the *LO* and *TO* modes of the Si-N bond.

Figure IV-1 also shows that the overlap intensity of *TO-LO* pair around 1000 cm⁻¹ decreases with the annealing. This may be due to a rearrangement of the atoms in the layer leading to a decrease of the disorder in the layer. *TEM* analyses on non-annealed and annealed layers (*Figure IV-2 (a) and (b)*, respectively) confirm this hypothesis. Thus the non-annealed layer presents distinct dark and bright zones indicating the presence of inhomogeneities while the annealed layer is homogeneous. The increase of disorder is corroborated by the increase of the overlap intensity of *TO-LO* pair around 1000 cm⁻¹.

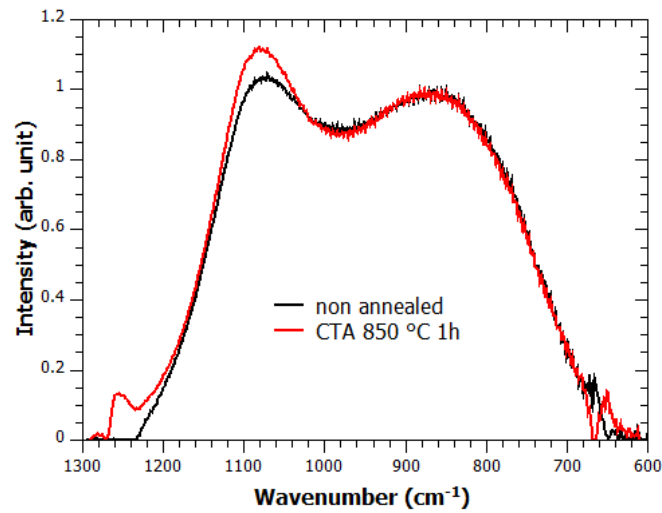


Figure IV-1: FTIR spectra of an annealed (red) and non-annealed (black) $\text{SiN}_x:\text{Tb}^{3+}-\text{Yb}^{3+}$ layers at Brewster incident angle.

It is important to note that no clusters are visible at the observation scale in both cases. The observation is backed up by the electron diffraction pattern (*EDP*) (*inset in Figure IV-2*) shows the pattern of the crystalline silicon substrate (dots) and a very diffuse ring which characterises an amorphous matrix.

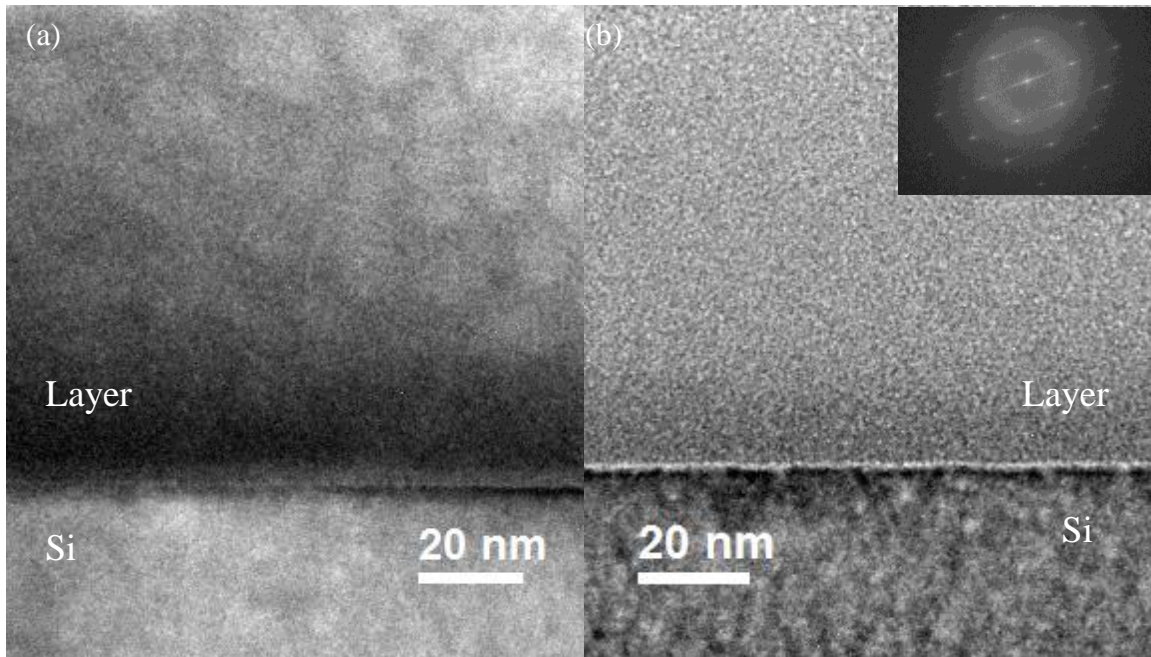


Figure IV-2: TEM pictures of a typical $\text{SiN}_x:\text{Tb}^{3+}-\text{Yb}^{3+}$ layer, non-annealed (a) and annealed at 850 °C during 1 h (b). The Si substrate is at the bottom and the layer on top. The inset in (b) corresponds to the EDP of $\text{SiN}_x:\text{Tb}^{3+}-\text{Yb}^{3+}$ layer with the Si substrate.

IV.2.1.2. Effect of the terbium and ytterbium target power densities

The influence of the rare earth ion incorporation on the microstructure is studied. For an increase of the RFP_{Tb} or the RFP_{Yb} , the Si-N bond LO peak of the $FTIR$ spectra shifts toward lower wavenumbers (Figure IV-3 (a) and (b)) while the refractive index increases (Figure IV-4). This might be due to the incorporation of large diameter rare earth ions in the matrix that may increase the disorder and generate defects [2,3]. However, as seen in the third chapter, previous studies [3,4] stated that, for a undoped matrix without hydrogen or oxygen, such behavior could be caused by a change in the $[N]/[Si]$ ratio.

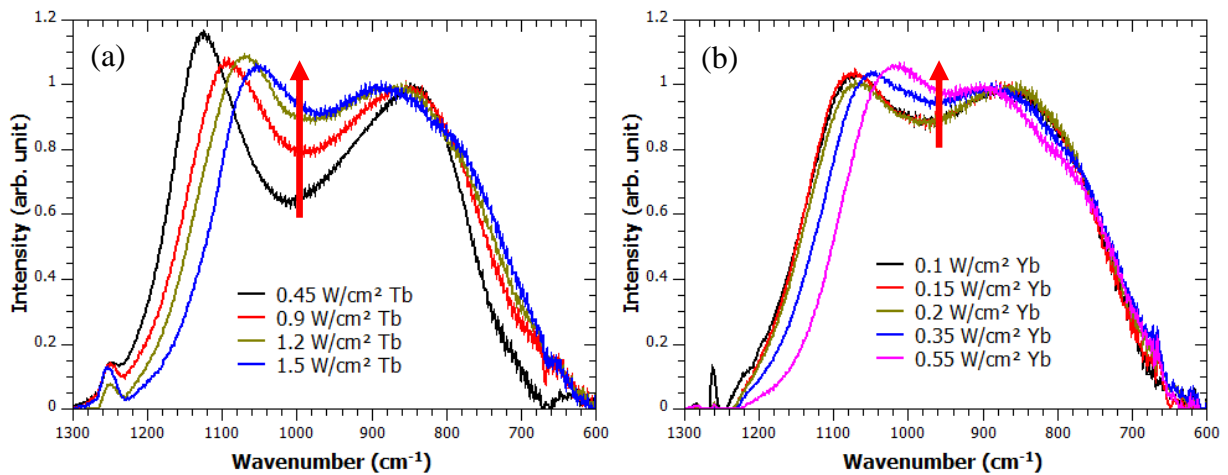


Figure IV-3: FTIR spectra recorded at Brewster angle of annealed (CTA 850 °C 1 h) Tb-Yb co-doped layers for different RFP_{Tb} and a RFP_{Yb} fixed at 0.3 W/cm² (a) and for different RFP_{Yb} and a RFP_{Tb} fixed at 1.2 W/cm².

The refractive indexes of the layers annealed by CTA were studied by ellipsometry spectroscopy for various target power densities. Figure IV-4 shows the refractive index of our layer as a function of the RFP_{Tb} for various RFP_{Yb} compared to the refractive indexes of Si_3N_4 and Si. As reported on Figure IV-4, all of the samples present a refractive index higher than that of Si_3N_4 . In a Tb and Yb free matrix, it would mean that the matrix contains an excess of silicon. However, in the case of doped-layers, the increase in the refractive index may also be due to the rare earth ion incorporation as observed in the case of $SiN_x:Tb^{3+}$ layer (see §III.3.2.1.). RBS analyses on undoped, doped, and Tb-Yb co-doped layers demonstrate that the relative proportions of Si and N remain constant at 43 % and 57 %, respectively (Table IV-1). Those results rule out the possibility of Si excess in the matrix. Thus, and similarly to the previous chapter, the redshift of the Si-N bond LO band position and the increase in the refractive index with RFP_{Tb} and RFP_{Yb} can be attributed to an increase of the matrix disorder for the former and to the incorporation of rare earth ions for the later. The increase of disorder is corroborated by the increase of the overlap intensity of $TO-LO$ pair around 1000 cm⁻¹.

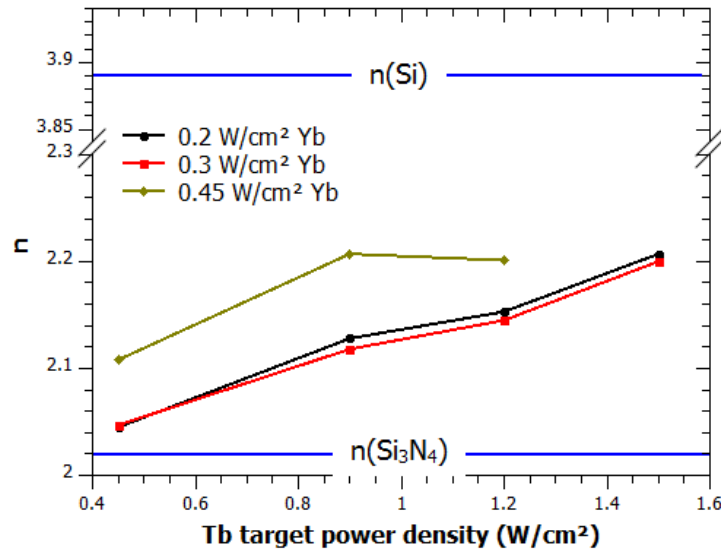


Figure IV-4: Refractive index at 1.95 eV of $\text{SiN}_x:\text{Tb}^{3+}-\text{Yb}^{3+}$ layer (deduced from ellipsometry) as a function of the RFP_{Tb} for different RFP_{Yb} . The blue lines represent the refractive index of Si, and Si_3N_4 , from top to bottom.

Sample	Si at.% (atoms/cm ²)	N at.% (atoms/cm ²)	Tb at.% (atoms/cm ²)	Yb at.% (atoms/cm ²)
1.2 W/cm ² Tb ; 0.2 W/cm ² Yb	38 % (300 x10 ¹⁵)	50.6 % (400 x10 ¹⁵)	10.1 % (80 x10 ¹⁵)	1.3 % (10 x10 ¹⁵)
1.2 W/cm ² Tb	38.3 % (300 x10 ¹⁵)	51.1 % (400 x10 ¹⁵)	10.6 % (79 x10 ¹⁵)	/
0.45 W/cm ² Tb	42.2 % (285 x10 ¹⁵)	56.4 % (380 x10 ¹⁵)	1.4 % (9.5 x10 ¹⁵)	/
SiN _x	42.9 % (360 x10 ¹⁵)	57.1 % (480 x10 ¹⁵)	/	/

Table IV-1: RBS analyses results after fitting the experimental curves of a standard Tb-Yb co-doped layer for undoped-, doped-, and Tb-Yb co-doped-layers. The measurement errors are: 10 % for the Si content, 10 % for the RE ions content, and 12.5 % for the N content.

We may note that the quantity of terbium ions incorporated for an identical value of RFP_{Tb} in the Tb-doped and Tb-Yb co-doped layers is very similar (from 80 x10¹⁵ to 79x10¹⁵ atoms/cm²). It

means that, in the case of the terbium ions incorporation, the concentration of this ion in the deposited layer does not vary the number and nature of the other species it is deposited with. In addition and as expected, increasing the RFP_{Tb} favors the terbium ions incorporation.

It is important to underline here again the difficulties we had to determine the composition of our samples. For the relative concentration of rare earth ions ($[Tb]/[Yb]$), The different measurement techniques give each a different value from 6.5/1 for the *RBS* to 50/1 for the *STEM-EELS* experiments. The *RBS* analysis of the *RE* ions concentration was difficult due to closeness of the Yb and Tb peaks that overlapped almost completely. A fit adjusting the species concentrations was needed to obtain the *RE* ions concentration. Further analyses are ongoing with the *XPS* to obtain more accurate results as well as the valence number of the *RE* ions. In the same way, *STEM-EELS* analyses are still running to have more accurate results as a function of the thickness of the layer. Metallic references of the Tb and Yb have been made but samples with a known concentration of *RE* would be even better to help decipher more accurately the *RE* peaks. In this work, the composition of the layer will be based on the *RBS* measurements that have been completed compared to the *XPS* and *STEM-EELS* ones that are still ongoing.

IV.2.2. Photoluminescence

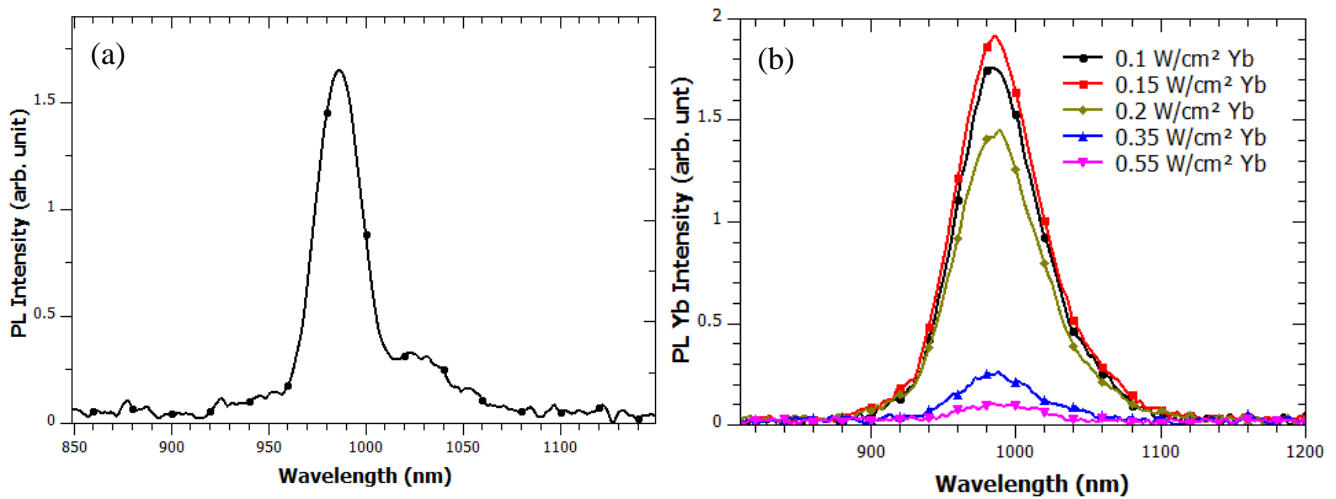


Figure IV-5: (a) Photoluminescence spectrum for an excitation wavelength of 285 nm measured with the [1200-300] grating. (b) Photoluminescence spectra for an excitation wavelength of 285 nm measured with the [600-750] grating.

In order to be able to observe and analyze the 990 nm-*PL* peak even for the weakest emitting layer, the photoluminescence spectra have been recorded using the [600-750] grating (Figure IV-5 (b)). The latter however favors the intensity at the expense of spectral resolution resulting in weaker resolved *PL* peak than with the [1200-300] grating. Figure IV-5 (a) represents the

photoluminescence of a typical Tb-Yb co-doped layer for the [1200-300] grating that is more dispersive and allows a higher resolution of the emission peaks at the expense of the intensity. The two peaks at 990 nm and 1025 nm coming from the $^2F_{5/2}$ to $^2F_{7/2}$ transition, characteristic of Yb^{3+} emission, are clearly identified.

IV.2.2.1. Effect of the terbium target power density

Contrary to the optimized RFP_{Tb} obtained in the previous chapter and fixed at 0.45 W/cm^2 , *Figure IV-6* shows that, whatever the power density used on the Yb target, the 990 nm- Yb^{3+} PL peak maximum intensity increases with RFP_{Tb} above this value and up to 1.2 W/cm^2 before decreasing. This feature is the signature that higher Tb^{3+} ion concentration is required to efficiently sensitize the Yb^{3+} . For $RFP_{Tb} > 1.2 \text{ W/cm}^2$ the PL decrease may be attributed to the disorder increase of the matrix, creating more non-radiative de-excitation channels. Another explanation could be a decreasing Tb^{3+} - Tb^{3+} distance that may favor the process of energy migration that enhances the probability to reach a defect. Such a process is detrimental for achieving an efficient energy transfer to Yb^{3+} ions.

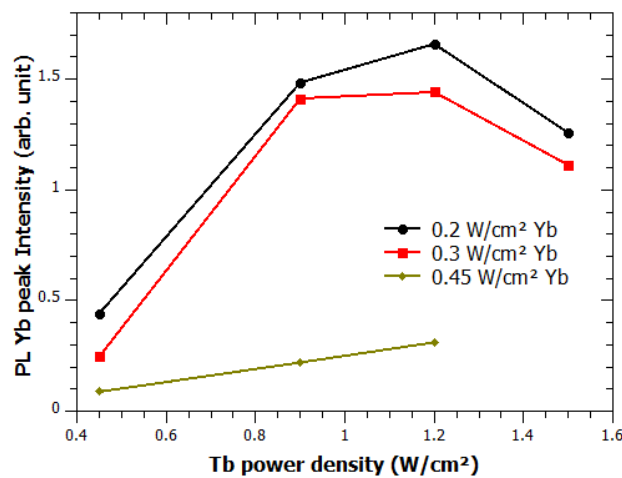


Figure IV-6: Yb^{3+} PL peak intensity as a function of the RFP_{Tb} for different RFP_{Yb} and for an excitation wavelength of 285 nm. The measurements have been carried out with the [600-750] grating.

It is important to note that, the optimized Tb-Yb co-doped layer is obtained for a higher RFP_{Tb} than the optimized Tb-doped layer. In addition, it contains 2.5 times more terbium than ytterbium (*Table IV-1*). This fact is conflicting with the DC principle that predicts the necessity of twice the ytterbium concentration than the terbium one in the system. We know from the previous chapter that increasing the RFP_{Tb} above 0.45 W/cm^2 does not increase the terbium emission but creates defects and/or migration between terbium ions close enough. However in the Tb-Yb co-doped system it increases the ytterbium emission. We also know that a terbium ion has to be very close to

a pair of ytterbium ions to favor an efficient cooperative energy transfer. Consequently, increasing the terbium ions quantity reduces the distance between terbium and ytterbium ions and thus favors the cooperative energy transfer (CET).

IV.2.2.2. Effect of the ytterbium target power density

Figure IV-6 displays an increase of the Yb^{3+} PL peak intensity with RFP_{Yb} up to 0.15 W/cm^2 , from which the Yb^{3+} peak intensity decreases. This evolution might have the same origin than in the Tb-doped layers case. It might be explained by either an increase of the disorder of the matrix and/or an energy migration process between Yb^{3+} ions. The effect of lower RFP_{Yb} on Yb^{3+} emission was then investigated. *Figure IV-7* shows the photoluminescence spectra of samples fabricated with $1.2 \text{ W/cm}^2 RFP_{\text{Tb}}$ and different RFP_{Yb} ranging from 0.1 to 0.55 W/cm^2 . An increase of the photoluminescence intensity for RFP_{Yb} up to 0.15 W/cm^2 followed by a drop is observed. This evolution evidences the higher sputtering yield of the Yb species compared to Tb ones, and demonstrates the critical role of the incorporation of Yb^{3+} ions in such doped layers. Before 0.15 W/cm^2 , we suppose that the number of optically active Yb^{3+} ions increases with the addition of Yb^{3+} ions, and thus, favors the Yb^{3+} emission intensity. After the Yb PL peak intensity reached a maximum for a RFP_{Yb} of 0.15 W/cm^2 , the drop in the emission intensity may be attributed to the incorporation of even more Yb ions, that leads to a concentration quenching process, or to an increase of defects density. So, deduced from *Figure IV-7*, **the sample with optimized PL is obtained for a RF power density of 1.2 W/cm^2 and 0.15 W/cm^2 applied on the Tb and Yb targets, respectively.**

In order to investigate the cause of the Yb^{3+} intensity drop, lifetime experiments were carried out on samples with varying power density on the Yb target (*Figure IV-8*). The lifetime curves present a non-singular exponential behavior, and therefore we use an average decay time model τ_m given by [5]:

$$\tau_m = \int_0^{\infty} \left(\frac{I(t)}{I_0} \right) dt . \quad \text{IV-1}$$

We observe that the Yb^{3+} lifetime stays constant for a RFP_{Yb} of 0.2 and 0.3 W/cm^2 and drops while RFP_{Yb} increases up to 0.45 W/cm^2 . XPS measurements have been carried out by Marie-Paule Besland from the Jean Rouxel Institute of Nantes. The results prove that all the ytterbium ions in our layers (even for a large ytterbium content -0.55 W/cm^2 -) have a valence of three (*Figure IV-9*). It means that there is no optically inactive Yb^{2+} in our layer. Consequently, this PL lifetime decrease characterizes the presence of supplementary non-radiative de-excitation channels such as defects or migration processes between Yb^{3+} ions ending in a defect [6].

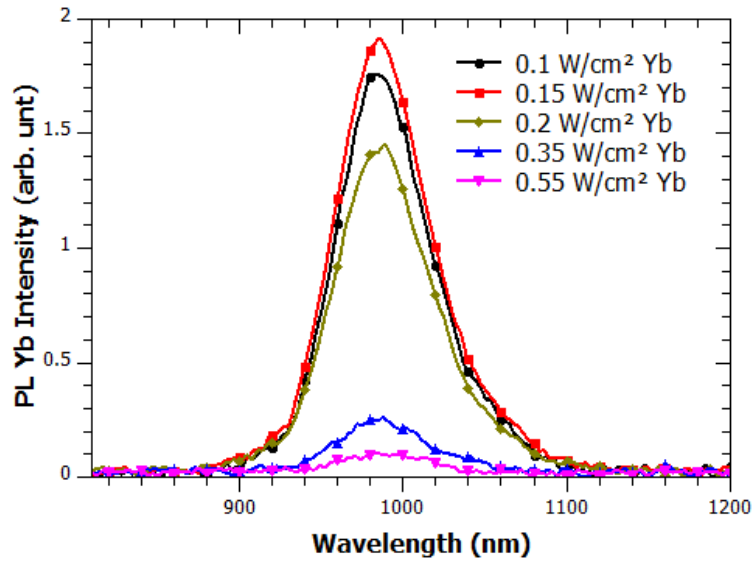


Figure IV-7: Photoluminescence spectra of Tb-Yb co-doped samples with various RFP_{Yb} and a RFP_{Tb} of 1.2 W/cm^2 . The samples have been excited using an excitation wavelength of 285 nm and the emitted light has been measured with the $[600-750]$ grating.

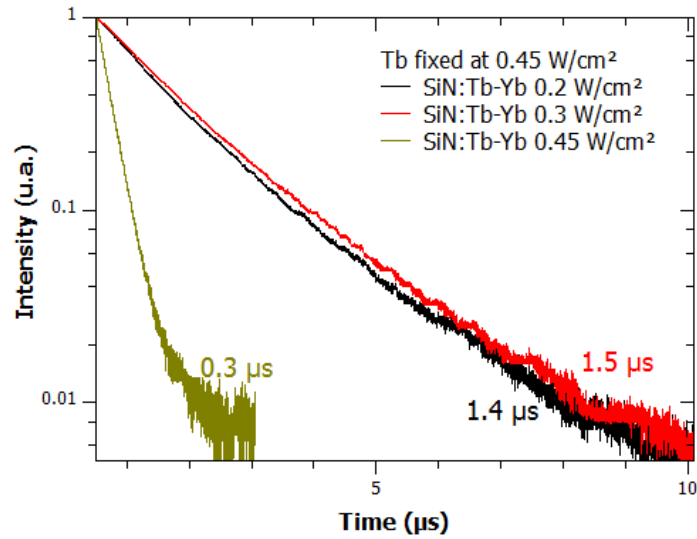


Figure IV-8: Time-resolved photoluminescence response of Yb^{3+} for different RFP_{Yb} under an excitation wavelength of 244 nm . The lifetimes corresponding to each curve are given in the same color.

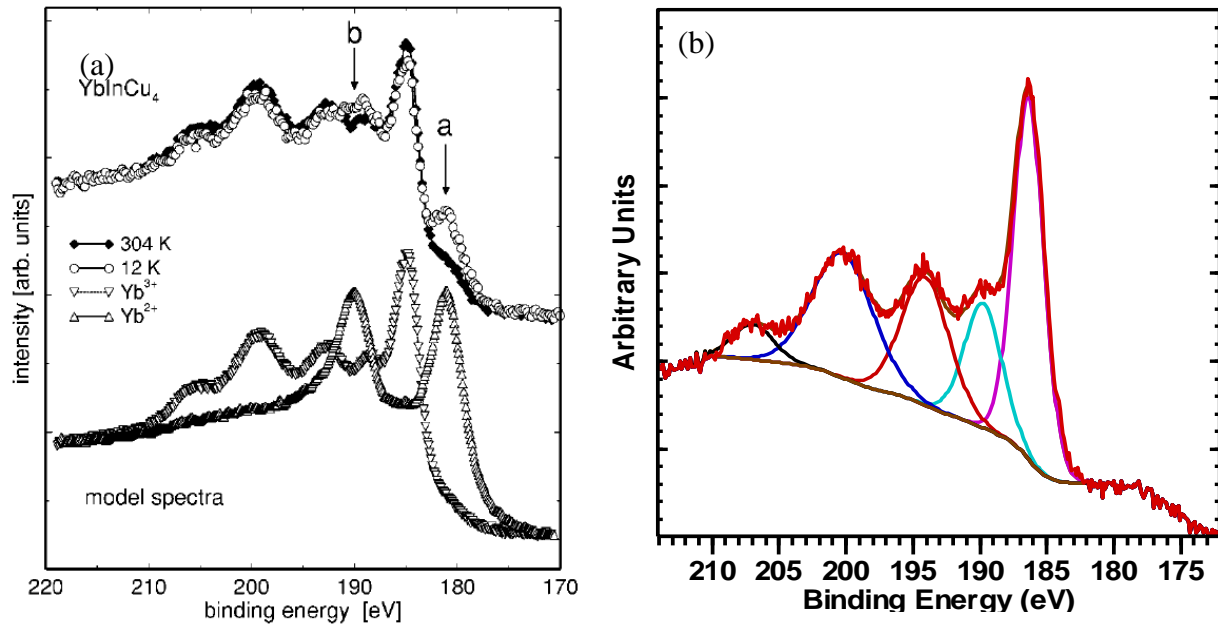


Figure IV-9: (a) XPS peaks characteristic of the Yb^{2+} and Yb^{3+} ions from [7] and (b) XPS peaks corresponding to a Tb-Yb co-doped layer (with $1.2 \text{ W/cm}^2 \text{ RFP}_{\text{Tb}}$ and $0.55 \text{ W/cm}^2 \text{ RFP}_{\text{Yb}}$).

IV.2.3. Other optical properties

In addition, to optimize a fabrication process compatible with the silicon solar cells, it is important to determine the impact that adding such layers will have on the light received and converted by the solar cell. For this purpose, the optical properties of our layer are studied.

Following the ellipsometry measurements, we compare the absorbance, transmittance, and reflectance efficiencies (A_{eff} , T_{eff} , and R_{eff}) as described in the second chapter (§II.4.1.) of the deposited layer to those of a standard Si_3N_4 layer on the same substrate.

It was found that the different deposited samples studied (for different power densities on the Tb and Yb targets) have comparable values of efficiency absorbance, reflectance, and transmittance. Thus, the quantity of rare earth incorporated does not influence significantly those optical properties (the maximum change is about 1 %).

Figure IV-10 (a), (b), and (c) show the absorbance, transmittance, and reflectance of our typical Tb-Yb co-doped deposited layer compared to a Si_3N_4 reference layer. We can see that the absorbance and transmittance of the Tb-Yb co-doped layer are higher and lower respectively than the reference particularly in the visible and IR ranges (550-1200nm). The absorbance efficiency A_{eff} is 5 % higher (5.6 % for 0.03 %) and the transmittance efficiency T_{eff} is 8 % lower (84.2 % for 92.2 %) for the Tb-Yb co-doped layer. It is useful in the UV part of the spectrum as it allows a better use of the UV photons, but it is less useful in the visible part of the spectrum as it absorbs photons that could be used by the solar cell below. The reflectance however seems to be comparable in the two layers

which is confirmed by the reflectance efficiency R_{eff} that is only 2 % higher (10.2 % for 7.8 %) for the Tb-Yb co-doped layer. It has thus the same anti-reflective properties as the Si_3N_4 .

Our Tb-Yb co-doped layer impairs only slightly the cell operation by absorbing more photons (and transmitting less photons) in the visible and IR spectral ranges. Its reflectance is however in part with the reference which means effective anti-reflective properties. The overall similarity of the optical properties between our sample and the Si_3N_4 ensures that our layers can be topped on silicon solar cell with a good prospect of efficiency improvement.

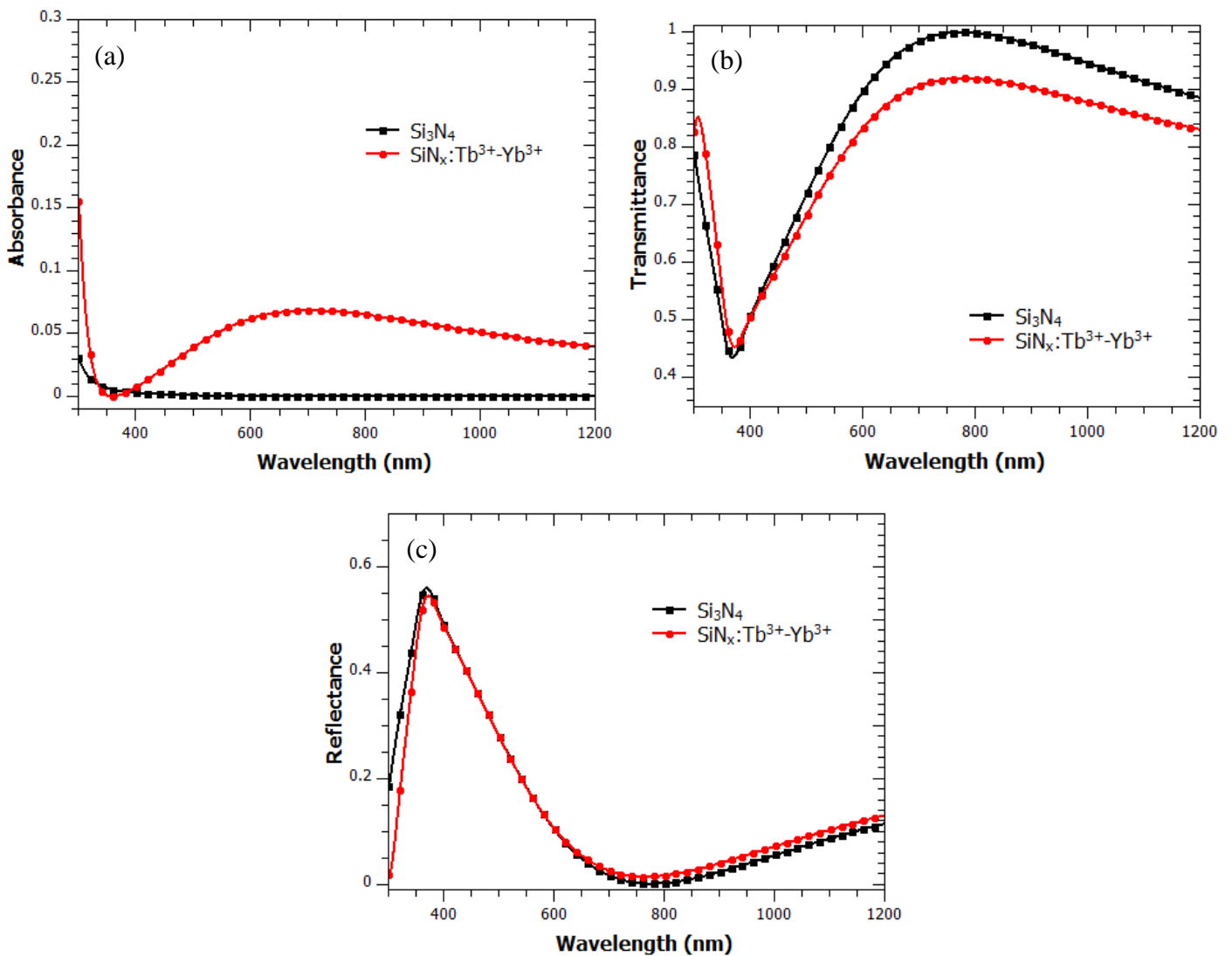


Figure IV-10: Absorbance A (a), Transmittance T (b), and Reflectance R (c) for a Si_3N_4 layer (black) and our typical Tb-Yb co-doped deposited layer (red).

IV.2.4. Conclusion

We have studied the down-conversion layer $\text{SiN}_x:\text{Tb}^{3+}-\text{Yb}^{3+}$. The study of the composition, the microstructure, and the optical properties of the samples allows a better understanding of the process. An optimized layer was achieved by means of reactive magnetron co-sputtering in a nitride rich atmosphere of Tb and Yb targets, with a RF power density applied of 1.2 W/cm² and 0.15 W/cm², respectively. The optical properties of our layer were found to be comparable to the ones of a Si_3N_4 coating, meaning that that our layers can be topped on silicon solar cell with a good prospect of efficiency improvement.

IV.3. Energy transfer and efficiency

In this part, we detail the down-conversion process occurring in the $\text{SiN}_x:\text{Tb}^{3+}-\text{Yb}^{3+}$ layer. The efficiency of the optimized DC layer is determined by a measurement of the external quantum efficiency (EQE) of the layer. Finally, we compare the $\text{SiO}_x\text{N}_y:\text{Tb}^{3+}-\text{Yb}^{3+}$ and $\text{SiN}_x:\text{Tb}^{3+}-\text{Yb}^{3+}$ samples, which exhibit the highest Yb^{3+} PL emission.

IV.3.1. Energy transfer from the terbium ions to the ytterbium ions

Figure IV-11 displays the photoluminescence spectra of the Tb-Yb co-doped samples for a 325 nm excitation wavelength. The Yb-doped sample emits a PL signal that is slightly above the measurement noise level around 985 nm while the Tb-Yb co-doped sample presents a distinct peak at 990 nm (Figure IV-11). This result evidences that (i) there is no direct energy transfer between the matrix and the ytterbium ions and (ii) terbium ions sensitize the Yb^{3+} ions under a UV excitation. A similar effect has been observed by An *et al.* in an oxynitride matrix SiO_xN_y [1]. In addition, as mentioned in the third chapter (§III.4.1.1.), the non-resonant excitation of Tb^{3+} ions witnesses the energy transfer (ET) occurring between the matrix and the Tb^{3+} ions.

Figure IV-12 presents the evolution of the Tb^{3+} ($^5\text{D}_4$ to $^6\text{F}_7$ energy transition) and the Yb^{3+} ($^2\text{F}_{5/2}$ to $^2\text{F}_{7/2}$ energy transition) maximum PL peak intensities for an increasing RFP_{Yb} . The 545 nm- Tb^{3+} intensity drops to the noise value of the measurement as soon as Yb^{3+} ions are incorporated in the film, suggesting that an efficient cooperative energy transfer takes place between Tb^{3+} and Yb^{3+} . The 990 nm- Yb^{3+} PL peak emission decreases with the rise of the RFP_{Yb} , i.e. the increase of the Yb^{3+} incorporation. This evolution in the matrix might be explained by an increase of the number of non-radiative centers due to the increasing content of RE ions, and/or by an increase of the probability of reaching the non-radiative centers due to energy migration process taking place between Yb^{3+} ions. **Thus, the presence of Yb^{3+} PL peak is a signature of double energy**

transfer, first between the matrix and the Tb^{3+} ions, and then the cooperative energy transfer between Tb^{3+} and Yb^{3+} ions.

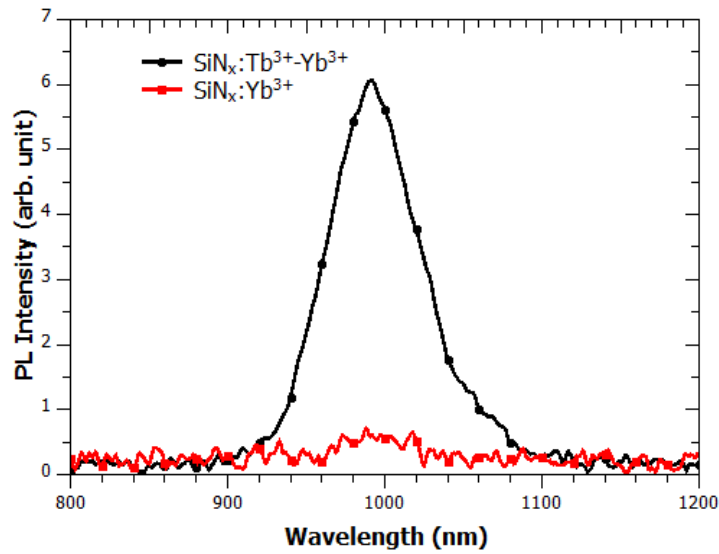


Figure IV-11: Photoluminescence curves of the typical Tb-Yb co-doped and Yb-doped deposited layers for a non-Tb resonant excitation wavelength of 325 nm. The emission is measured with the [600-750] grating.

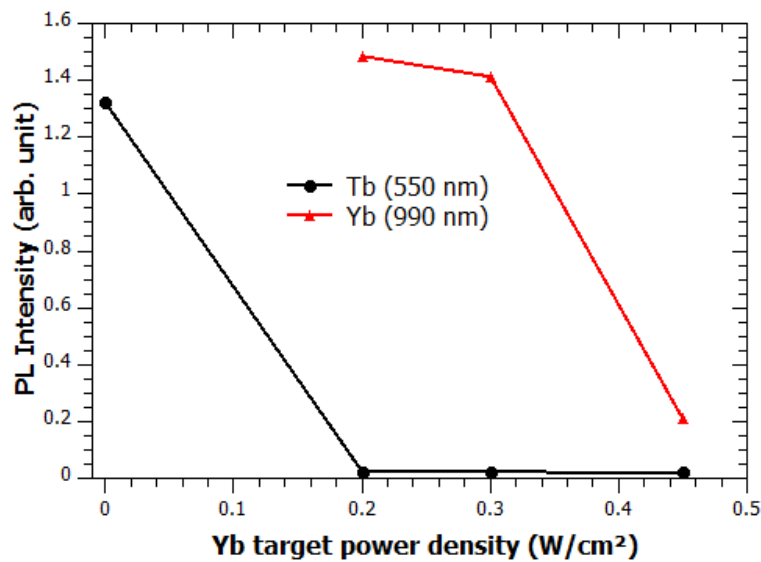


Figure IV-12: Tb^{3+} and Yb^{3+} PL peak intensities of a Tb-Yb co-doped layer as a function of the RFP_{Yb} for an excitation wavelength of 285 nm. The emission is measured with the [600-750] grating.

The *PLE* spectrum of the Tb-Yb co-doped system for a detection wavelength of 985 nm, displayed on *Figure IV-13*, exhibits a large band between 240 and 290 nm (4.3 to 5.2 eV) followed by a continuous decrease with the wavelength. For wavelengths below 450 nm (2.75 eV), the *PLE* signal decreases to the limit of detectability (noise limit). This spectrum is comparable to the *PLE* spectrum of the terbium for a detection wavelength of 550 nm in term of spectral position (§III.4.1.3.) with a slight broadening. Since there is no evident direct excitation of terbium ions, the matrix absorbs the energetic photons and transfers its energy to the terbium ions that themselves transfer to the ytterbium ions. An energy level scheme of the energy transfers occurring in our samples is drawn from the photoluminescence results on *Figure IV-13*. In this figure, we observe that due to the discrete nature of the Tb^{3+} ions energy levels and to the energy of 5D_4 level located at around 2.58 eV, the energy transfer from the matrix to the Tb^{3+} ion may occur preferentially from the matrix UV levels to the Tb^{3+} ions levels above 5D_4 . Those levels with an energy above the 5D_4 energy level match the energy of matrix band between 240 and 290 nm, and 330 nm could be 4F_75d , $^5H_{6,7,8}$, and $^5L_{6,7,8}$ respectively. Energy transfer to those upper levels may be followed by a non-radiative allowed transition to the 5D_4 level of Tb^{3+} ions from which cooperative energy transfer to Yb^{3+} ions may occur.

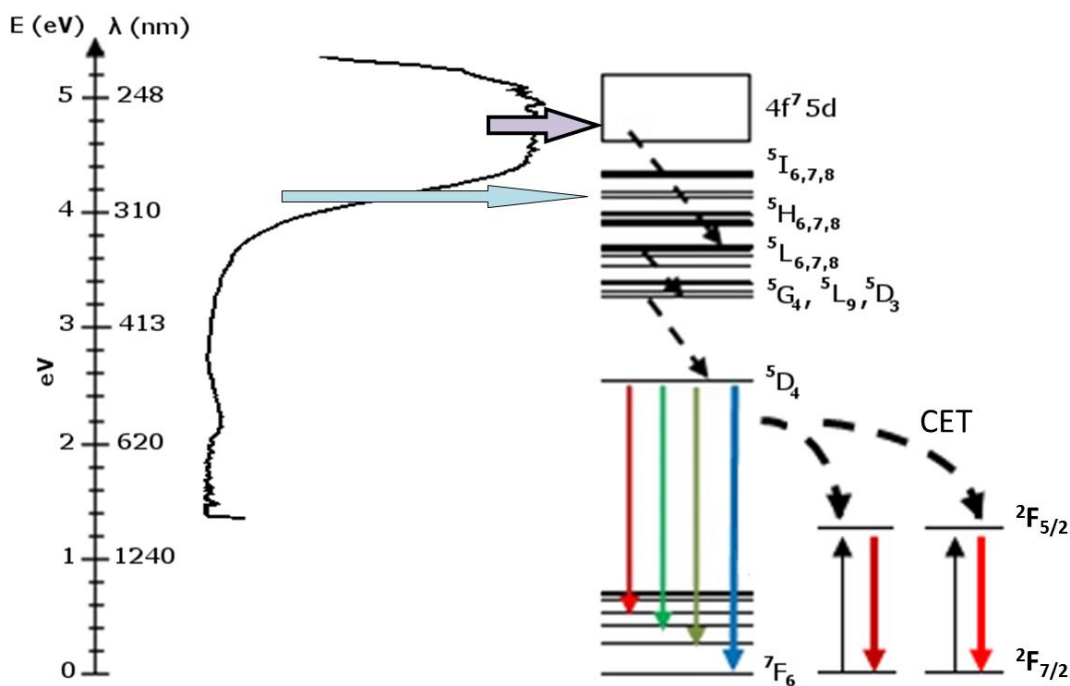


Figure IV-13: PLE spectrum of the $SiN_x:Tb^{3+}-Yb^{3+}$ system for a detection wavelength at 985 nm and schematic diagram of the energy levels of the down-conversion mechanism with the radiative de-excitation (photon emission) in colored arrows, the non-radiative de-excitation in black straight dashed line arrows, the energy transfer in big blue arrows, and the cooperative energy transfer in black curved dash line arrows.

IV.3.2. Down-conversion system efficiency

IV.3.2.1. Comparison with a previous study

a) Composition

The concentrations of the different elements in the deposited layers are deduced from the *RBS* measurements (*Table IV-1*, sample: $RFP_{Tb} = 1.2 \text{ W/cm}^2$; $RFP_{Yb} = 0.2 \text{ W/cm}^2$). Those values are converted in percentage (at.%) and compared to the results obtained for the oxynitride $\text{SiO}_x\text{N}_y:\text{Tb}^{3+}-\text{Yb}^{3+}$ layers [1]. Only the percentage of rare earth ions are shown here: 10.1 at.% of Tb^{3+} ions and 1.3 at.% of Yb^{3+} ions for our optimized layer, whereas, in the oxynitride matrix it was found 1.8 at.% of Tb^{3+} ions and 2.0 at.% of Yb^{3+} ions for the previous one.

A microstructural study on the same annealed $\text{SiN}_x:\text{Tb}^{3+}-\text{Yb}^{3+}$ layer using a high resolution transmission electron microscope (*HRTEM*) (*Figure IV-14*) shows that at the observation scale the layer is homogeneous with no segregation of species (no cluster). This picture coupled with the *RBS* concentrations evidence the larger incorporation of rare earth ions in our matrix (SiN_x) than in the previous one (SiO_xN_y) without clustering of rare earth elements as expected.

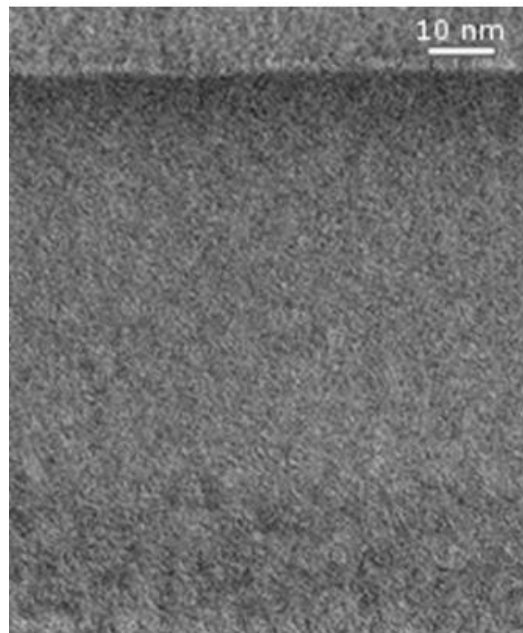


Figure IV-14: HRTEM picture of a typical $\text{SiN}_x:\text{Tb}^{3+}-\text{Yb}^{3+}$ layer with the Si substrate at the top and the layer at the bottom.

b) Down-conversion layer efficiency

Another of our objectives is to develop a Tb-Yb co-doped layer that have a higher *PL* intensity of the Yb^{3+} peak than the Tb-Yb co-doped SiO_xN_y layer developed during the precedent work of Y-T An. The optimized Tb-Yb co-doped SiN_x layer obtained in this work is thus compared to a similar Tb-Yb co-doped SiO_xN_y [13]. In *Figure IV-15*, the *PL* intensity at 990 nm of our more luminescent samples that was analyzed by *RBS* ($\text{SiN}_x-1.2\text{Tb}-0.15\text{Yb}$) is found to be 5.6 times more intense than the more luminescent sample obtained on the $\text{SiO}_x\text{N}_y:\text{Tb}^{3+}-\text{Yb}^{3+}$ system [1]. The objective of a higher *PL* peak intensity is here again reached and, from this point, we also go further and determine how much more light a Si *SC* topped with our Tb-Yb co-doped SiN_x layer would receive compared to one topped with the Tb-Yb co-doped SiO_xN_y layer.

Following the same reasoning than in the previous chapter (see §III.4.2.), the Yb^{3+} excited state ratio, in this case, is $N^* \text{SiN}_x:\text{Tb}^{3+}-\text{Yb}^{3+}(\text{Yb}^{3+})/N^* \text{SiO}_x\text{N}_y:\text{Tb}^{3+}-\text{Yb}^{3+}(\text{Yb}^{3+}) = 5.6$, which demonstrates the higher *PL* efficiency of the $\text{SiN}_x:\text{Tb}^{3+}-\text{Yb}^{3+}$ system.

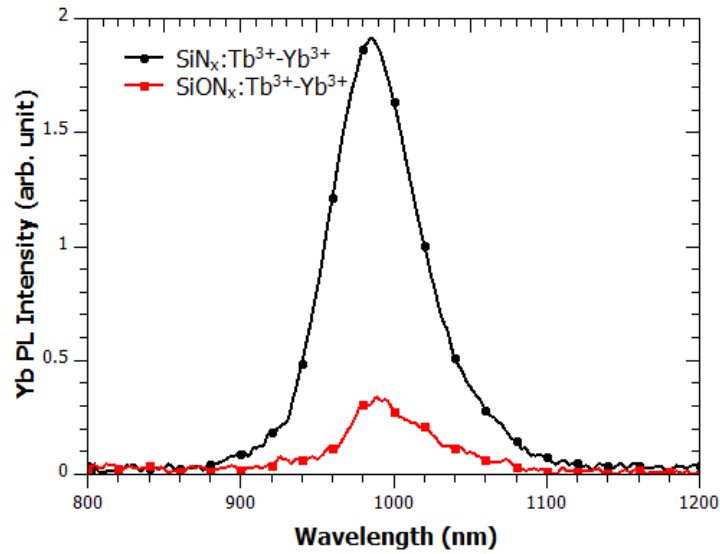


Figure IV-15: Photoluminescence spectra of the best samples obtained of $\text{SiN}_x:\text{Tb}^{3+}-\text{Yb}^{3+}$ and $\text{SiO}_x\text{N}_y:\text{Tb}^{3+}-\text{Yb}^{3+}$ co-doped matrices for an excitation wavelength of 285 nm measured with the [600-750] grating.

The normalized absorbance of both $\text{SiO}_x\text{N}_y:\text{Tb}^{3+}-\text{Yb}^{3+}$ and $\text{SiN}_x:\text{Tb}^{3+}-\text{Yb}^{3+}$ samples exhibiting the highest Yb^{3+} *PL* emission are estimated to be 21.2 % and 32.5 %, respectively, for an excitation at 285 nm and a photon flux of 1.9×10^{15} photons/cm². This difference can be here again attributed to opto-geometrical differences between the two studied layers, which have different thicknesses (225 nm and 81 nm, respectively) and different refractive indexes at 1.95 eV (1.742 and 2.151, respectively).

The luminescence ratios in the layer, in the air, and in the substrate obtained thanks to the extended transfer matrix method (*ETMM*) program given in *Table IV-2* show that the Tb-Yb co-doped SiN_x layer transfers more to the *SC* (considered here as Si) than the Tb-Yb co-doped SiO_xN_y one.

Still using the reasoning of the third chapter and knowing that the Yb^{3+} excited state ratio of nitride DC layer (Figure IV-15) was found to be 5.6 times higher than the one for oxynitride layers with the same PL experimental conditions (1.9×10^{15} photons/cm² at 285 nm), the internal efficiency ratio is:

$$\eta^{\text{int}}(\text{SiN}_x : \text{Tb}^{3+} - \text{Yb}^{3+}) / \eta^{\text{int}}(\text{SiN}_x\text{O}_y : \text{Tb}^{3+} - \text{Yb}^{3+}) = 4.77. \quad \text{IV-2}$$

Here again, this internal efficiency increase of the nitride DC layer compared to the thicker oxynitride one might be attributed to one or several of the following improvements: (i) the optically active RE content, (ii) the DC conversion, and (iii) the 985nm photons propagation.

Similarly to the third chapter, the ratio of global efficiency in the silicon SC is evaluated:

$$\eta^{\text{glo}}(\text{SiN}_x : \text{Tb}^{3+} - \text{Yb}^{3+}) / \eta^{\text{glo}}(\text{SiN}_x\text{O}_y : \text{Tb}^{3+} - \text{Yb}^{3+}) = 8.6. \quad \text{IV-3}$$

This ratio shows the improvement of the global efficiency of the DC-SiN_x layer transmitted to the silicon substrate compared to the thicker DC-SiN_xO_y one (assumed to be representative of the silicon SC). **For the conditions of thickness and refractive index employed in this work, the silicon, and thus the silicon solar cells, would receive 8.6 times more light at 985 nm from the DC-SiN_x layer compared to the thicker Tb-Yb co-doped SiN_xO_y one for an excitation at 285 nm.**

$\eta^{\text{ext}}(\%)$	Air	Layer	Silicon
$\text{SiN}_x : \text{Tb}^{3+} - \text{Yb}^{3+}$	16.3	61.2	22.5
$\text{SiN}_x\text{O}_y : \text{Tb}^{3+} - \text{Yb}^{3+}$	21.4	59.4	19.2

Table IV-2: Luminescence efficiencies of the Tb-Yb co-doped SiN_x and SiO_xN_y matrices in the air, the layer, and the silicon.

IV.3.2.2. Time-resolved photoluminescence and lifetime based efficiency

In order to determine the time decay based efficiency of the down-conversion process between the terbium ions to the ytterbium ones, time-resolved photoluminescence measurements of Tb^{3+} are performed on Tb-Yb co-doped layers deposited with a RFP_{Tb} fixed at 0.45 W/cm^2 and varying RFP_{Yb} . The internal quantum yield may be calculated thanks to the lifetime deduced from the fitting (exponential curves) of the spectra obtained and the following relation [1]:

$$\eta_{QE} = \eta_{Tb}(1 - \eta_{ETE}) + 2\eta_{ETE} \quad \text{IV-4}$$

With η_{Tb} the efficiency of the excitation of the terbium ions assumed to be equal to 1 here since we study only the cooperative transfer [9,10], and η_{ETE} the efficiency of the cooperative energy transfer from the terbium ions to the ytterbium ions given by:

$$\eta_{ETE} = 1 - \left(\frac{\tau_{Tb_Yb}}{\tau_{Tb}} \right) \quad \text{IV-5}$$

With τ_{Tb_Yb} the lifetime of the terbium ions in the Tb-Yb co-doped system and τ_{Tb} the lifetime of the terbium ions in the Tb-doped system.

Thus *Equation IV-4* may be written as:

$$\eta_{QE} = 2 - \left(\frac{\tau_{Tb_Yb}}{\tau_{Tb}} \right) \quad \text{IV-6}$$

For the Tb-doped system, the terbium lifetime is recorded at the detection wavelength of 543 nm and is reported *Figure IV-16*. A lifetime of $5 \mu\text{s}$ is deduced from the fit by mean lifetime model (§II.3.3.4.) of the curve. However, for the Tb-Yb co-doped system, no lifetime was recordable due to signal lower than the background noise level. This fact may have two explanations. The incorporation of ytterbium might have increased the disorder that quenched the terbium emission. Previous discussions (§ IV.2.2.) and the successful measurement of the ytterbium lifetime for the same layers (*Figure IV-8*) prove this supposition wrong. In addition, the terbium emission has been shown to decrease to the background noise when Yb^{3+} are incorporated in the layers (*Figure IV-12*). Thus, the terbium signal being below the detection threshold, for the calculation of the quantum efficiency we consider the worst-case scenario of $0.1 \mu\text{s}$ corresponding to the detection threshold of our setup.

Equation IV-6 is thus written by:

$$\eta_{QE} = 2 - \left(\frac{0.1}{5} \right) = 1.98 \quad \text{IV-7}$$

From this experiment, **the efficiency of the down-conversion process in the $\text{SiN}_x:\text{Tb}^{3+}\text{-Yb}^{3+}$ system is of 198 % and the energy transfer from the terbium ions to the ytterbium ions is total.**

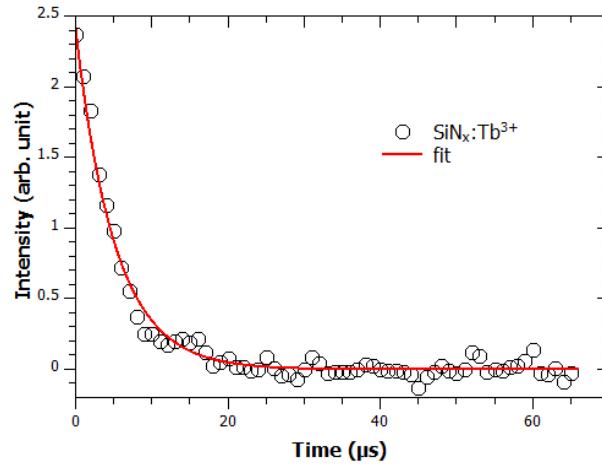


Figure IV-16: Time-resolved photoluminescence spectrum of the terbium ions in a $\text{SiN}_x:\text{Tb}^{3+}$ layer ($RFP_{\text{Tb}} = 1.2 \text{ W/cm}^2$) for a detection wavelength of 543 nm.

IV.3.3. Conclusion

We have studied the cooperative energy transfer between Tb^{3+} and Yb^{3+} in the SiN_x matrix. The optimized layer obtained was compared to the more efficient sample produced during a previous study on $\text{SiO}_x\text{N}_y:\text{Tb}^{3+}-\text{Yb}^{3+}$, and found to have a 5.6 times higher *PL* efficiency for a photon flux of 1.9×10^{15} photons/cm² at 285 nm. A 4.77 times higher internal efficiency corresponding to the *DC* conversion and propagation of the signal at 985 nm (Yb^{3+}) efficiencies was found. Moreover, an efficiency of the *DC* layer emission into the silicon was found 8.6 times higher than the one with $\text{SiO}_x\text{N}_y:\text{Tb}^{3+}-\text{Yb}^{3+}$. Another one of our objectives is thus reached. Considering the similarity of the silicon substrate and a silicon solar cell material, the latter efficiency increase is promising for future applications on this *DC* layer stacked over a real silicon solar cell. The lifetime based internal quantum yield of 198 % deduced from the lifetime measurements, although uncertain, is also promising.

IV.3. Multilayer system

In the study described above, the Tb-Yb co-doped monolayer has been optimized and the cooperative energy transfer from the terbium ions to the ytterbium ions is demonstrated. The cooperative energy transfer depends greatly of the distance between the terbium and ytterbium ions. Thus a way to improve the emission at 985 nm could consist in tuning the Tb-Yb distance. For this purpose, a $\text{SiN}_x:\text{Yb}^{3+}/\text{SiN}_x:\text{Tb}^{3+}$ multilayer where the Tb^{3+} - Yb^{3+} distance is managed has been developed and optimized to favor the emission in the infrared region. Once again, the $\text{SiN}_x:\text{Yb}^{3+}/\text{SiN}_x:\text{Tb}^{3+}$ layer is optimized by determining the deposition parameters leading to the higher ytterbium *PL* peak intensity. In this part, the layers are deposited in our laboratory by *RF* reactive magnetron co-sputtering of a pure silicon target and metallic terbium and ytterbium ones in a nitrogen-rich plasma on a silicon P-type *CZ* wafer. The deposition is performed with the values of the Si target power density RFP_{Si} , the plasma pressure P , the nitrogen ratio rN_2 , the substrate-target distance d and the substrate rotation fixed at 4.5 W/cm², 3 mTorr, 20 %, 10 cm, and 20 rpm, respectively. The *RF* power density applied on the terbium target (RFP_{Tb}) varies from 0.45 to 3.75 W/cm² while the *RF* power density applied on the ytterbium target (RFP_{Yb}) is varied from 0.1 to 0.2 W/cm². The deposition time of each sublayer is tuned to vary thicknesses from 1 nm to 6 nm for the Tb-doped sublayer and 1 nm to 5 nm for the Yb-doped sublayer. Unless otherwise stated, the layers are annealed by *CTA* at 850 °C for 1 h under nitrogen flow. First, the system is optimized through the ytterbium *PL* peak intensity by adjusting the RFP_{Tb} , the RFP_{Yb} , and the thicknesses of the two sublayers. The microstructure and composition of the obtained multilayers (*MLs*) are studied and a comparison with the monolayers is undertaken.

IV.3.1. Principle

As discussed in the first chapter, the efficiency of the cooperative energy transfer depends on the distance between the terbium and ytterbium ions and evolves by a coefficient inversely proportional to this distance power 6. In our layers, the *RE* ions are only dopants so their concentration is low and the probability of having a terbium ion close enough of two ytterbium ones is low. For this purpose, a MLs system composed of a 25 stacks of a pattern consisting in the couple Yb-doped and Tb-doped sublayers as schematized on *Figure IV-17*, is deposited on top of silicon wafers. Such a multilayer system allows a better management of the rare earth ions concentration in each sublayers, as well as of the Tb-Yb interaction distance by comparison to the composite layer.

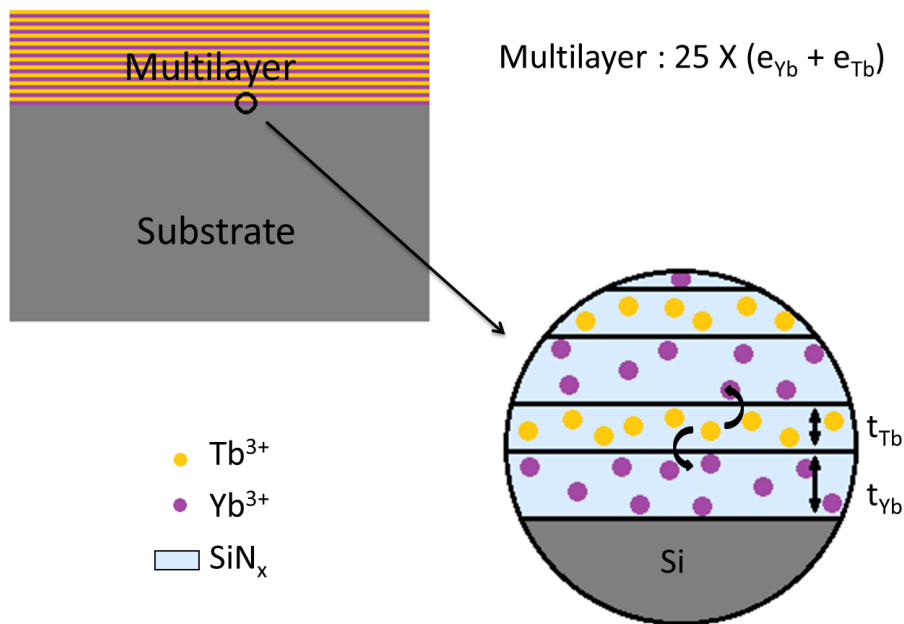


Figure IV-17: Scheme of the $SiN_x:Yb^{3+}/SiN_x:Tb^{3+}$ multilayers deposited by RF reactive magnetron co-sputtering on top of a c-Si wafer.

IV.3.2. Effects of the deposition parameters

The deposition parameters, that are the RFP_{Tb} , the RFP_{Yb} , the thicknesses of the Tb-doped and Yb-doped sublayers, are optimized by means of the *PL* intensity.

IV.3.2.1. Terbium target power density

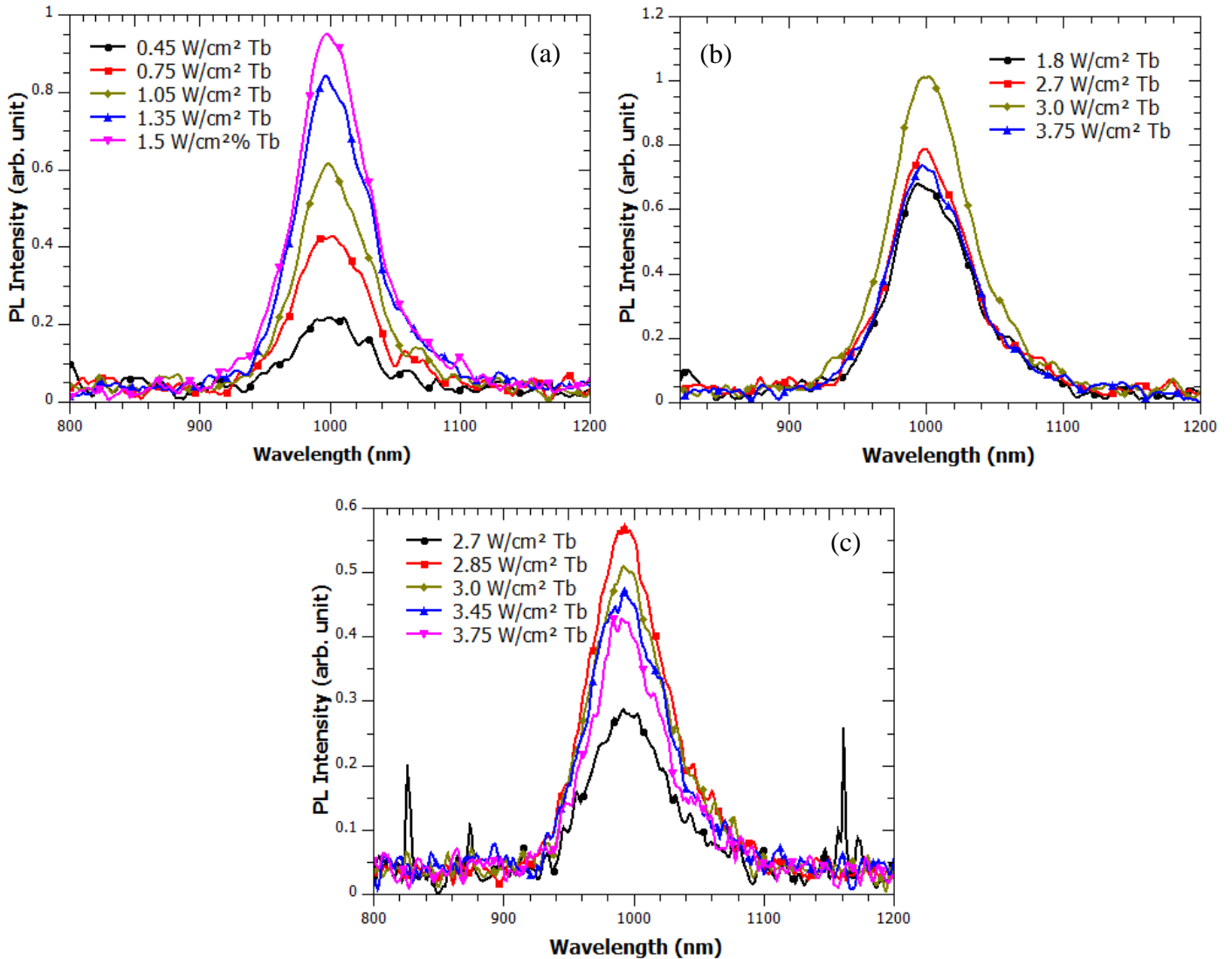


Figure IV-18: Photoluminescence spectra of the $\text{SiN}_x:\text{Yb}^{3+}/\text{SiN}_x:\text{Tb}^{3+}$ multilayer for an excitation wavelength of 285 nm and the [600-750] grating, for different RFP_{Tb} ranging from 0.45 to 1.5 W/cm^2 (a), 1.8 to 3.75 W/cm^2 (b), and 2.7 to 3.75 W/cm^2 (c) and for a RFP_{Yb} fixed at 0.15 W/cm^2 . The Yb- and Tb-doped sublayer thicknesses have been fixed at 1.2 nm and 2.6 nm, respectively.

The analysis of the effect of RFP_{Tb} is made in three steps. The first deposition session focuses on the value range of RFP_{Tb} defined in the previous parts (§III.3.2.3. and § IV.2.2.1.) for a RFP_{Yb} fixed at 0.15 W/cm^2 . The resulting PL spectra are exhibited on Figure IV-18 (a) on which one can see that the Yb^{3+} PL peak intensity increases up to the maximum value fixed (1.5 W/cm^2). Keeping the same parameters, the second deposition session consists in increasing the RFP_{Tb} to reach the maximum PL intensity at 985nm. Figure IV-18 (b) displays the resulting PL curves. The maximum PL intensity is obtained for RFP_{Tb} value of 3.0 W/cm^2 . The last depositing session has for objective of restraining the range of RF powers with a selection of RFP_{Tb} values closer from each other. The

corresponding *PL* spectra are showed on *Figure IV-18 (c)*. The optimum value found is 2.85 W/cm².

In this context of *MLs*, the *PL* intensity at 985 nm evolves similarly than for monolayer system but with a maximum emission achieved for a much higher *RFP_{Tb}*. The quenching mechanisms observed previously for composite layer (defects formation and/or migration ending by a defect) appear later for the *MLs* structure.

IV.3.2.2. Ytterbium target power density

Similarly to the previous part, the study of the effect of *RFP_{Yb}* has been carried out in two steps. The goal of the first deposition session is to determine roughly the value of *RFP_{Yb}* allowing to obtain the maximum *PL* intensity at 985nm. *Figure IV-19(a)* exhibits the recorded *PL* spectra for a *RFP_{Tb}* fixed at 1.5 W/cm². We can see that the higher intensity is obtained for the lower value of *RFP_{Yb}* (0.1 W/cm²). The second step consists in determining the optimal *RFP_{Yb}* with a higher accuracy. *Figure IV-19 (b)* shows that the value of 0.15 W/cm² leads to a higher *PL* intensity for a *RFP_{Tb}* fixed at 1.8 W/cm². However, the difference with the previous one is negligible, under the 10 % uncertainty of the measurement. The quenching of the photoluminescence with the increase of *RFP_{Yb}* has the same origins than the ones previously described. The optimum value of *RFP_{Yb}* is taken at 0.15 W/cm² but 0.1 W/cm² may also be used.

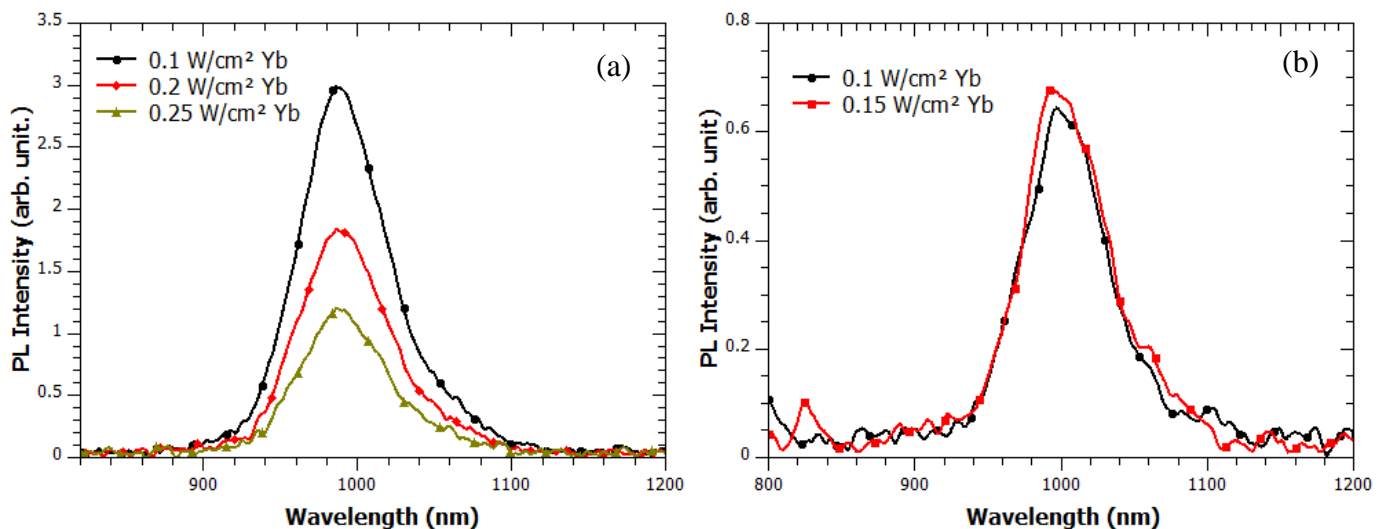


*Figure IV-19: Photoluminescence spectra of the SiN_x:Yb³⁺/SiN_x:Tb³⁺ multilayers for an excitation wavelength of 285 nm and the [600-750] grating. The values of *RFP_{Yb}* are ranging from 0.1 to 0.25 W/cm² while the *RFP_{Tb}* is fixed at 1.5 W/cm² (a), and from 0.1 to 0.15 W/cm² and a *RFP_{Tb}* fixed at 1.8 W/cm² (b). The Tb-doped and Yb-doped sublayer thicknesses have been fixed to 1.2 nm and 2.6 nm, respectively.*

IV.3.2.3. Terbium-doped sublayer thickness

As the management of the distance of interaction between the *RE* ions is essential to optimize the cooperative energy transfer, the sublayer thickness has to be optimized. *Figure IV-20* displays the *PL* spectra of *MLs* for different values of the Tb-doped sublayer thickness (t_{Tb}) for RFP_{Tb} , RFP_{Yb} , and Yb-doped sublayer thickness (t_{Yb}) fixed at 2.85 W/cm², 0.15 W/cm², and 3 nm, respectively. The higher *PL* intensity is obtained for the 1.75 nm-thick Tb-doped sublayer but the *PL* intensity achieved with t_{Tb} of 2.6 nm is very close. As using less material entails a price decrease, thinner layers are favored. The Tb-doped sublayer thickness is thus fixed at 1.75 nm.

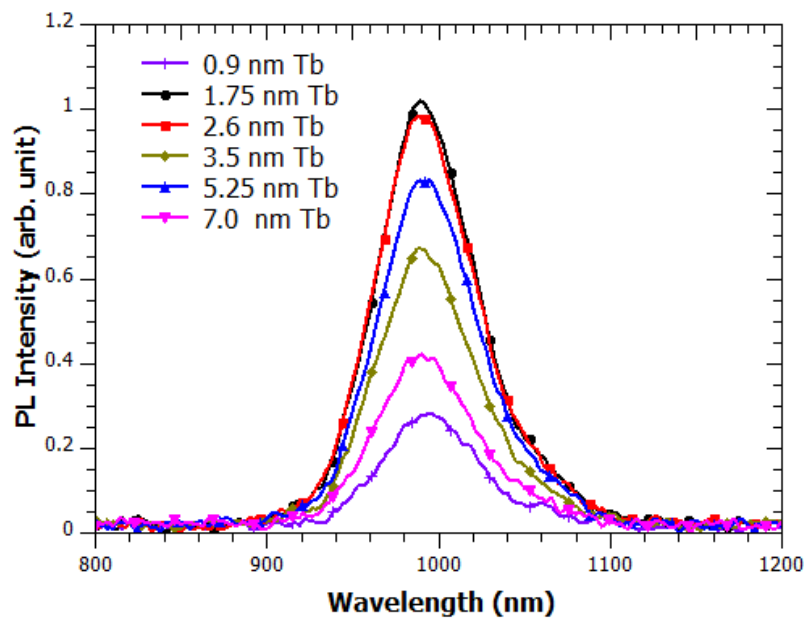


Figure IV-20: Photoluminescence spectra of the $\text{SiN}_x:\text{Yb}^{3+}/\text{SiN}_x:\text{Tb}^{3+}$ multilayers for an excitation wavelength of 285 nm and the [600-750] grating for different Tb-doped sublayer thickness and a RFP_{Tb} fixed at 2.85 W/cm², a RFP_{Yb} fixed at 0.15 W/cm², and a Yb-doped sublayer thickness fixed at 1.75 nm.

IV.3.2.4. Ytterbium-doped sublayer thickness

The PL spectra of MLs recorded for different Yb-doped sublayer thicknesses (t_{Yb}) and a RFP_{Tb} , RFP_{Yb} , and t_{Tb} fixed at 2.85 W/cm², 0.15 W/cm², and 1.75 nm, respectively is exhibited on Figure IV-21. The higher PL intensity is clearly obtained for the 1.75 nm thick Yb-doped sublayer.

Thus the optimum MLs system is obtained for RFP_{Tb} , RFP_{Yb} , t_{Tb} and t_{Yb} , of 2.85 W/cm², 0.15 W/cm², 1.75 nm and 1.75 nm, respectively.

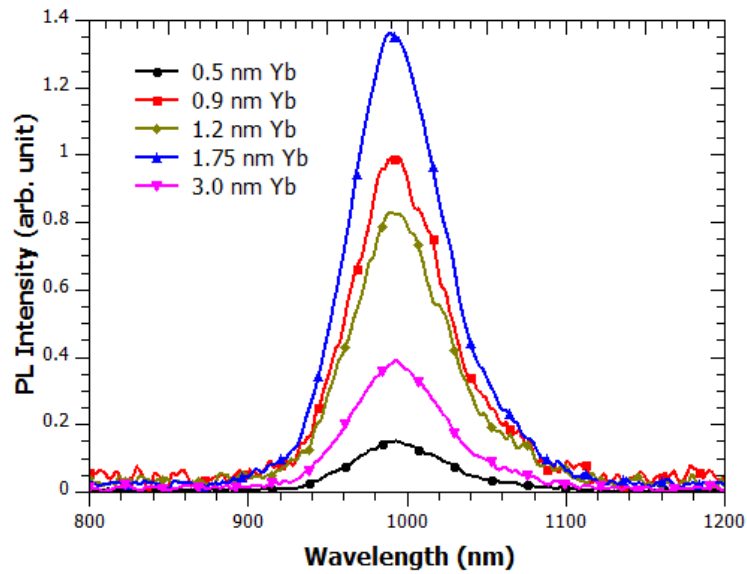


Figure IV-21: Photoluminescence spectra of the $\text{SiN}_x:\text{Yb}^{3+}/\text{SiN}_x:\text{Tb}^{3+}$ multilayers for an excitation wavelength of 285 nm and the [600-750] grating for different Yb-doped sublayer thicknesses (t_{Yb}) and a RFP_{Tb} fixed at 2.85 W/cm², a RFP_{Yb} of 0.15 W/cm², and a t_{Tb} of 1.75 nm.

IV.3.3. Composition properties

The *TEM* picture of a typical annealed *MLs* displayed on *Figure IV-22* shows that the *RE*-doped sublayers are well defined and separated with the *Tb*-doped sublayers presenting a darker contrast. Considering that their atomic weight number is similar, the contrast difference is an evidence of higher incorporation of Tb^{3+} ions than Yb^{3+} ones. In the two cases (annealed or non-annealed) the *Tb*-doped and *Yb*-doped sublayers have the same thickness of around 1.75 nm and 1.75 nm, respectively.

There is no evidence of the presence of any clusters at the observation scale in any of the sublayers, thus proving that such a nitride matrix may be able to incorporate a large amount of *RE* ions without cluster formation.

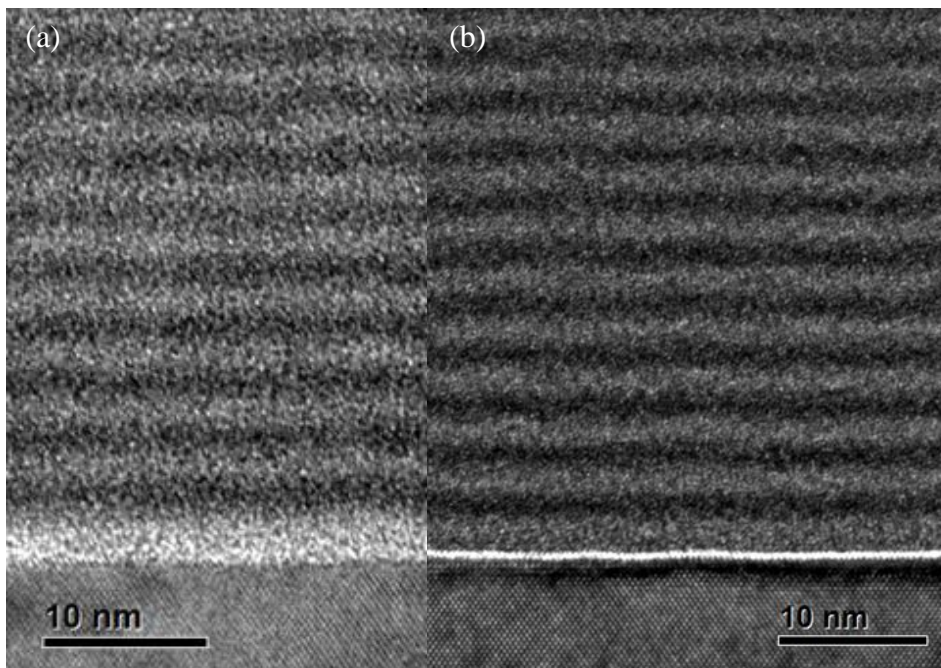


Figure IV-22: HRTEM picture of a typical non-annealed (a) and annealed at 850 °C (CTA 1 h) $\text{SiN}_x\text{:Yb}^{3+}/\text{SiN}_x\text{:Tb}^{3+}$ multilayer (b) with the Si substrate at the bottom and the layer at the top.

IV.3.3. Comparison with the monolayer system

The optimized multilayer obtained is compared to ones of the optimized monolayer previously detailed. It is worth noting that the *PL* spectra are normalized to the *Yb*-doped thickness (t_{Yb}) as we focus only on the Yb^{3+} emission. So, the thickness of the monolayers is entirely taken into account while for multilayers only the cumulative thicknesses of the *Yb*-doped sublayers are taken into account. In this context, *Figure IV-23* shows that the *Yb* peak intensity in *MLs* is 1.5 times higher than the one of the monolayer.

Similarly to the reasoning used in the previous chapter (see §III.4.2.) and above (IV.3.2.1.b)), an Yb^{3+} excited state ratio of $N_{multi}^*(\text{Yb}^{3+})/N_{mono}^*(\text{Yb}^{3+}) = 1.5$ is found demonstrating the higher *PL* efficiency of the multilayer system.

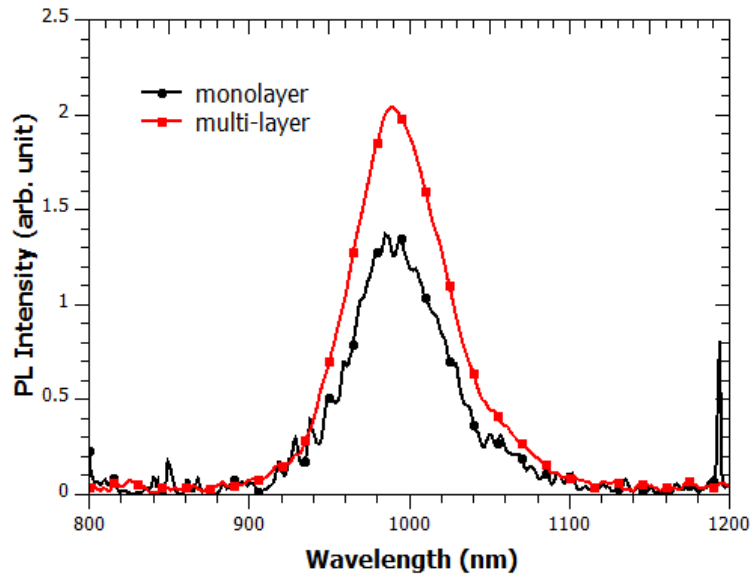


Figure IV-23: Photoluminescence spectra of the monolayer and multilayer systems for an excitation wavelength of 285 nm measured with the [600-750] grating.

In this case, the normalized absorbance of both $\text{SiN}_x:\text{Tb}^{3+}-\text{Yb}^{3+}$ and $\text{SiN}_x:\text{Yb}^{3+}/\text{SiN}_x:\text{Tb}^{3+}$ samples exhibiting the highest Yb^{3+} *PL* emission are estimated to be 32.5 % and 27.1 %, respectively, for an excitation at 285 nm and a photon flux of 1.9×10^{15} photons/cm². This difference can be once again attributed to opto-geometrical differences between the two studied layers, which have different thicknesses 81 nm and 93 nm and different refractive indexes 2.151 and 2.108, respectively at 1.95 eV.

The luminescence ratios in the layer, in the air, and in the substrate obtained thanks to the extended transfer matrix method (*ETMM*) program given in *Table IV-3* show multilayer transfers more to the *SC* (modeled here by the Si) than the monolayer.

Still using the same reasoning and knowing that the Yb^{3+} excited state ratio of multilayer (*Figure IV-23*) was found to be 1.5 times higher than the one for monolayers with the same *PL* experimental conditions (1.9×10^{15} photons/cm² at 285nm), the internal efficiency ratio is:

$$\frac{\eta_{multi}^{int}}{\eta_{mono}^{int}} = 1.87. \quad \text{IV-8}$$

Once again, the internal efficiency improvement of the multilayer compared to the $\text{SiN}_x:\text{Tb}^{3+}-\text{Yb}^{3+}$ monolayer can be attributed to: (i) an increase of the optically active *RE* content, (ii) an improvement in the *DC* conversion efficiency, or/and (iii) an improvement of the 985 nm photons propagation in the layer.

Similarly, the ratio of global efficiency of *DC* layers with emission in the Si substrate leads to:

$$\frac{\eta^{glo}_{multi}}{\eta^{glo}_{mono}} = 1.6 . \quad \text{IV-9}$$

This ratio shows the improvement of the global efficiency of the multilayer compared to the $\text{SiN}_x:\text{Tb}^{3+}-\text{Yb}^{3+}$ monolayer (assumed to be representative of the silicon *SC*). **For the conditions of thickness and refractive index employed in this work and an excitation at 285 nm, the silicon, and thus the silicon solar cells, would receive 1.6 times more light at 985 nm from the multilayer compared to the $\text{SiN}_x:\text{Tb}^{3+}-\text{Yb}^{3+}$ monolayer.**

η^{lum} (%)	Air	Layer	Silicon
mono	16.3	61.2	22.5
multi	15.7	61.2	23.1

Table IV-3: Luminescence ratio of the mono- and multilayers in the air, the layer, and the silicon.

IV.3.4. Conclusion

The $\text{SiN}_x:\text{Yb}^{3+}/\text{SiN}_x:\text{Tb}^{3+}$ multilayer structure has been optimized through the *PL* intensity at 985 nm with the goal of increasing the down-conversion efficiency. The optimum *MLs* system is obtained for RFP_{Tb} , RFP_{Yb} , t_{Tb} , and t_{Yb} fixed at 2.85 W/cm², 0.15 W/cm², 1.75 nm, and 1.75 nm, respectively. Microstructure analyses show well-defined sublayers. This system has been compared to the $\text{SiN}_x:\text{Tb}^{3+}-\text{Yb}^{3+}$ monolayer one and found to have a Yb^{3+} *PL* peak 1.5 times more intense. Thus the silicon cell would receive 1.6 times more light thanks to *MLs* than monolayers.

IV.4. Conclusion

In this work, both the Tb-Yb co-doped monolayer and multilayer systems have been optimized in order to obtain a *DC* layer that emits a maximum intensity at 985 nm (ytterbium peak) and that exhibits anti-reflective properties. Studies of the composition, the microstructure, and the optical properties enabled a better understanding of the requirements for obtaining such a layer. The optimized monolayer has been achieved for a plasma pressure of 3 mTorr, a nitrogen ratio of 20 %, a 1.2 W/cm² power density on the terbium target, and a 0.15 W/cm² power density on the ytterbium target. The optimized multilayer has been obtained for a plasma pressure of 3 mTorr and a nitrogen ratio of 20 % for the host-matrix, a 2.85 W/cm² power density on the terbium target and a thickness of 1.75 nm for the Tb-doped sublayers, and a 0.15 W/cm² power density on the ytterbium target and a thickness of 1.75 nm for the Yb-doped sublayers.

The cooperative energy transfer from the terbium ions to the ytterbium ones has been evidenced. Moreover, a second of our objective is reached as the Tb-Yb co-doped monolayer *DC* system is found to have a *PL* efficiency 5.6 times higher and a emission toward the wafer 8.6 times higher than a similar system constituted of a SiO_xN_y host-matrix.

The multilayer system is found to transfer 1.6 times more light to the Si *SC* than the monolayer one. The two systems will be used on top of silicon solar cells to try and determine the effects of the layers on the *SC* efficiency.

Bibliography

- [1] Y.-T. An, C. Labbé, J. Cardin, M. Morales, F. Gourbilleau, Highly Efficient Infrared Quantum Cutting in Tb³⁺- Yb³⁺ Codoped Silicon Oxynitride for Solar Cell Applications, *Adv. Opt. Mater.* 1 (2013) 855–862.
- [2] M. Ippolito, S. Meloni, Atomistic structure of amorphous silicon nitride from classical molecular dynamics simulations, *Phys. Rev. B.* 83 (2011) 165209. doi:10.1103/PhysRevB.83.165209.
- [3] O. Debieu, R.P. Nalini, J. Cardin, X. Portier, J. Perrière, F. Gourbilleau, Structural and optical characterization of pure Si-rich nitride thin films, *Nanoscale Res. Lett.* 8 (2013) 1–13.
- [4] E. Bustarret, M. Bensouda, M.C. Habrard, J.C. Bruyère, S. Poulin, S.C. Gujrathi, Configurational statistics in a-SixNyHz alloys: A quantitative bonding analysis, *Phys. Rev. B.* 38 (1988) 8171–8184. doi:10.1103/PhysRevB.38.8171.
- [5] A.F. van Driel, I.S. Nikolaev, P. Vergeer, P. Lodahl, D. Vanmaekelbergh, W.L. Vos, Statistical analysis of time-resolved emission from ensembles of semiconductor quantum dots: Interpretation of exponential decay models, *Phys. Rev. B.* 75 (2007). doi:10.1103/PhysRevB.75.035329.
- [6] K. Petermann, D. Fagundes-Peters, J. Johannsen, M. Mond, V. Peters, J.J. Romero, S. Kutovoi, J. Speiser, A. Giesen, Highly Yb-doped oxides for thin-disc lasers, *J. Cryst. Growth.* 275 (2005) 135–140. doi:10.1016/j.jcrysgro.2004.10.077.
- [7] S. Schmidt, S. Hüfner, F. Reinert, W. Assmus, X-ray photoemission of Yb In Cu 4, *Phys. Rev. B.* 71 (2005). doi:10.1103/PhysRevB.71.195110.
- [8] D. Navarro-Urrios, Y. Lebour, O. Jambois, B. Garrido, A. Pitanti, N. Daldosso, L. Pavesi, J. Cardin, K. Hijazi, L. Khomenkova, F. Gourbilleau, R. Rizk, Optically active Er³⁺ ions in SiO₂ codoped with Si nanoclusters, *J. Appl. Phys.* 106 (2009) 93107. doi:10.1063/1.3253753.
- [9] R.T. Wegh, H. Donker, K.D. Oskam, A. Meijerink, Visible Quantum Cutting in LiGdF₄:Eu³⁺ Through Downconversion, *Science.* 283 (1999) 663–666. doi:10.1126/science.283.5402.663.
- [10] P. Vergeer, T.J.H. Vlugt, M.H.F. Kox, M.I. den Hertog, J.P.J.M. van der Eerden, A. Meijerink, Quantum cutting by cooperative energy transfer in YbxY_{1-x}PO₄:Tb³⁺, *Phys. Rev. B.* 71 (2005) 14119. doi:10.1103/PhysRevB.71.014119.

Chapter V: Application to silicon solar cells

V.1. Introduction

After having optimized our frequency conversion layer, either the down-shifting (*DS*) system with the Tb-doped layer or the down-conversion (*DC*) systems that consists in co-doped mono-or multi-layer with the Tb^{3+} - Yb^{3+} couple, we have tested their efficiency on silicon solar cells. This is the purpose of this chapter in which *DS* and *DC* layers have been deposited on industrial silicon solar cells provided by the E-Ton Solar company (Taiwan, www.e-tonsolar.com) through a collaboration with the Prof. Ing-Song Yu from the Department of Materials Science and Engineering of the National Dong Hwa University (Hualien –Taiwan).The optical and electrical properties (I-V, Reflectance, Internal Quantum Efficiency, ...) of the solar cell topped with such frequency conversion layer (*DC* or *DS* layers) are then measured and analyzed.

In the first part of this chapter, the operating principle and the fabrication process of the silicon solar cell will be described. Then, we will detail how we adapted the fabrication steps of our layers to the Si *SC* fabrication requirements. In the last part, an example of the annealing temperature influence on the characteristic of the *SC* is detailed.

V.2. Prerequisite to the deposition on silicon solar cells

V.2.1. Solar cell operating principle

The photovoltaic (PV) solar technic used PV cells composed of two semiconductor materials. The first doped with bore has an excess of positive charge carriers (holes) and is called type P semiconductor. The second doped with phosphor has an excess of negative charge carriers (electrons) and is called type N semiconductor. When those two semiconductors are placed on top of each other, at the equilibrium, the electrons of the N material and the holes of the P material diffuse to the interfacial zone or P-N junction where they recombine. Fixed charges linked to the lattice on either side of the interfacial zone (positive in the N material and negative in the P one) are left without electrical compensation and create an electric field from the N material to the P one. This electric field goes against the diffusion mechanism and, at equilibrium, the diffusion currents in the two materials are compensated by conduction currents driven by this local electric field. Photons absorption in the cell (*Figure V-1*) leads to generation of electron/hole pairs (excitons) in the three zones, called photogeneration. In the P and N zones, some of the minority charges carriers, electrons and hole respectively, diffuse to and through the P-N junction toward the opposite zone (N and P) thanks to diffusion currents. In the P-N junction, the charge carriers are split by the electrical field and sent toward the N material for the electrons, and the P materials for the holes which generated the photocurrent.

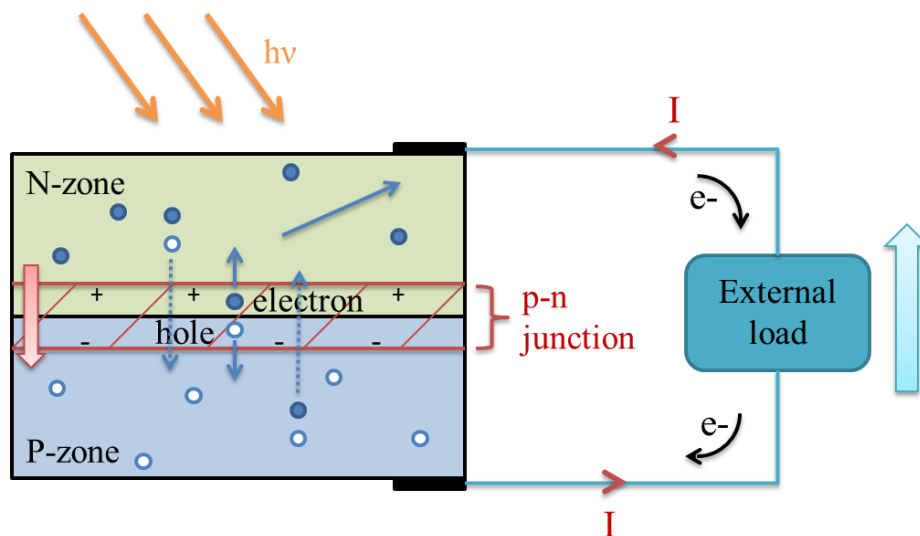


Figure V-1: Photovoltaic solar cell diagram.

V.2.2. Fabrication process

Our optimized silicon nitride based layers (*DC*, *DS* and non-doped layers) described in the two previous chapters have been tested on Si solar cells. *Figure V-2* represents schematically the fabrication steps of such devices. The steps not involving the deposition of our layers follow the standard procedure developed by the E-Ton Solar Company.

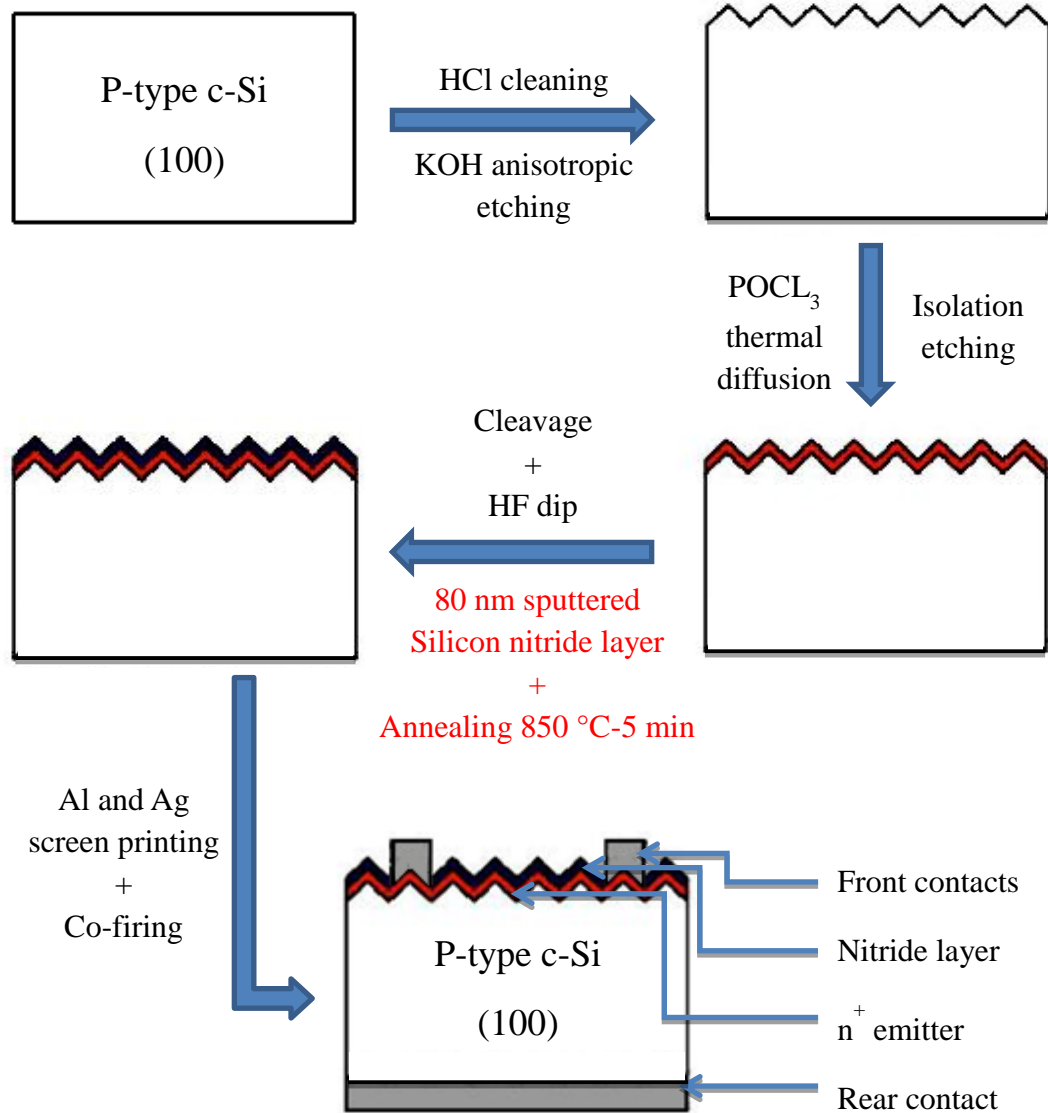


Figure V-2: Schematic of the fabrication process of a Si solar cell with our silicon nitride layers (step in red) [3].

A 200 μm -thick monocrystalline P-type Si wafer is chemically cleaned with HCl before being textured into pyramid-shape structures using a KOH etching. It then undergoes a N doping via a POCL₃ diffusion at 850 °C during 30 min. Afterwards, an isolation etching process is performed to remove the N-type Si edges and backsides. The cells are cleaved from the wafer. A classical removed native oxide procedure is applied using a HF acid before the deposition of a 80 nm-thick

silicon nitride based layer by means of *PECVD* (plasma-enhanced chemical vapor deposition) technique. This step will be replaced by means of our *RF* magnetron sputtering process using the optimized fabrication conditions described above. After the deposition of the *RF*-sputtered layer, an additional post annealing treatment with adapted temperature and time is performed to favor the recovering of non-radiative traps. The last step of the process consists in screen-printing of Ag-front contacts and Al-back contacts followed by a co-firing¹ [1,2] to passivate the interface *SC*/silicon nitride layer.

It is important to note that here our layers deposited instead of the standard anti-reflective silicon nitride layer does not contain 40 at.% hydrogen of the *PECVD* approach that enables the interface passivation by diffusion in the Si wafer during the co-firing.

Once the deposition process of our layers is adapted to Si *SC*, the optimized Tb-doped-, Tb-Yb co-doped-, multi- and undoped-layers are deposited on industrial Si *SC*. The solar cells produced by the company, cut and sent to us for the deposition step of the frequency conversion layers. After this step and an appropriate annealing treatment, the *SCs* were then sent back to Taiwan where the end of the fabrication process and/or measurements takes place.

Figure V-3 (a) shows that the pyramids of the textured cell are very large which allows for a uniform covering of the surface by the sputtering technique. It is confirmed by *Figure V-3 (b)* displaying the *TEM* picture of a Tb-Yb co-doped layer deposited on top of the textured *SC* where the layer follows the surface of the pyramids uniformly.

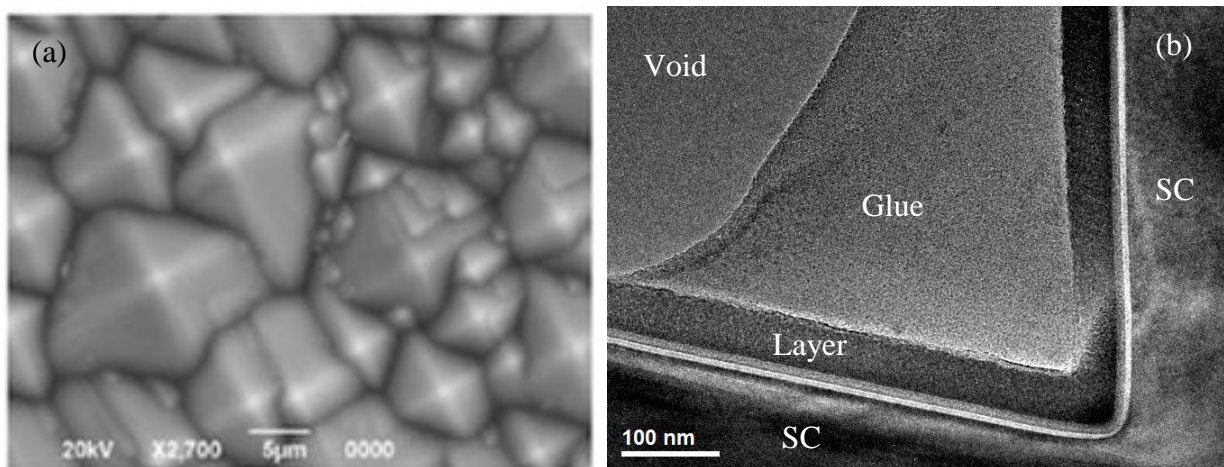


Figure V-3: (a) SEM picture of the textured surface of a SC on which our layer is deposited. (b) xTEM picture of one of our layer deposited on a SC.

¹The co-firing of screen-printed metal contacts is a standard process in crystalline silicon solar cells industry that consists in forming simultaneously the front and back grid contact by a sophisticated temperature profile annealing with typical ramps of 60-80 °C/s during 16-20 s.

V.3. Adaptation of the fabrication parameters of our layers to the silicon solar cell system

Experiments have been carried out to improve our layers compatibility with the *SCs*. The luminescence, the reflectance and the lifetime of the minority carriers of the samples (*SC* + layer) are measured before metallization and co-firing. The cell *EQE* is then measured.

V.3.1. 1st round -Efficiency improvement

For the first round, a Tb-doped-, Tb-Yb co-doped-, and undoped-layers are deposited on Si *SC* following the fabrication process described on §V.2.2.. The two first layers deposited on the Si *SC* are annealed by *CTA* at 850 °C during 5 min while the third is annealed by *CTA* at 850 °C during both 5 and 20 min for the co-doped layer. Indeed, annealing at 850 °C is likely to destroy the P-N junction integrity. Therefore, the annealing time is decreased to keep the same level of Yb³⁺ *PL* intensity of the layer while sparing the P-N junction.

It is worth noting that the reflectance obtained for our layer deposited on a Si wafer and a Si *SC* are widely different and cannot be compared (*Figure V-4*). This difference may be due to the difference in fabrication process and notably the nanostructuration of the *SC* surface that enhances the anti-reflective properties of the system. Thus, only layer deposited on a bare Si wafer will be analyzed.

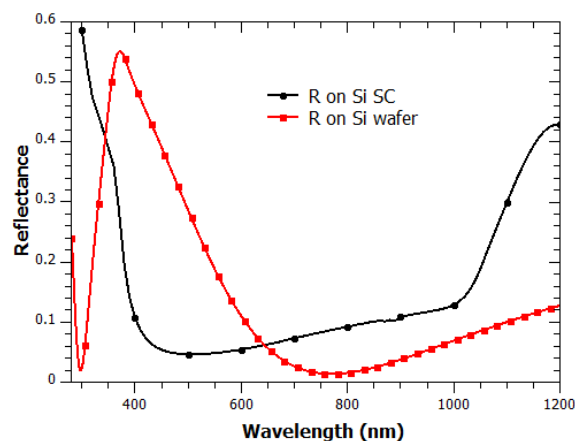


Figure V-4: Reflectance spectra of a sample deposited on top of a Si SC and on a bare Si wafer.

Figure V-5 (a) represents the *EQE* spectra of Si SC topped with the undoped-, Tb-doped-, and Tb-Yb co-doped-layers. The *EQE* of the SC topped with the co-doped layer annealed for 20 min is not represented as the measurements were impossible. This is the result of the combination of high temperature annealing (850 °C) and duration (20 min) that destroys the P-N junction. However, the *EQE* measurement was possible for the Tb-Yb co-doped layer annealed at the same temperature but during a shorter duration (5 min). This demonstrates that the change of the annealing duration is a possible way to obtain efficient *DC (DS)* layers while keeping the P-N junction integrity.

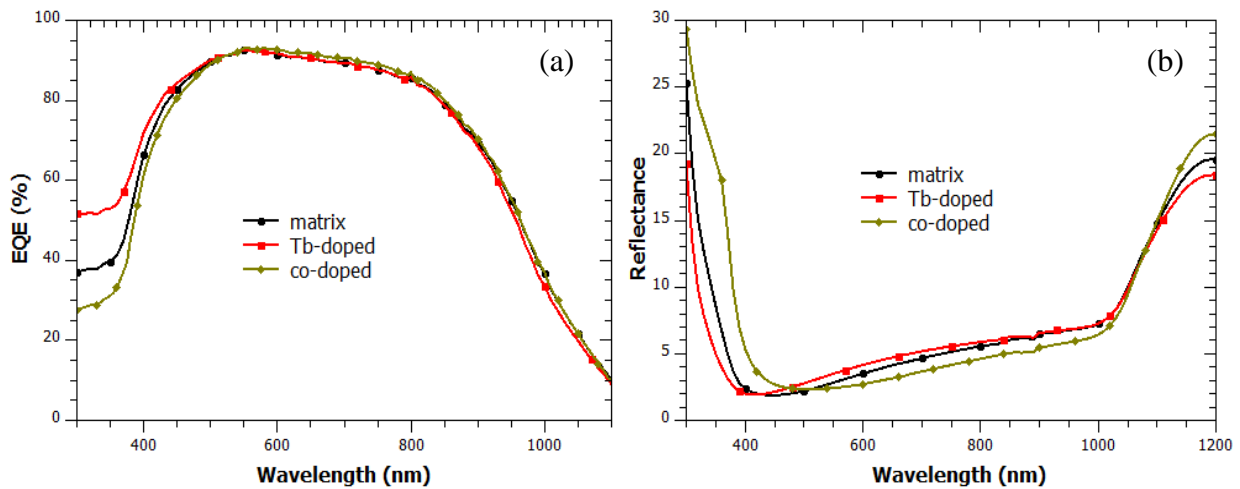


Figure V-5: (a) *EQE* and (b) reflectance spectra of Si SC topped with the undoped-, Tb-doped-, and Tb-Yb co-doped-layers.

Comparing the optical characteristic of the SC topped with the undoped- and the Tb-doped-layer, we can see that the later presents an increased *EQE* by 15 % in the UV range (300-400 nm) while being similar on the rest of the spectrum (or slightly below in the IR range). This result shows that the *EQE* is larger for UV photons thanks to the Tb-doped layer. In addition, Figure V-5 (b) displaying the reflectance of SC topped with our layers (undoped- and Tb-doped-layers) shows that the Tb-doped layer has a lower reflectance in the UV range which allows for a bigger part of those photons, to be absorbed by the layer or transmitted to the cell. Regarding the *EQE* spectrum, the Tb-doped layer acts as a down-shifting layer that may improve the solar cell efficiency in the UV part of the solar spectrum.

The comparison of these results with the Tb-Yb co-doped layer reveals that their behavior is similar on the visible and IR ranges but the Tb-Yb co-doped layer displays a much lower *EQE* in the UV range (25 % to the undoped- and 46 % to the Tb-doped- layer). This decrease may be attributed to the optical path (couple refractive index/thickness) that influences greatly the anti-reflective properties of the layers. The standard AR-layer refractive index and thickness being optimized at 80 nm for a refractive index n equal to 2.02 (at 1.95 eV), a higher refractive index requires a thinner layer in order to keep the same optical path and thus the same anti-reflective properties as shown by the modeling made in the third chapter (*Figure III-9*). However, we can see in *Table V-1* that the Tb-Yb co-doped layer has a higher refractive index and larger thickness which results in a larger reflectance in these thickness and refractive index range. In addition, the higher reflectance in the UV range displayed on *Figure V-5 (b)* would decrease the part of the photons possibly used by the layer and the cell which will decrease even more the efficiency. To improve the efficiency of such a layer, its thickness should be reduced as the refractive index will most likely remain constant.

Layer	n (1.95 eV)	Thickness
AR layer	2.02	80 nm
Undoped layer	2.04	80 nm
Tb-doped layer	2.03	70 nm
Tb-Yb co-doped layer	2.15	86 nm

Table V-1: Refractive index at 1.95 eV and thickness of the undoped-, Tb-doped-, and Tb-Yb co-doped- layers deposited on top of Si SCs as well as for a standard anti-reflective (AR) layer.

V.3.2. Deposition and annealing temperatures studies

The necessity of annealing our layers after deposition is illustrated by *Figure V-6* that displays the *PL* spectra of the terbium ion for non-annealed- or annealed-layers using the rapid thermal annealing process (*RTA* for 10 min). The *PL* intensity of Tb^{3+} peaks for the annealed layers is at least 7 times higher than for the non-annealed one. It shows the main importance of the annealing step in our layers optimization.

The optimal annealing temperature was first determined for the Tb-doped layers at 850 °C (*Figure V-6*) and then checked for the Tb-Yb co-doped ones. Below 850 °C, the increase of the *PL* intensity (of either the Tb^{3+} or Yb^{3+} peaks) is attributed either to the thermal passivation of non-radiative defects [4] or the relaxation/rearrangement of the matrix that improve its order [5]. After 850 °C, the decrease of the *PL* intensity is mostly due to the concentration quenching and/or the increase of the defects density [5] that will quench the *PL*.

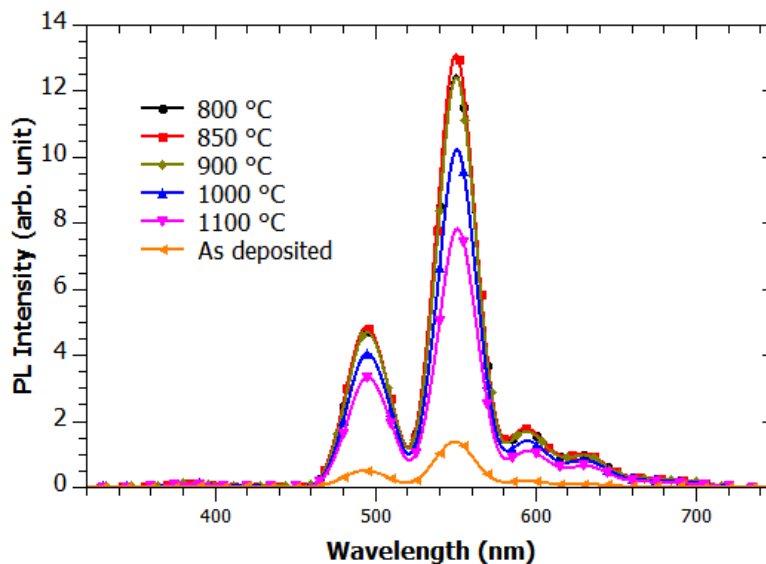


Figure V-6: Photoluminescence spectra of the terbium ions for different annealing temperatures by RTA during 10 min.

For all the studies presented in the third and fourth chapters, the 1 h-CTA 850 °C annealing was applied; however, a possible degradation of the P-N junction by such a high temperature annealing has to be taken into account in the fabrication process of photovoltaic cells. Indeed, above 700 °C the P and B dopant diffusion increases drastically, which may destroy the P-N junction. Consequently, solutions have to be found by adapting the deposition temperature as well as the annealing one to the silicon solar cell requirements while keeping as intense as possible, the emission intensity at 980 nm.

V.3.2.1. Annealing temperature adaptation

To prevent dopants diffusion, the annealing temperature has to be decreased to around 600 °C. At this temperature, the SC can be annealed up to 1 h without any detrimental effect on photovoltaic behavior. However, the Tb^{3+} -and/or Yb^{3+} - PL peak intensities reach a maximum for 850 °C as shown previously (Figure V-6) and are almost 2 times lower for an annealing temperature of 600 °C (Figure V-7). The effect of duration at this lower temperature has been analyzed. For that we annealed several times at 600 °C during 10 min using the RTA furnace one layer. For each annealing step a PL experiment has been carried out. The resulting PL spectra are shown on Figure V-7 alongside spectra of a non-annealed- and annealed-layer (CTA 850 °C 1 h). The PL intensity stays constant with the number of annealing times. Therefore, another solution has to be found to keep a high PL intensity while decreasing the annealing temperature.

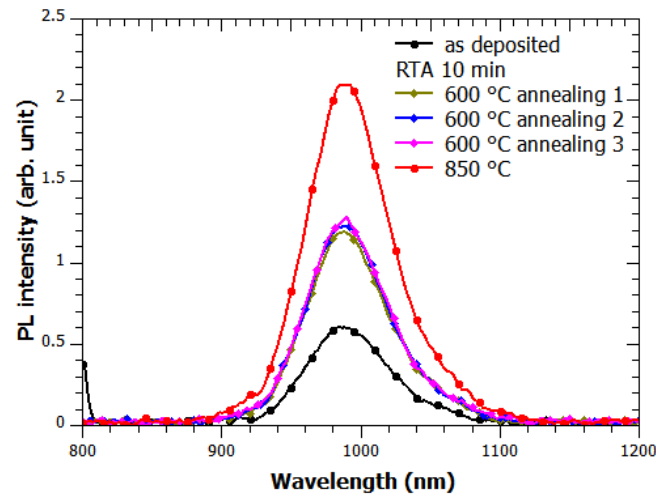


Figure V-7: Photoluminescence of the Yb^{3+} peak for an increasing number of annealing times.

The results indicate that, in our case, the Yb^{3+} PL peak intensity of the annealed layers does not depend of the number of annealings but on the energy reached during the annealing ($k_B T$ with k_B the Boltzmann constant). This phenomenon seems to be activation energy dependent, which might correspond to several reasons like atomic reorganizations, non-radiative defects recovering, ...

TEM analyses performed in Caen (Figure V-8) on non-annealed-, 600 °C, and 850 °C annealed-layers show that the inhomogeneity present in the non-annealed layer is recovered with annealing at both 600 °C or 850 °C.

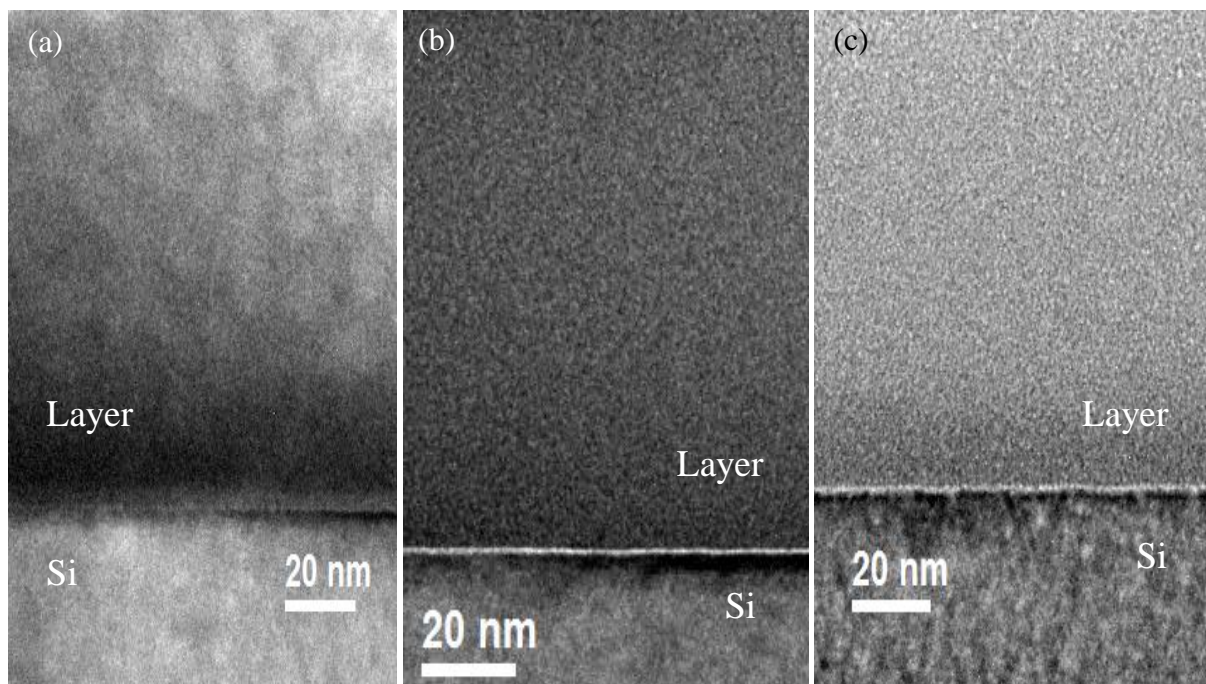


Figure V-8: TEM pictures of a non-annealed (a), 600 °C (b), and 850 °C (c) annealed characteristic Tb-Yb co-doped layer.

V.3.2.2. Deposition temperature adaptation

Modifying only the annealing temperature does not lead to a satisfactory *PL* intensity. To increase the efficiency of our layers, the deposition temperature is increased to 350 °C and 500 °C. The *PL* emission of the layers obtained are compared on Figure V-9 (a) after an annealing at 600 °C during 10 min. Increasing the deposition temperature to 350 °C and 500 °C improves the *PL* intensity 2.5 times and 3 times, respectively.

Figure V-9 (b) compares the Yb^{3+} *PL* peak intensity of samples deposited at 200 °C and annealed 1 h at 850 °C using the *CTA* with samples deposited at 500 °C and annealed during 10 min at 600 °C but with the *RTA* approach. The two layers have mostly the same Yb^{3+} *PL* peak intensity allowing the use of these new fabrication conditions for inserting our *DC* layer in the solar cell fabrication process.

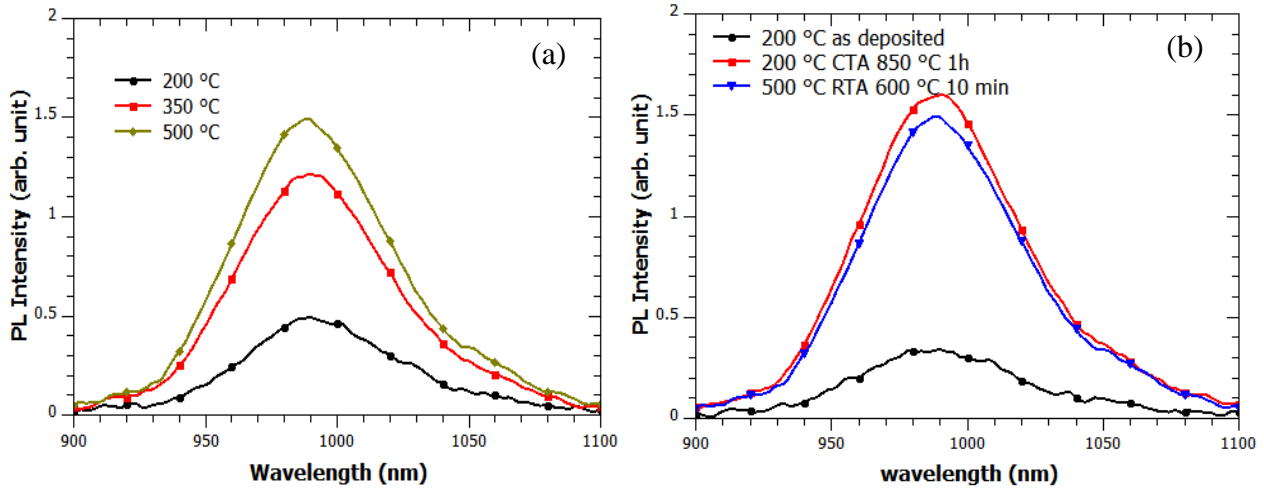


Figure V-9: PL curves of layers annealed by RTA at 600 °C during 1 min for different deposition temperatures (a). Photoluminescence spectra of the standard sample deposited at 200 °C and annealed with 1 h-CTA 850 °C, and of the layer deposited at 500 °C and annealed with 10 min-RTA 600 °C (b). The PL experiments have been performed with an excitation wavelength of 285 nm and the [600-750] grating

V.3.3. Conclusion

EQE measurements performed on *SC* topped with the undoped-, Tb-doped-, and Tb-Yb co-doped- layers, determined a 15 % improvement of the cell efficiency while topped with the Tb-doped layers that used the down-shifting process instead of the undoped one. However the *SC* topped with Tb-Yb co-doped layer has an efficiency 25 % lower than the undoped one which demonstrates the need to improve the fabrication process of our frequency conversion layer to be compatible with the *SC* fabrication requirements. In fact, the annealing process, optimized and applied for our *DC* layer, uses a temperature too high that may destroy the P-N junction by diffusion of the dopants. In order to adapt the fabrication process of our layer to the silicon solar cell one, tests have been made while decreasing the annealing temperature from 850 °C to 600 °C. A satisfying compromise is found by increasing the deposition temperature to 500 °C that allows to decrease the annealing temperature to 600 °C while obtaining the same *PL* intensity level than layers deposited at 200 °C and annealed at 850 °C.

V.4. Improvement of the fabrication process

The optimization of the fabrication process of the Si SCs topped with our frequency conversion layer is very complex as it depends of many parameters. Several of them were studied such as the deposition and annealing temperatures, the annealing time, but also the use of mono- or multilayers. However, we will focus on one specific case which is the annealing temperature.

V.4.1. Study of the annealing temperature

Tb-Yb co-doped layers deposited at 500 °C and annealed by means of *RTA* during 5 min at 650, 750, and 850 °C are studied. First of all, the lifetime of their minority carriers has been measured using the procedure described in the second chapter (II.3.3.). The resulting values are presented on *Table V-2*. Such a measurement before the screen-printing and the co-firing, is an indication of quality of the P-N junction and thus of the efficiency of the future cell. Indeed, standard Si SCs have a lifetime of minority carriers around 10 μs. A system having a lifetime of minority carriers close to that value will potentially be an efficient one while a system having a lifetime of minority carriers lower will be inefficient. In *Table V-2*, we can see that the lifetime of minority carriers decreases with the increase of the annealing temperature. The lifetime of minority carriers of 1.99 μs is obtained at 850 °C which witness the P-N junction degradation and would lead to a low SC efficiency.

After the co-firing, *EQE* and *I-V* measurements are performed and an *IQE* curve is obtained from the following formula:

$$IQE = (1 - R)EQE \quad V-1$$

The *IQE* and *I-V* curves obtained are exposed on *Figure V-10* and the cell parameters deduced from the *I-V* curves are shown on *Table V-2*. The efficiency is calculated following the equation:

$$\eta = \frac{V_{OC} I_{SC} FF}{P_{in}} \quad V-2$$

With P_{in} the incident light (sun or optical) power, V_{OC} the open-circuit voltage, I_{SC} the short-circuit current and FF the fill factor.

The open-circuit voltage V_{OC} of a standard mono-Si SC is of 0.73 V [6]. We can see in *Table V-2* that the V_{OC} of our samples is stable and quite high and close to the reference mentioned above (20 % difference).

The short-circuit current J_{SC} of a standard mono-Si SC is between 28 and 35 mA/cm² [6]. The values obtained for our layers are lower by 20 % but for the one annealed at 650 °C that is lower by 50 %. Usually the J_{SC} and the efficiency η have the same evolution which is seen also in the case of our samples (*Table V-2*).

The lifetime of minority carriers for the different annealing temperatures are reported in *Table V-2*. We can see that the minority carriers have the higher lifetime in the 650 °C annealed layer, followed by the ones in the 750 °C annealed layer. In the 850 °C annealed layer-case, the value measured is very low which means that they recombine much faster than in the layers annealed at lower temperature. This is the sign of a P-N junction of lower quality and, thus, confirmed the fact that annealing at 850 °C damages the P-N junction of the SCs.

In the same *Table V-2*, are exposed the calculated efficiency of the layers annealed at various temperatures. The higher efficiency is obtained for the 750 °C annealed layer, followed by the 850 °C, and the 650 °C layers. Those results differ from the lifetime of the minority carriers ones as the efficiency not only takes into account the quality of the P-N junction but also the number of minority carriers generated in the cell, the shunt and series resistances, ...

The fill factor of a standard mono-Si SC is between 0.83 and 0.85 [6]. The *FF* of our layers is very low (less than half the standard value) which may be explained by bad contacts on the top and on the back. This is mainly due to the non-standard size and shape of our cells with respect to the ones of company process. Indeed, due to the maximum size of substrate that can be placed in our sputtering machine (4"), cells are cut by cleaving the 15x15 cm² industrial cell. Such a procedure gives rise to non-homogeneous shape and size which are at the origin of some inhomogeneities during the co-firing step in the industrial process. For this same reason, the *EQE* measurements are difficult to compare which prevent us to compare our Tb-Yb co-doped- and undoped- layers.

Annealing Temperature (°C)	Lifetime (μs)	V _{OC} (V)	J _{SC} (mA/cm ²)	FF	η (%)
650	8.21	0.58	13.12	0.40	3.04
750	7.06	0.57	22.84	0.35	4.52
850	1.99	0.55	23.16	0.31	3.95

Table V-2: SCs parameters obtained by I-V measurements and lifetime of minority carriers for various annealing temperatures.

The study of the *IQE* spectra (*Figure V-10 (a)*) reveals that the 650 °C annealed layer has a higher *IQE* from 300 to 1000 nm, above 1000 nm the 750 °C annealed layer is above. However, the shoulder observed above 1000 nm for the 750 °C annealed layer is the sign of a poor passivation at the bottom of the cell and/or loose contacts at the back of the cell. Those problems originate from a process not adapted to the cells we deposited on. In a similar way, the shoulder observed below 400 nm is the sign of a poor passivation at the top of the cell, typically at the interface between the cell and the anti-reflective layer thus our layers in this case. The 850 °C-annealed layer has an *IQE* lower on the whole spectra range which is consistent with its low lifetime of minority carriers.

The study of the I-V curves (*Figure V-10 (b)*) shows the much lower J_{SC} of the 650 °C annealed layer observed before. We can also see that the I-V curves do not have the appearance of the ones of standard SCs and composed of (i) a slightly sloped region above 0 V, (ii) a steeply region below V_{OC} , and (iii) a bend in the curve at the maximum power point. In our case, the curves are steeper in region (i) and less steep in region (ii) which result in almost no bend (region (iii)) [6,7]. Only the 650 °C annealed layer I-V curve has an appearance slightly rectangular.

The steeper region (i) originates from an increased shunt conductivity (decreased shunt resistivity) that is due to either shunt paths in the cell or in the cell interconnects that bypass the cell junction without creating power.

The less steep region (ii) originates from an excessive series resistance in the cell, in the wiring, or in the electrical interconnections of the wiring.

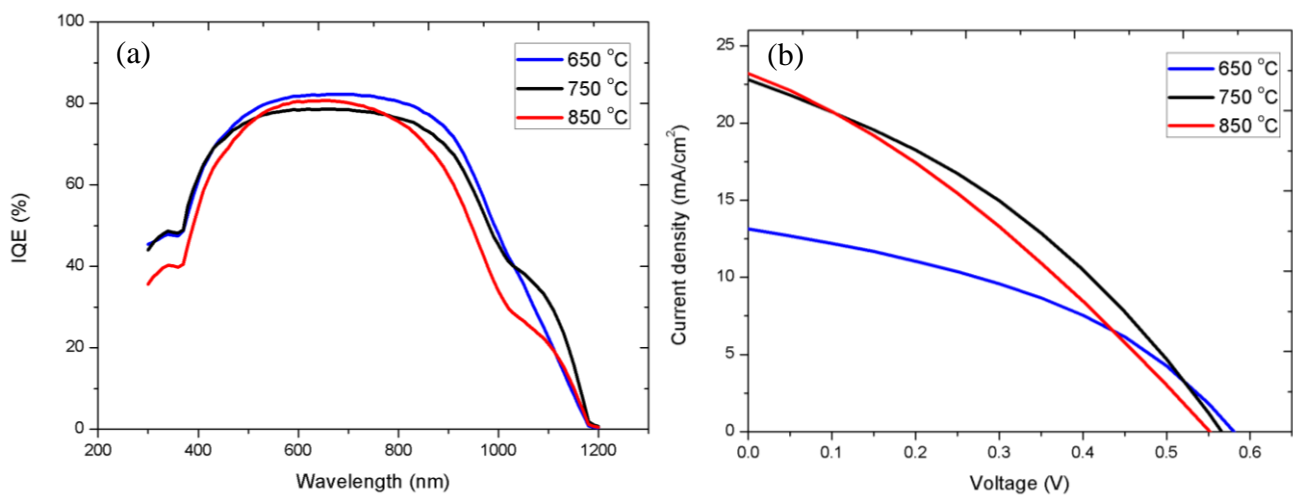


Figure V-10: (a) IQE spectra and (b) I-V curve for various annealing temperature for a RTA process during 5 min.

V.4.2. Conclusion

Due to the huge number of parameters that have to be considered, the complete optimized deposition process of our *DC* layer on the top of the Si solar cells is complex and not fully achieved yet. The annealing temperature is taken as an example to show the difficulties encountered. Passivation problems at the top of the cell (layer/cell interface) but also at the bottom as well as high series resistance and shunt conduction decreasing the performances of the system are evidenced. New depositions of those layers have to be carried out to confirm those first results. The layer should be deposited on 7x7 cm laser cut cells which would assure a more reproducible process.

V.5. Conclusion

In this work, our *DC* layers are deposited on industrial Si *SCs* in order to determine the additional efficiency obtained thanks to those layers. Both Tb-doped- and Tb-Yb co-doped layers are found to increase the cell efficiency by 15 % and 30 % respectively when compared to a cell topped with our undoped layer that is used as a reference because close to the standard anti-reflective layer usually used. The study of the annealing and deposition temperature is studied through the *PL* intensity. It was determined that a layer deposited at 500 °C and annealed at 650 °C has a *PL* intensity similar to a layer deposited at 200 °C and annealed at 850 °C. The temperatures thus involved will then not destroy the P-N junction.

This work also allow for an optimization of the deposition of our layers in order to adapt it as best to the Si *SCs* requirements. Several parameters have thus been studied but only the annealing temperature influence is detailed in this chapter. This example is used to outline the various issues encountered (passivation, shunt resistance, series resistance, ...) that have to be overcome before obtaining an efficient system.

Bibliography

- [1] A. Schütt, J. Carstensen, J.M. Wagner, H. Föll, Local Characterization of Co-Firing-Induced Inhomogeneities of Conventional mc-Si Solar Cells, (n.d.). <http://www.tf.uni-kiel.de/matwis/amat/publications/pdf/schcar2013a.pdf> (accessed July 12, 2016).
- [2] P.J. Richter, F.J. Bottari, D.C. Wong, Rapid Metallization Paste Firing of Crystalline Silicon Solar Cells, Inter PV. (2011). http://www.interpv.net/tech/tech_view.asp?idx=726&part_code=020080031&page=1.
- [3] J. Chen, Recent Developments on Silicon Based Solar Cell Technologies and their Industrial Applications, in: Energy Effic. Improv. Smart Grid Compon., INTECH, 2015. <http://www.intechopen.com/books/energy-efficiency-improvements-in-smart-grid-components/recent-developments-on-silicon-based-solar-cell-technologies-and-their-industrial-applications>.
- [4] S. Yerci, Rui Li, S.O. Kucheyev, T. van Buuren, S.N. Basu, L. Dal Negro, Visible and 1.54 μm Emission From Amorphous Silicon Nitride Films by Reactive Cosputtering, IEEE J. Sel. Top. Quantum Electron. 16 (2010) 114–123. doi:10.1109/JSTQE.2009.2032516.
- [5] E. San Andrés, A. del Prado, F.L. Martínez, I. Mártel, D. Bravo, F.J. López, Rapid thermal annealing effects on the structural properties and density of defects in SiO₂ and SiN_x:H films deposited by electron cyclotron resonance, J. Appl. Phys. 87 (2000) 1187. doi:10.1063/1.371996.
- [6] PVEducation, (n.d.). <http://www.pveducation.org/>.
- [7] Guide to Interpreting I-V Curves.pdf, (n.d.). <http://resources.solmetric.com/get/Guide%20to%20Interpreting%20I-V%20Curves.pdf> (accessed June 28, 2016).

Conclusion and perspectives

In this thesis work, we developed down-conversion (*DC*) and down-shifting (*DS*) layers destined to be topped on silicon solar cells in order to improve their efficiency. The frequency conversion processes (*DC* or *DS*) are enabled by doping of the SiN_x matrix with the couple of rare earth ions Tb^{3+} - Yb^{3+} and with the rare earth ion Tb^{3+} , respectively. The layers are deposited by radio-frequency reactive magnetron co-sputtering and their fabrication is compatible with the silicon PV industry.

In a first phase, the composition and the optical properties of the undoped matrix are studied as a function of the nitrogen ratio and the plasma pressure. The goal was to obtain a layer fulfilling the criteria required of a frequency conversion layer as well as of an anti-reflective one. Thus the layer has to have a high absorbance and low transmittance in the UV part of the spectrum (below 550 nm -above 2.25 eV-) and a low absorbance and high transmittance in the rest of the spectrum. A low reflectance on the whole spectrum is also required. Because of the monotony of the refractive index, the values of the absorbance and reflectance efficiencies are similar on the whole spectrum. In order to preserve the primary efficiency of the solar cell, the layer developed shading of the cell should be reduced to a minimum. Thus the high transmittance and low absorbance in the visible and IR parts of the spectrum are favored. The deposition parameters are fixed at 20 % nitrogen ratio and 3 mTorr plasma pressure.

In a second phase, the matrix is doped with terbium ions with the aim of obtaining a maximum intensity of photoluminescence of the Tb^{3+} peaks at 629 nm, 594 nm, 550 nm, and 493 nm. The values of the nitrogen ratio and plasma pressure previously mentioned lead to a maximum Tb^{3+} PL peak intensity that confirmed the choice of these parameters. The composition and optical properties among which photoluminescence are then studied as a function of the terbium target power density. An optimum is found for 0.45 W/cm² while concentration PL quenching is observed for higher values. The optimized layer obtained is compared to a $\text{SiO}_x\text{N}_y:\text{Tb}^{3+}$ layer from a previous study and found to transmit 2.14 times more light to the substrate (solar cell).

In a third phase, the matrix is doped with the couple of rare earth ions terbium and ytterbium, the system is optimized through the search for maximum photoluminescence. The composition and optical properties of the system are studied as a function of the power densities of the terbium and ytterbium targets. An optimum is found for 1.2 W/cm² and 0.2 W/cm² respectively, and concentration quenching is observed for higher values in both cases. The optimized layer obtained is compared to a $\text{SiO}_x\text{N}_y:\text{Tb}^{3+}$ - Yb^{3+} layer from a previous study and found to transmit 8.6 times more light to the substrate (solar cell).

A multilayer system composed of a stack of alternating sublayers of the ytterbium- or terbium-doped matrix is studied as a way to control more easily the rare earth concentration in each sublayer. Here again, composition and optical properties are analyzed, and the power density on the terbium and ytterbium targets as well as the sublayers thickness are optimized through the search of a maximum photoluminescence intensity. The optimized values are 2.85 W/cm² and 0.15 W/cm² power densities on the terbium and ytterbium targets respectively and a thickness of 1.75 nm for

both the Tb-doped- and Yb-doped- sublayers. The optimized multilayer obtained is compared to the optimized monolayer and found to transmit 1.6 times more light to the substrate (solar cell).

The energy transfers taking place in our systems have been determined. The matrix first absorbs the high energy photons and transfers them to the high energy levels and band of the terbium ions ($4f^75d$ energy band and the 4F_7 and $^5H_{6,7,8}$ energy levels) thanks to the electronic transfer between the conduction band and the defects level ($=N^{\cdot}$) and/or the pair electron/hole recombination over the bandgap of the matrix. The terbium ions de-excite non-radiatively toward the 5D_4 level from which the radiative transitions (*DS* process) or the quantum cutting (*DC* process) toward two ytterbium ions take place.

Finally, our optimized layers are adapted to and deposited on silicon solar cells and efficiency measurements are performed. This study show that depositing at 500 °C and annealing at 650 °C lead to similar Yb *PL* peak intensities than depositing at 200 °C and annealing at 850 °C. As annealing at 850 °C for any amount of time damages the PN-junction of the cell, the first process is chosen. Various parameters are also varied to improve the efficiency gain. The analyze of an example, demonstrated the difficulties encountered due to passivation process of both the layers and the contacts which could lead to losses mechanisms such as shunt conductance, series resistance, ... A comparison between the Tb-Yb co-doped and the undoped layers showed an increase by 30% of the cell efficiency while topped with the Tb-Yb co-doped layer.

Thus our objectives to develop Tb-doped- and Tb-Yb co-doped- layers that have a higher *PL* intensity of the Tb^{3+} and Yb^{3+} peaks respectively than the Tb-doped- and Tb-Yb co-doped- SiO_xN_y layers developed during the precedent work of Y-T An are reached. In addition, we demonstrate that our layers also transmit more light to the solar cell than those of the precedent work. The main objective is partially reached as we deposited our optimized (down-conversion and anti-reflective) layers on industrial solar cells. However, the coupling of those layers with the silicon solar cells is still a work in progress.

From this point, several studies may be undertaken:

- The deposition of our optimized frequency conversion layers on industrial solar cells has to be continued in order to develop layers that improve the efficiency of the cell without hindering its usual operating. For this purpose, a more reproducible fabrication (cell + conversion layer) has to be used such as laser cutting 7×7 cm² cells that can be inserted in our co-sputtering machine in order to improve the contacts formation at the front and the back of the cell and increase the reliability of the various measurements performed. In this case, the comparison between the conversion layers (*DS*, *DC* mono- and multi-layer) with the undoped one has to be redone to confirm our current results.
- The frequency conversion layers optimized during this work may be coupled with silver nanoparticles that would increase absorption of the UV photons thanks to their plasmonic effect. The silver nanoparticles are deposited on top of the wafer and covered by the frequency conversion layer. The size and distribution of the nanoparticles control the wavelength at which the plasmonic effect takes place. This way, this wavelength may be

tuned to fit the absorption wavelength of the terbium ions and thus enhanced the conversion process.

- Another approach would be to use a matrix with aluminum that allows for a very high incorporation of rare earths before concentration quenching and clustering and thus may increase the conversion efficiency.
- The phenomena that happen during annealing for various temperatures, time and processes used may be determine to better understand and control the layers annealing.
- The behavior of the various species involved in the plasma during the deposition in the co-sputtering machine would be also interesting to study in order to better control the deposition of the layers.

Annex 1: Matrix representation and formulation

The sample is modeled as shown in *Figure A1-1* by a semi-infinite substrate topped by an isotropic thin film of thickness, d , with or without roughness. The roughness is modeled by a layer composed of the thin film material mixed with air following the Effective Medium Approximations (*EMA*), on top of the thin layer. The refractive indexes of the medium (air, *EMA*, thin layer and substrate) are mentioned as n_{air} , n_{EMA} , n_{tl} , and n_{sub} .

The sample is illuminated by an electro-magnetic (*EM*) monochromatic wave which wavelength may vary over a 300 to 1200 nm range. This wave is described by an electric field vector, \vec{E} , a magnetic field factor, \vec{B} , and the wave factor, \vec{k} , perpendicular to one another. The calculations are made for a transverse electric mode (*TE*) wave inducing $E_x = E_z = 0$, and $E_y \neq 0$. The incident angle of the wave is noted θ_{inc} .

The electric field amplitude is of the form:

$$E_y(x) = E(x)e^{i(\omega t - \beta z)} \quad A1-1$$

With β is the z component and κ is the x component of the propagation wave vector, and ω the angular frequency.

Part of the incident light is transmitted within the layer and part is reflected back. So the electric field is a superposition of the two waves traveling opposite to each other in the positive and negative directions of x , E_+ and E_- :

$$E_y(x) = E_+(x)e^{-i\kappa_x x} + E_-(x)e^{i\kappa_x x} = A(x) + B(x) \quad A1-2$$

With $\pm\kappa_x$ is the x component of the wave factor, $A(x)$ and $B(x)$ are constant in the positive and negative direction of x .

$A(x)$ and $B(x)$ are considered at five positions at the top and bottom of each interfaces $x = 0$, $x = d'$, and $x = d$ as shown in *Figure A1-1*. They may then be written as:

$$A_1 = A(x = 0^-) \text{ and } B_1 = B(x = 0^-)$$

$$A'_2 = A(x = 0^+) \text{ and } B'_2 = B(x = 0^+)$$

$$A_2 = A(x = d'^-) \text{ and } B_2 = B(x = d'^-)$$

$$A'_3 = A(x = d'^+) \text{ and } B'_3 = B(x = d'^+)$$

$$A_3 = A(x = d^-) \text{ and } B_3 = B(x = d^-)$$

$$A'_4 = A(x = d^+) \text{ and } B'_4 = B(x = d^+)$$

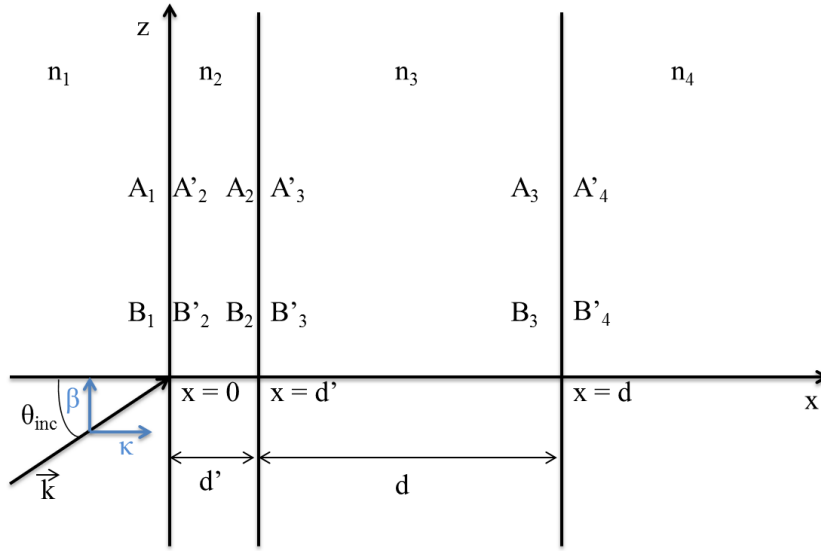


Figure A1_1: Thin layer sample model.

The $A(x)$ and $B(x)$ are thus no longer continuous at the interfaces. The amplitude of the field before and after the interfaces can be represented as column vectors and linked by:

$$\begin{aligned}
 \begin{pmatrix} A_1 \\ B_1 \end{pmatrix} &= D_1^{-1} D_2 \begin{pmatrix} A'_2 \\ B'_2 \end{pmatrix} \\
 \begin{pmatrix} A'_2 \\ B'_2 \end{pmatrix} &= P_2 \begin{pmatrix} A_2 \\ B_2 \end{pmatrix} = \begin{pmatrix} e^{i\Phi_2} & 0 \\ 0 & e^{-i\Phi_2} \end{pmatrix} \begin{pmatrix} A_2 \\ B_2 \end{pmatrix} \\
 \begin{pmatrix} A_2 \\ B_2 \end{pmatrix} &= D_2^{-1} D_3 \begin{pmatrix} A'_3 \\ B'_3 \end{pmatrix} \\
 \begin{pmatrix} A'_3 \\ B'_3 \end{pmatrix} &= P_3 \begin{pmatrix} A_3 \\ B_3 \end{pmatrix} = \begin{pmatrix} e^{i\Phi_3} & 0 \\ 0 & e^{-i\Phi_3} \end{pmatrix} \begin{pmatrix} A_3 \\ B_3 \end{pmatrix} \\
 \begin{pmatrix} A_3 \\ B_3 \end{pmatrix} &= D_3^{-1} D_4 \begin{pmatrix} A'_4 \\ B'_4 \end{pmatrix}
 \end{aligned}
 \tag{A1-3}$$

Where D_1 , D_2 , D_3 , and D_4 are the dynamical matrices of the wave for the different media as describe above and given by:

$$\begin{aligned}
 D_i &= \begin{pmatrix} 1 & 1 \\ \frac{\kappa_i}{k_0} & -\frac{\kappa_i}{k_0} \end{pmatrix} \\
 D_i^{-1} &= \begin{pmatrix} \frac{1}{2} & \frac{1}{2} \frac{k_0}{\kappa_i} \\ \frac{1}{2} & -\frac{1}{2} \frac{k_0}{\kappa_i} \end{pmatrix}
 \end{aligned}
 \tag{A1-4}$$

For TE waves

$$D_i = \begin{pmatrix} \frac{\kappa_i}{k_0 n_i} & \frac{\kappa_i}{k_0 n_i} \\ n_i & -n_i \end{pmatrix} \quad \text{For } TM \text{ waves} \quad A1-5$$

$$D_i^{-1} = \begin{pmatrix} \frac{1}{2} \frac{n_i k_0}{\kappa_i} & \frac{1}{2n_i} \\ \frac{1}{2} \frac{n_i k_0}{\kappa_i} & -\frac{1}{2n_i} \end{pmatrix}$$

With $i = 1, 2, 3$, and 4 . β and κ are the z and the x components of the wave propagation vector, respectively.

θ_i is the wave angle in each medium and related to κ_i by:

$$\beta = n_i \frac{\omega}{c} \sin \theta_i \quad \text{and} \quad \kappa_i = n_i \frac{\omega}{c} \cos \theta_i \quad A1-6$$

P_2 and P_3 are the propagation matrices which account for the propagation of the wave through the media 2 and 3 given by:

$$P_i = \begin{pmatrix} e^{i\kappa_i l} & 0 \\ 0 & e^{-i\kappa_i l} \end{pmatrix} \quad A1-7$$

With $l = d'$ in the medium 2 and $l = d$ in the medium 3.

Knowing all the previous relations, the amplitude of the field going through the whole sample can be expressed as:

$$\begin{pmatrix} A_1 \\ B_1 \end{pmatrix} = D_1^{-1} D_2 P_2 D_2^{-1} D_3 P_3 D_3^{-1} D_4 \begin{pmatrix} A'_4 \\ B'_4 \end{pmatrix} \quad A1-8$$

Or

$$\begin{pmatrix} A_1 \\ B_1 \end{pmatrix} = M \begin{pmatrix} A'_4 \\ B'_4 \end{pmatrix} = \begin{pmatrix} m_{11} & m_{12} \\ m_{21} & m_{22} \end{pmatrix} \begin{pmatrix} A'_4 \\ B'_4 \end{pmatrix} \quad A1-9$$

Thus the column vectors that represent the plane wave in each medium are related by a product of 2×2 matrices in sequence. Each sides of an interface are linked by a dynamical matrix and the propagation within the media is modeled by a propagation matrix.

In our study, the silicon wafer (medium 4) is considered as semi-infinite thus $B'_4 = 0$. The Equation A1-9 may then be written as:

$$\begin{pmatrix} A_1 \\ B_1 \end{pmatrix} = \begin{pmatrix} m_{11} & m_{12} \\ m_{21} & m_{22} \end{pmatrix} \begin{pmatrix} A'_4 \\ 0 \end{pmatrix} \quad 163$$

The reflection and transmission coefficients of the total sample can then be determined:

$$r_{glob} = \left(\frac{B_1}{A_1} \right)_{B'_4=0} \quad \text{A1-11}$$

And

$$t_{glob} = \left(\frac{A'_4}{A_1} \right)_{B'_4=0} \quad \text{A1-12}$$

Thanks to the *Equation A1-10*, we obtain:

$$r_{glob} = \frac{m_{21}}{m_{11}} \quad \text{A1-13}$$

And

$$t_{glob} = \frac{1}{m_{11}} \quad \text{A1-14}$$

To obtain the reflectance and transmittance, the following equations may be applied:

$$R = |r_{glob}|^2 = \left| \frac{m_{21}}{m_{11}} \right|^2 \quad \text{A1-15}$$

And

$$T = \frac{\kappa_4}{\kappa_1} |t_{glob}|^2 = \frac{\kappa_4}{\kappa_1} \left| \frac{1}{m_{11}} \right|^2 \quad \text{A1-16}$$

From this point the absorption, A, may be calculated from:

$$A = 1 - T - R \quad \text{A1-17}$$

Annex 2: Single emitter modeling

The emission of a film is influenced by several factors such as its thickness, the emitters distribution, their population density in the ground and excited states, the lifetime of the carriers, the absorption, and the emission cross-sections. Ellipsometric obtained data as well as data from literature were used in the model developed. This model is based on the same 2x2 matrices as in *Annex 1* but transposed in 3x3 matrices as employed by Boucher et al. [20]. The example in the following is valid for all the other matrices:

$$P_i = \begin{pmatrix} e^{ik_i l} & 0 \\ 0 & e^{-ik_i l} \end{pmatrix} \longrightarrow P_i = \begin{pmatrix} e^{ik_i l} & 0 & 0 \\ 0 & e^{-ik_i l} & 0 \\ 0 & 0 & 1 \end{pmatrix}$$

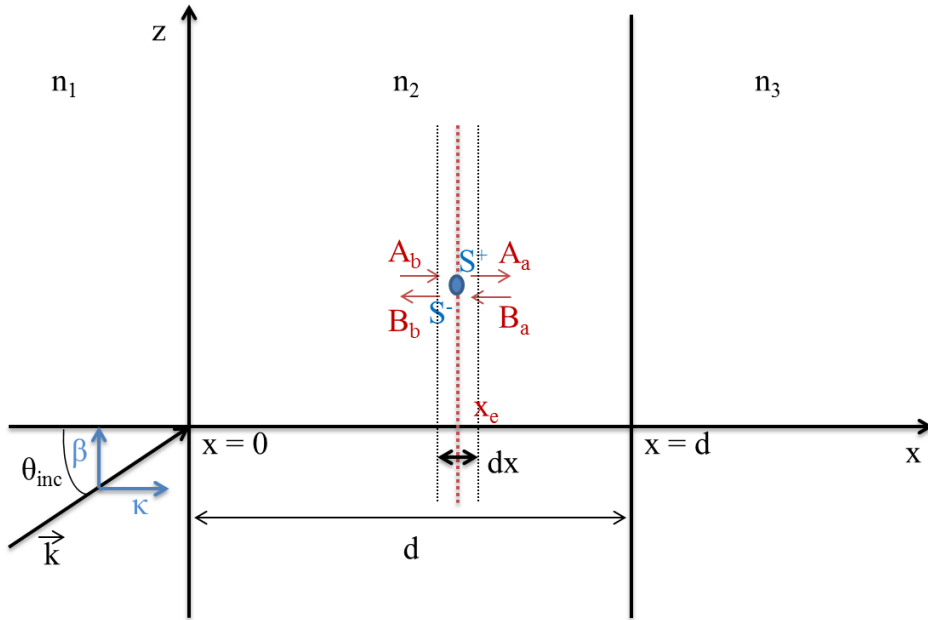


Figure A2_1: Single emitter in the thin film at x_e

We consider now a single emitter placed at a position x_e in the layer (medium 2) (*Figure A2-1*). The emitter is considered to emit in the two directions of x (positive and negative). The amplitude of the waves is noted S^+ and S^- respectively. Indeed, the emitter is constructed as an isotropic source composed of three electric dipole sources as described by Benisty et al. [18].

In these conditions, we write the waves amplitudes before and after the emitter (following the x axe) as:

$$A_b = A(x = x_e^-) \text{ and } B_b = B(x = x_e^-)$$

$$A_a = A(x = x_e^+) \text{ and } B_a = B(x = x_e^+)$$

A2-1

At $x = x_e$, we have:

$$\begin{aligned} A_a &= A_b + S^+ \\ B_a &= B_b - S^- \end{aligned} \quad \text{A2-2}$$

Those equations highlight that the amplitude of the waves traveling in the positive and negative directions is a combined contribution of the pump (light illuminating the sample) and the emitter.

The field amplitude of the wave before and after the emitter can be linked using the matrix formulation:

$$\begin{pmatrix} A_b \\ B_b \\ 1 \end{pmatrix} = \begin{pmatrix} 1 & 0 & -S^+ \\ 0 & 1 & +S^- \\ 0 & 0 & 1 \end{pmatrix} \begin{pmatrix} A_a \\ B_a \\ 1 \end{pmatrix} \quad \text{A2-3}$$

As the emitter is placed in the middle of the layer, its amplitude can be linked to the field amplitude at the interface with the air ($x = 0^+$) and at the interface with the substrate ($x = d^-$) by the propagation matrix in the layer:

$$\begin{pmatrix} A'_2 \\ B'_2 \\ 1 \end{pmatrix} = \begin{pmatrix} e^{ik_2x_e} & 0 & 0 \\ 0 & e^{-ik_2x_e} & 0 \\ 0 & 0 & 1 \end{pmatrix} \begin{pmatrix} 1 & 0 & -S^+ \\ 0 & 1 & +S^- \\ 0 & 0 & 1 \end{pmatrix} \begin{pmatrix} e^{ik_2(d-x_e)} & 0 & 0 \\ 0 & e^{-ik_2(d-x_e)} & 0 \\ 0 & 0 & 1 \end{pmatrix} \begin{pmatrix} A_2 \\ B_2 \\ 1 \end{pmatrix} \quad \text{A2-4}$$

Which simplified gives:

$$\begin{pmatrix} A'_2 \\ B'_2 \\ 1 \end{pmatrix} = \begin{pmatrix} e^{ik_2d} & 0 & -e^{-ik_2d}S^+ \\ 0 & e^{-ik_2d} & e^{-ik_2d}S^- \\ 0 & 0 & 1 \end{pmatrix} \begin{pmatrix} A_2 \\ B_2 \\ 1 \end{pmatrix} \quad \text{A2-5}$$

Following the same matrix principle as described above the amplitudes of the field at the interface but inside the layer can be linked to the amplitudes of the field at the interfaces but outside of the layer (roughness layer and substrate) using the dynamical matrices D_i and D_i^{-1} :

$$\begin{pmatrix} A_1 \\ B_1 \\ 1 \end{pmatrix} = D_1^{-1}D_2 \begin{pmatrix} e^{ik_2d} & 0 & -e^{-ik_2d}S^+ \\ 0 & e^{-ik_2d} & e^{-ik_2d}S^- \\ 0 & 0 & 1 \end{pmatrix} D_2^{-1}D_3 \begin{pmatrix} A'_3 \\ B'_3 \\ 1 \end{pmatrix} \quad \text{A2-6}$$

This global matrix formulation is applied for each wavelength separately. Hence, when we consider a wavelength emitted by the emitter, the input wave $A_1 = 0$. Indeed, the incident wavelength is different from the emitted one. The wave B_1 going out of the sample toward the air is only due to the wave produced by the emitter and that goes in the negative direction of x . Therefore, we can

$$\begin{pmatrix} 0 \\ B_0^- \\ 1 \end{pmatrix} = D_1^{-1} D_2 \begin{pmatrix} e^{ik_2d} & 0 & -e^{-ik_2d} S^+ \\ 0 & e^{-ik_2d} & e^{-ik_2d} S^- \\ 0 & 0 & 1 \end{pmatrix} D_2^{-1} D_3 \begin{pmatrix} B_s^+ \\ 0 \\ 1 \end{pmatrix} \quad A2-7$$

note $B_1 = B_0^-$. In addition, the outgoing wave toward the substrate is also only due to the wave produced by the emitter, thus $A_3^+ = B_s^+$. As the substrate is a semi-infinite medium there is no backward wave and $B_3^- = 0$. The last equation takes the form:

A global matrix M is obtained:

$$\begin{pmatrix} 0 \\ B_0^- \\ 1 \end{pmatrix} = \begin{pmatrix} m_{11} & m_{12} & m_{13} \\ m_{21} & m_{22} & m_{23} \\ 0 & 0 & 1 \end{pmatrix} \begin{pmatrix} B_s^+ \\ 0 \\ 1 \end{pmatrix} \quad A2-8$$

We can thus calculate the positive and negative travelling emitted fields by:

$$B_s^+ = -\frac{m_{13}}{m_{11}} \quad A2-9$$

And

$$B_0^- = \frac{m_{23}m_{11} - m_{13}m_{21}}{m_{11}} \quad A2-10$$

The intensities of the emitted waves traveling in opposite directions are then calculated with the following equations:

$$I_s^+ = \frac{c\epsilon_0 n |B_s^+|^2}{2} \quad A2-11$$

And

$$I_s^- = \frac{c\epsilon_0 n |B_0^-|^2}{2} \quad A2-12$$

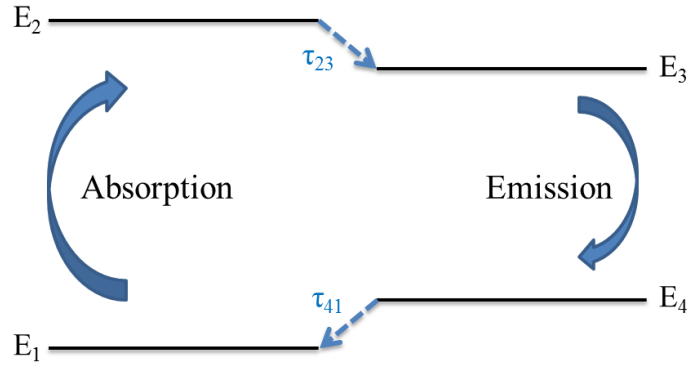


Figure A2_2: 4 levels system.

In order to calculate the emission intensity of the N emitters, the population rate equations have to be known. To estimate the population density, the absorption and emission mechanisms are described by a four levels system (Figure A2-2). After the absorption, a non-radiative de-excitation takes place followed by a spontaneous or stimulated emission (with $E_{abs} > E_{em}$) and another non-radiative de-excitation to come back in the initial energy level. The emission does not happen immediately, the time the electron stays in the E_3 energy level before emission is the carriers' lifetime. The population rate equations are:

$$\frac{dN_1}{dt} = -\sigma_{abs}\phi N_1 + \frac{N_4}{\tau_{41}} \quad A2-13$$

$$\frac{dN_2}{dt} = \sigma_{abs}\phi N_1 - \frac{N_2}{\tau_{23}} \quad A2-14$$

$$\frac{dN_3}{dt} = \frac{N_2}{\tau_{23}} - \left(\sigma_{em}\phi + \frac{1}{\tau_{34}} \right) N_3 \quad A2-15$$

$$\frac{dN_4}{dt} = -\frac{N_4}{\tau_{41}} + \left(\sigma_{em}\phi + \frac{1}{\tau_{34}} \right) N_3 \quad A2-16$$

With σ_{abs} and σ_{em} the absorption and emission cross-sections in m^2 , respectively, τ_{21} the transmission time from level 1 to level 2, τ_{23} , τ_{34} , and τ_{41} the decay times from their respective levels, and ϕ the photon flux (photons/ m^2).

The population excited by the standing wave in the layer has a decaying and sinusoidal profile depth following the shape of the pump intensity profile with depth. We consider a sublayer of the film smaller than the period of the incident pump standing wave, dx . The number of emitters n_e in excited state in this sublayer dx can be estimated by:

$$N_e = N_3(x_e) S dx \quad A2-17$$

With $N_3(x_e)$ the emitters concentration obtained at stationary regime and S the surface of the light beam so the volume of interaction is $V = S dx$.

Annex 3: List of the bonds between the Si, N, H, and O elements and their bands wavenumber in a SiO_xN_y:H material.

Position (cm ⁻¹)	Mode	Name	Bond
3500	stretching		N-H ₂ [21]
3450	stretching		SiN-H ₂ [22]
3360	stretching		N-H [21,23]
3350	stretching		Si ₂ N-H [22]
3340	stretching		N-H [24,25]
3320	stretching		N-H [26]
2220			N ₃ -Si-H [27]
2190	stretching		Si-H [21]
2180	stretching		Si-H [26]
2170			N ₂ H-Si-H [27]
2160			Si-H [24]
2150	stretching		N ₂ Si-H [22]
2150	stretching		NSi-H ₂ [22]
2150	stretching		Si-H [25]
2150	stretching		N ₂ Si-H [23]
2140			N ₂ Si-Si-H & NHSi Si-H [27]
2140			Si-H ₃ [22]
2100			Si ₂ N Si-H [27]
2100	stretching		Si-H ₂ [22]
2090			Si-H [22]
2090	stretching		Si-H ₂ [23]
2060			Si ₂ H-Si-H [27]
2000			Si ₃ Si-H [27]
1550	bending		Si-N-H ₂ [22,26]
1215-1256	stretching	LO ₃	Si-O [28]
1200	bending		N-H [25]

1180	bending		N-H [26]
1170	rocking		Si ₂ N-H [22]
1165	rocking		Si ₂ N-H [23]
1140	bending		N-H [21]
1060	asymmetric stretching	TO ₃	Si-O [29]
1050	asymmetric stretching	TO ₃	Si-O
1050-1070	stretching	LO	Si-N [30]
1050	symmetric stretching	LO	Si-N ₄ [21]
1030	stretching	LO	Si-N [26]
907			Si-H ₃ [22]
890			Si-H ₂ [22]
875			Si-H [22]
845			Si-H ₂ [22]
880	stretching	TO	Si-N [26]
860		TO	Si-N [29]
850		TO	Si-N ₄ [24]
840	symmetric stretching	TO	Si-N [25]
810-840		TO	Si-N [31]
650	wag-rocking		Si-H [25]
645	wagging		Si-H [23]
630	wagging		Si-H [22]
630	wagging		Si-H ₂ [22]
630	wagging		Si-H ₃ [22]
400-600	breathing		Si-N [23]
480	breathing		Si-N [26]
475	symmetric stretching		Si-N [25]

Résumé

Cette thèse porte sur le développement de couches à conversion de fréquence basse à base de silicium permettant une augmentation du rendement des cellules solaires au silicium. Des couches de SiN_x dopées avec le couple de terres rares terbium et ytterbium sont élaborées par co-pulvérisation cathodique magnétron radiofréquence. Les propriétés optiques de la matrice hôte non dopée sont étudiées avant le dopage. Elle est ainsi optimisée (via les paramètres de dépôt) dans le but d'obtenir une matrice propice à la conversion en fréquence tout en étant antiréfléctive. Les systèmes matrice dopée terbium puis matrice dopée terbium et ytterbium sont ensuite optimisés pour obtenir une émission de photoluminescence des ions terbium et ytterbium respectivement la plus intense possible après une excitation dans l'*UV*. Les mécanismes de transfert de l'énergie entre la matrice et les ions terbium puis entre ces derniers et les ions ytterbium sont détaillés. Le transfert d'énergie coopératif qui a lieu entre les ions terbium et ytterbium lors de la conversion basse (ou down conversion) est très dépendant de la distance entre les ions. Ainsi, un système multicouches alternant les couches dopées avec des ions terbium et des ions ytterbium est développé pour permettre l'excitation d'un plus grand nombre d'ions Yb^{3+} et donc augmenter l'efficacité du système. L'influence de cette approche sur les propriétés des couches à conversion de fréquence et sur le processus de conversion basse est détaillée. Enfin, une étude sur les couches optimisées déposées sur des cellules solaires Si produites industriellement est menée pour déterminer l'influence de ces couches sur l'efficacité des cellules solaires.

Mots clés : Pulvérisation cathodique, Conversion de fréquence, Nitrure de silicium, Terres rares, Cellules solaires au silicium, Photoluminescence, Couche mince, Transfert d'énergie

Abstract

This thesis work focuses on the development of silicon based down-conversion layers allowing the improvement of the silicon solar cells efficiency. SiN_x terbium and ytterbium co-doped layers are produced by radio-frequency reactive magnetron co-sputtering. The optical properties of the undoped SiN_x host matrix are investigated and optimized prior doping to obtain a layer suitable for the down-conversion process and keeping anti-reflective properties. The systems with the terbium-doped matrix and terbium-ytterbium co-doped matrix are optimized with the aim of achieving an intense photoluminescence emission from Tb^{3+} ions and Yb^{3+} ions respectively through a wide UV domain excitation. The energy transfer mechanisms between the matrix and the terbium ions and then between those last ions and the ytterbium ones are detailed. The cooperative energy transfer taking place between Tb^{3+} - Yb^{3+} ions involved in the down-conversion process is highly dependent on the distance between the two ions. Thus, in order to achieve a higher quantum efficiency, a multilayer approach based on alternating stack of Tb- and Yb-doped sublayers has been developed to increase the number of excited Yb^{3+} ions. The effect of this approach on the frequency conversion process is discussed in details. Lastly, the optimized layers are deposited on industrial silicon solar cells in order to determine the influence of those layers on the solar cells efficiency.

Key words: Sputtering, Down-conversion, Silicon nitride, Rare earths, Silicon solar cells, Photoluminescence, Thin film, Energy transfer